

REPORT DOCUMENTATION PAGE				Form Approved OMB No. 0704-0188	
Public reporting burden for this collection of information is estimated to average 1 hour per response, including the time for reviewing instructions, searching existing data sources, gathering and maintaining the data needed, and completing and reviewing this collection of information. Send comments regarding this burden estimate or any other aspect of this collection of information, including suggestions for reducing this burden to Department of Defense, Washington Headquarters Services, Directorate for Information Operations and Reports (0704-0188), 1215 Jefferson Davis Highway, Suite 1204, Arlington, VA 22202-4302. Respondents should be aware that notwithstanding any other provision of law, no person shall be subject to any penalty for failing to comply with a collection of information if it does not display a currently valid OMB control number. <b>PLEASE DO NOT RETURN YOUR FORM TO THE ABOVE ADDRESS.</b>					
1. REPORT DATE (DD-MM-YYYY) 21-01-2010		2. REPORT TYPE Doctoral Thesis		3. DATES COVERED (From - To)	
4. TITLE AND SUBTITLE  Charging Effects on Fluid Stream Droplets for Momentum Exchange Between Spacecraft				5a. CONTRACT NUMBER	
				5b. GRANT NUMBER	
				5c. PROGRAM ELEMENT NUMBER	
6. AUTHOR(S) Thomas B. Joslyn (University of Colorado)				5d. PROJECT NUMBER	
				5f. WORK UNIT NUMBER 50260542	
7. PERFORMING ORGANIZATION NAME(S) AND ADDRESS(ES)  Air Force Research Laboratory (AFMC) AFRL/RZSA 10 E. Saturn Blvd. Edwards AFB CA 93524-7680				8. PERFORMING ORGANIZATION REPORT NUMBER  AFRL-RZ-ED-TP-2010-027	
9. SPONSORING / MONITORING AGENCY NAME(S) AND ADDRESS(ES)  Air Force Research Laboratory (AFMC) AFRL/RZS 5 Pollux Drive Edwards AFB CA 93524-7048				10. SPONSOR/MONITOR'S ACRONYM(S)	
				11. SPONSOR/MONITOR'S NUMBER(S) AFRL-RZ-ED-TP-2010-027	
12. DISTRIBUTION / AVAILABILITY STATEMENT  Approved for public release; distribution unlimited (PA #10048).					
13. SUPPLEMENTARY NOTES For submission to the Graduate Faculty of the University of Colorado at Colorado Springs, CO.					
14. ABSTRACT  This dissertation presents the results of research on a novel satellite propulsion concept that relies on the constant transfer of momentum through projection of silicon oil droplet streams through space. The system is primarily applicable to satellites flying side-by-side in formation that require a constant distance between them in order to conduct certain missions such as interferometric synthetic aperture radar observations. Rational for selection of the silicone oil DC705 as the best working fluid is presented. Droplet size, velocity, and spacing needed for station keeping of various satellite mass and separation distance combinations is evaluated. Droplet streams of diameters demonstrated in this study and speeds demonstrated in past research can satisfy propulsion needs of reasonably sized satellites in any earth orbit with at least a kilometer of separation. A continuous droplet stream system requires an order of magnitude less mass than comparable electric propulsion systems and two orders of magnitude less power. The focus of this study is droplet charging in space due to various mechanisms associated with ambient plasma and photoemissions.					
15. SUBJECT TERMS					
16. SECURITY CLASSIFICATION OF:			17. LIMITATION OF ABSTRACT	18. NUMBER OF PAGES	19a. NAME OF RESPONSIBLE PERSON
a. REPORT	b. ABSTRACT	c. THIS PAGE			Dr. Andrew Ketsdever
Unclassified	Unclassified	Unclassified	SAR	196	19b. TELEPHONE NUMBER (include area code) N/A

**CHARGING EFFECTS ON FLUID STREAM  
DROPLETS FOR MOMENTUM EXCHANGE  
BETWEEN SPACECRAFT**

by

THOMAS B. JOSLYN

A dissertation submitted to the Graduate Faculty of the

University of Colorado at Colorado Springs

in partial fulfillment of the

requirements for the degree of

Doctorate in Philosophy

Department of Mechanical and Aerospace Engineering

2009



This dissertation for Doctorate of Philosophy degree by  
Thomas B. Joslyn  
has been approved for the  
department of Mechanical and Aerospace Engineering  
by

---

Andrew Ketsdever, Chair

---

Scott Trimbolli

---

James Stevens

---

Linda Krause

---

Steven Tragesser

---

Date

## Abstract

This dissertation presents the results of research on a novel satellite propulsion concept that relies on the constant transfer of momentum through projection of silicon oil droplet streams through space. The system is primarily applicable to satellites flying side-by-side in formation that require a constant distance between them in order to conduct certain missions such as interferometric synthetic aperture radar observations. Rational for selection of the silicone oil DC705 as the best working fluid is presented. Droplet size, velocity, and spacing needed for station keeping of various satellite mass and separation distance combinations is evaluated. Droplet streams of diameters demonstrated in this study and speeds demonstrated in past research can satisfy propulsion needs of reasonably sized satellites in any earth orbit with at least a kilometer of separation. A continuous droplet stream system requires an order of magnitude less mass than comparable electric propulsion systems and two orders of magnitude less power.

The focus of this study is droplet charging in space due to various mechanisms associated with ambient plasma and photoemissions. Droplet charging is modeled analytically and numerically, primarily with the in-space material charging software called NASCAP. Predicted low earth orbit (LEO) charging is less than a few volts relative to the ambient plasma. Droplets in GEO charge slightly positive in the sun and slightly negative in eclipse during nominal geomagnetic conditions. During high geomagnetic activity, droplets in GEO reach several kilovolts negative potential, which is sufficient to induce Coulomb break-up. Eclipsed polar orbiting droplets reach negative charge potentials of -26V. Lorentz forces will impair droplet collection in the GEO and polar environments but can be mitigated by producing larger droplets and using faster transit speeds between satellites.

A numerical model was developed to simulate droplet stream dispersion caused by electric fields acting between charged droplets. This dispersion can be abated substantially by increasing droplet spacing, which is possible using solenoid valve technology evaluated in laboratory testing. Laboratory charging of DC705 using an extreme ultraviolet lamp in vacuum was conducted. Droplet charge potentials measured in more than 200 experiments were within 4% of NASCAP photoemission simulation predictions. This close correlation indicates that the DC705 material properties determined in this study and the NASCAP algorithm are appropriate for prediction of photoemission charging of DC705.

## Acknowledgements

Credit for devising the concept of using fluid stream propulsion to maintain a set distance between side-by-side formation satellites belongs to two individuals at the University of Colorado. Dr. Steve Tragesser realized the need for such a propulsion system and Dr. Andrew Ketsdever realized that momentum transfer with fluid streams could satisfy that need.

Many individuals contributed to my pursuit of identifying and then analyzing the challenges associated with this topic. My advisor Dr. Andrew Ketsdever provided guidance and instruction every step of the way, with both this topic and a previous one that proved to be a dead end. Taylor Lilly has also provided technical support and advice with both topics and helped troubleshoot problems from computer code to vacuum chamber components. Dr. Linda Krause of the Physics Department at the U.S. Air Force Academy was very helpful with charge modeling and learning to use NASCAP. Dr. Victoria Davis at SAIC was also helpful in understanding the capabilities, limitations and intricacies of NASCAP.

Several research assistants have also helped me at various times: Jeff Atkinson with droplet generation, Jordan Olliges with Labview and with my previous topic, Barry Cornell with vacuum chamber operation, Sean Hammerlan with high-speed camera operation, and Shawn Laabs with Thermal Desktop. Ron Wilkinson, Calvin Roberts and Steve Jernigan provided the advice and skill needed to build and operate dozens of components and instruments for various experiments.

My work was supported by two organizations within the Air Force: The Astronautics Department at the Air Force Academy sponsored my PhD slot and I am very grateful to General (ret.) Mike DeLorenzo and Col Martin France who allowed me the opportunity to pursue it. Air Force Research Lab (Propulsion Directorate: Advanced Concepts Division) provided funding for the equipment and materials needed to carry out experimentation in this study.

My deepest debt of gratitude is to my family, especially my two sons, Ben and Taylor, who have sacrificed countless irreplaceable hours of quality time with Dad and endured many boring weekend hours in the lab “with” Dad. Your love, support and patience is truly appreciated!

## Table of Contents

CHARGING EFFECTS ON FLUID STREAM DROPLETS FOR MOMENTUM EXCHANGE BETWEEN SPACECRAFT	i
Abstract	iv
Acknowledgements	v
Tables	ix
Figures	x
Chapter 1: Introduction and Related Research	1
A. Motivation for Tandem Satellites	2
B. Fluid Selection and Droplet Generation	4
C. System Performance and Comparison with Ion Engines	8
D. Summary of Non-Charging Impediments to Droplet Stream Propulsion	12
E. Relevance of Droplet Charging to Droplet Stream Propulsion	13
Chapter 2: Analytic Models of Charging of Droplets in Space	14
A. Characterizing the LEO and Auroral Charging Environments	14
B. Characterizing the Geosynchronous Charging Environment	21
C. Space Charging Theory	23
D. Space Charging Theory Applied to Silicone Oil Droplets	29
E. Droplet Charge Prediction by Analytic Methods	32
F. Properties Affecting Secondary Emission of Electrons	39
G. Photoemission of Electrons in DC705	48
Chapter 3: Numerical Charging Simulations	51
A. NASA Charging Analyzer Program (NASCAP) Limitations	52

B.	Material Properties in NASCAP	55
C.	Results of GEO Simulations	61
D.	Results of LEO and Auroral Simulations	69
E.	Summary of Droplet Charging in LEO, GEO, and Auroral Environments	76
Chapter 4:	Effects of Electric and Magnetic Fields on Droplet Motion	79
A.	Small Charge Induced Drift Forces Considered	79
B.	Lorentz Forces Caused by Earth's Magnetic Field	82
C.	Charge Induced Droplet Breakup	86
D.	Electric Field Forces Acting Between Droplets	88
E.	Droplet Drift Due to Electric Field Interactions	90
F.	Computer Simulation of Electric Field Induced Droplet Dispersion	93
G.	Plasma Damping of Electric Fields between Droplets	97
Chapter 5:	Droplet Charging Experimentation	101
A.	Experimental Method and Setup	101
B.	DC705 Capacitor Charging Experiment Setup	106
C.	Droplet Charging and Deflection Experiment Setup and Method	111
D.	Droplet Charging Experimental Results	114
E.	Comparison of Experimental Results to NASCAP Results	119
F.	Comparison of Experimental Results to SimIon Simulation Results	120
Chapter 6:	Conclusions and Recommendations	123
Appendix 1:	Tandem Satellite Propulsion Needs and Droplet Stream Capabilities	126
Appendix 2:	Past Droplet Stream Research	132
Appendix 3:	Heat Transfer Considerations for Fluid Stream Propulsion	136



Appendix 4. Droplet Stream Formation	144
Appendix 5. Evaporation Losses and Additional Fluid Requirements	153
Appendix 6. Effects of Drag in LEO	156
Appendix 7. Effects of Solar Radiation Pressure	160
Appendix 8. Effects of Atomic Oxygen on Candidate Fluids	162
Appendix 9: Optimization and Design Tools	164
Appendix 10: Lee Solenoid Micro Valve Specifications	167
Appendix 11: Photodiode Specifications and Output	170
Appendix 12: Droplet Dispersion Simulation Code (for Matlab)	173
Bibliography	177
References	178

## Tables

Table 1. Candidate LDR Fluids and their Properties at 20°C. <sup>6</sup> .....	5
Table 2. Low and High Altitude Auroral Environment Fontheim Parameters Used in this Study. ....	20
Table 3. GEO Charging Environments Used in this Study. ....	23
Table 4. DC705 Material Properties Selected for Use by NASCAP. ....	55
Table 5. Dielectric Constants and Strength of Select Materials and Silicone Oil. <sup>52</sup> .....	56
Table 6. Summary of Equilibrium Potentials (maximum sunlit surface and minimum eclipsed surface) and Time to Reach Equilibrium in the Environments Analyzed.....	76
Table 7. Cyclotron Periods for 1mm Droplet at Several Voltage Potentials .....	80
Table 8. Secondary Lorentz Force Drift Due to Transit Velocity .....	85
Table 9. Direction and Speed Stability of DC704 Droplet Streams. ....	90
Table 10. DC705 Capacitor Results. ....	107
Table 11. Capacitance Change in Second DC705 Capacitor Experiment. ....	109
Table 12. Droplet Diameter Statistical Results.....	115
Table 13. Radiation Equivalent Biot Numbers for a 1mm Droplet .....	138
Table 14. Radiation from Fluid Stream Pairs at Similar levels of Thrust (100m Transit).....	143
Table 15. Drift of Droplets due to Solar Radiation Pressure in 50 seconds .....	160
Table 16. Notional Mission Parameters and Resulting Stream Propulsion Specifications.....	166

## Figures

Figure 1. Droplet Stream Propulsion Concept in which Momentum is Exchanged Between Satellites Creating a Continuous Displacement Force from the Reference Orbit Centerline. ....	1
Figure 2. Tandem X Formation Orbit Configuration Providing Various Baseline Distances from which Interferometric Synthetic Aperture Radar will be Performed in 2010. ....	3
Figure 3. DC705 and DC704 Molecules Chemical Structure wherein Hexagon Rings represent Benzene Rings: $C_6H_6$ (From Koizumi, 1996). ....	6
Figure 4. Vapor Pressures of Fluid Candidates Versus Temperature where a Vapor Pressure of $1.0 \times 10^{-5}$ results in Loss of 1/3 of the Mass of a Stream in 10 Years. ....	7
Figure 5. Fluid in Transit Between Two 1km Spaced LEO Satellites at 300km Altitude for Various Stream Transit Velocities. ....	9
Figure 6. Comparison of Ion Thruster Consumed Propellant with Equivalent Thrust Droplet Stream Evaporation Losses at the Same Thrust Level. ....	10
Figure 7. Power and Specific Impulse of Various Electric Propulsion Systems Currently Used in 4 Missions, Each with a Different Range of Required Power and Specific Impulse. Droplet Stream Propulsion has Specific Impulse greater than 60,000 seconds and Power Requirements of Less than 0.05 kW (from Sutton, 2003). ....	11
Figure 8. One and Three Dimensional Maxwellian Velocity Distributions. Left Chart Describes the Portion of Particles with a Particular Velocity Magnitude and Direction in One Dimension. Right chart Describes the Portion of Particles with a Particular Speed. (From Chen, 2006). ....	15
Figure 9. Ion Composition in LEO (from Hastings and Garrett, 1996). ....	16
Figure 10. Auroral Electron Flux Energy Distribution during High (left image) and more Nominal (right image) Magnetospheric and Solar Activity. The 4.9keV Peak is due to the High Energy Plasma Beam Induced by the Magnetic Field (from Fontheim et al, 1982). ....	19
Figure 11. ATS-5 Electron (top) and Ion Distribution Functions with Single and Double Maxwellian Fits (from Hastings, 1996). ....	22
Figure 12. Charging Sources in the Space Plasma Environment. ....	24
Figure 13. Charging Processes at the Surface of a Dielectric Material (after Hastings, 1996). ....	26
Figure 14. Incidence Angle Definition and Typical charge density profile for a dielectric material (graph from Katz et al, 1977). ....	28
Figure 15. Charging Processes Affecting DC705 Droplets. ....	30
Figure 16. Floating Potential Resulting from Atmospheric Plasma in LEO and in Auroral Eclipse during low auroral activity (at 500km). ....	36
Figure 17. Predicted Floating Potential at Energy Levels Approaching those of Auroral Beams. ....	37
Figure 18. Maximum, Nominal, and Minimum Auroral Electron Number Flux Distribution (MIL-STD- 1809). ....	37
Figure 19. Comparison of Actual and Experimental Backscattering Yields. ....	40
Figure 20. Example Electron Secondary Yield as a function of Incident Energy (from Davis, 2008). ....	42
Figure 21. Calculated DC705 vs. Actual Teflon Secondary Electron Yield. ....	43
Figure 22. Predicted Secondary Electron Yield for DC705 and Teflon at 0 and Various Incidence Angles. ....	44
Figure 23. Penetration Range of Electrons (Actual for Teflon and Kapton, Estimated for DC705) ....	46
Figure 24. Estimate of Relative Charge Density Profile for DC705 Due to Secondary Electrons Based on Calculated Range Penetration in DC705 and Known Profiles for Insulating Materials (After Katz, 1977). ....	47
Figure 25. Solar Irradiance at UV Wavelengths Measured by SORCE Satellite. ....	48
Figure 26. Photoemission of Electrons for DC705 & DC704 (from Koizumi et al.) ....	50
Figure 27. Nominal Solar Output (solid line) and Photoelectron Yield for Silicon Oil (dashed line plotted against the right ordinate). ....	50
Figure 28. Comparison of Charging of Sunlit and Anti-sun Surfaces on Sunlit Droplets and Eclipsed Surface Elements on Spheres with Four Different Diameters. ....	53
Figure 29. DC705 Sphere in NASA Worst-case GEO in Eclipse (top) and in Sun (bottom). Photoemission of Electrons Results in a More Positive Charge on the Sunlit Hemisphere. ....	58
Figure 30. Strong Auroral Charging of a 20cm DC705 Sphere in Sun with 7500m/s Velocity in the y-axis	

and Sunlight aligned with the x-axis. ....	59
Figure 31. Comparison of Hemispheric Charging Impacted by Velocity and Solar Incidence. ....	60
Figure 32. DC705 Sphere in NASA Worst-case Sunlit GEO Environment after 0.2 sec. Early Stages of Plasma Sheath Development are Evident Near the Droplet Surface. ....	62
Figure 33. DC705 Sphere in NASA Worst-case GEO environment after 1.5 sec. ....	63
Figure 34. DC705 Sphere in NASA Worst-case GEO after 10 sec. ....	64
Figure 35. DC705 Sphere at Equilibrium in NASA Worst-case GEO after 300 sec. ....	64
Figure 36. DC705 Spheres in NASA Worst-case GEO ....	65
Figure 37. NASCAP Simulation of DC705 alongside SPENVIS and NASCAP Simulations of Teflon Spheres in Eclipse. All Simulations are in NASA's Worst-case GEO Charging Environment. In Sunlit Droplets, the Most Positive and Negative Potentials are found on the Sunlit and Anti-sun Surfaces, Respectively. ....	66
Figure 38. NASCAP Charging Results for Strong GEO Charging Environments. This chart shows the First 0.50 seconds of the severe GEO charging data presented in Figure 37 with more resolution on both axes. ....	67
Figure 39. Nominal GEO Environment DC705 Sphere Charging (first series plotted against left ordinate, other 4 plotted against right ordinate. ....	68
Figure 40. 2mm DC705 Cubes in Strong DMSP Eclipse Environment after 0.01 seconds. ....	70
Figure 41. 2mm DC705 Cubes in Strong DMSP Eclipse Environment after 0.5 seconds. ....	70
Figure 42. DC705 Spheres in DMSP Sunlit Environment with Elevated Geomagnetic activity. ....	71
Figure 43. DC705 Spheres in DMSP Sunlit Environment with Elevated Geomagnetic activity. ....	72
Figure 44. Transition from Eclipse to Sun in a Strong 800km Auroral Charging Environment. ....	73
Figure 45. Nominal Auroral Droplet Charging. Top curve shows Maximum Potential on Sunlit Surface Elements (right ordinate). Eclipse results are shown in the Bottom Three Curves (plotted against left ordinate). Ram Surfaces Acquire a Slightly more Positive Charge while and Sunlit Surfaces Charge more Strongly Positive. ....	74
Figure 46. Transition from Eclipse to Sun in a Moderate, High Altitude, Auroral Environment At 0.15 seconds, exposure to the sun occurs causing a momentary spike of +21V and establishes a new maximum (positive) equilibrium on the sunlit surfaces. The anti-solar side experiences a similar momentary spike of +12V before returning to negative charge equilibrium. In the simulation depicted the maximum number of time steps supported by NASCAP was used. ....	75
Figure 47. Droplet Charge Density as it relates to Diameter. ....	78
Figure 48. Direction of Lorentz Force Defined by the Cross Product of the Charged Object's Velocity and External Magnetic Field. ....	83
Figure 49. Velocity Change due to Primary Lorentz Force at Nominal Charge Levels ....	84
Figure 50. Worst-case Lorentz Drift and Velocity Change over a 1km Transit Distance. ....	86
Figure 51. DC705 Droplet Breakup as a Function of Diameter and Voltage. ....	87
Figure 52. Alignment of Charged Droplets Forcing Upper Droplet Out of Nominal Dispersion Cone. ....	91
Figure 53. Off-Centerline Drift of a 1mm Droplet during a 1km Transit as a Function of Velocity (for a 26V droplet) and as a Function of Potential (for a droplet transiting at 20m/s). ....	92
Figure 54. Dispersion Simulation Results for 5000 Uncharged Droplets after 50 second transit. ....	93
Figure 55. Charged Droplet Impact Point for 2mm Droplets after 50 second Transit. ....	94
Figure 56. Histogram of Impact Distance from Centerline for a Droplet Stream Charged to 100V Potential. ....	95
Figure 57. Maximum Miss Distance vs. Velocity for 100V Droplets. Diameter = 1 to 5mm, Spacing = 0.5 to 3 Diameters. Ratio of Diameter to Droplet Spacing = 1 to 2. ....	95
Figure 58. Results of Transit Simulations with Different Gap Distances between Droplets. Power Law Curve Fits to Simulation Data indicate an Inverse Relationship between Maximum Miss Distance and Droplet Diameter. ....	96
Figure 59. Debye Length as a Function of Altitude. ....	98
Figure 60. Spectral Radiance of 30W Deuterium Lamp Used to Simulate Solar EUV (From Hamamatsu, 2007). ....	102
Figure 61. Comparison of Solar Irradiance at 121-123 nm to Lamp Irradiance. ....	104
Figure 62. Solar and Lamp Irradiance with Photoemission Yield on Right Ordinate ....	104
Figure 63. Photoelectron Currents for Lamp and Sun. ....	105

Figure 64. DC705 Fluid Filled Capacitor Experiment Setup in which Change in Capacitance is Measured following Irradiation of DC705 with an EUV Lamp.....	106
Figure 65. Second DC705 Capacitor Experiment Setup .....	108
Figure 66. Droplet Impact Location Sensor composed of Separate Wire Mesh Capacitors, each Capable of Detecting Impacting Charged Droplets. ....	110
Figure 67. Charged Droplet Experiment in which Droplets are Charged with EUV then Deflected by Charged Plates. Displacement is Measured using High Speed Imagery. ....	111
Figure 68. Droplet Before and After Impact with a Ruler Tilted Away from Field of View. ....	114
Figure 69. Displacement Results for the 2.4mm Diameter Droplet Series. Lamp# Refers to Lamp Positions 1, 2, and 3, which were positioned 21, 29, and 39 Centimeters, respectively, from the Droplet Charging Path. ....	116
Figure 70. Series 3 (1.2mm) Droplet Deflection Results. Lamp# Refers to Lamp Positions 1, 2, and 3, which were positioned 21, 29, and 39 Centimeters, respectively, from the Droplet Charging Path. ..	117
Figure 71. Average Droplet Potential at Nearest and Farthest Lamp Positions. Lamp# Refers to Lamp Positions 1 and 3, which were positioned 21 and 39 Centimeters, respectively, from the Droplet Charging Path. Error Bars Reflect One Standard Deviation in Measured Droplet Displacement as well as Uncertainty in Voltage Potential due to One Standard Deviation in Droplet Mass Variation. ....	118
Figure 72. Droplet Potential as a Function of Lamp Distance. Vertical Error Bars Reflect One Standard Deviation in Measured Droplet Displacement and Droplet Mass Variation. ....	118
Figure 73. Comparison of NASCAP and Experiment Results for DC704 Spheres. Lamp# Refers to Lamp Positions 1, 2, and 3, which were positioned 21, 29, and 39 Centimeters, respectively, from the Droplet Charging Path. Vertical Error Bars Reflect One Standard Deviation in Measured Droplet Displacement and One Standard Deviation in Voltage Potential due to Droplet Mass Variation. ....	120
Figure 74. Actual and SimIon Predicted Deflection of 2.4mm Droplets Charged at Closest Lamp Position. Error Bars Reflect One Standard Deviation in Measured Droplet Displacement as well as Uncertainty in Voltage Potential due to One Standard Deviation in Droplet Mass Variation. ....	121
Figure 75. Reference Frame used in Development of Equations used to Describe the Forces Required to Maintain Tandem Satellite Formation Position (From Tragesser, 2007). ....	126
Figure 76. Thrust Required in GEO and Produced by LDR Streams .....	128
Figure 77. Thrust Required in LEO and Maximum Demonstrated Stream Capabilities .....	129
Figure 78. LEO Thrust Required as a function of Spacecraft Mass and Thrust Possible by Increasing Diameter and Velocity Slightly .....	130
Figure 79. Liquid Droplet Radiator Concept (from Totani et al., 2002). ....	132
Figure 80. Silicon Oil Rotating Collector Designed by Grumman Aerospace Corp. for AFRL. (from AFRPL TR-85-082, 1985). ....	133
Figure 81. Collection of Uniform (left) and Non-uniform (right) Droplet Streams (from Totani et al., 2002) .....	134
Figure 82. Emissivity Results for DC704 Samples; 0.6mm thick film on the left, 0.3mm on the right (from White, 1987).....	139
Figure 83. Spherical Radiation to 80K Model vs. Thermal Desktop Results (1mm diam in eclipse). ....	140
Figure 84. Cooling Results for 1mm droplet using "2/3 to 3K" Model and Thermal Desktop .....	141
Figure 85. Equilibrium Temperature for Various Diameters and Exposure Times (0.61 emissivity) .....	141
Figure 86. 2mm Droplet Cooled in Eclipse then Exposed to Full Sun (Temperature vs. Time) .....	142
Figure 87. Transformation of Fluid Column to Droplet Stream (from Totani et al, 2002) .....	144
Figure 88. Uniform Droplet Formation Envelope (from Muntz and Dixon, 1984). ....	146
Figure 89. Droplet Velocity and Chamber Pressure for Several Orifice Diameters .....	148
Figure 90. Electrical Power Required Generating Fluid Pressures at 1km Spacing in LEO .....	149
Figure 91. DC705 Required Velocity and Operating Frequency for a Range of Droplet Diameters .....	151
Figure 92. Fluid in Transit 1km Spaced LEO Satellites .....	153
Figure 93. Loss of DC705 Fluid due to Evaporation in 10 Years for 1km Spacing in LEO .....	154
Figure 94. Angle of Incidence of Particles Impacting a Droplet. ....	156
Figure 95. Drag Coefficient vs. Specular Reflectance of Neutrals at 300km .....	157
Figure 96. Drift off Centerline of Droplets and Satellites Due to Drag During 10 Seconds of Transit .....	158
Figure 97. Design Process for a Droplet Stream Propulsion System .....	165
Figure 98. Measured and Advertised Lamp Output between 120-180 nm.....	171

## Chapter 1: Introduction and Related Research

The research presented here evaluates momentum exchange through fluid streams as a means of maintaining side-by-side spacing between a pair of formation satellites. Droplet streams of very low vapor pressure silicone oil are generated on each spacecraft and projected through space to a receiving satellite. The receiving satellite collects the droplet stream and pumps the fluid to heat exchangers on warm spacecraft components removing heat from those components while warming the fluid. Fluid is pressurized further in a droplet generator where a return stream is produced and sent back to the originating satellite to begin the process again. The concept might look like Figure 1 in which two spacecraft are travelling in the horizontal direction while imaging the Earth below.



**Figure 1. Droplet Stream Propulsion Concept in which Momentum is Exchanged Between Satellites Creating a Continuous Displacement Force from the Reference Orbit Centerline.**

The side-by-side satellites use streams of small silicon oil droplets continuously exchanged to produce the force needed to maintain constant separation. This study investigated various aspects of generating and collecting such a droplet stream including the many environmental forces acting to

disturb droplets from their intended path between satellites. This dissertation focuses on one aspect of the study: droplet charging in the space environment and the impact of charging on the concept viability. To date, no one has studied the impact of droplet charging in the space environment on long distance collection.

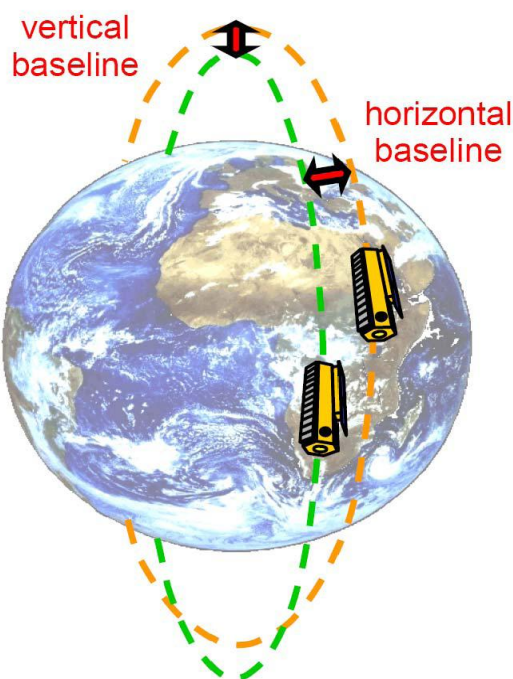
### **A. Motivation for Tandem Satellites**

In the past decade, the advantage of satellite formations to the field of remote sensing gave rise to several proposals for their implementation. The first satellite formation to fly is likely to be a satellite pair called Tandem-X. These spacecraft are under development by the German Space Agency and are expected to be operational by 2010. The nearly identical Tandem-X satellites will provide the first bi-static synthetic aperture radar (SAR) platform in space. This technique is expected to provide topographic resolution one the order of 1cm.<sup>1</sup>

To achieve a side-by-side configuration, Tandem-X utilizes two offset polar orbits depicted in Figure 2. Because of the ever-changing TanDEM-X separation distance, the formation is ill-suited for frequent, repeat observations of the Earth and is fundamentally unable to achieve the same separation baseline over all parts of the Earth. Such consistency of baseline is necessary for consistent coverage of the entire Earth and for timely detection of surface changes. Conceptually, tandem spacecraft with constant spacing would be desired.

Since tandem, side-by-side satellites are each in orbits around the center of the Earth their orbits cross twice every period and they tend to converge on each other unless a continuous separation force counteracts this convergence. The magnitude of the separation force required is proportional to the total mass of the two spacecraft and their separation distance. Appendix 1 presents work by Tragesser<sup>2</sup> to quantify this force and analysis of the various sizes and velocities of droplet streams needed for various spacecraft masses and separation distances. In GEO, the thrust force is 20 to 100 mN while in LEO, 100 to 1000 mN is required for satellites between 100 and 1000kg with 1km spacing. Droplet streams of the size

produced in this study and of the velocity produced in other studies are capable of providing several Newtons of thrust. It is possible to generate the necessary momentum transfer with a single pair of droplet streams to separate satellites with an average mass of several thousand kilograms more than a kilometer apart. Appendix 1 presents work by Tragesser<sup>2</sup> to quantify this force and analysis of the various sizes and velocities of droplet streams needed for various spacecraft masses and separation distances. In GEO, the thrust force is 20 to 100 mN while in LEO, 100 to 1000 mN is required for satellites between 100 and 1000kg with 1km spacing. Droplet streams of the size produced in this study and of the velocity produced in other studies are capable of providing several Newtons of thrust. It is possible to generate the necessary momentum transfer with a single pair of droplet streams to separate satellites with an average mass of several thousand kilograms more than a kilometer apart.



**Figure 2. Tandem X Formation Orbit Configuration Providing Various Baseline Distances from which Interferometric Synthetic Aperture Radar will be Performed in 2010.**



A range of formation separation distances between tens of meters to at least one kilometer is useful to the remote sensing community.<sup>3</sup> Polar orbit is both a desirable place to fly remote sensing satellites in formation and a challenging environment to perform droplet transfer due to dramatic changes to the auroral plasma charging environment during periods of high solar and geomagnetic activity. The focus of this study is on obstacles to using the concept in GEO, LEO<sup>i</sup>, and polar orbit. Primarily this study focuses on the effects of these very different plasma-charging environments on droplet transport.

Droplet streams in space were first proposed in the 1980s for use in radiating waste heat on large space structures. The National Aviation and Space Administration (NASA) and the Air Force (USAF) funded the Liquid Droplet Radiator (LDR) program that demonstrated feasibility of droplet streams and developed technologies for generating and collecting them in space. A description of this program, its findings, and the technologies applicable to a droplet stream propulsion system is found in Appendix 2. More than two dozen articles in the literature describe the formation and use of droplet streams in the space environment. Of note, is work done in the 1980s by researchers at the University of Washington,<sup>4</sup> the University of Southern California (USC)<sup>5</sup>, NASA's Glenn Research Center<sup>6</sup> and Air Force Research Laboratory (AFRL).<sup>7</sup> NASA and the USAF funded studies by several contractors that resulted in proven technologies for fluid stream generation and collection. NASA researchers also conducted drop testing of LDR components in free fall.<sup>8</sup> Many of the technologies developed for the LDR program would be equally useful for droplet stream propulsion.

## **B. Fluid Selection and Droplet Generation**

---

<sup>i</sup> For this study LEO is defined as less than 650km and between 0 and 55 degrees inclination. This is non-auroral space where atomic oxygen ions are the dominant ion species.<sup>18</sup>

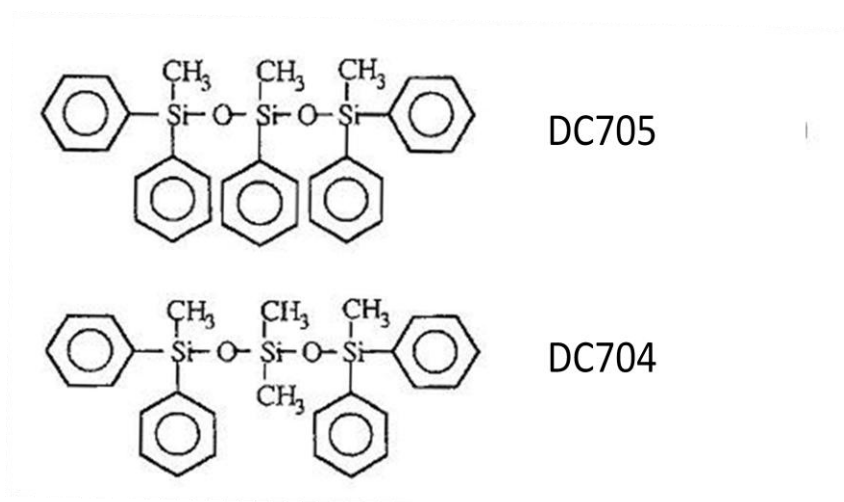
Several types of low vapor pressure fluids were considered for use in a droplet stream propulsion system. LDR researchers considered the fluids in Table 1 and the fluid selected by NASA and the USAF in the 1980s was trimethyl pentaphenyl siloxane which is a silicone based oil known best by its trade name Dow Corning 705 (DC705).<sup>6</sup> DC705 is a good LDR fluid because of its low vapor pressure and relatively low viscosity at nominal satellite operating temperatures. DC705 is still the working fluid of choice for LDR designs and was selected for LDR testing performed by Japanese researchers as recently as 2005.<sup>9</sup>

**Table 1. Candidate LDR Fluids and their Properties at 20°C.<sup>6</sup>**

Fluid	Vapor Pressure (Torr)	Molecular Weight (amu)	Viscosity (centistokes)
DC705	$3 \times 10^{-10}$	546	175
Fomblin Z25	$3 \times 10^{-12}$	9500	355
Krytox 16256	$3 \times 10^{-14}$	11000	2560
Krytox 1502	$6 \times 10^{-7}$	1465	17

A Polyphenyl Ether diffusion pump oil called Santovac 5 was also considered in this study because of its resistance to oxygen and radiation degradation.<sup>10</sup> Santovac 5 has a vapor pressure that is very similar to that of DC705 but is considered less desirable because its viscosity is 1000 centistokes (cst) at 27° C which is about five times higher than that of DC705 (175 cst at 25°C). Low viscosity is advantageous because it allows droplet stream production at a lower reservoir pressure. Other fluids considered include another silicone oil called DC704 and a synthetic hydrocarbon called Neovac SY. Both fluids are desirable for their relatively low viscosity, which is 39-40 centistokes at 25°C.<sup>11</sup> The vapor pressure of DC704 is  $2.6 \times 10^{-6}$  Pa ( $2 \times 10^{-8}$  Torr) at 25° C while Neovac SY has a vapor pressure of  $1.3 \times 10^{-6}$  Pa ( $1 \times 10^{-8}$  Torr).

DC704 and DC705 have similar density; 1070 kg/m<sup>3</sup> for DC704 and 1097 kg/m<sup>3</sup> for DC705. The fluids differ chemically by a single methyl group, which is replaced by a fifth Benzene ring (C<sub>6</sub>H<sub>6</sub>) in DC705 as seen in Figure 3. Previous research shows that charging properties of DC704 and DC705 are very similar.<sup>12</sup> For these reasons, much of the research presented in this report is quite applicable to both DC704 and DC705. In fact, DC704 was used as a less expensive alternative for some charging experiments performed in support of this research.

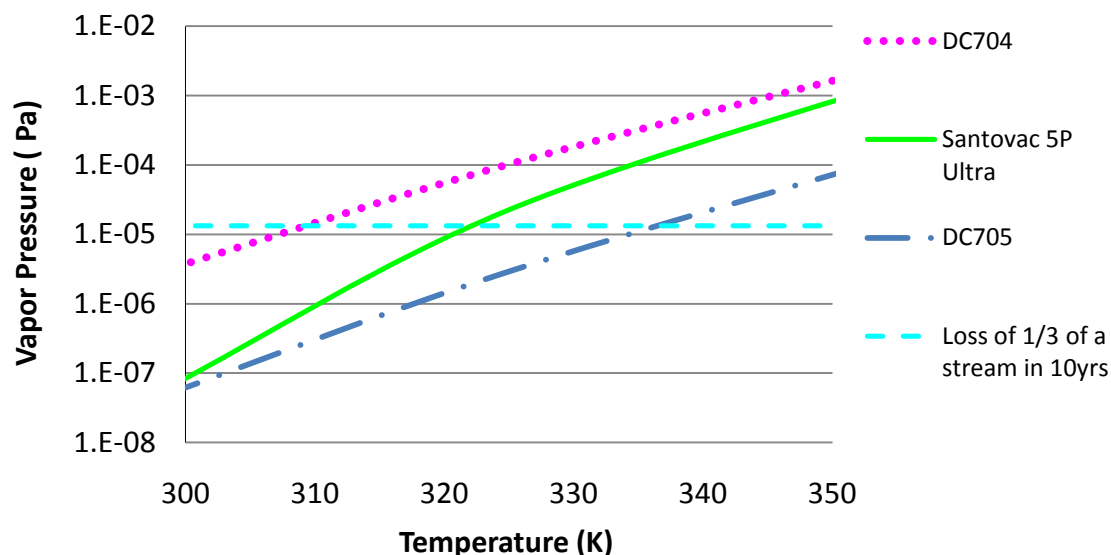


**Figure 3. DC705 and DC704 Molecules Chemical Structure wherein Hexagon Rings represent Benzene Rings: C<sub>6</sub>H<sub>6</sub> (From Koizumi, 1996).**

As seen in Figure 4, the vapor pressure of silicone oils, and other fluids considered, increases significantly as a function of temperature. As a result, DC705 is only practical for use at temperatures below 350K. For most spacecraft, this temperature limit is quite reasonable since it is rare for spacecraft components to require operation at temperatures exceeding 350K. Spacecraft cooling systems can be designed that avoid producing droplet streams with temperatures greater than this. Indeed, one of the advantages of having fluid on-board is the active temperature control it affords the spacecraft through control of fluid flow and using the propulsion system itself as a liquid droplet radiator.

DC704 vapor pressure is nearly two orders of magnitude higher than that of DC705. Thus, more fluid loss through evaporation is expected with DC704 than with DC705. Analysis of DC704 for LDR applications concluded that fluid loss due to evaporation is significant at operating temperatures expected on high temperature satellites considered for LDR.<sup>4</sup> The horizontal dashed line in the chart shows the vapor pressure at which 1/3 of the mass of fluid in space at any given time is lost through evaporation over a 10-year period. If fluid temperature is less than 310K, the loss of DC704 through evaporation is less than half a liter over 10 years for reasonable streams. This fluid temperature limit is reasonable for most satellites and indicates that DC704 is a viable candidate for droplet stream propulsion if fluid temperature is kept low. The lower viscosity of DC704 gives it advantages over DC705 in terms of power required to pump the

fluid up to the desired pressure. For this study, DC705 was the primary fluid evaluated but charging characteristics of DC704 and DC705 are very similar so charging results are quite applicable to either fluid.



**Figure 4. Vapor Pressures of Fluid Candidates Versus Temperature where a Vapor Pressure of  $1.0 \times 10^{-5}$  results in Loss of 1/3 of the Mass of a Stream in 10 Years.**

It is necessary to break up a fluid column into uniform droplets to prevent randomly sized droplets from forming due to the tendency for a fluid column to minimize its surface area. This phenomenon, called Rayleigh instability, causes breakup into droplets of random size at about 3 stream diameters from the producing orifice.<sup>13</sup> Droplets of varying size are affected differently by drag and other forces described in this study resulting in a very large impact region at the receiving satellite, making collection difficult. Droplet generators developed for the LDR program were based on vibration-induced breakup of a fluid column into droplets. This mature technology pioneered by Lord Rayleigh is described in Appendix 4.

Micro solenoid valves are a proposed new method of droplet generation. This technology was developed in the decade following cancellation of the LDR program and is currently used in spacecraft applications. These valves can operate for several million cycles and are capable of generating a droplet stream for 3-5 years. Testing of two types of micro solenoid valves was carried out for this study and indicates that this technology can produce droplet streams of sufficient uniformity, size, and speed needed for virtually any type of droplet stream propulsion system envisioned in this study. When compared to

piezoelectric droplet generators, solenoid generators have less fluid loss at startup and shutdown and can produce droplets with very large gap distance between droplets. In Chapter 4 it is shown that electric field interactions cause droplets to drift off of the intended path during transit. Such dispersion of droplets from centerline increases impact area and is the chief problem associated with droplet charging. Larger gaps between droplets reduce electric field strength between droplets and the resulting dispersion from centerline.

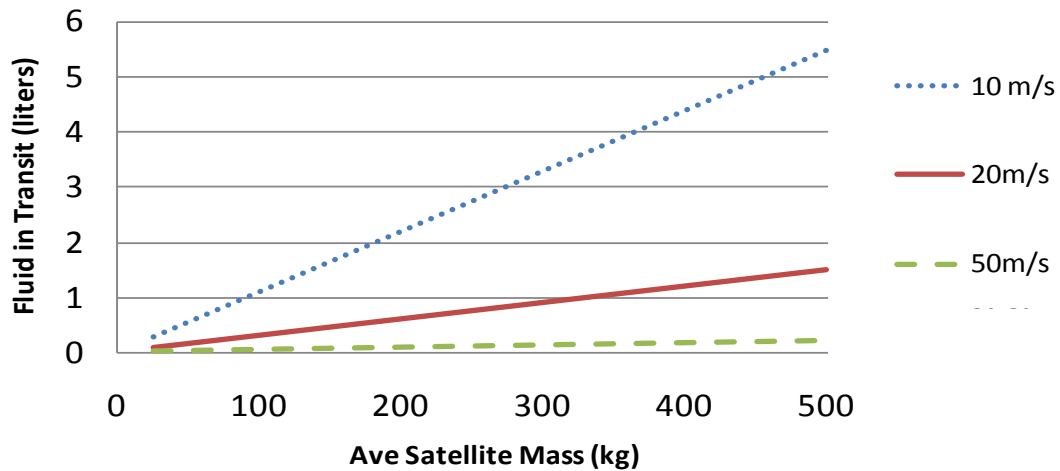
### **C. System Performance and Comparison with Ion Engines**

GEO satellite propulsion needs are low and can be satisfied by a single opposing pair of droplet streams using already proven stream size and velocity. Droplet streams of demonstrated size and speed extended over a 1km distance require less than 100mL of silicone oil in transit at any one time. The need for additional fluid beyond that which is in transit will be discussed later but, even after accounting for expected fluid loss and extra fluid needed to ensure correct collector and pump operation, the impact of fluid propulsion on a typical GEO satellite's mass budget is less than 2% of system mass.

In LEO where the propulsion need is much greater, the need for larger droplet diameters results in a need for more fluid in transit. The chart in Figure 5 compares fluid in transit over a 1km distance between two 300km LEO satellites. Droplet stream speed has a significant effect on the amount of fluid in transit because slower droplets spend more time in transit and because slower speeds require more fluid mass to provide the required momentum exchange. A transit velocity of only 10m/s requires about 5 liters of fluid in transit to maintain 1km spacing of 500kg satellites whereas a transit velocity of 50m/s has about 70 ml of fluid in transit.

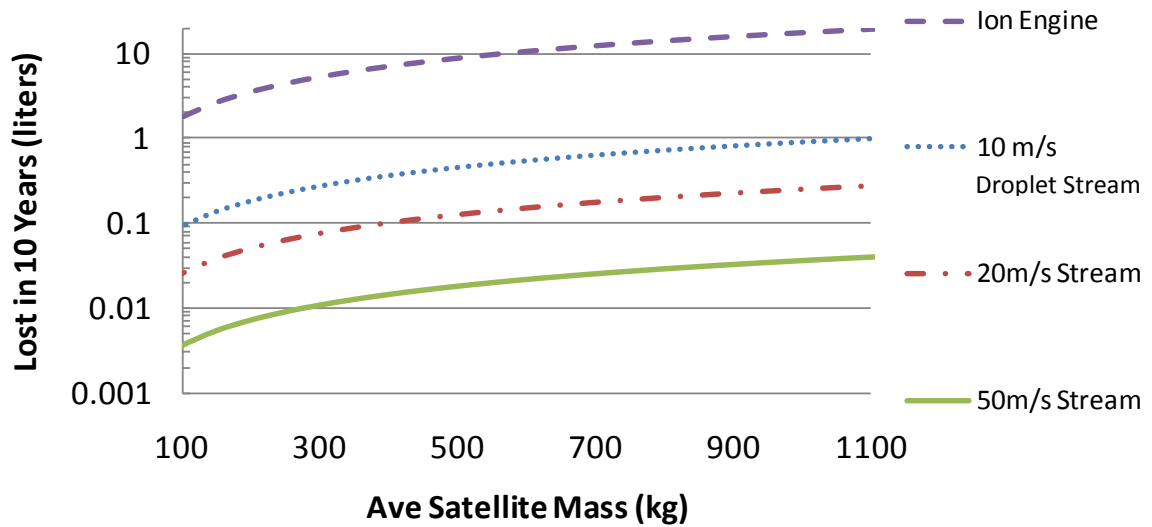
Appendix 5 includes a discussion of how much additional fluid is required in feed lines and to account for evaporation losses. The amount of fluid needed on each satellite is roughly equal to 3 times the amount of fluid in transit. About 9kg of DC705 is needed to maintain 1km separation of two 500kg satellites in LEO with a transit speed of 20m/s. This represents less than 2% of the total spacecraft mass and displaces some mass otherwise needed for a conventional thermal control system (TCS). Based on the

mass of components developed for the LDR program<sup>14</sup> it is estimated that a droplet stream propulsion system for LEO satellites will require less than 6% of a spacecraft's mass budget.



**Figure 5. Fluid in Transit Between Two 1km Spaced LEO Satellites at 300km Altitude for Various Stream Transit Velocities.**

Low thrust propulsion to maintain a tandem spacecraft formation can be provided by Ion Engines or other forms of electric propulsion. Such thrusters operate with a specific impulse (Isp) on the order of 6000 seconds. In Figure 6 the amount of propellant used by an EADS Astrium RIT-22 Ion Thruster is compared to droplet stream fluid losses due to evaporation from a 1mm diameter stream. Fluid mass consumed is shown on a logarithmic ordinate as a function of spacecraft mass. The chart shows that ion engines consume about 11 times more propellant than a 20m/s droplet stream propulsion system and three orders of magnitude more propellant mass than a 50m/s stream system. Based on these estimates, a 1mm diameter, 20m/s stream has an Isp of about 60,000 seconds. Isp for a 3mm, 50m/s stream is on the order of 9 million seconds and the efficiencies of faster and larger streams are even higher.

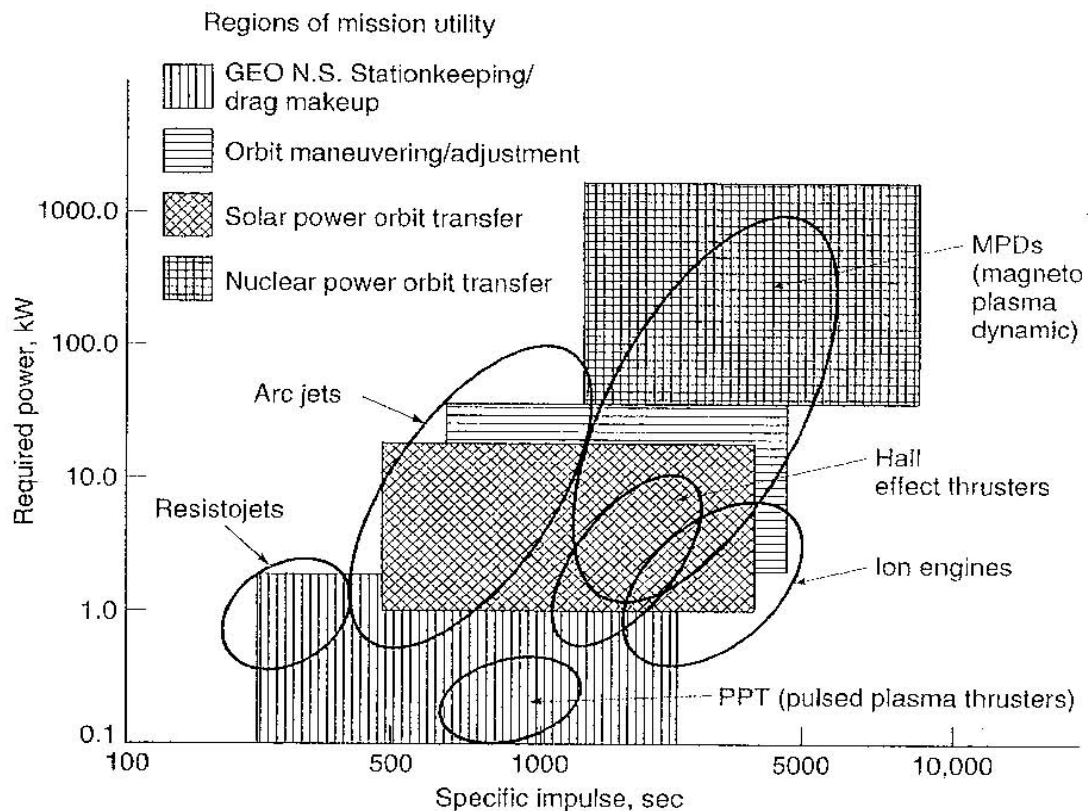


**Figure 6. Comparison of Ion Thruster Consumed Propellant with Equivalent Thrust Droplet Stream Evaporation Losses at the Same Thrust Level.**

In addition to specific impulse, system mass was analyzed to properly compare ion thrusters with droplet stream systems. LDR system components applicable to droplet stream propulsion include fluid pumps, collector structure, reservoir, feed lines, heat exchangers, flow directing valves and droplet generator solenoid valves. In addition, a pointing platform may be required for the droplet generator unless satellite attitude control systems can ensure stream pointing accuracy. A first order approximation of system dry mass of 10-20kg was calculated using component masses reported by NASA and AFRL.<sup>7</sup> By comparison a RIT-22 Ion thruster weighs 7kg (dry mass) and six of them are required on each satellite to provide the same thrust provided by opposing 2mm, 50m/s droplet streams.<sup>15</sup>

Although specific impulse of droplet stream propulsion is an order of magnitude higher than most electric propulsion systems this alone does not put droplet stream technology in a class of its own. When faced with the option of flying ion engines on a 500kg satellite that total 100kg, or an unproven droplet stream system weighing just 20 kg, many spacecraft designers will accept the mass penalty of the proven system. Where droplet streams show clear advantage over electric propulsion is in the areas of thrust and power. A single RIT-22 consumes over 5kW of power whereas a droplet stream system providing the same thrust as six RIT-22 engines is estimated to use less than 50W. The same ion engine produces less

than  $1/6^{\text{th}}$  the thrust of a relatively small and slow droplet stream. For most satellites, this 600 to 1 difference in continuous required power is more significant than a 5-fold mass savings and puts droplet stream propulsion in its own class. Figure 7 compares the performance of existing electric propulsion systems used currently used in orbit. Droplet stream propulsion is literally off the chart in both directions with power requirements below 100 Watts and specific impulse typically much more than 100,000 seconds.



**Figure 7. Power and Specific Impulse of Various Electric Propulsion Systems Currently Used in 4 Missions, Each with a Different Range of Required Power and Specific Impulse. Droplet Stream Propulsion has Specific Impulse greater than 60,000 seconds and Power Requirements of Less than 0.05 kW (from Sutton, 2003).**



#### **D. Summary of Non-Charging Impediments to Droplet Stream Propulsion**

As droplets travel between satellites, they are exposed to the near Earth environment which affects the path that the droplets follow and the chemical makeup of the droplet material itself. In this study, the forces of drag and solar radiation pressure were quantified and these results are presented in Appendix 6 and 7 respectively. Solar pressure forces are negligible at all altitudes and result in off-course droplet drift of less than a few millimeters. Drag is significant below 600km and acts to slow droplet orbital velocity much more than the orbit velocity of the sending and receiving satellites. In this way, drag alters the trajectory of transiting droplets. The direction and magnitude of drag forces are relatively predictable and can be compensated for by projecting a stream that leads the target collector sufficiently. A droplet stream pointing control system will require a feedback sensor that can detect droplet impact location. A prototype of such a device was developed and tested in this study and is described in Chapter 5.

Heat transfer within and from droplets is analyzed in Appendix 8. Heat transfer within a droplet via conduction is significantly faster than radiation of heat from the surface. Analysis shows that surface radiation is slow enough that droplets 1mm in diameter will not freeze during transits of several kilometers at reasonable speeds (20m/s). Larger or faster droplets can travel further without freezing. The amount of waste heat that various droplet streams can dissipate is presented in Appendix 8. For the same amount of thrust, small droplets dissipate more heat from the host satellite than large droplets do.

Radiation and atomic oxygen may damage the molecular structure of the fluid and could lead to changes in viscosity, electromagnetic energy absorption, bulk conductivity, and possibly other properties. Some study of the effects of DC705 exposure to ionizing radiation and atomic oxygen was accomplished for the LDR program. DC705 was exposed to positive ions for more than 72 hours without a significant effect. This research recommends further testing to identify and quantify possible long-term viscosity changes.<sup>16</sup> A more detailed description of ion bombardment testing of DC705 from the LDR program is presented in Appendix 8. In this study, DC705 samples were exposed to ionizing levels of EUV light and then analyzed using infrared spectroscopy. Samples exposed to EUV for 15 and 30 minutes showed no change the chemical makeup of the fluid.

## **E. Relevance of Droplet Charging to Droplet Stream Propulsion**

Once the utility of droplet stream momentum transfer was established and the more obvious impediments to its implementation were quantified the focus of this study turned to the issue of droplet charging in space. Exposure to the plasma and radiation environment of space results in negative or positive charging of any material. Droplet charge is a concern for several reasons discussed in detail in Chapter 4. Charged droplets will experience Lorentz forces associated with interaction with electric and magnetic fields. Electric fields between charged droplets will cause droplets to repel one another, which alters their trajectory between satellites. If droplet charge gets high enough, it will cause droplets to break up into smaller droplets of various diameters and with trajectories altered from that of the original droplet.

The rest of this dissertation concerns the focus of this study, droplet charging in space. Chapter 2 discusses the methods used to quantify the plasma and radiation environments in LEO, GEO and auroral space. Droplet charging theory is discussed and how it was applied to predict charging of silicone oil through analytical and numerical methods. Chapter 3 discusses numerical modeling tools used in this study, particularly NASA Charge Analysis Program (NASCAP). Each of the materials properties used by NASCAP is discussed along with the method used to determine an appropriate value for DC705 property. Chapter 5 details two experiments conducted in a vacuum chamber to verify and quantify droplet charging of silicone oil by an Extreme Ultraviolet (EUV) lamp. Results of experimental charging correlate well with NASCAP numerical predictions of droplet charging due to EUV radiation from the sun. Experiment results were also used to refine the material property used by NASCAP to predict the rate at which electrons are removed from DC705 by incident high-energy photons.

## Chapter 2: Analytic Models of Charging of Droplets in Space

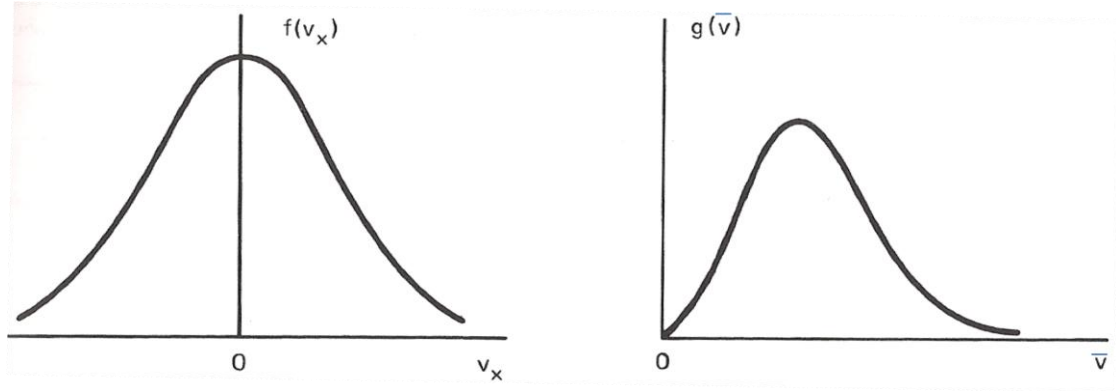
Silicone oil was chosen for its low vapor pressure and relatively low viscosity. However, this semi-conducting dielectric material can charge to significant levels in the plasma environment of space. Because of the influence of Earth's magnetic field, the plasma environment varies significantly as a function of orbit inclination and altitude. Objects in LEO at latitudes below 60 degrees reside in a relatively benign surface-charging environment. Here high-energy particles are shielded by Earth's magnetic field and low energy plasma from photoionization of atmospheric constituents dominates. At latitudes greater than 60 degrees auroral phenomenon can expose orbiting bodies to much higher energy plasma that can vary significantly with time and produce strong localized charging environments. In GEO, high-energy plasma dominates, especially during strong magnetospheric activity.

Knowledge of the flux density and energy distribution of incident particles and photons is needed to determine how much charge develops on the surface of a dielectric material in space. Knowledge of the energy flux density of electrons, in particular, is essential because electron fluxes in any orbit are much greater than those of ions, which typically have a negligible impact on the surface potentials of tested spacecraft materials.<sup>17</sup> This chapter begins with sections on characterizing the LEO, GEO and auroral environments. Space charging theory is then discussed along with how it relates to properties of the exposed material. Finally, the environment and materials properties are combined in a simplified method of charge determination for a DC705 droplet in LEO eclipse.

### A. Characterizing the LEO and Auroral Charging Environments

It has been shown that in low latitude LEO, particle collisions are frequent enough that plasma is in thermal equilibrium. The velocity distribution of isotropic LEO plasma in one dimension ( $x$ ) is depicted on the left in Figure 8.  $f(v_x)$  is the fraction of the total number of incident particles expected as a function of velocity. Integrating  $f(v_x)$  from negative to positive infinity yields unity. This distribution is centered on

zero because particle motion is random and motion in the positive and negative x direction has an equal probability. The width of this distribution describes the temperature of the plasma. A higher plasma temperature produces a broader distribution curve.<sup>29</sup>



**Figure 8. One and Three Dimensional Maxwellian Velocity Distributions. Left Chart Describes the Portion of Particles with a Particular Velocity Magnitude and Direction in One Dimension. Right chart Describes the Portion of Particles with a Particular Speed. (From Chen, 2006).**

Atoms in the upper atmosphere are heated by various radiation sources and will ionize if the thermal energy exceeds the ionization energy of the particular atomic species. In the LEO region between 180 and 650-1000 km, atomic oxygen is the most prevalent ion species. Above 650-1000 km hydrogen ions (protons) dominate. The relative concentrations of ions in LEO are shown in Figure 9. Although temperature ( $T$ ) is the same for ions and electrons in LEO, the particle mass,  $m$ , is much higher for ions than it is for electrons. Because of this, thermal velocity, defined by Equation 1, is higher for electrons than it is for ions:

$$v_{th} \equiv (2\kappa T/m)^{1/2} \quad (1)$$

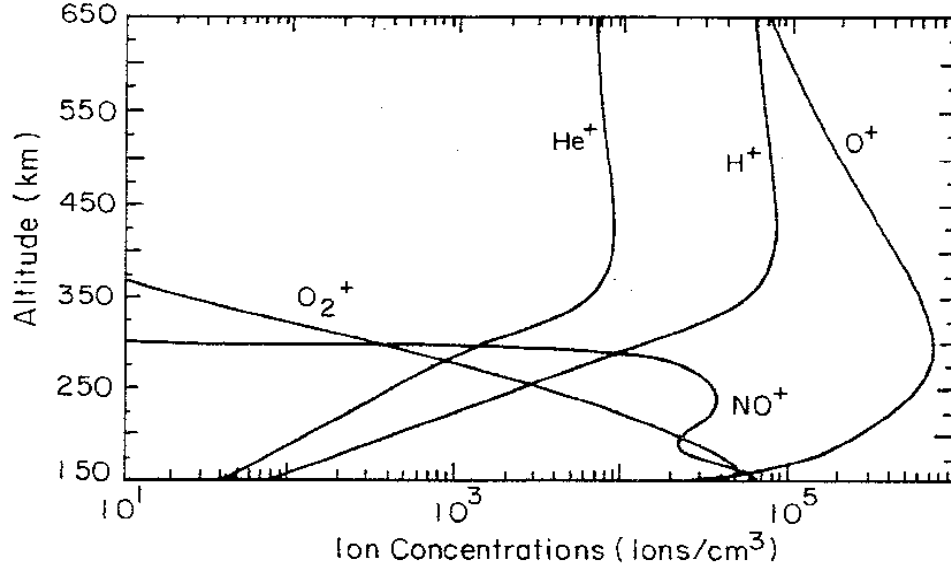
Here  $\kappa$  is the Boltzmann constant  $\kappa = 1.380658 \times 10^{-23}$  J/K and  $\kappa T$  is the average thermal energy of the population of particles. The average magnitude of velocity is determined by:<sup>20</sup>

$$\bar{v} = 2\sqrt{\pi}v_{th} = \sqrt{8\kappa T/\pi m} \quad (2)$$

and the mean translational kinetic energy of a population is given by:<sup>18,20</sup>

$$E_{ave} = 3\kappa T/2 = m\bar{v}^2/2 \quad (3)$$

$\kappa T$  can be expressed in joules but is more often expressed in electron volts (eV) where, 1 eV =  $1.602177 \times 10^{-19}$  J. The temperature corresponding to a thermal energy of 1 eV is 11600 K.<sup>19</sup>



**Figure 9. Ion Composition in LEO (from Hastings and Garrett, 1996).**

It is common to describe a population by its temperature or by its average thermal energy ( $\kappa T$ ) thus a 2 eV plasma has a mean translational kinetic energy ( $E_{ave}$ ) equal to 3 eV in three dimensions.<sup>20</sup> The right-hand chart in Figure 8 describes the speed distribution of incident particles and is a Maxwellian distribution defined by the following equation:<sup>20</sup>

$$g(\bar{v}) = 4\pi\bar{v}^2 \left( \frac{m}{2\pi\kappa T} \right)^{3/2} \exp \left( -\bar{v}^2 / v_{th} \right) \quad (4)$$

The energy state of incident particles in an environment along with the plasma density and material properties is all needed for accurate prediction of droplet charging.

One of the more likely missions to employ droplet stream propulsion is remote sensing. These spacecraft will likely utilize a polar orbit in order to provide global coverage. The environment in polar orbit differs significantly from that of lower inclination LEO because high-energy plasma is channeled by the magnetic field toward the Earth and through the auroral regions. Auroral electrons typically have

energy levels of several keV, and are capable of more severe charging than the electrons encountered at lower latitudes. Objects in polar orbit encounter these annular regions above the geomagnetic poles for very short durations four times each orbit. Droplets that transit between satellites in auroral space will experience a much stronger plasma charging environment than droplets transiting at lower latitudes.

Charging of droplets at LEO altitudes differs significantly from charging in GEO because of the large population of low energy plasma subject to attraction or repulsion by a charged object. Electron concentrations in LEO peak at about 300km altitude and vary from about  $1 \times 10^5 \text{ cm}^{-3}$  at night during low geomagnetic activity to  $1 \times 10^6 \text{ cm}^{-3}$  during high geomagnetic activity in the daytime.<sup>28</sup> In GEO, electron number density can vary from a nominal 1.0 electron per cubic cm to a peak density of 1.7 electrons per cubic cm. More important than number density, however, is the energy state of particles entering the near Earth environment, which is mainly influenced by geomagnetic activity. In GEO, energy flux can increase by an order of magnitude from a nominal  $2 \times 10^{12}$  to nearly  $2 \times 10^{13} \text{ eV/cm}^2 \text{ s sr}$  during high geomagnetic activity. Similar increases in energy flux can be seen in the high auroral regions during high geomagnetic activity.<sup>20</sup>

Droplet charging in low latitude LEO was estimated by analytic methods and through numerical simulations, which showed that it is a rather benign charging environment relative to GEO or auroral space. Thus, in this study, emphasis was placed on accurately predicting nominal and peak charging encountered by polar orbiting droplet streams. The auroral regions, like the rest of LEO, contain neutral particles and low energy ions from the atmosphere. However, the auroral zones also contain a significant population of high-energy plasma particles, particularly during periods of high geomagnetic activity. Auroral flux of high-energy electrons with an average temperature between 10eV and 20keV can reach  $10^{10} \text{ electrons/cm}^2 \text{ s}$ . The composition of this ever-changing plasma environment is quite complex, more complex (though less extreme) than geosynchronous environments. As a result, energy flux distributions that characterize the ambient plasma populations in the auroral regions are more complex than those used to predict the charging environment in low latitude LEO and GEO.

To characterize the flux of particles in the orbit environment affecting a droplet it is necessary to determine a number density and particle velocity probability distribution. The time rate of change of

charged particles into the volume of space surrounding a droplet is proportional to the net flow of particles into and out of the volume and the production (ionization) and loss (recombination) of charged particles. Mathematically, this is described by the following equation: <sup>20</sup>

$$\frac{dn}{dt} = (-\nabla n \vec{v}) + Q - L \quad (5)$$

where  $n$  = the charge particle number density,  
 $\vec{v}$  = the bulk flow velocity,  
 $Q$  = the ionization rate,  
 $L$  = the rate of recombination.

In non-polar LEO, the ambient low energy plasma is in thermal equilibrium and  $\frac{dn}{dt}$  is equal to zero, and the normalized probability distribution can be accurately (to a first order) described by a Maxwellian distribution. <sup>20</sup>

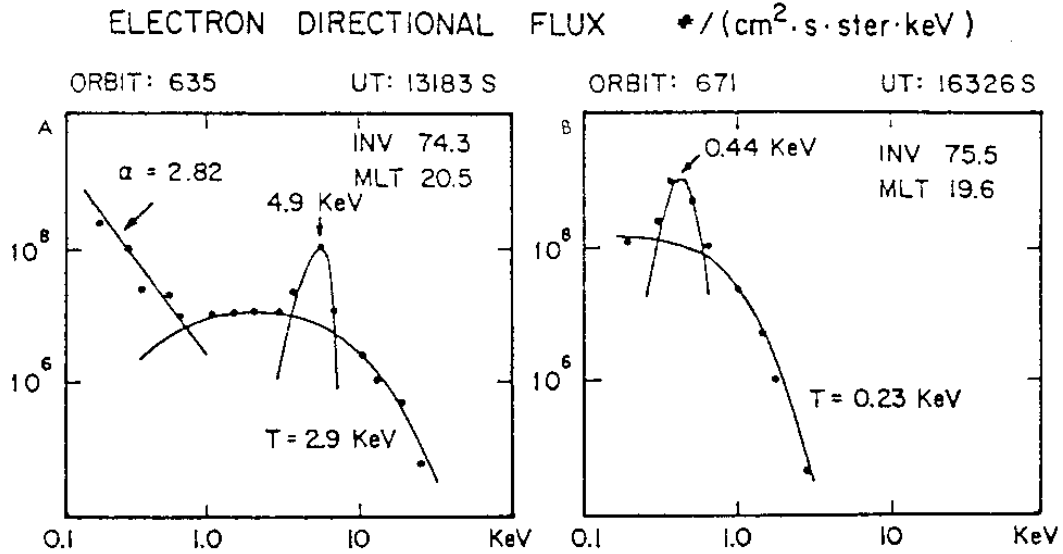
In the Auroral portion of a polar orbit electron velocity distribution is more complex and is not described accurately by a Maxwellian distribution. Hastings and Garrett (1996) use a Gaussian distribution with a full-width half maximum (FWHM) of 3.2 degrees but admit that more complex models account for more variations in the auroral plasma. <sup>23</sup> Figure 10 shows a comparison of actual levels of electron flux densities recorded by spacecraft passing through the auroral region. The figure also shows Fontheim curve fits to the data that accurately describe the flux density as a function of particle energy. A Fontheim distribution is described by the superposition of four terms defined in the following equation:

$$\text{Flux}(E) = \underbrace{\sqrt{\frac{e}{2\pi\theta m_e}} \frac{E}{\theta} n \exp\left(-\frac{E}{\theta}\right)}_{\text{Term 1}} + \underbrace{\pi \zeta_{\max} E \exp\left(-\frac{E}{\theta_{\max}}\right)}_{\text{Term 2}} + \underbrace{\pi \zeta_{\text{gauss}} E \exp\left(-\left(\frac{E_{\text{gauss}} - E}{\Delta}\right)^2\right)}_{\text{Term 3}} + \underbrace{\pi \zeta_{\text{power}} E^{-\alpha}}_{\text{Term 4}} \quad (6)$$

where  $n$  = density of the low-energy ionospheric plasma,  
 $e$  = electron elementary charge,  
 $m_e$  = the mass of an electron,  
 $\theta$  = temperature of the low-energy ionospheric plasma.

The impact of the power law component term exponent,  $\alpha$ , is seen in the first plot in Figure 10 where it describes low energy electron flux during high geomagnetic activity. The various  $\zeta$  terms, as well as  $\theta_{\max}$

$E_{gauss}$  and  $\Delta$  are constants that will be discussed in the next section. The flux density calculated using the Fontheim distribution equation has the units  $(\text{eV ster m}^2)^{-1}$ .



**Figure 10. Auroral Electron Flux Energy Distribution during High (left image) and more Nominal (right image) Magnetospheric and Solar Activity. The 4.9keV Peak is due to the High Energy Plasma Beam Induced by the Magnetic Field (from Fontheim et al, 1982).**

A parametric analysis of the four components of charged particle flux used by NASCAP for auroral charging analysis was performed to identify which components have the greatest impact on DC705 charging. Each environmental input was varied one-by-one in NASCAP charging simulations using a range of values from historical satellite environmental data provided by the Solar Data Analysis Center at NASA's Goddard Spaceflight Center,<sup>21</sup> and from Tribble<sup>28</sup> and Hastings.<sup>23</sup> The parametric analysis determined that the Fontheim component with the greatest impact on maximum surface potential (by at least a factor of 3) was the Gaussian term. This knowledge was then used to select the Fontheim fits to satellite observed auroral data most likely to result in high levels of droplet charging.

NASA's Space Environment Effects (SEE) group at Marshall Space Flight Center has adopted the Fontheim distribution method for characterizing the electron flux in the auroral environment. SEE offers a software tool called the Space Environment Effects Handbook<sup>22</sup> that lists Fontheim parameters that fit data



from auroral observations made by various polar orbiting satellites. DMSP environment data was selected for most analysis because these satellites operate in a 500-800km orbit and because data from these satellites covers a period of more than 35 years. The combination of high-energy electron flux rates and lower flux rates of low energy plasma at DMSP altitudes provides an environment capable of charging droplets to higher potentials than lower altitude polar orbits where low-energy plasma mitigates charge.<sup>23</sup> Values for nominal and strong low altitude auroral environment parameters used in this study are listed in the first two columns of Table 2.

**Table 2. Low and High Altitude Auroral Environment Fontheim Parameters Used in this Study.**

<b>Auroral Environment Parameter</b>	<b>DMSP Strong</b>	<b>DMSP Nominal</b>	<b>DMSP Weak</b>	<b>Freja High Altitude Strongest</b>
Low E Plasma Density ( $\text{m}^{-3}$ )	$3.55 \times 10^9$	$3.55 \times 10^9$	$3.0 \times 10^9$	$1.2 \times 10^8$
Low E Plasma Temp (eV)	0.2	0.2	0.2	0.3
Fraction Hydrogen	0.1	0.1	0.09	0.9
Maxwellian Current ( $\text{Am}^{-2}$ )	$1.40 \times 10^{-6}$	$1.00 \times 10^{-6}$	$3.800 \times 10^{-7}$	$2.86 \times 10^{-9}$
Maxwellian Temperature (eV)	8000	5000	3200	5000
Maxwellian Coefficient ( $\text{Am}^{-2}$ )	$4.35 \times 10^4$	$7.96 \times 10^4$	$7.37 \times 10^4$	227.1
Maxwellian Density ( $\text{m}^{-3}$ )	$5.81 \times 10^5$	$5.25 \times 10^5$	$2.49 \times 10^5$	1500
Gaussian Current ( $\text{Am}^{-2}$ )	$1.40 \times 10^{-5}$	$1.00 \times 10^{-5}$	$8.50 \times 10^{-6}$	$5.78 \times 10^{-7}$
Gaussian Energy (eV)	$2.40 \times 10^4$	$1.10 \times 10^4$	$3.50 \times 10^4$	1500
Gaussian Width (eV)	$1.60 \times 10^4$	1000	$1.80 \times 10^4$	3000
Gaussian Coefficient ( $\text{Am}^{-2}$ )	$4.08 \times 10^4$	$1.02 \times 10^4$	$1.51 \times 10^4$	$1.2 \times 10^5$
Gaussian Density ( $\text{m}^{-3}$ )	$7.77 \times 10^6$	$4.19 \times 10^6$	$4.19 \times 10^6$	$5.23 \times 10^5$
Power Law Current ( $\text{Am}^{-2}$ )	$6.70 \times 10^{-7}$	$1.12 \times 10^{-7}$	$6.7 \times 10^{-8}$	$3.34 \times 10^{-6}$
First Power Law Energy (eV)	50.0	50.0	50.0	0.5
Second Power Law Energy (eV)	$1.60 \times 10^6$	$1.60 \times 10^6$	$1.60 \times 10^6$	$6.5 \times 10^4$
Power Law Exponent	1.10	1.10	1.05	1.90
Power Law Coefficient ( $\text{Am}^{-2}\text{eV}^{-1}$ )	$3.05 \times 10^{11}$	0	$2 \times 10^{10}$	$3.2 \times 10^{12}$
Power Law Density ( $\text{m}^{-3}$ )	$1.03 \times 10^6$	0	$9 \times 10^4$	$1.281 \times 10^8$
Total Electron Current ( $\text{Am}^{-2}$ )	$-5.86 \times 10^{-5}$	$-5.35 \times 10^{-5}$	$-5.35 \times 10^{-5}$	$-9.9 \times 10^{-7}$

These parameters come from fits to data collected by DMSP satellites over several decades and are therefore very accurate predictions of worst-case and nominal auroral charging.

Following analysis with sets of DMSP Fontheim distribution data, similar data for a higher altitude auroral environment gathered by the Freja spacecraft was used to simulate high altitude auroral conditions. Freja was launched in 1992 and operated for 3 years in a polar orbit between 1500 and 1700 km

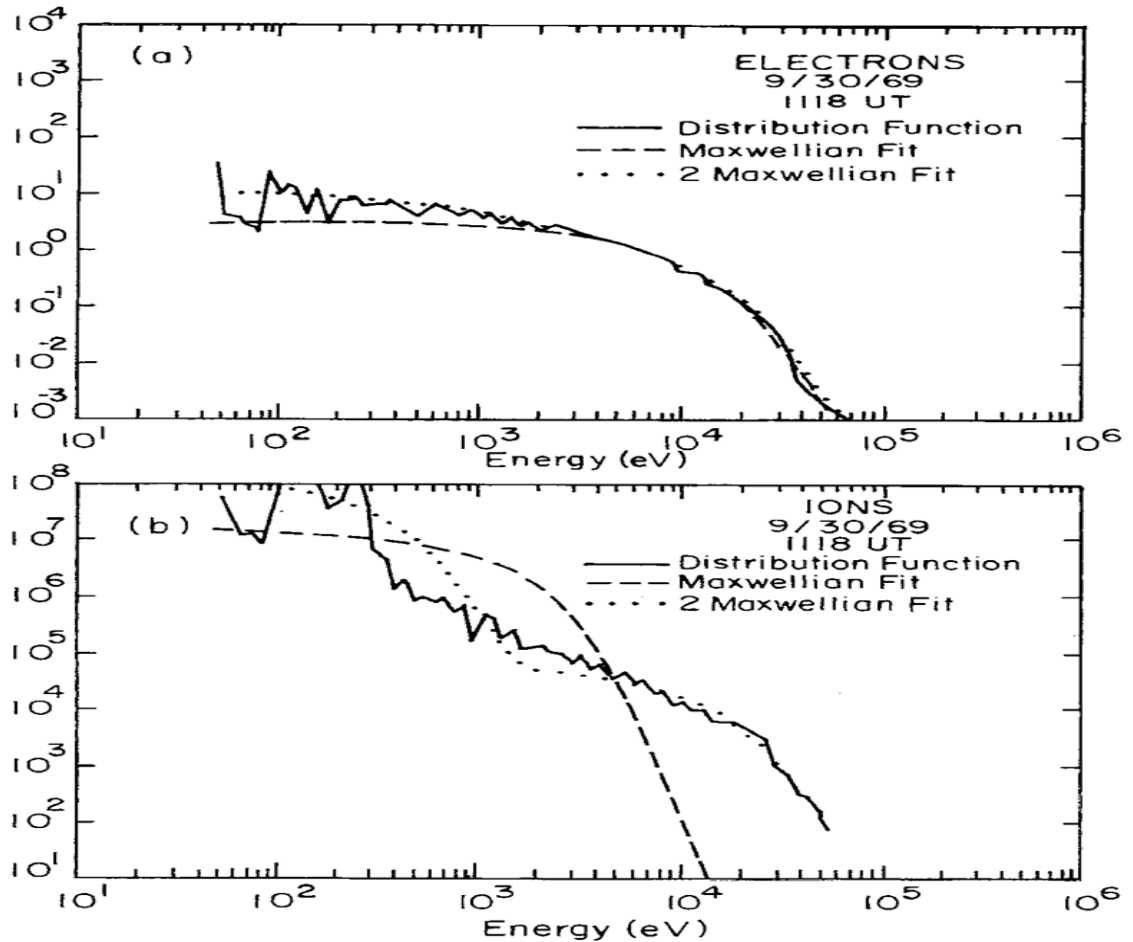
altitude. Freja auroral events are less frequent than DMSP events but sometimes occur in sunlight whereas DMSP events peak exclusively in eclipse. Freja data includes Fontheim fits to five charging events associated with geomagnetic activity of low to moderate severity.<sup>24</sup> The fourth column in Table 2 contains terms of a Fontheim fit to high altitude (1500km) auroral environment data collected by the Freja satellite. Despite its high altitude, it did not collect data on charging environments stronger than the worst-case DMSP environment in Table 2. Consequently, simulations of droplet charging using Freja high altitude auroral data resulted in weaker charging of droplets than the strong DMSP environment did.

## **B. Characterizing the Geosynchronous Charging Environment**

In GEO the mean free path of particles is much greater and collisions are infrequent enough that ions and electrons often have a different average thermal energy. Figure 11 shows electron and ion flux distribution data from the Applications Technology Satellite (ATS) satellite. The environment depicted is based on 10 days between 1969 and 1972 that represent a wide range of geomagnetic activity. Plasma injection events occurring at local midnight were selected to isolate variations associated with a single event. Collision frequency is low enough in this data that ion and electron flux distribution of the ATS-5 data does not follow a Maxwellian profile.<sup>32</sup> Studies of environmental data from ATS and the Spacecraft Charging AT High Altitudes (SCATHA) spacecraft have determined that an accurate distribution function in GEO requires at least four moments. To provide more analytic simplicity to spacecraft designers, Garrett and DeForest<sup>25</sup> derived Maxwellian representations of the plasma distribution functions from the four primary moments. These single and double Maxwellian representations (dashed lines) are shown in Figure 11 alongside actual flux data from the ATS-5 spacecraft.

The single Maxwellian tends to underestimate the density of low-energy electrons while providing an accurate representation of the high-energy distribution of electrons. The single Maxwellian tends to underestimate the density of both low and high-energy ions and is not as well suited to describing the ion distribution as it is at describing electron distributions. Since electron processes tend to dominate charging in GEO, a single Maxwellian is usually accurate enough for practical spacecraft design purposes.<sup>32</sup> In fact,

the original NASA design guideline, published in 1986, describes the worst-case GEO charging environment with a single Maxwellian distribution.<sup>26</sup>



**Figure 11. ATS-5 Electron (top) and Ion Distribution Functions with Single and Double Maxwellian Fits (from Hastings, 1996)**

Results of charging simulations of DC705 in both single and double Maxwellian distribution environments are presented in the next chapter and show that the highest level of charging resulted when a double Maxwellian distributions was used. This is believed to be the case because the double Maxwellian predicts a higher density of low energy electrons that cause negative charging through deposition.

Parameters for three charged particle distribution models of GEO environments used in this study are shown in Table 3. The ionic composition is assumed 100%  $H^+$  in all three distributions. The first two of these models are defined by NASA-TP-23613 and are known as the NASA worst-case GEO environment.<sup>23</sup>

These worst-case parameters are single and double Maxwellian distribution fits to SCATHA and ATS-6 satellite data. Both distributions provide a high flux of high-energy electrons capable of charging certain spacecraft materials to some of the largest negative potentials ever seen.<sup>26</sup> These distributions constitute the worst-case NASA design guidelines specified by Purvis et al,<sup>26</sup> in 1984 and revised by JPL scientists in 2005.<sup>26</sup> These guidelines have remained the standard for surface electrostatic charging among U.S. spacecraft designers for over two decades.<sup>27</sup> The last plasma distribution in Table 3 is a nominal GEO charging environment. This nominal environment represents average GEO environment conditions as reported by the SCATHA and ATS-6 spacecraft.

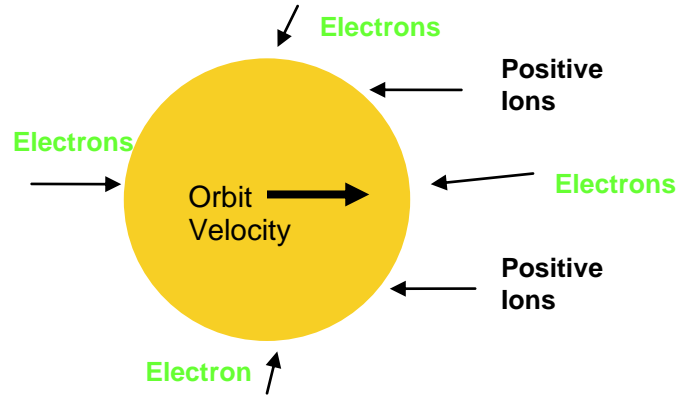
**Table 3. GEO Charging Environments Used in this Study.**

<b>Environmental Parameter</b>	<b>NASA Worst-case</b>	<b>NASA Worst-case</b>	<b>Nominal GEO</b>
Distribution	Single Maxwellian	Double Maxwellian	Double Maxwellian
Electron Density ( $\text{m}^{-3}$ )	$1.1 \times 10^6$	$1.2 \times 10^6$	$7 \times 10^5$ ; $2.25 \times 10^5$
Electron Temperature (eV)	$1.2 \times 10^4$	$1.6 \times 10^4$ ; 1000	400; 8200
Ion Density ( $\text{m}^{-3}$ )	$2.4 \times 10^5$	$2.4 \times 10^4$ ; 8820	$6 \times 10^5$ ; $4 \times 10^5$
Ion Temperature (eV)	$2.95 \times 10^4$	$2.95 \times 10^4$ ; 111	450; $1.9 \times 10^4$
Electron Current ( $\text{A/m}^2$ )	$3.3 \times 10^{-6}$	$4.1 \times 10^{-6}$	$9.6 \times 10^{-7}$
Ion Current ( $\text{A/m}^2$ )	$2.5 \times 10^{-8}$	$2.5 \times 10^{-8}$	$2.2 \times 10^{-8}$

### **C. Space Charging Theory**

As objects move through space they come into contact with ambient electrons and ions from the sun and Earth's atmosphere that constitute the plasma environment of space. Free electrons in near-earth space move in all directions at very high speeds that are about 200km/s, more than an order of magnitude higher than orbital velocities. Consequently, electrons impact orbiting bodies from all directions as depicted in Figure 12. In contrast, positively charged ions in near-earth space have an average velocity magnitude ( $\bar{v}$ ) of only about 1km/s. This is significantly slower than orbit velocity, and ions tend to hit the ram side of orbiting bodies much more frequently than the wake side. The velocity of electrons is about two orders of

magnitude greater than that of ions and the resulting flux of electrons to the surface is up to 50 times greater than the flux of ions to the surface.<sup>23</sup> Because electrons have a flux rate so much higher than that of ions they tend to play a more significant role in determining the charge of materials in space than ions do.



**Figure 12. Charging Sources in the Space Plasma Environment.**

Atoms near a surface absorb low energy electrons and materials in LEO and Polar orbit tend to charge negatively under nominal geomagnetic conditions when incident electron energies are low. As the surface material is charged, a plasma sheath forms around the object and Coulomb repulsion forces become sufficient to reflect some inbound electrons. As a result, negative charging in LEO due to plasma is limited to just a few volts, even during high geomagnetic activity.<sup>28</sup> The presence of low energy (cool) atmospheric plasma in LEO and Polar orbits has a similar charge limiting effect for objects that are charged positively by secondary electron production or photoemission of electrons at the surface. As the surface charges positively, electron deposition rates increase as fewer electrons are reflected.

A droplet in the ambient space plasma acts like an isolated electrical probe. As such, it adopts an electrostatic potential consistent with charge collection as modeled by Maxwell's equations.<sup>29</sup> Hastings and Garret<sup>23</sup> have shown that the divergence of the Poisson equation and Ampere's law yield the following relationship for a sphere in a space plasma environment:

$$\frac{\partial \rho}{\partial t} + \nabla \cdot \vec{j} = 0 \quad (7)$$

Here  $\rho$  is the charge density and  $\vec{j}$  is the incident current density at the object's surface. Integrating over the space outside of the sphere and applying the divergence theorem yields

$$\frac{\partial Q}{\partial t} = I_{net} \quad (8)$$

where  $Q$  is the total charge of the sphere (in Coulombs) and  $I_{net}$  is the net current at the surface. To determine the charge of an object immersed in a plasma it is necessary to solve the net current equation while simultaneously solving Poisson's equation for charge density:<sup>23</sup>

$$-\rho = \epsilon_0 \nabla^2 \phi = e(n_i - n_e) \quad (9)$$

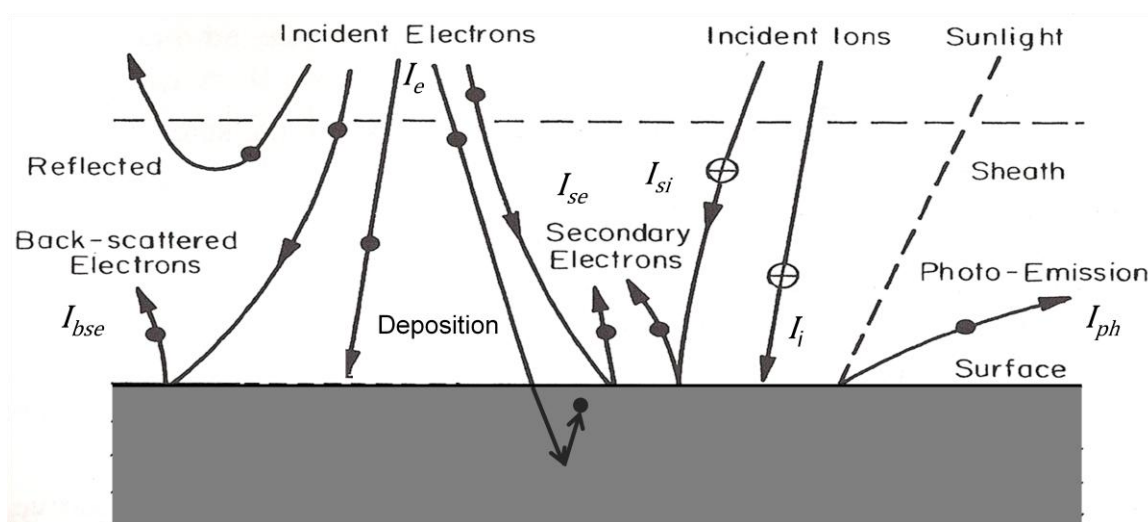
where  $\epsilon_0$  is the permittivity constant of free space,  
 $\phi$  is the local charge potential (Volts),  
 $e$  is the charge of an electron (C),  
 $n_e$  is the local electron density ( $\text{m}^{-3}$ ),  
 $n_i$  is the local ion density ( $\text{m}^{-3}$ ).

An object in space is exposed to many different processes that add or remove electrons at the surface. Determining the net current at the surface of an object is a matter of determining and then summing the current due to each of these processes. Quantifying net current is complicated by the fact that the processes that add or remove electrons from the surface are also influenced by the surface charge. Secondary electrons with sufficient kinetic energy to escape in one instant may be retained by a more positively charged surface in the next. Consequently, the most accurate charge determination algorithms are iterative, solving for the charge density and potential of the elements of a mesh of small volumes for a time step and then repeating the process for the next time step. Mathematically, the current balance for a droplet at a floating electrostatic potential ( $V$ ) is expressed as:<sup>30</sup>

$$I_{net}(V) = I_e(V) - [I_i(V) + I_{se}(V) + I_{si}(V) + I_{bse}(V) + I_{ph}(V)] \quad (10)$$

where  $I_e$  is the incident electron current on the surface,  
 $I_i$  is the incident ion current,  
 $I_{se}$  is the secondary electron current caused by the incident electrons,  
 $I_{si}$  is the secondary electron current caused by the incident ions,  
 $I_{bse}$  is the backscattered incident electrons,  
 $I_{ph}$  is the secondary electron current caused by incident photons.

Each of the terms inside the square brackets in the net current equation represents a process that removes electrons from the object or, much less frequently, adds positive ions to the object. Terms inside the brackets reduce current flow to the object and result in negative (or less positive) charging of the material. Processes that result in positive charging are principally caused by the removal of electrons from atoms in the surface material by energetic particles or photons entering the surface. An electron or ion entering a material with an energy state above the material's ionization potential may produce one or more secondary electrons. An inbound electron is slowed through random elastic collisions with nuclei and penetrates a certain distance into the material (usually tens of Angstroms).<sup>23</sup> Electrons penetrate farther into low-density materials because there are fewer nuclei and less likelihood of collisions. When an electron is slowed sufficiently, Coulomb force interaction with other electrons bound to atoms within the material may liberate those electrons from their parent atoms. These free electrons are called secondary electrons.



**Figure 13. Charging Processes at the Surface of a Dielectric Material (after Hastings, 1996).**

Secondary electrons may escape the material, be conducted by the material, or be absorbed by other atoms in the material depending on the energy state of the secondary and on material properties discussed in the remainder of this chapter. Incident ions and photons of sufficient energy can also produce secondary electrons. These sources of secondaries are generally less significant than incident electrons but their impact on DC705 charging is discussed in the next section and is accounted for by NASCAP simulations. Figure 13 provides an overview of the various processes that result from the impact of charged

particles or photons at the surface of a dielectric material. As the surface charge increases, low energy electrons or ions can be reflected, reducing the rate of plasma deposition.

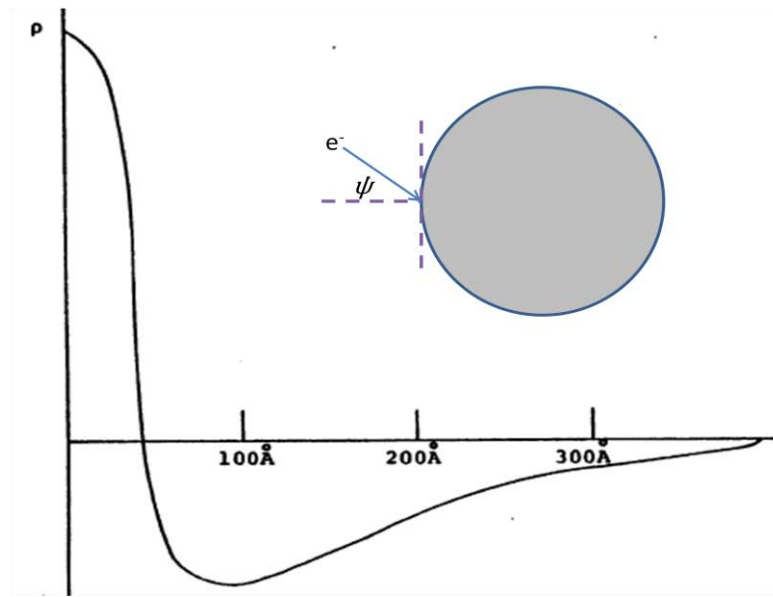
Electrons can also be backscattered by interaction with atomic nuclei so that the electron's trajectory is changed without much energy loss and the electron escapes the material. Capture of low energy electrons by atoms in the material, called deposition, results in negative material charging. High-energy electron impacts can result in a net negative or net positive charge on an object. Because of the range of effects an incoming electron or ion can have, probability distributions are used to describe the yield of secondary electrons for a given material as a function of incident electron energy. This yield is used to quantify the resulting current to or from a material as a function of the flux density and energy distribution of incoming electrons. The effect of each of these processes depends on material properties described in the next section.

Secondary electrons are produced within an atom at a range of energy states called the valence band. Conducting materials such as metals have a conduction band adjacent to the valence band. In conductors, secondary electrons require very little energy to move into the conduction band and free electrons flow readily throughout the material. In an insulating material, there is a band gap between the valence and conduction energy bands that is sufficiently high that very few secondary electrons can reach it. As a result, secondaries are not slowed by interactions with other electrons and can often escape the surface of an insulating material causing positive charging in the material. In a semi-conductor, the band gap is small enough to allow some secondary electrons to reach the conduction band and travel throughout the material just as in a conductor. Some secondaries will escape the material completely as they typically do in an insulator. Others will not escape, limiting the amount of positive charge that develops in a semi-conductor to levels below the levels that develop in an insulator.

The higher the energy state of an incident electron, the more deeply into a material it is likely to penetrate before producing secondary electrons. The greater the penetration depth, the less likely secondaries are to escape the material surface before being absorbed by other atoms. Absorption of secondary electrons liberated by deeply penetrating high-energy electrons is called deep bulk surface charging and results in negative charging of dielectric materials typically hundreds of Angstroms beneath the surface. The charge density profile produced within a typical dielectric material exposed to a nominal



space environment is shown in Figure 14. Within a few tens of angstroms of the surface a positively charged layer forms due primarily to emission of secondary electrons and photoemissions. Beyond several tens of Angstroms, a distribution of negative charge is seen that is the result of stopped incident electrons and deep bulk surface charging.<sup>31</sup> Figure 14 also shows the definition of incidence angle,  $\psi$ , of incoming electrons to the surface of a sphere. The larger the incidence angle, the greater the likelihood that liberated electrons will reach the surface and contribute to the secondary electron current. The method NASCAP uses to account for incidence angle is discussed in the next chapter.



**Figure 14. Incidence Angle Definition and Typical charge density profile for a dielectric material (graph from Katz et al, 1977)**

The total secondary yield of electrons from a surface,  $\delta$ , is defined as the average number of emitted electrons produced by the surface per incident electron. This total yield is composed of true secondary electrons,  $\delta_s$ , and backscattered electrons,  $\eta$ , as in the following equation:  $\delta = \delta_s + \eta$ . The backscattering rate,  $\eta$ , is the average number of incident electrons scattered from the surface. Essentially, these electrons are reflected from the surface and leave the surface with more energy than true secondary electrons. Backscattered electrons have an energy distribution that is usually peaked close to the primary incident energy and most of these electrons have an energy state of more than 50eV. Experiments done to

determine true secondary yield rates for DC705 caused by incident electrons were found in the literature and are presented later in this chapter.

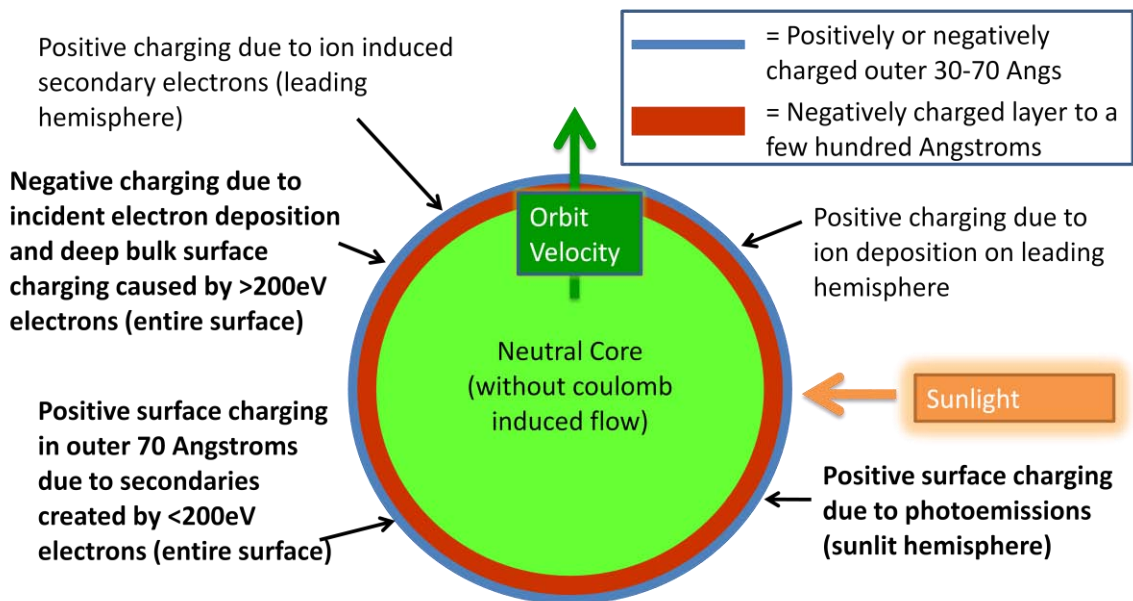
High-energy photons from the sun play a role in charging DC705 droplets because of their ability to couple with electrons. If photon energy is sufficient (at least 7.2eV for DC705) there is a certain probability that the photon will impart enough energy to liberate an electron within an atom of the material. This process is the photoelectric effect and results in photoemission of electrons called photoelectrons. For Earth orbiting spacecraft, the current due to photoemissions is generally  $10\text{-}40\text{ }\mu\text{A}/\text{m}^2$  and is usually less significant than other sources of secondary electrons, particularly in GEO and auroral space.<sup>32</sup>

#### **D. Space Charging Theory Applied to Silicone Oil Droplets**

The first particles to affect a newly formed droplet exposed to the sun are solar photons travelling at the speed of light. Photons above the electron binding energy for DC705 give the droplet a positive surface charge by liberating photoelectrons from the material. This initial positive charge due to photoemissions is followed by low energy electron deposition inducing a negative charge and secondary electron production producing a positive charge. The charged surface attracts oppositely charged particles from the surrounding plasma and the first layer of a plasma sheath is formed. This layer, in turn, attracts particles from the ambient plasma with charge opposite that of the first layer. In this manner, the sheath grows and dampens the surface potential until it reaches a thickness at which the surface potential is completely shielded and has zero potential relative to the ambient plasma.

Droplet orbital velocity determines which side of the droplet is exposed to positive ions. In LEO, below about 650km, most ions are atomic oxygen atoms ionized by solar EUV radiation. Above 1000km protons are the dominant ion species, and ions in GEO are almost exclusively protons.<sup>23</sup> In LEO, the droplet's orbital velocity is greater than that of most ambient ions. Because of this, most ion impacts occur on the leading hemispheric surface. Electron velocities are more than an order of magnitude greater than orbital velocities and therefore electron impacts occur nearly uniformly around the droplet's spherical

surface. Distribution of differential hemispheric charge is limited because DC705 is a relatively poor conductor. The various effects acting on a droplet that is moving perpendicular to the sunward direction are summarized in Figure 15 where the processes that are typically the most significant are in bold text:



**Figure 15. Charging Processes Affecting DC705 Droplets.**

The fact that DC705 is a liquid allows for movement of charged molecules within the fluid sphere. Positively charged molecules in the outer layer are attracted to underlying negatively charged molecules, which can lead to mixing of ions in the charged outer region of the droplet. If such mixing occurs on time scales below the transit time of droplets, the result will be a more uniform distribution of charge over the entire droplet surface. In sunlit droplets Coulomb forces may also induce fluidic flow from the sunlit side to the more negatively charged shaded side.

Fluidic mixing of charged molecules may lead to the repulsive transport of charged molecules into the underlying neutral core of a droplet. Movement of ions into the neutral core of a droplet will result in an influx of more neutral molecules to the surface that could contribute to more absorption of secondaries and a more negative overall droplet charge. This mechanism was not quantified for this study and is assumed to have a negligible effect. The redistribution of charge through fluidic flow promotes uniform charge on all surfaces. The timescale on which this will occur was not quantified and but is believed to be significantly

less than the transit time of droplets. It will be shown in the next chapter that eclipsed droplets have nearly uniform charge without fluidic flow and can be treated as point masses. In chapter 4 is shown that uniform charge distributions cause the strongest inter-droplet electric fields resulting in droplet dispersion from the intended centerline path between satellites.

In LEO, charged particles from the sun are, on average, much more energetic than particles from the Earth's upper atmosphere and are more likely to ionize surface materials. Unlike neutral particles, charged particles are influenced by electromagnetic fields that are often produced by spacecraft components. Thus, certain surfaces of spacecraft can experience a greater fluence of charged particles due to their proximity to on-board electromagnetic fields. Since droplets, transiting hundreds of meters, will only experience artificial magnetic fields when close to the sending or receiving satellite, they will experience an unaltered flux of charged particles for the bulk of their transit time. This study does not consider the impact of on-board spacecraft magnetic fields and assumes that droplets are only affected by the unaltered ambient plasma environment.

Total sheath thickness is characterized by the Debye length and it is generally assumed that a sheath extends several Debye lengths from the surface of a spacecraft. Particles a few Debye lengths away from a charged body are effectively screened from the body by the plasma.<sup>28</sup> The point where the electric potential of a body is completely screened from the surrounding plasma is called the Child-Langmuir distance.<sup>32,33</sup> this distance is commonly used in the analysis of electric field strength surrounding a spacecraft and was calculated for a DC705 droplet at various surface voltage potentials. However, an assumption made in development of the Child-Langmuir law is that the sheath is thin relative to the radius of the material surface, which is not the case for droplets of the size being considered. Calculation of Child-Langmuir distance using conventional spacecraft charging equations for Droplets in LEO results in a distance equal to 5 Debye lengths for a 5V surface potential and 15 Debye lengths for a 25V surface potential. These results violate the rule of thumb 3 Debye length estimate of sheath thickness and indicate that more rigorous methods of characterizing the potential surrounding a droplet are needed.

The potential in the plasma near a charged surface  $V$  is given by the Poisson equation:

$$-\rho = \epsilon_0 \nabla^2 \phi = e(n_i - n_e) \quad (11)$$

The computer based charge simulation code; NASCAP solves this equation by applying the specified environment flux distribution electron and ion densities in an iterative process while developing the sheath at the surface and recalculating the particle densities accordingly. One advantage this gives NASCAP, over other charge modeling codes, is its ability to calculate accurate electric fields in the surrounding plasma.<sup>32</sup> NASCAP employs the Boundary Element Method as developed by Brebbia<sup>34</sup> as a means for relating fields and potentials in the surrounding plasma to sources at the surface. This method, originally developed for thermal analysis of surface cracking in materials, allows rapid summation of the coulomb fields in the sheath.<sup>50</sup> This allows rapid determination of changes in plasma densities, current flow to/from the surface and a new solution to Poisson's equation to determine changes in electrostatic potential that occur during the time step. The time step is determined by the equation  $\tau = \Delta V j / c$  where  $j$  is the maximum surface current density,  $c$  is the capacitance per unit area, and  $\Delta V$  is an approximate change in potential during the time step.<sup>50</sup>

### E. Droplet Charge Prediction by Analytic Methods

Models predicting material charging in the space environment are derived from electric probe theory that stems from early work by Irving Langmuir. Langmuir probes on spacecraft and in laboratories are widely used to characterize the surrounding plasma environments.<sup>35</sup> In this study, electric probe theory was applied to the problem of a droplet charging in space in order to better understand the magnitude of the applicable charging mechanisms and to make a first order prediction of equilibrium droplet charge to compare with results from iterative computer based tools. The goal of analytic charging analysis is to quantify the floating voltage potential ( $V_f$ ) of a material. An object at floating potential has a zero net current at the surface and a balance between the attraction of ambient ions, the repulsion of ambient electrons and the production of secondary electrons.

A droplet in LEO eclipse, during nominal geomagnetic conditions, experiences low secondary electron production because there are few high-energy incident electrons or photons. Electrons are

collected much more readily than ions because of the speed difference between the two particle types. Because ion deposition only occurs on the leading hemisphere, it is expected that this hemisphere will charge more positively than the trailing hemisphere. Several mechanisms contribute to a more uniform charge distribution on a droplet. Since the leading hemisphere charge density is less negative, Poisson's equation,  $-\rho = \epsilon_0 \nabla^2 \phi$ , dictates that the electrostatic potential of the leading hemisphere surface is weaker. The weaker surface potential results in a greater density of electrons in the sheath surrounding the leading hemisphere. A higher concentration of electrons in the sheath results in a greater flux of electrons to the surface and mitigation of positive surface charge. In this way, the sheath itself tends to mitigate non-uniform charging of the droplet.

Another mechanism working to distribute charge more evenly around the surface of a droplet occurs at the boundary of the leading and trailing sheaths. Here electric field forces between particles tend to distribute charged particles more evenly between the leading and trailing sheaths and subsequently throughout each sheath. Because DC705 is a semiconductor, some distribution of electrons is accomplished through conduction that contributes to a more uniform charge distribution. The mechanisms of charge redistribution in the plasma sheath just described, as well as those associated with fluidic flow in droplets described previously all contribute to more uniform distribution of charge in droplets. Moreover, these mechanisms occur in droplets in any orbit and in both eclipse and sun. In low latitude LEO where secondary electron production is low, the strongest surface charge occurs when a droplet is in eclipse. A sunlit hemisphere will incur a positive or less negative charge and the charge redistribution methods will tend to mix positively and negatively charged molecules and reduce the peak magnitude of charge on any surface. Thus, the most useful equation for a LEO droplet is one that describes potential in eclipse. The derivation of an analytic formula for the equilibrium floating potential of an eclipsed droplet in low latitude LEO follows.

When a droplet is created in LEO eclipse, the initial charging process is electron deposition at the surface. This results in a negative surface charge on the entire droplet surface. As a result, no positively charged ions are repelled and the flux of ions to a droplet is simply a function of the ion number density ( $n_i$ ) times the velocity of the droplet relative to the ion population ( $v_0$ ) times the cross sectional area of the

droplet ( $A_i$ ). Current due to ions is then found by multiplying the ion flux by the elementary charge as shown by:<sup>20,28</sup>

$$I_i = en_i v_0 A_i \quad (12)$$

where  $n_i$  = ambient ion density (equal to electron density in a quasi-neutral plasma),

$e$  = electron elementary charge,

$A_i$  = area collecting ions (cross sectional area of the droplet sphere that is perpendicular to relative flow of ions),

$v_0$  = orbital speed (assumed to be much greater than ion thermal speed).

Since average electron velocity is much greater than orbital velocity, it is assumed that droplets are stationary relative to electrons. If a neutral plane is inserted into a population of particles with random motion, half of the particles in the population will have a velocity component moving toward the plane and the other half will move away from the plane. This approximates the situation at the surface of a droplet before it has acquired a charge potential. Bird has shown that the particle flux into such a plane is given by<sup>36</sup>

$$\Gamma_{\text{random}} = n\bar{v}/4 \quad (13)$$

Where  $n$  is the number density of the population surrounding the neutral plane and  $\bar{v}$  is the average particle speed in the population. The number of electrons impacting the surface of a neutral droplet is then approximated by  $\Gamma_{\text{random}}$  times the droplet surface area,  $A_e = 4\pi r^2$ .

A charged droplet with a surface potential,  $\phi$ , influences the number density of the surrounding plasma. A positive potential attracts more electrons to the surface vicinity while a negative potential reduces this number. Plasma density is high enough in non-polar LEO to assume that electrons in the ambient plasma are in thermodynamic equilibrium.<sup>23,28,29</sup> Ludwig Boltzmann showed that a set of electrons in thermal equilibrium will assume a density in accordance with the following equation known as the Boltzmann relation for electrons:<sup>20</sup>

$$n_{\text{surf}} = n_e \exp\left(\frac{\phi e}{\kappa T_e}\right) \quad (14)$$

where  $n_{surf}$  = the local or surface electron number density ( $m^{-3}$ ),  
 $n_e$  = the ambient electron number density outside of the sheath ( $m^{-3}$ ),  
 $\phi$  = the voltage potential at the position of interest (Volts)  
 $\kappa$  = the Boltzmann constant =  $1.381 \times 10^{-23}$  (J/K),  
 $e$  = electron elementary charge,  
 $T_e$  = average electron temperature.

If a LEO eclipsed droplet is at an equilibrium charge potential where the net current at the surface is zero then the droplet must have a negative charge to repel enough electrons for the deposition of electrons and ions to be equal.

Substituting the local number density for  $n$  in equation 13 and multiplying by surface area and the fundamental charge of an electron,  $e$ , yields the following equation for current:<sup>28</sup>

$$I_e = eA_e \left[ \frac{\bar{v}_e n_e}{4} \exp\left(\frac{\phi e}{\kappa T_e}\right) \right] \quad (15)$$

Here the term inside square brackets is the electron flux rate to the droplet surface from the fully developed sheath.

For a droplet at floating potential, current due to incident electrons must equal current due to ions. Setting the two current sources equal to each other results in the following equation:

$$en_i v_0 A_i = \frac{n_e e A_e \bar{v}_e}{4} \left[ \exp\left(\frac{e\phi}{\kappa T_e}\right) \right] \quad (16)$$

Rearranging terms, and assuming that  $\phi$  is equal to the droplet floating potential,  $V_{fl}$ , yields the following equation for floating potential:

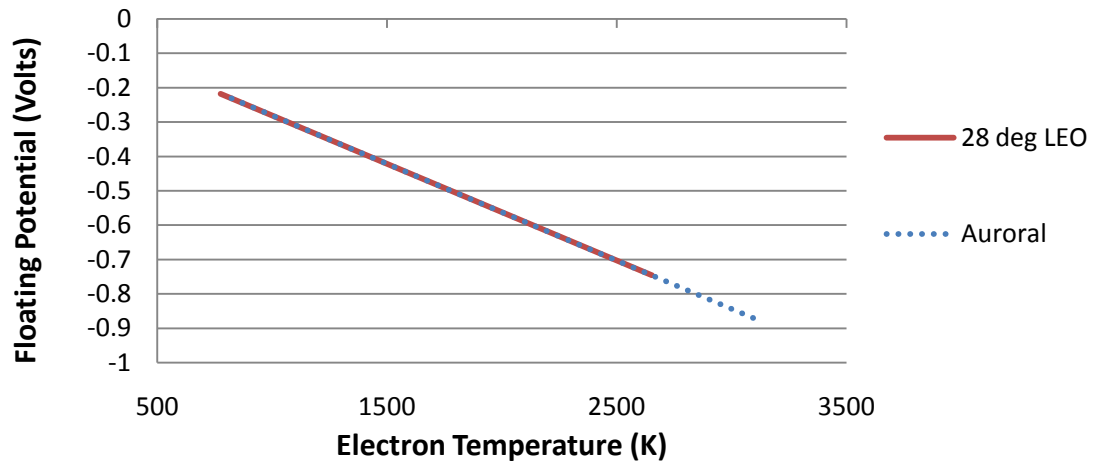
$$V_{fl} = \frac{\kappa T_e}{e} \ln\left(\frac{4v_0 A_i n_i}{\bar{v}_e A_e n_e}\right) \quad (17)$$

The effective area exposed to ions coming from only one direction is equal to the cross sectional area of a droplet ( $A_i = \pi r^2$ ) while the entire surface is impacted by electrons with random motion over a surface 4 times larger. The number density of electrons is roughly equal to the number density of ions. Thus, the floating potential for a sphere reduces to:

$$V_{fl\_sphere} = \frac{\kappa T_e}{e} \ln\left(\frac{v_0}{\bar{v}_e}\right) \quad (18)$$



Here  $T_e$  is the average electron temperature. The calculated floating potential using Equation 18 is shown in Figure 16 for the range of electron mean temperatures expected in LEO and the atmospheric (cool) plasma in Polar orbit. Minimum to maximum values for electron temperatures from the International Reference Ionosphere (IRI) for a 400km, 28 degree inclined orbit and a 500km, sun-synchronous orbit, were used in these calculations.<sup>23</sup> The range of electron temperatures presented represents the range seen at 500km over the course of a solar cycle (as predicted by the IRI model).

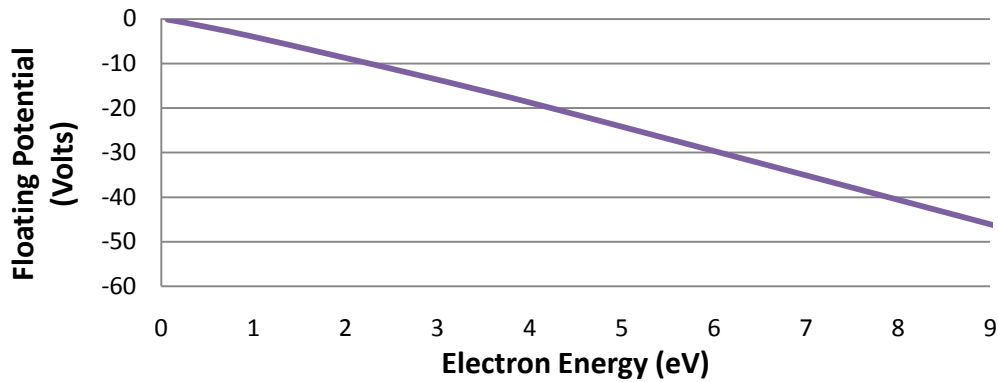


**Figure 16. Floating Potential Resulting from Atmospheric Plasma in LEO and in Auroral Eclipse during low auroral activity (at 500km).**

The results presented in Figure 16 for polar orbit reflect charging induced by low-energy plasma from the atmosphere, but not high-energy plasma in the aurora. High-energy influxes can occur nominally but are more common during periods of high auroral activity associated with high magnetospheric activity. Variations in Earth's magnetic field can cause the number flux density of plasma to vary by a factor of five.<sup>23</sup> Auroral activity results in an influx of plasma at energy states orders of magnitude greater than the state of low-energy plasma from the atmosphere. This plasma is attracted to the poles by the geomagnetic field and therefore tends to impact a droplet on the hemisphere facing away from Earth as it transits polar orbiting satellites.

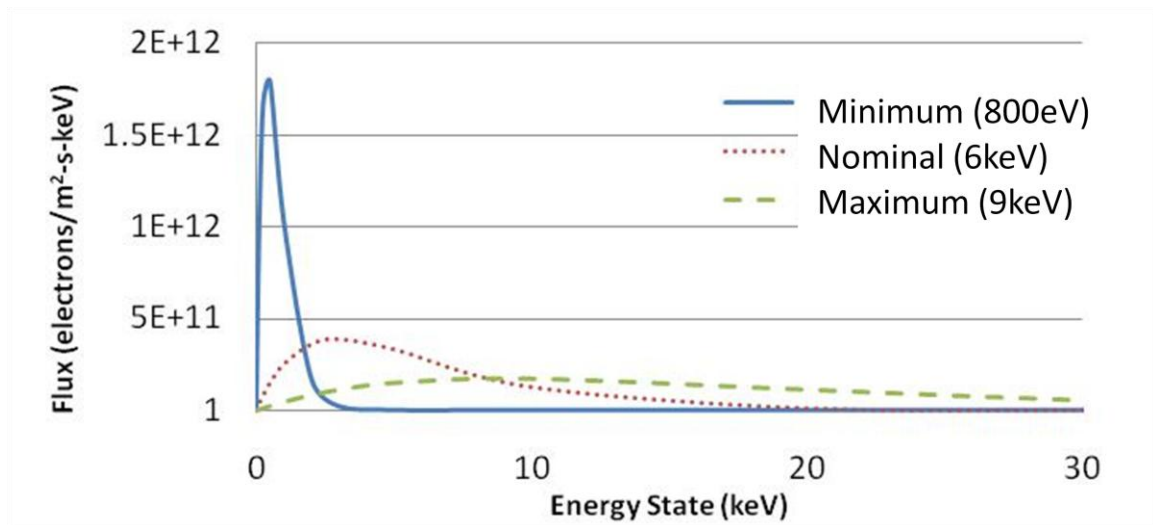
Floating potential for electron energies seen during moderate auroral activity was calculated with equation 18 and is presented in Figure 17. These results are more negative than in reality because electrons at the higher energy states on the ordinate will result in some secondary electron production that is not

accounted for, and will cause the droplet to charge more positively and the curve to become more flat at higher electron energy states.



**Figure 17. Predicted Floating Potential at Energy Levels Approaching those of Auroral Beams.**

High-energy electrons can also result in deep bulk surface charging which incurs a negative charge to the droplet. Later in this chapter it is shown that deep bulk surface charging is expected in DC705 with normally incident electrons at energy levels above 250eV. Accounting for secondary electrons and deep bulk surface charging analytically in auroral droplets is difficult because of the highly variable nature of electron densities and energy states of auroral particles.



**Figure 18. Maximum, Nominal, and Minimum Auroral Electron Number Flux Distribution (MIL-STD-1809).**

The wide variation of electron energy distribution is evident in Figure 18 that shows number flux density in auroral space as predicted by MIL-STD-1809 (1991).<sup>23</sup> This chart reveals that periods of minimum auroral activity have significant levels of flux at energies below 250eV where secondary electron production is high. However, even during minimum levels of auroral activity, the average energy of precipitating electrons is about 800eV and a significant portion of the incident electrons will cause deep bulk surface charging. During nominal conditions the average energy is 6000eV and during maximum auroral activity average the average energy state is 9000eV.

The high-energy state of auroral plasma beams implies that there is very little secondary electron production in both the nominal and maximum situations. Indeed, if the droplet presented a flat surface perpendicular to the beam the material would experience deep bulk surface charging almost exclusively. However, electrons with high incidence angles to the surface are more likely to produce secondaries that escape the material. As a result, it is expected that the hemisphere exposed to an auroral beam of electrons will have a more negative charge beneath surfaces that are more normal to the beam and a more positive charge on surfaces that are highly inclined to the beam. The worst-case scenario for maximizing droplet charge magnitude is one in which very few secondaries are emitted. Thus a droplet modeled as a flat surface positioned perpendicular to the auroral beam with primarily deep bulk surface charging will assume a conservatively negative floating potential. In the presence of low-energy plasma, such a strongly negative droplet will repel low energy electrons, and attract low energy ions present in auroral space.

Auroral ions are often ignored in descriptions of auroral charging of materials since number flux density of ions to a surface is typically 50 times less than that of electrons.<sup>23</sup> As with auroral electrons, auroral ions come in a variety of energy states but unlike electrons, studies to characterize these energy distributions were not found in the literature. Attempts were made in this study to analytically predict the impact of much droplet charge on ion attraction and flux rates. The results of this analysis indicate that electrostatic forces on a droplet with a charge of -9V are strong enough to accelerate atomic oxygen ions less than a millimeter from the surface to speeds an order of magnitude greater than orbital speed. However, given the uncertainty of auroral ion energy levels, incorporation of altered ion flux rates was not incorporated into the analytic auroral charging model described in this section.

The analytic approach to predicting floating potential discussed in this section assumes the droplet is in eclipse. Accounting for the direct effects on a material of photoemissions analytically is possible given the relatively constant nature of the photon flux from the sun in the EUV region of interest. However, photoemissions make a droplet charge more positively and the high number of low energy electrons in LEO and the auroral zones limit positive charging of droplets. Thus, there is little utility gained by incorporating photoemission current into the floating potential equations for LEO or the auroral zone where the magnitude of negative charge is the greatest concern. It will be shown in chapter 4 that solar effects are beneficial to the droplet stream concept and therefore photoemission of electrons was not modeled analytically. The impact of photoemission was analyzed numerically using NASCAP.

#### **F. Properties Affecting Secondary Emission of Electrons**

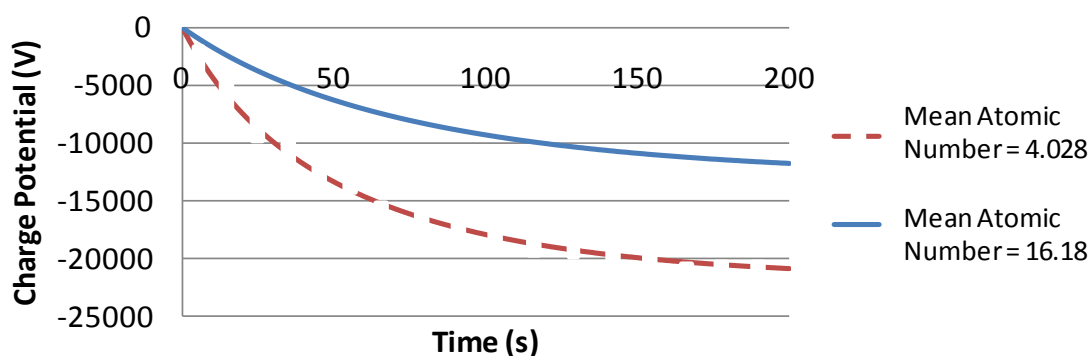
The first of the key charging properties used by NASCAP is average atomic number. Total atomic number is known for DC705 and is computed directly from the chemical formula for DC705 that contains 3 silicon atoms linked to each other by 2 oxygen atoms. Each silicon atom is also bound to a methane molecule ( $\text{CH}_3$ ). Additionally, the middle silicon atom is bound to a Benzene ring ( $\text{C}_6\text{H}_5$ ) and the two outside silicon atoms are bound to two Benzene rings (see Figure 3). A DC705 molecule has a molecular weight of 546AMU. To determine the average atomic number for DC705 the total atomic number is divided by the total number of atoms in the molecule, which is 72. The resulting average atomic number is 4.028 AMU.

Atomic number is significant to charging of DC705 because of its impact on backscattering of electrons. NASCAP determines backscattering yield using a theory developed by Everhart<sup>37</sup> and extended by McAfee.<sup>38</sup> This theory assumes a normal incidence angle backscattering yield  $\eta$  that matches experimental data and is determined by the following relationship:<sup>31</sup>

$$\eta = 1 - \left(\frac{2}{e}\right)^a \quad (19)$$

where  $e$  is the natural log base,  $a = 0.0375 Z$  and  $Z$  is the mean atomic number of the material. Using DC705 properties this equation results in a backscattering yield of 0.05. A study by Issikawa and Goto<sup>39</sup> measured the inelastically reflected primary electrons with energies above 50eV for several silicon oils bombarded by electrons from a plasma asher. Their study determined that the fraction of inelastically reflected primary electrons is 0.17 for both DC704 and DC705. The value of mean atomic number in the equation above that would produce yield rates of 0.17 is 16.18.

Mean atomic number is only used by NASCAP to determine backscattering yield rates (and nothing else) so mean atomic number was set to 16.18 in NASCAP to quantify the impact of the demonstrated DC705 backscatter rate on droplet charging. A larger value of average atomic number results in a larger backscattering yield and a more positive droplet charge so the expectation is that the atomic number based on experimental backscatter results will result in a more positive equilibrium charge and a less conservative result. To validate this prediction, NASCAP simulations of droplets with each mean atomic number were run and the results are shown in Figure 19:



**Figure 19. Comparison of Actual and Experimental Backscattering Yields.**

As predicted, the higher experimental backscatter rates determined by Issikawa and Goto result in a more positive surface charge than theoretical yield rates do. This indicates that backscattering yield rates produced by the Everhart theory are lower than rates seen in experiment. Thus, using the Everhart theory to calculate backscattering yield rates provides a conservative estimate of negative surface potential reached. The Everhart theory has been used successfully to model backscattering rates in spacecraft materials for

more than 25 years.<sup>49</sup> For these reasons, it was decided to use this theory to calculate backscattering rates in NASCAP simulations done in this study.

The Everhart theory is extended to incidence angles other than normal in NASCAP by the large-angle scattering theory and by the experiments of Darlington and Cosslett<sup>40</sup> which determined that the angular dependence of backscattering is approximated by:

$$\eta(\psi) = \eta_o \exp(\eta_1 (1 - \cos\psi)) \quad (20)$$

where  $\eta_o$  is the normal incidence angle backscattering yield and the value of  $\eta_1$  is the yield obtained by assuming total backscattering at glancing incidence angles,  $\eta_1 = -\log \eta_o$ .

Electron energy below 10 keV results in higher backscattering yield than electrons with energy levels above 10keV and the increase is almost independent of atomic number. This component of backscattering can be approximated by:<sup>37</sup>

$$\delta \eta_o = 0.1 \exp\left[-\frac{E}{5}\right] \quad (21)$$

where  $E$  is incoming electron energy in keV. At energies below 50eV, the backscattering coefficient becomes very small. It is also impossible to distinguish backscattering and secondary emission of electrons below 50eV experimentally. NASCAP accounts for this using a factor determined by a Heaviside step function ( $H$ ) applied in the following manner:<sup>50</sup>

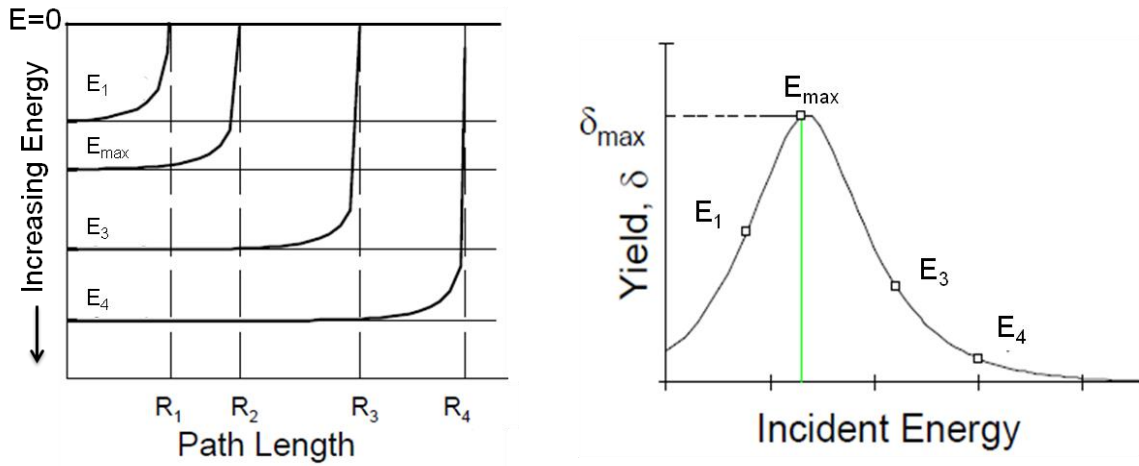
$$H(E - 50\text{eV}) \left[ \frac{1}{\log 20} \right] \log\left(\frac{E}{50\text{eV}}\right) \quad (22)$$

NASCAP incorporates the backscattering assumptions and equations presented above into one equation that describes backscattering yield as a function of incoming electron energy ( $E$ , measured in keV):

$$\eta_o = H(1 - E)H(E - 0.05) \left( \frac{1}{\log 20} \right) \log\left(\frac{E}{0.05}\right) + H(E - 1) \times \left[ \frac{e^{-E/5}}{10} + 1 - \left(\frac{2}{e}\right)^{0.037Z} \right] \quad (23)$$

The rate of backscattered electrons is determined by exposing the object of interest to electrons at flux density and energy levels corresponding to the environment specified. The only material property affecting backscattering in the equation above is mean atomic number,  $Z$ . Moreover, the only properties affected by mean atomic number in NASCAP are backscattering and true secondary electron emission.

The next identified material property with a significant impact on droplet charging is  $\delta_{max}$ , which is the most probable number of secondary electrons that are emitted following electron impacts with the surface. The left-hand chart in Figure 20 shows the manner in which, on average, electron energy state drops off as a function of electron penetration range. The slowing rate of electrons is non-linear and results in an asymptotic curve with energy dropping rapidly once the incident electron has slowed enough to have stronger elastic collisions with nuclei within the material. The secondary yield curve is a plot of number of secondary electrons emitted per incident electron which is a function of the incident energy of the primary incoming electron,  $E$ .  $\delta_{max}$  represents the average number of electrons emitted per incoming electron and  $E_{max}$  is the incident electron energy state where  $\delta_{max}$  is maximized.<sup>50</sup>

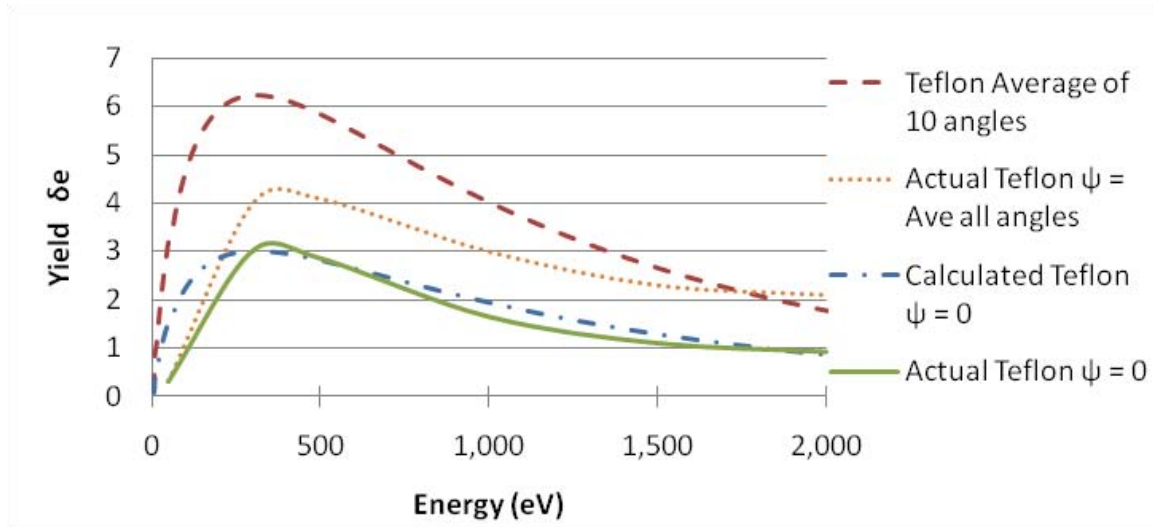


**Figure 20. Example Electron Secondary Yield as a function of Incident Energy (from Davis, 2008).**

Experiments have shown that yield curves for secondary electron emission have a universal shape regardless of the material. Particles with small impact energies do not have enough energy to displace electrons. High-energy electrons do not spend enough time near surface atoms to displace electrons and, when slowed, are too deep for displaced electrons to escape the material. In the Goto and Issikawa study, DC705 was bombarded with a pulsed electron beam in the range of 50-2000 eV. The study revealed that the maximum secondary electron yield for DC704 and DC705 was peaked at 1.9 and occurred when electron energy was 200eV.<sup>39</sup> Based on these experimental results, 200eV was used as the value for  $E_{max}$  and 1.9 was chosen for  $\delta_{max}$  for DC705 in this study. NASCAP uses the following equation to determine the secondary electron yield as a function of the incidence angle ( $\psi$ ) as well as  $E_{max}$  and  $\delta_{max}$ :<sup>32</sup>

$$\delta_e(E, \psi) = \frac{1.114 \delta_{max}}{\cos \psi} \left( \frac{E_{max}}{E} \right)^{0.35} \left\{ 1 - \exp \left[ -2.28 \cos \psi \left( \frac{E_{max}}{E} \right)^{1.35} \right] \right\} \quad (24)$$

Teflon was recommended by several experts in space charging as a conservative first order approximation of DC705 properties.<sup>ii,iii,iv</sup> To verify the accuracy of calculated DC705 secondary electron yields, a comparison was made between known Teflon yields Teflon yields calculated with equation 24. Known values for Teflon  $E_{max}$  and  $\delta_{max}$  are 300eV and 3.0 respectively, as reported by Hastings and Garrett and confirmed elsewhere.<sup>23,41</sup> Results of this comparison are presented in Figure 21 and show that values of predicted and actual Teflon secondary yield at normal incidence agree fairly well.



**Figure 21. Calculated DC705 vs. Actual Teflon Secondary Electron Yield.**

At certain energies, below 300 eV ( $E_{max}$ ), the two curves differ by about 50% but this disparity is offset at higher energy states and the areas under the two curves appear quite close. In contrast, the predicted yield of Teflon at 10 different angles between 0 and 90 degrees is significantly greater than the actual Teflon yield at all angles. This indicates that NASCAP may overestimate secondary yields for insulators by about

<sup>ii</sup> Mandell, Myron J. SAIC, San Diego, CA. Private communication. August, 2008.

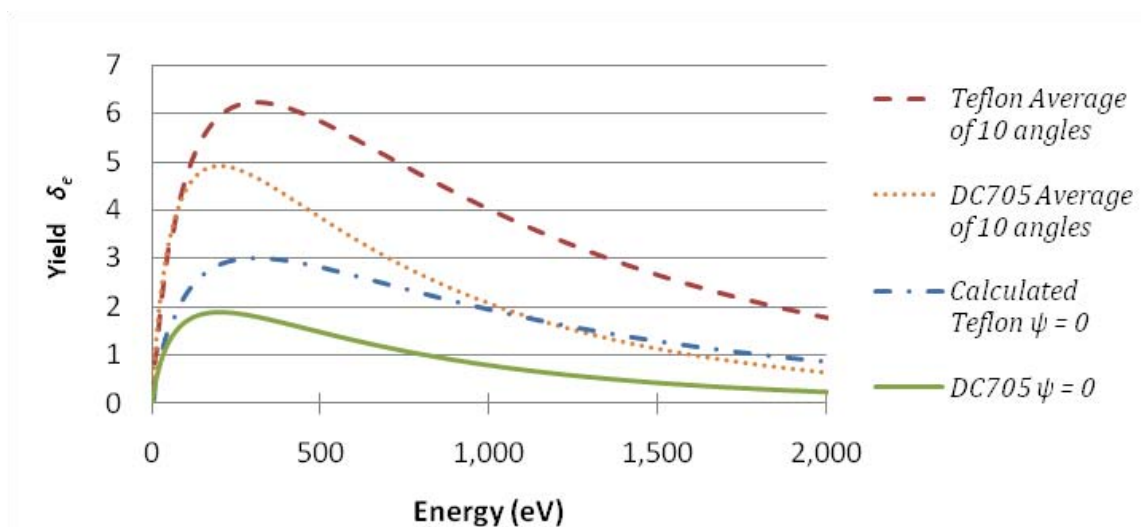
<sup>iii</sup> Lai, S.T. AFRL, Hanscom AFB, MA. Private communication. August 13, 2008.

<sup>iv</sup> Dennison, J.R. Utah State University, Dept. of Physics. Private communication August, 2008.



50% at lower energy states commonly seen in nominal auroral and GEO environments. This error is less significant during solar events when average electron energies in these environments can exceed 2keV and the NASCAP equation (equation 24) appears to predict secondary yield more accurately. The Validity of the equation used by NASCAP to predict secondary electron yield was studied by Katz, et al.<sup>31</sup> The Katz study found that there are differences for some materials between actual yield and that predicted by NASCAP but that these differences do not affect the accuracy of overall charge density by more than a few percent.

A four-way comparison was made of secondary electron yield at various incidence angles for Teflon and DC705 and results are shown in Figure 22. Teflon and DC705 yields were calculated and averaged for the incidence angles of 0, 10, 20, 30, 40, 50, 60, 70, 80 and 90 degrees. The bottom two curves describe the normal (zero degree) incidence angle yield for DC705 and Teflon. These results match expectations of a lower yield for DC705 than for Teflon at all energy levels.



**Figure 22. Predicted Secondary Electron Yield for DC705 and Teflon at 0 and Various Incidence Angles.**

The average yield of 10 incidence angles at  $E_{max}$  for DC705 is 150% greater than the yield at  $\psi = 0$ . The average yield of 10 incidence angles at  $E_{max}$  for Teflon is 115% greater than the yield at  $\psi = 0$ . This amounts to about a 20% greater increase in yield in DC705 than in Teflon. Charge predictions made by the NASCAP model compare well with actual space charging data for many other insulating materials in the

literature.<sup>50</sup> Since predicted DC705 secondary yields mirror predicted Teflon yields at a level expected for a semi-conductor, it is felt that NASCAP will provide a reasonably accurate overall charge prediction just as it does for Teflon, other insulators, and other semi-conductors tested to date.<sup>31</sup>

The material properties that describe the penetration range of electrons (also known as the stopping power of the material) were identified as moderately significant for determining droplet charge. The range is the average depth to which the electrons can penetrate the material as they are slowed by energy loss to the material lattice. NASCAP uses a biexponential equation to determine the range  $R$  (in angstroms) which is given by Feldman's formula:<sup>42</sup>

$$R = b_1 E^{q_1} + b_2 E^{q_2} \quad (25)$$

Here  $E$  is the energy of maximum yield ( $E_{\max}$  described previously) and is expressed in keV. In NASCAP, the  $b$  and  $q$  terms above must be specified for the material of interest. These properties are usually obtained through empirical testing of materials.

Empirical range parameter fits to stopping power data was not found in the literature for silicone oils. When stopping power parameter fits are not available, NASCAP developers recommend estimating range with a mono-exponential form of Feldman's formula.<sup>45</sup> Here Feldman's empirical relationships can be applied by connecting  $b$  and  $q$  from Feldman's equation to atomic data in the following manner:<sup>42</sup>

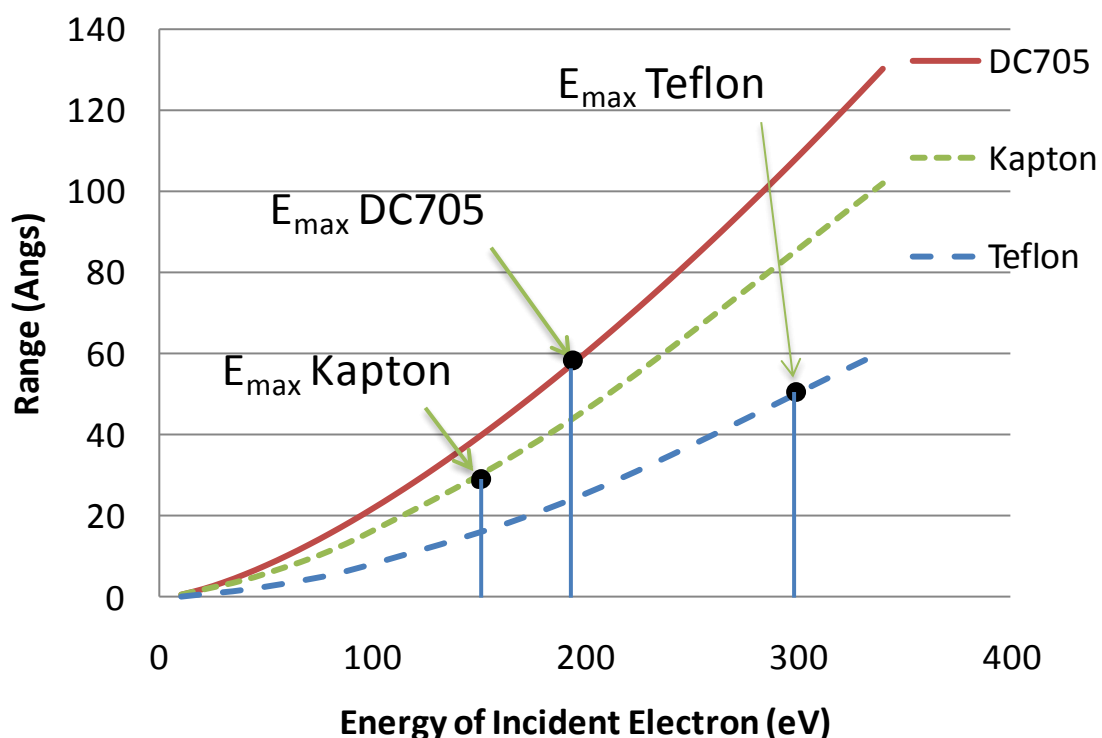
$$R = b E^q \quad (26)$$

where  $E$  is in keV,  $R$  is in angstroms and

$$q = \frac{1.2}{(1 - 0.29 \log_{10} Z)} \quad b = \frac{250 W}{\rho_{\text{mass}} Z^{(q/2)}} \quad (27)$$

where  $W$  is the average molecular weight of the material,  $Z$  is the average atomic number, and  $\rho_{\text{mass}}$  is the mass density in  $\text{g/cm}^3$ . Estimated penetration range for DC705 is shown in Figure 23 alongside actual penetration range results for two commonly used insulators on spacecraft, Kapton and Teflon. These results show a range of penetration for DC705 that is twice that of Teflon and about 50% greater than that of Kapton for the same incident electron energy state. This result matches expectations since the density of DC705 ( $1.08 \text{ g/cm}^3$ ) is lower than that of Teflon ( $1.6 \text{ g/cm}^3$ ) or Kapton ( $2.15 \text{ g/cm}^3$ ). The greater range of

DC705 is also due to its relatively low average atomic number and average molecular weight, which are equal to or lower than those of both Kapton and Teflon.



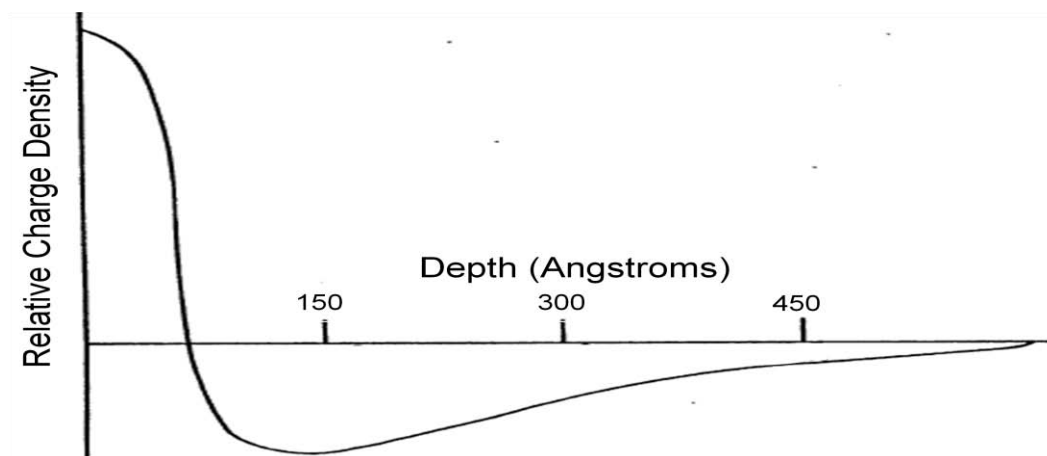
**Figure 23. Penetration Range of Electrons (Actual for Teflon and Kapton, Estimated for DC705)**

NASCAP simulations were run using Teflon range parameters determined using equation 27 and simulation results were then compared with results for known Teflon bi-exponential range parameter charging. The resulting peak positive charge was 7% less than the peak positive charge that resulted from using Teflon range parameters. The minimum equilibrium surface charge of a DC705 droplet in DMSP auroral space was 40% more positive when charged using Feldman's range parameters than with Teflon range parameters. The equilibrium potential in this simulation was -24V using Feldman's formula and -43V using Teflon range parameters. These results are in keeping with the general expectation of a smaller charge magnitude in a semi-conductor than in an insulator.<sup>23,28,31</sup>

Ion-induced secondary emission describes the secondary emission of electrons due to ion impact. NASCAP treats the resulting yield as a two-parameter fit. "Proton Yield" is the yield for 1 keV normally

incident protons and “Proton Maximum” is the proton energy that produces the maximum electron yield. The secondary emission properties due to the impact of ions other than protons are assumed identical to the proton values for the same energy state.<sup>48</sup> Electron yield due to proton impacts was not found in the literature and Teflon material properties were assumed in this case. Variations of proton yield from Teflon properties 50% up and down showed less than a 5% impact on droplet charge indicating that proton impacts have limited impact on surface charge. This matches the general expectation that ions play an insignificant role in spacecraft charging due to their low energy relative to electrons.<sup>23</sup>

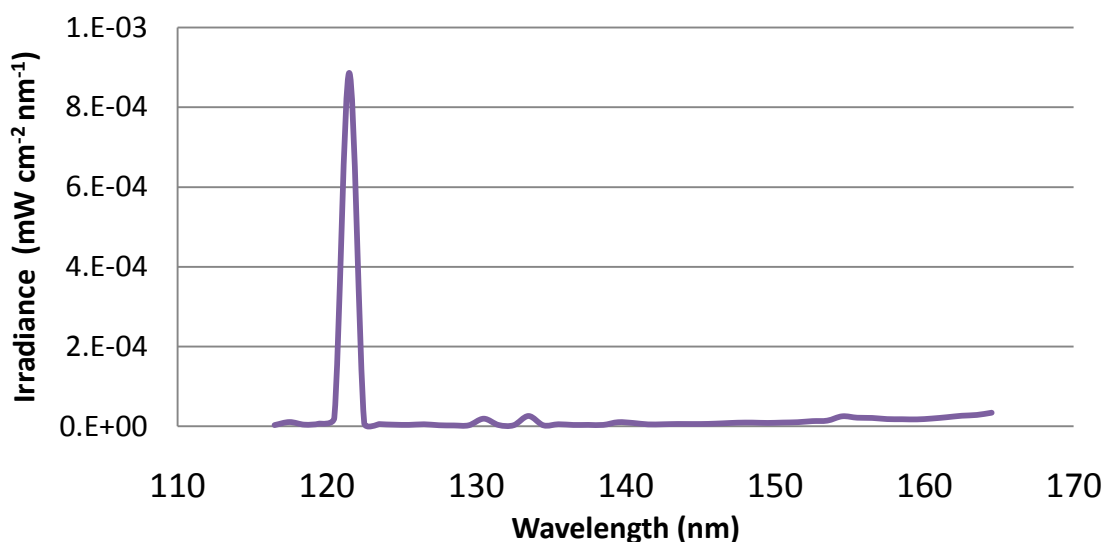
Applying the estimated electron penetration range values for DC705 to a general charge density profile for a dielectric material yields the normalized charge density profile shown in Figure 24. Here secondary electron production produces a significant number of electrons that escape the surface and charge the material positively. Electrons come from all incidence angles and are slowed by the material before producing secondary electrons. Production of escaping secondary electrons peaks at about 60 Angstroms for electrons entering at an angle normal to the surface ( $\psi = 0$ ). Electrons entering normal to the surface and reaching 60 Angstroms have an average energy state of 200eV. Electrons with a greater angle of incidence produce secondary electrons closer to the surface and these secondaries are more likely to escape the material than those produced at greater depths. Escaping secondaries leave behind positively charged molecules that are responsible for the positive charge density that peaks at the surface.



**Figure 24. Estimate of Relative Charge Density Profile for DC705 Due to Secondary Electrons Based on Calculated Range Penetration in DC705 and Known Profiles for Insulating Materials (After Katz, 1977).**

### G. Photoemission of Electrons in DC705

The final material property critical to droplet charging is photoemissions which is the yield of photoelectrons from surface material exposed to UV sunlight. The UV spectrum of solar radiation reaching near-earth space is shown in the following figure.<sup>43</sup> The chart shows average irradiance for a 24-hour periods on 31 October 2003 during a period of high solar activity that disabled a Japanese satellite in 2003. These measurements are presented for a select range of UV wavelengths that extend down to the photoelectric threshold of DC705. This data was collected by the Solar Radiation and Climate Experiment (SORCE) satellite which resides in a 645 km, 40 degree orbit and is operated by the Laboratory for Atmospheric and Space Physics at the University of Colorado in Boulder, Colorado.<sup>44</sup> The data presented above was compared to satellite data archived by NASA Goddard over a 20 year period.<sup>45</sup> The NASA Goddard data shows that flares like the one that resulted in solar irradiance shown occur roughly every 11 years and can reach an irradiance level 42% above nominal at wavelengths below 130nm and 30% above nominal at wavelengths above 130nm. The largest event monitored from space, in 1983, was particularly strong and reached 200% of nominal at wavelengths below 130nm.



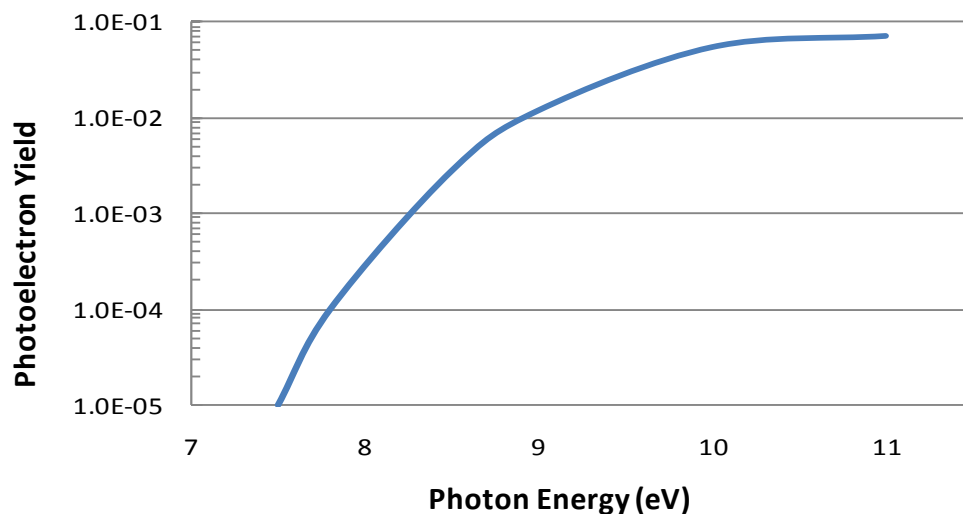
**Figure 25. Solar Irradiance at UV Wavelengths Measured by SORCE Satellite.**

Photons with wavelengths shorter than 165nm (1650 Å) have a thermal energy greater than 7.5eV which is the threshold energy sufficient to eject measurable numbers of electrons from DC704 and DC705. This threshold energy was discovered by Koizumi, Lacmann and Schmidt<sup>46</sup> who looked at DC704 and DC705 photoelectron emissions involving the absorption of a photon, ionization of a silicon oil molecule, electron transport to the liquid/vacuum interface and escape into a vacuum. Incident photons are absorbed by a molecule of the liquid at distances between  $x$  and  $x+dx$  beneath the surface with a probability of  $\mu e^{-\mu x} dx$ , where  $\mu$  is the photoabsorption coefficient.

In the Koizumi et al study,<sup>46</sup> a thin liquid film of DC705 and DC704 was applied to cathodes in vacuum and irradiated with ultraviolet light from a deuterium discharge lamp. The vacuum ultraviolet light was monochromatized and fell on the cathode through an anode mesh. Current induced by photoelectron emissions was measured as a function of photon energy. The relative light intensity was monitored by the fluorescence of Sodium Salicylate. Division of the current by the intensity of the fluorescence gave the relative photoelectron emission yield. The study looked at normal incidence of UV light on DC705 and DC704 and determined that the threshold photon energy required to liberate an electron for both fluids is 7.5 +/- 0.2 eV. The yield ratio of electrons released to photons absorbed ( $Y_{\text{sun}}$ ) is shown in Figure 26 where yield peaks at about 73 electrons emitted for every 1000 photons and occurs at about 11eV incident photon energy. Note that the ordinate of the graph is logarithmic and that the yield between 7.5 and 8.5 eV is roughly described by the following equation:

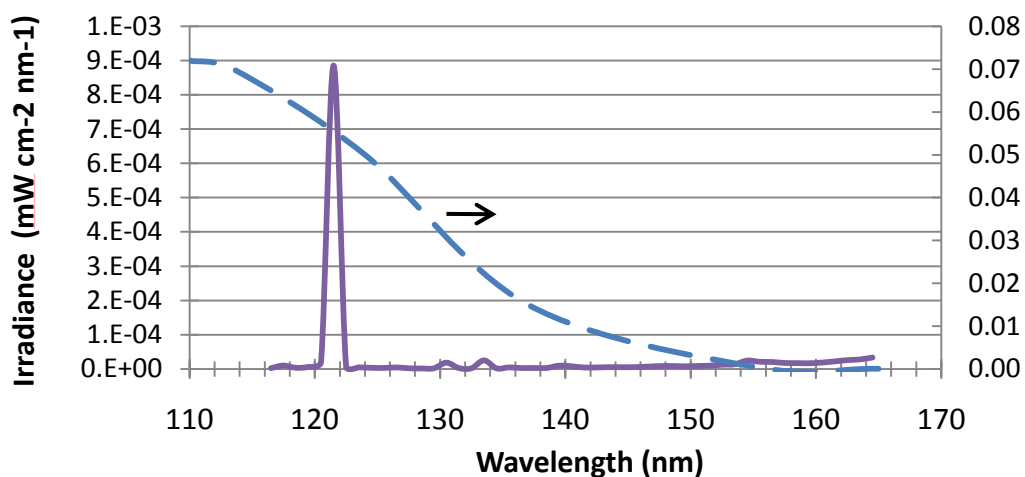
$$Y \propto (E_{\text{photon}} - 7.5)^3 \quad (28)$$

Results for DC704 and DC705 are indistinguishable from each other providing strong justification for the use of DC704 in photoemissions charging experimentation instead of the more costly DC705.



**Figure 26. Photoemission of Electrons for DC705 & DC704 (from Koizumi et al.)**

Overlaying the nominal solar output chart with the quantum yield data as a function of wavelength instead of energy yields the chart in Figure 27.



**Figure 27. Nominal Solar Output (solid line) and Photoelectron Yield for Silicon Oil (dashed line plotted against the right ordinate).**

This chart highlights the dramatic contribution of the Lyman Alpha spike in solar energy from the sun in the EUV part of the spectrum near 121.6nm (about 10eV). DC705 droplets in space due to photoemissions are dominated by these 10eV photons that produce a photoelectron yield of about 0.055.

### Chapter 3: Numerical Charging Simulations

Three professional charge modeling software tools were employed in this study to predict droplet charging. Results of these models were compared with each other and to analytic calculations to validate them to a first order approximation. The first spacecraft charging code employed in this research was NASA's Space Charge Expert System (SCES) distributed by NASA's Space Environment Effects (SEE) office.<sup>22</sup> This code has a library of materials from which to choose but does not contain DC705 or allow modification of other material properties to more closely approximate DC705 properties. The SCES code was run for a 1mm diameter Teflon sphere placed in a 300km nominal auroral environment and in a nominal low latitude LEO environment. The SCES simulation with Teflon predicted a peak charge on the sunlit hemisphere of +4.5 volts in auroral space and +2V at lower latitudes. In eclipse the SCES estimated a -6.2V potential on a Teflon sphere in nominal auroral conditions and -2.5V at lower latitudes.

Another charge estimation tool called SPENVIS was used to give a first order estimate of droplet charge in GEO and auroral space. This program is made available through the European Space Agency<sup>47</sup> and, like SCES, does not allow modification of material properties. Since Silicone oil was not a material in the SPENVIS database, Teflon was selected to give an approximation of droplet charge. Results of SPENVIS simulations compare very well with Teflon charging results from SCES and with NASCAP results for Teflon charging. SPENVIS results are presented in the next chapter alongside results from NASCAP simulations in the same or similar environments. SPENVIS does not allow modeling of spherical objects so an isolated Teflon patch was positioned on a flat panel surface for estimation of charge. As with SCES, SPENVIS has no 3-D surface modeling and therefore provides no estimation of charge variations between adjoining surfaces or of the difference in charge between sunlit and shaded sides.

The most powerful tool employed is NASA Charging Analyzer Program (NASCAP) ver. 3.2 developed by Science Applications International Corporation (SAIC) for the USAF and NASA. NASCAP incorporates and builds upon the algorithms of three separate models developed over several decades for LEO, GEO, and polar orbits. These algorithms were validated with laboratory testing and charging data from sensors on many different satellites with different surface materials operating in a diverse range of orbit environments and altitudes.<sup>48</sup> NASCAP considers geometry and numerous material properties



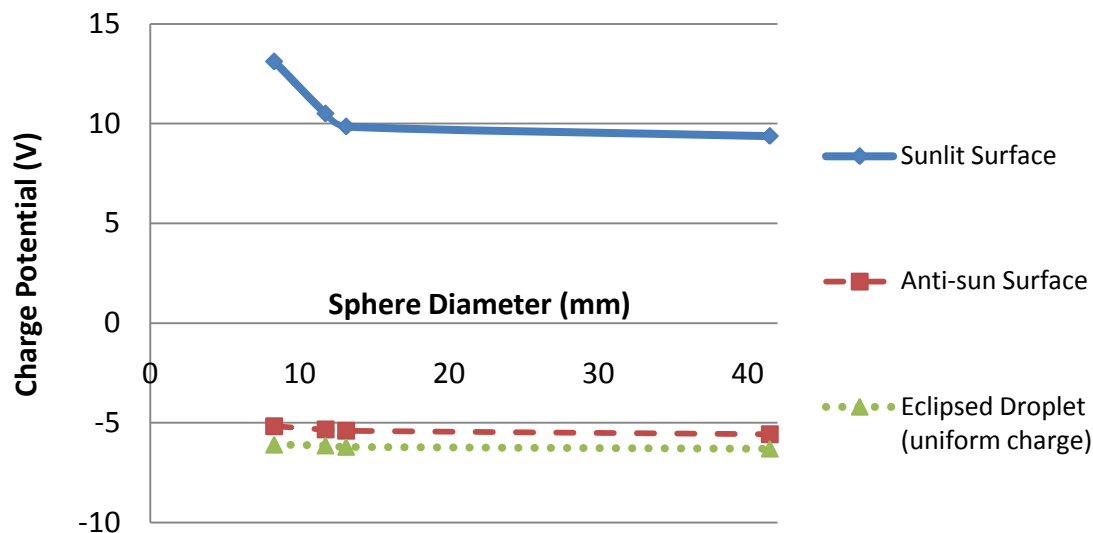
allowing a charge prediction that is specific to non-traditional shapes and materials. The Maxwell probe formulation used by NASCAP to determine charge is, in principle, exact for a sphere in an isotropic, Maxwellian plasma.<sup>49</sup> Hundreds of NASCAP simulations were conducted in this study to predict charging of droplet streams exposed to different orbital environments. NASCAP was also employed to evaluate the impact of various DC705 material properties on charging to estimate error due to uncertainties about these properties.

NASCAP is a better tool for modeling droplet charging because of its 3-D object surface modeling capability that allows for complex geometries. It is widely used by industry and government and has the ability to account for the effects of object velocity and direction of sun exposure for various surface elements. NASCAP algorithms and methods are referred to in spacecraft charging literature quite often.<sup>23,30,33</sup> Objects in NASCAP are composed of surface elements that form the shell of an object whose thickness can be specified as a material property. The code uses 16 materials property inputs and 12 environmental parameters. The complex geometries, custom materials properties, and diverse environmental inputs make NASCAP an appropriate tool for accurately predicting charging of a spherical DC705 droplet transiting space. Of particular importance to this study is NASCAP's ability to create materials by allowing the user to specify certain material properties.

#### **A. NASA Charging Analyzer Program (NASCAP) Limitations**

The most significant limitation of NASCAP for modeling droplets is that it cannot analyze surface elements with dimensions less than 1.3 millimeters on a side.<sup>50</sup> This makes construction of a spherical objects of the size desired for fluid streams impossible without merging of nodes and distortion from a spherical shape. The smallest sphere NASCAP can analyze is 8.3mm in diameter so an investigation was made into the differences between charging of large and small spheres. A comparison was made between large and small spheres to identify whether charging of small droplets can be modeled accurately using larger droplets with the same material properties. In this study, 8.3, 11.7, 13.3, 41.8 and 200 millimeter

diameter spheres were simulated in the same auroral plasma environment. Results of these simulations are shown in Figure 28 and indicate that larger spheres can accurately predict average (nearly uniform) charging of smaller spheres in eclipse where potential in large spheres differed by less than 3.3% from that of large spheres. Similarly, minimum charge on the surface facing away from the sun (“Min Chrg” in the figure) decreased less than 7.8% as sphere diameter was increased.



**Figure 28. Comparison of Charging of Sunlit and Anti-sun Surfaces on Sunlit Droplets and Eclipsed Surface Elements on Spheres with Four Different Diameters.**

In all surface elements, droplet charge trends more negative as diameter increases. This can be explained by the fact that voltage potential of a sphere decreases as capacitance increases  $V = Q/C$  and, as equation 32 shows, capacitance increases with droplet diameter. Charge on the surface normal to the sun (“Max chrg” in the figure) varied 28.5% between the 8.3mm and the 41mm diameter spheres. The steep initial slope of the sunlit surfaces in Figure 28 is most likely explained by the small size of the droplet surface relative to the thickness of the plasma sheath. Large spheres provide a slightly conservative (more negative) estimate of charging in droplets that are smaller than 8.3mm but an estimate of maximum positive charging that is significantly less than that seen in smaller droplets. Because of this, spherical droplet simulations were only used to quantify the most negative charge on droplets in each environment. Prediction of maximum positive charge on faces normal to the sun was accomplished using cubes that can be much smaller (1.3mm per side) in NASCAP.

To verify that cubes provide results applicable to spherical droplets, an investigation was made into the differences between charging of cubes and spheres using NASCAP. This study simulated charging of variously sized spheres and cubes in a LEO environment, an auroral environment, and a GEO environment to identify surface charging differences. The results of simulations comparing eclipsed LEO charging of similarly sized cubes and spheres show that the relatively uniform potential, relative to the ambient plasma, on any surface is nearly the same on the spheres as it is on cubes. Charging of similarly sized spheres and cubes in the auroral and GEO environments paralleled the LEO charging results where equilibrium charge on any surface differed by less than 5% between shapes for all three eclipsed environments.

When both spheres and cubes are exposed to the sun in LEO, GEO, and auroral space simulations the surfaces on both objects directly facing and opposite the sun charge to similar levels. These faces correspond to the maximum and minimum surface charge of the objects. Comparison of minimum charge potential reached by surfaces on cubes and spheres showed a difference of less than 5% while comparison of maximum potential showed a difference of less than 12%. The equilibrium minimum and maximum potentials reached by a DC705 sphere are consistently lower (more negative) than those reached by a DC705 cube with the same surface area. These results indicate that sun exposed droplets modeled as cubes provide an estimate of charging that is  $< 12\%$  more positive than the actual charging of surfaces of a sphere normal to the sun and  $< 5\%$  more positive than surfaces normal to, but facing away from, the sun. In this study, cube droplet simulations were used to quantify the maximum (most positive) droplet surface charge for each environment.

A cube cannot accurately predict photoemissions on sphere surfaces that are neither normal nor parallel to the sun. Spherical charging is also complicated by the impact of droplet velocity that leads to more positive charging on the leading edge hemisphere in LEO and polar orbits. This effect can be modeled on cubes by directing the droplet velocity perpendicular to the vector to the sun. The resulting charge on the ram surface of a cube is very close to the maximum positive charge on a sphere surface that is normal to the droplet velocity. However, simple cube geometry cannot accurately capture the full range of charge seen on surfaces of the ram hemisphere or sun-facing hemisphere of a sphere.

## B. Material Properties in NASCAP

The material properties used by NASCAP to model charging are shown in Table 4. Values for DC705 properties in the left half of the table were either provided by the manufacturer or found in the literature.<sup>51,46,12</sup> Values in the right half of the table were determined using theoretical equations, or estimated from Teflon properties.

**Table 4. DC705 Material Properties Selected for Use by NASCAP.**

<u>Material Property</u>	<u>DC705 Value</u>		<u>Material Property</u>	<u>DC705 Value</u>
Average Atomic Number	4.028		Maximum Secondary Yield due to Protons	0.455
Secondary Electron Maximum Yield (normal incidence)	2.0 electrons/electron		Energy of Maximum Secondary Yield due to Protons	140 eV
Maximum Photoelectron Yield (normal incidence)	0.073 electrons/photon		Surface Resistivity	$1 \times 10^{16}$ ohms/m <sup>2</sup>
Dielectric Constant	2.5		Range Coefficient	0.627
Thickness	Drop Radius (m)		Range Exponent	1.455
Bulk Conductivity	$1.0 \times 10^{-12}$ ohms <sup>-1</sup> m <sup>-1</sup>			
Average Atomic Weight	7.583 amu			
Density	1097 kg/m <sup>3</sup>			

A parametric study was conducted to quantify the relative effect of each material in the right half of the table on droplet equilibrium charge as determined by NASCAP. Each property was varied by an amount within a reasonable range to quantify the impact on equilibrium surface charge reached in the GEO and auroral environments. Reasonable range of variation of each parameter was determined by researching properties for semi-conducting materials (typically Silicon) and insulating material (typically Teflon). Electron penetration range was estimated using theoretical equations described later in this chapter. Maximum secondary yield due to protons and the energy causing maximum yield were both found to affect equilibrium charge by less than 1% when known values for Teflon were used for these properties.

Dielectric constant is a measure of dielectric strength, which is the strongest electric field that can exist in a dielectric material before electrical breakdown (discharge) occurs. The dielectric constant of a

material describes the factor by which the capacitance of two charged parallel plates changes when that material is used to fill the gap between the two plates. This is described by the following equation:<sup>52</sup>

$$C = \kappa C_o \quad (29)$$

where  $C_o$  is capacitance with a vacuum separating the charged plates,  $C$  is the capacitance after insertion of the dielectric material, and  $\kappa$  is the dielectric constant specific to the dielectric material. Similarly, voltage potential of the capacitor separated by vacuum is decreased by  $1/\kappa$  when the dielectric material is inserted between plates as in the following relationship:

$$V = \frac{V_o}{\kappa} \quad (30)$$

where  $V_o$  is the electrostatic voltage measured with vacuum separating two charged plates and  $V$  is the electrostatic voltage measured with the dielectric material between the charged plates. The dielectric constant of silicone oil was used in this study and is listed in Table 5 along with the dielectric constants and dielectric strengths of several similar materials.<sup>52</sup>

**Table 5. Dielectric Constants and Strength of Select Materials and Silicone Oil.**<sup>52</sup>

Material	Dielectric Constant $\kappa$	Dielectric Strength (MV/m)
Vacuum	1.00000	n/a
Air	1.00059	3
Fused Quartz	3.78	8
Pyrex Glass	5.6	14
Teflon	2.1	60
<b>Silicone Oil</b>	2.5	15

Bulk conductivity and density were identified in product literature and clarified through communications with a Dow Corning Applications Engineer.<sup>v</sup> Both of these values vary slightly with

---

<sup>v</sup> Private telephone conversation with Mr. James Wright, Applications Engineer, Dow Corning Corp. June 15, 2008.

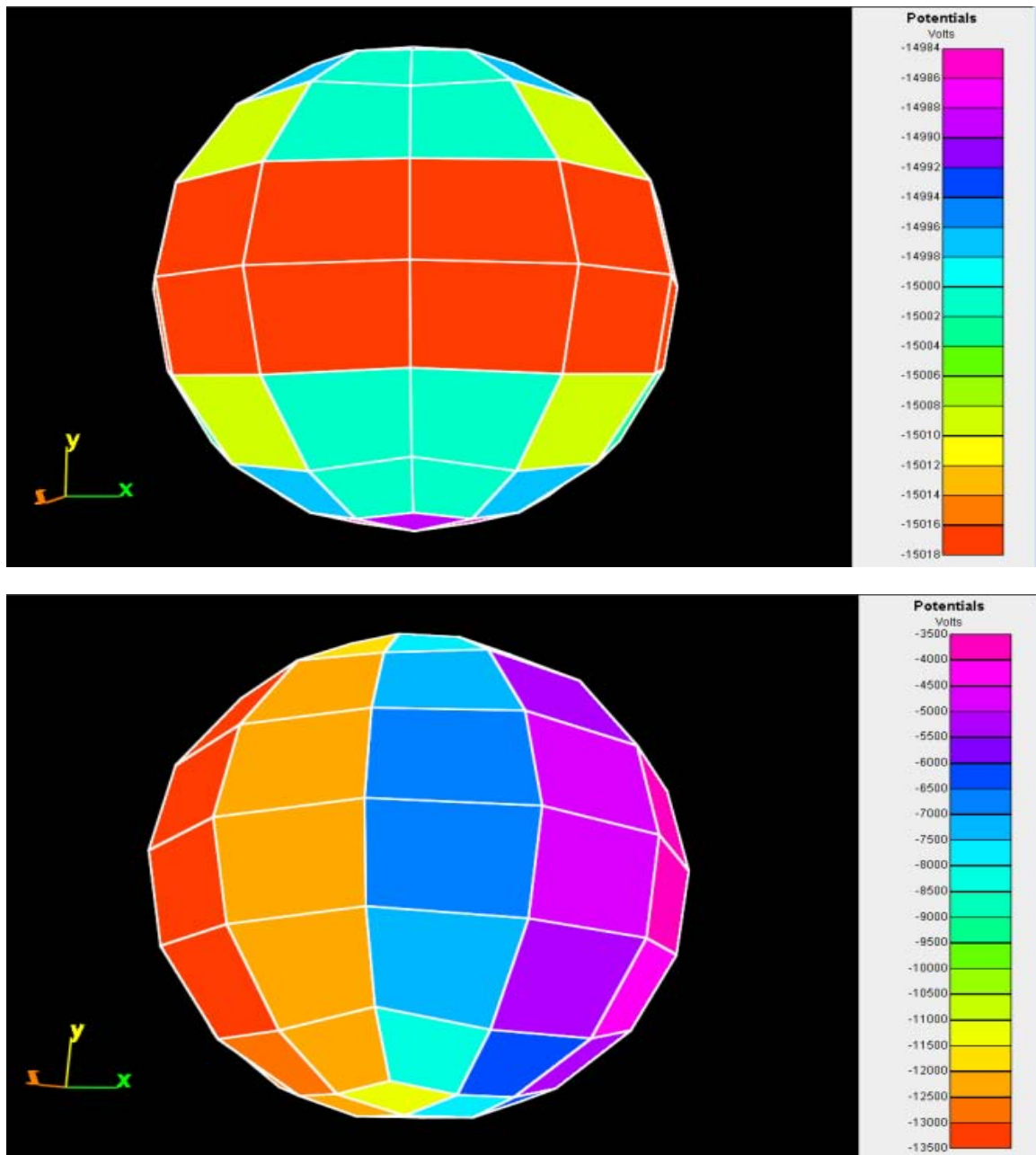
temperature but varied less than 0.1% over the range of temperatures (200-350K) considered in this study. Simulations were performed to evaluate the effect of this slight variation in conductivity and density. These simulations show that slight variations in conductivity and density have no noticeable effect on equilibrium charge. The values of conductivity and density, listed in Table 4, were used for all simulations performed in this study.

Variation of material thickness had little effect on equilibrium charge in NASCAP simulations. Two thicknesses, 0.5mm and 4mm, were evaluated on an 8.3mm sphere in both a GEO environment and in an auroral environment. This matched expectations since electron penetration range calculations discussed later in this chapter predict electron penetration distance much less than a half millimeter in DC705 for energy states typical of electrons produced by the sun. Once material thickness was determined to have little impact on charging, droplet radius was used for material thickness in simulations of spheres in this study. Material thickness of cubes was also varied with the same results as in spheres. Cube material thickness was set equal to half of the length of each side in cube simulations.

NASCAP assumes that the electron yield per photon is equal to the yield caused by normal incidence multiplied by the cosine of the angle of incidence to the sun ( $\psi_{sun}$ ). Thus, the photocurrent from a surface exposed to the sun is given by the formula:

$$i_{photo} = Y_{sun} (Area\ exposed) \cos \psi_{sun} \quad (31)$$

where  $i_{photo}$  is the current from the droplet surface to the ambient plasma.  $Y_{sun}$  is the normal incidence angle yield determined by Koizumi et al.<sup>46</sup> (a maximum of 0.073 electrons per photon for both DC-704 and 705). The effect of photoemissions is graphically evident in NASCAP simulation results in Figure 29. Here two drops are shown, the first in eclipse and the second in full sun with the sun in line with the x-axis. The color legend to the right of the images shows that the eclipsed droplet exhibits a nearly uniform negative potential of -15kV relative to the NASA worst-case plasma environment described in Chapter 2. In contrast, the sun exposed drop has a similar uniform low potential on its shaded side and a less negative charge potential on its sun facing side. The greatest voltage potential relative to the ambient plasma is -13.5kV on the surfaces directly opposite the sun. The droplet exhibits negative charge on all of its surfaces but the surfaces normal to the sun have a potential 10kV more positive than their counterparts on the shaded hemisphere.



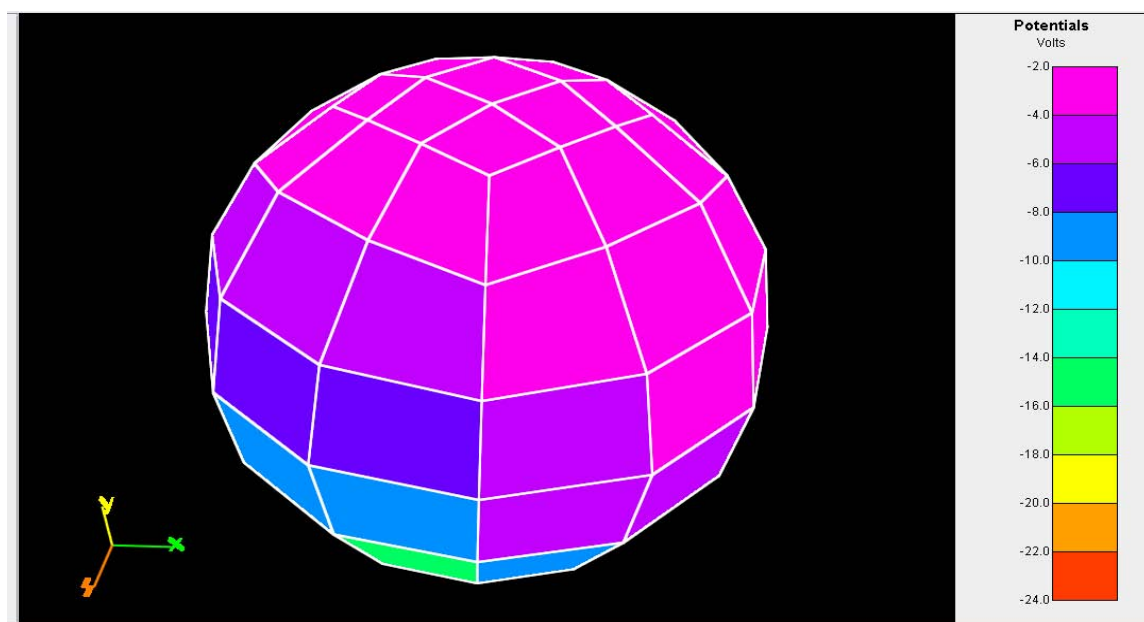
**Figure 29. DC705 Sphere in NASA Worst-case GEO in Eclipse (top) and in Sun (bottom).**

**Photoemission of Electrons Results in a More Positive Charge on the Sunlit Hemisphere.**

NASCAP uses the surface resistivity parameter from Table 4 times a geometrical factor to determine the surface resistance between two adjacent surface elements. Surface resistivity is due to the migration of electrons along the surface layer, possibly aided by adsorbed impurities and defects. A negative value indicates that the material is a conductor. This property was found to change charge levels

by less than 5% when surface resistivity was varied between values for silicon and values for Teflon. The surface resistivity value of Teflon was used for charging simulations in this study because it tended to yield a more negative surface charge, which, in the strongest charging environments, is more conservative.

Despite the relative insignificance of ion-induced charging compared to electron charging the effect of ion bombardment on the leading hemisphere of a droplet is noticeable. In Figure 30 a sun-lit auroral DC705 sphere is oriented with the x-axis pointing to the sun, the y-axis pointing in the direction of orbit travel at 7500 m/s and the z-axis pointing in the direction of droplet transit at 100 m/s. The leading (top) hemisphere is more positively charged by the low energy positive ions and protons (90% oxygen, 10% hydrogen in the case depicted). The bottom or wake hemisphere is more negatively charged, particularly on the shaded left hemisphere where photoelectrons are not emitted. Not surprisingly, the relatively insignificant 100m/s transit velocity has no noticeable effect on charge distribution.

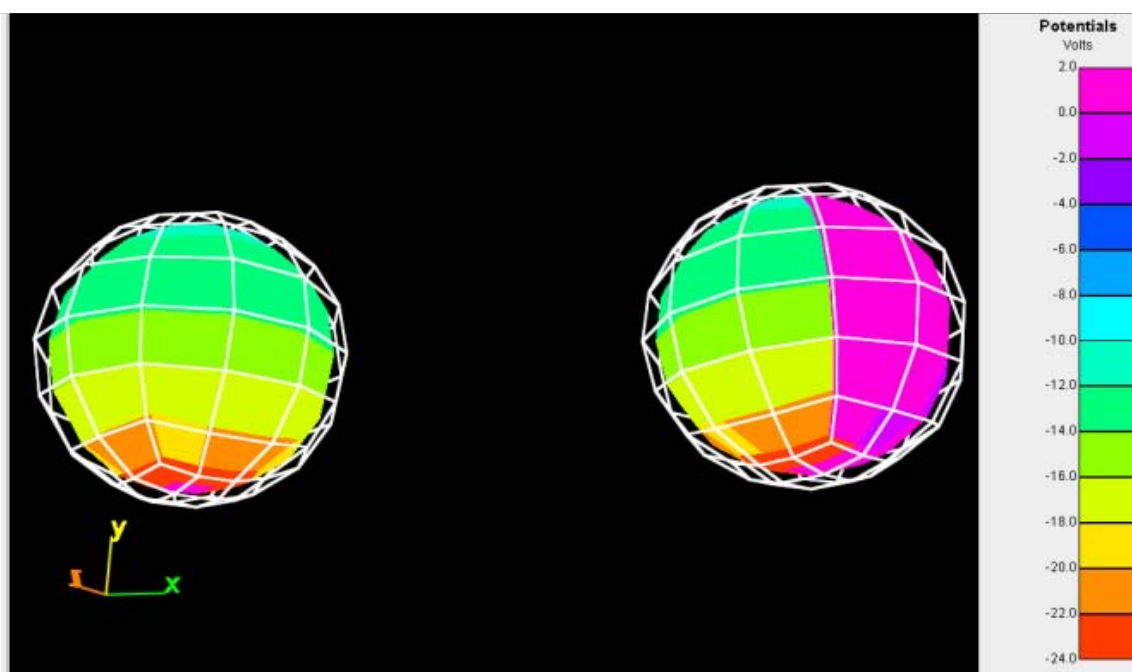


**Figure 30. Strong Auroral Charging of a 20cm DC705 Sphere in Sun with 7500m/s Velocity in the y-axis and Sunlight aligned with the x-axis.**

Using smaller (8.3mm diameter) droplets and adding a second droplet positioned in the shadow of the first yields the equilibrium surface charge shown in Figure 31. The right droplet in Figure 31 has a distribution of charge similar to the much larger (20cm diameter) droplet in Figure 30. Droplets in Figure



30 and Figure 31 are exposed to the same strong auroral charging environment measured by a DMSP satellite during high auroral activity. Both 8.3mm and 20cm spheres as well as 1mm cubes display charge potentials that differ by less than 0.5V from each other on surfaces normal to the sun. Note that the y-axis is rotated back into the page in Figure 31 relative to Figure 30 to better show the wake side of the droplets. In Figure 31 the ram hemisphere of both droplets has a more positive charge. Note that the very bottom surface of the left droplet receives some sunlight and develops a positive charge. This effect is not seen in droplets more closely spaced.



**Figure 31. Comparison of Hemispheric Charging Impacted by Velocity and Solar Incidence.**

Poisson's equation, which is the foundational equation that NASCAP solves to determine droplet charge, applies to matter in any state. However, NASCAP is not designed to account for the internal dynamics of a charged liquid. The liquid state has little effect at the atomic level where electrons are energized and ions created. At the inter-molecular level, like charges repel each other causing dilution of charge concentrations and a more uniformly distributed charge within droplets. In a sun-exposed droplet, this will likely result in negatively charged molecules migrating to the (more) positively charged sun-facing hemisphere. This migration will tend to mitigate the dipolar charging expected in sun-exposed droplets and lead to a more uniform charge distribution. Sunlit droplets are likely to have a charge distribution similar to

that of droplets in eclipse but with a more positive overall charge. Droplets in eclipse will likely see a migration of charged droplets from the surface into the interior of the droplet resulting in a charge distribution more uniform throughout the sphere. The rate of migration depends on the level of charge and was not quantified in this study. Both of these charge distribution mechanisms support the assumption described in the next chapter that droplets can be treated as point charges when analyzing droplet interactions that affect their trajectory between satellites.

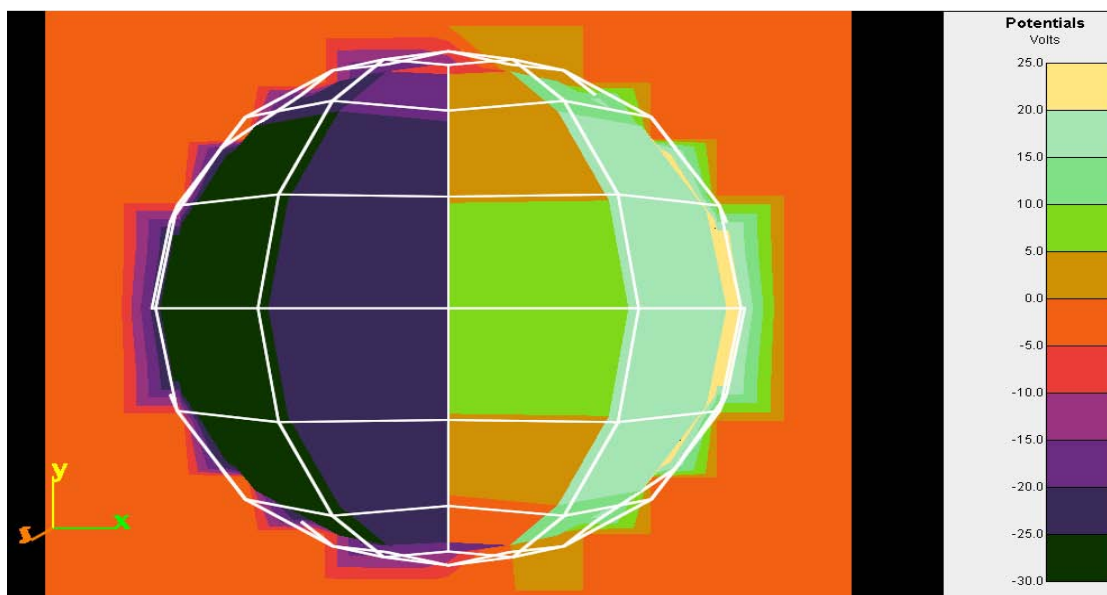
Once material properties of DC705 were identified for use in NASCAP, simulations were performed to evaluate droplets in different plasma environments. 8.3mm diameter DC705 spheres and 1.3mm cubes were simulated in isolation, as pairs and as strings of three. For LEO and Polar orbit simulations, velocity was usually assigned in the Y direction at 7.5 km/s and deviations from this practice will be noted. The sun vector was aligned with the X-axis in sunlit simulations presented in this report unless otherwise noted. A transit velocity of 20 or 100 m/s was assigned to the Z-axis in at least a dozen simulations but results showed no significant effect of this velocity on corresponding ram or wake hemispheres. In four instances, droplets were charged with and without transit velocity and there was no difference in minimum, maximum, or average charge potential between the two cases. As a result, transit velocity was not considered in later simulations to limit the time required to run simulations which can take several hours. Orbital velocity is not considered in GEO simulations because of the slower orbital speed and the absence of low-energy positive ions that play a significant role in mitigating negative charge at lower altitudes.

### **C. Results of GEO Simulations**

In this study, NASCAP charging simulations of DC705 droplets in GEO were performed for nominal conditions and during high magnetospheric activity. The strong GEO charging environment is NASA's worst-case design guideline described in Chapter 2. These simulations show that droplet charging in GEO during nominal geomagnetic activity varies significantly from charging during peak geomagnetic

activity. Nominal GEO charging results in positive surface potentials caused by secondary electrons produced by electrons with energy states between about 10 and 300eV. During high magnetospheric activity, the proportion of electrons with energy states above 300eV is much greater and negative deep surface charging processes dominate. Here, secondary electrons are created hundreds of Angstroms inside the material and, along with the incident electron, are absorbed by other molecules instead of escaping the material. This results in a gradual negative charging of the material.

The series of figures that follow show various stages of plasma sheath development around a DC705 droplet exposed to a high magnetospheric GEO environment. In these simulations, a grid was constructed in a plane that bisects the droplet to display contours of electric field potential in the space surrounding the droplet. These contours are evidence of the presence of a plasma sheath that screens the surface potential from the surrounding plasma or from electric fields of nearby objects. Sunlit spheres are exposed to photons coming from the right side of the image, resulting in positive charging of the right hemisphere due to photoemission of electrons.

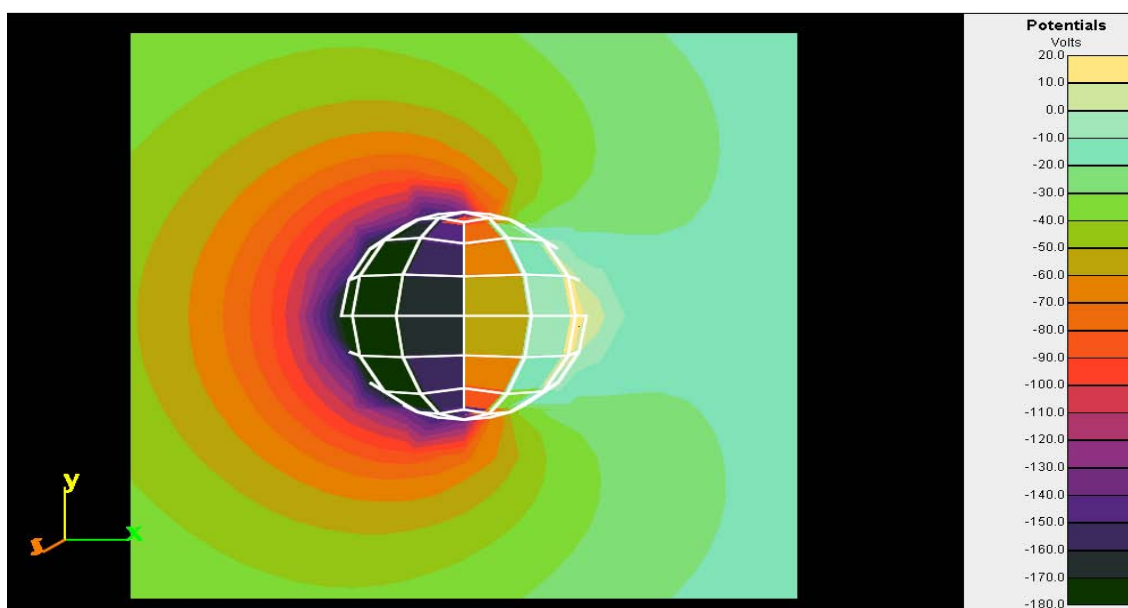


**Figure 32. DC705 Sphere in NASA Worst-case Sunlit GEO Environment after 0.2 sec. Early Stages of Plasma Sheath Development are Evident Near the Droplet Surface.**

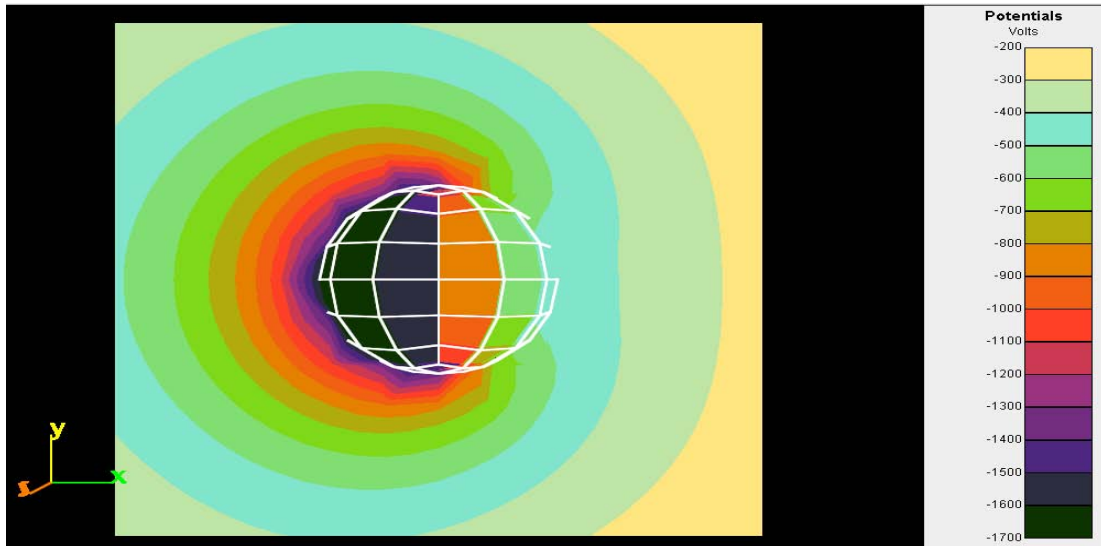
Figure 32 shows a droplet 0.2 seconds after exposure to a sunlit worst-case GEO environment.

The sunlit hemisphere is completely charged positive with the surfaces most normal to the sun charged to +25V potential. Photons charged this hemisphere positive in hundredths of a second and at 0.2 seconds; it is starting to charge negatively. The anti-solar side is completely negative and the surfaces directly opposite the sun are at -30V, roughly opposite their counterpart surfaces on the sunlit side of the sphere. The orange field surrounding the sphere represents a potential of roughly zero relative to the surrounding plasma and black is beyond the edge of the cut-plane grid. The very beginnings of a sheath are visible at 0.2 seconds but the transition from droplet surface potential to zero potential is still very abrupt. At lower altitudes, where plasma flux densities are higher, sheath development is usually complete in less than half of a second and droplet surface elements are already at equilibrium charge.

Figure 33 shows the same worst-case GEO droplet's surface and sheath potential after 1.5 seconds of exposure. The sunlit surfaces are still predominantly positive but some surfaces on the sunlit hemisphere that are further from normal to incoming photons have a negative charge. The anti-solar hemisphere has a negative charge that is almost uniform. The potential in the sheath surrounding the droplet is now negative in all directions except for a small part of the sheath above the positive surfaces where the potential remains positive out to about 1mm from the surface. Electrostatic potential is strongly negative on all surface elements except those most normal to the sun. The average surface potential is already about -120V.

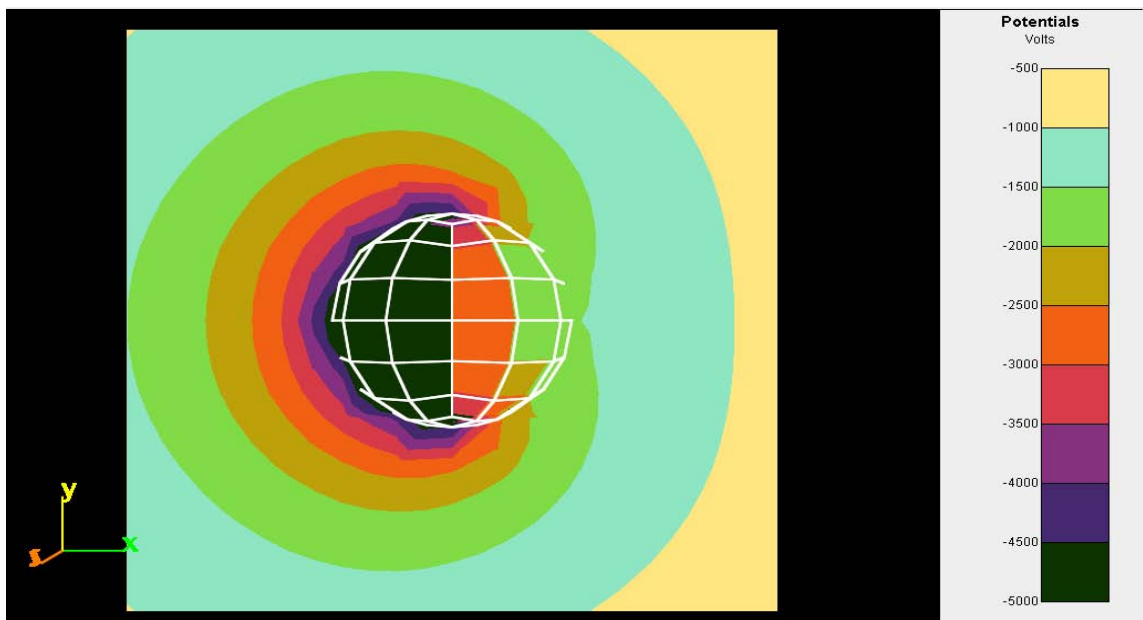


**Figure 33. DC705 Sphere in NASA Worst-case GEO environment after 1.5 sec.**



**Figure 34. DC705 Sphere in NASA Worst-case GEO after 10 sec.**

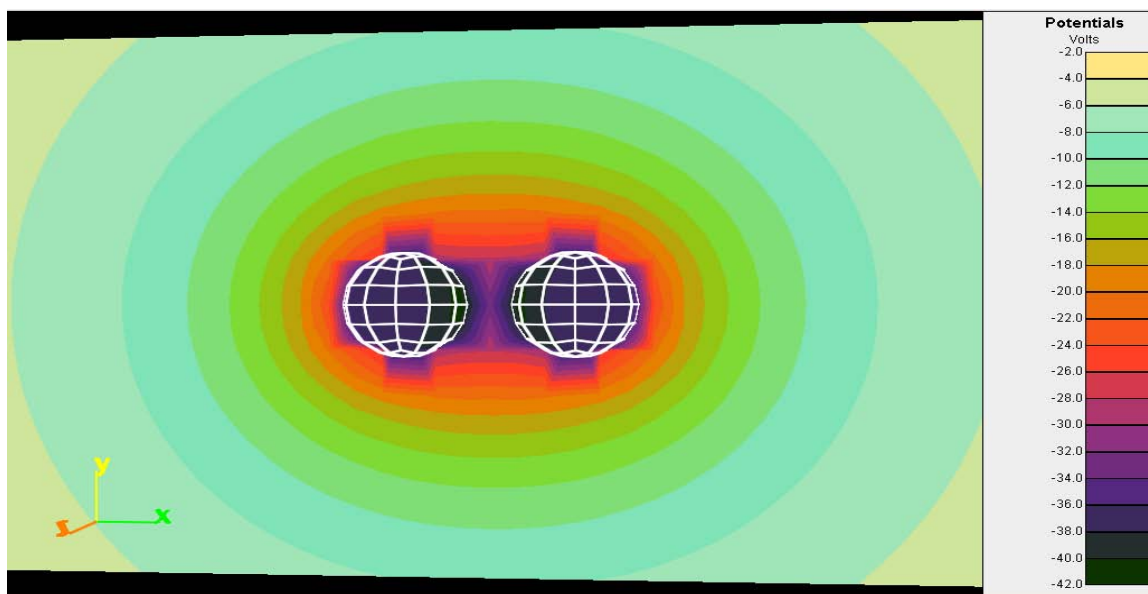
Figure 34 shows droplet surface and sheath potentials after 10 seconds of charging. Sheath development is not yet complete but there is a negative potential on all surfaces and throughout the sheath. After 10 seconds of the strongest GEO charging expected, the droplet has a negative surface potential greater than -200V on every surface element. Analysis in the next chapter will show that uniform surface potential of 350V can induce Coulomb breakup in droplets with a diameter 1mm or less.



**Figure 35. DC705 Sphere at Equilibrium in NASA Worst-case GEO after 300 sec**

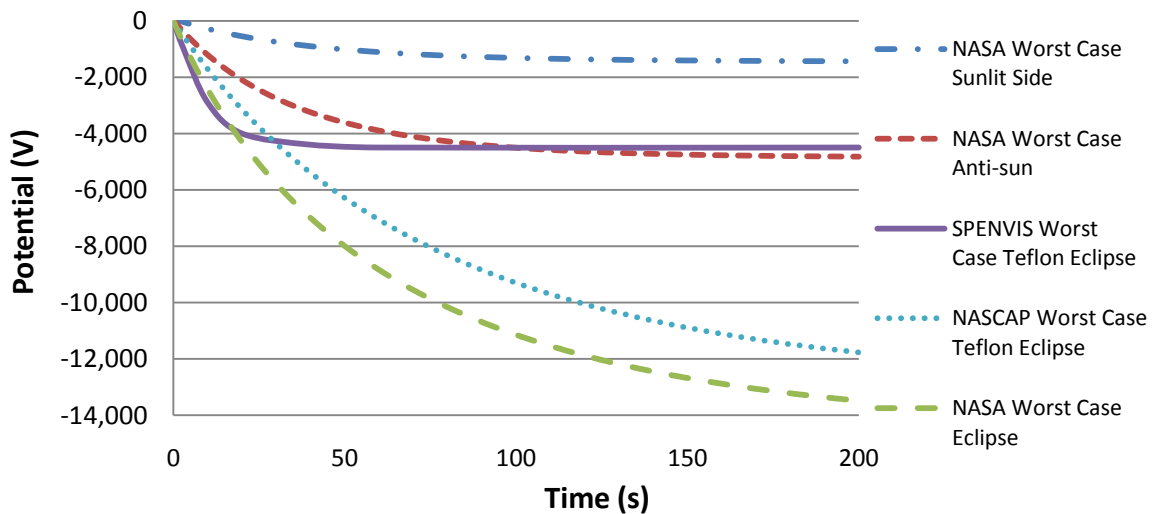
The same droplet is depicted in Figure 35 after 300 seconds. At this point surfaces have reached equilibrium potential, and the sheath is fully formed. Droplet charge is now above the level required to induce Coulomb breakup in small droplets. The impact of droplet breakup in to sub-droplets is discussed in the next chapter. In GEO eclipse, equilibrium potential is nearly uniform on all surface elements of a sphere. The equilibrium charge variation was analyzed in six eclipse simulations, and in all cases the maximum and minimum surface elements differed by less than 3%. When neighboring droplets have a small enough gap between them, their plasma sheaths overlap.

Figure 36 shows two 8.3mm spheres separated by a 4mm gap in an eclipsed NASA worst-case GEO environment. The sheaths of the two droplets merge and create an interactive sheath. If more droplets are added in series, a nearly cylindrical sheath forms around the stream of droplets. Electrostatic potential inside the gap drops off much less with distance than it does above surfaces not facing another droplet. The higher potential in the gap region results in electric field forces between droplets that are damped very little by the plasma sheath. Inside the gap, electric field strength still drops with distance and is proportional to:  $\frac{e^{-r}}{r}$ . This proportionality is used in Chapter 4 to quantify electric field strength between droplets when plasma damping in the space between droplets is negligible.



**Figure 36. DC705 Spheres in NASA Worst-case GEO**

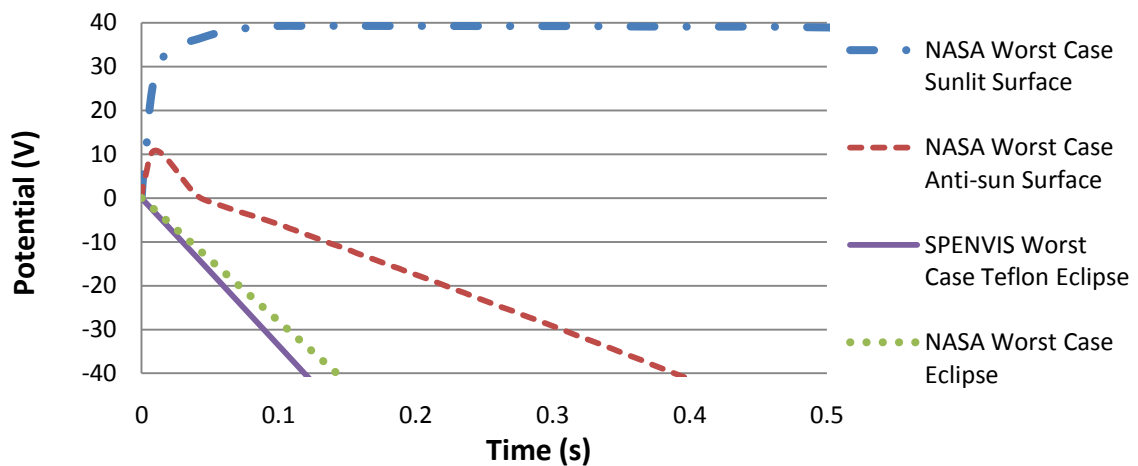
It can take several minutes for droplets to reach equilibrium potential in GEO during high geomagnetic activity. Results of charging of a single 8.3mm DC705 droplet in the NASA Worst-case environment are shown in Figure 37. The chart includes results from simulations run in both eclipse and in sunlight. Sunlit surfaces in the chart below refer to the surfaces on the particular droplet most normal to the sun while anti-sun surfaces are those on the side of the droplet opposite the sun with the most negative charge potential. The plot shows the long period of time required to reach equilibrium charge in GEO during high geomagnetic activity. At reasonable transit speeds, droplets transiting spacecraft in GEO are unlikely to reach equilibrium potential before being collected. Droplets charged in the sun reach significantly more positive equilibrium charges than those in eclipse. The average charge of all surface elements on a sunlit droplet is about 75% less negative than the nearly uniform potentials reached by droplets in eclipse.



**Figure 37. NASCAP Simulation of DC705 alongside SPENVIS and NASCAP Simulations of Teflon Spheres in Eclipse. All Simulations are in NASA's Worst-case GEO Charging Environment. In Sunlit Droplets, the Most Positive and Negative Potentials are found on the Sunlit and Anti-sun Surfaces, Respectively.**

Teflon was simulated in strong GEO using NASCAP and the ESA charging model, SPENVIS to compare results with DC705 results. Surprisingly, both SPENVIS and NASCAP Teflon eclipse estimates are less negative than estimates for eclipsed DC705. This result is counter to the expectation that the strong

insulator, Teflon, will charge more strongly than DC705, a semi-conductor. One explanation for the stronger charge potential seen in DC705 is lower density that allows greater electron penetration depth. This results in more pronounced deep bulk surface charging in DC705 than in Teflon. The most important finding of these simulations of high magnetospheric charging in GEO is that charge levels are above those at which droplet breakup occurs, even with very fast streams. Figure 38 shows the first 0.50 seconds of the severe GEO charging data presented in Figure 37 with more resolution on both axes. One surprising result of the presence of sunlight is that positive charging occurs during the first few hundredths of a second on the anti-sun side. Movement of ions from the sheath above the sunlit side to the anti-sun side is the presumed cause of this initial positive charging, however, the nature of this initial positive charging is not well understood.



**Figure 38. NASCAP Charging Results for Strong GEO Charging Environments. This chart shows the First 0.50 seconds of the severe GEO charging data presented in Figure 37 with more resolution on both axes.**

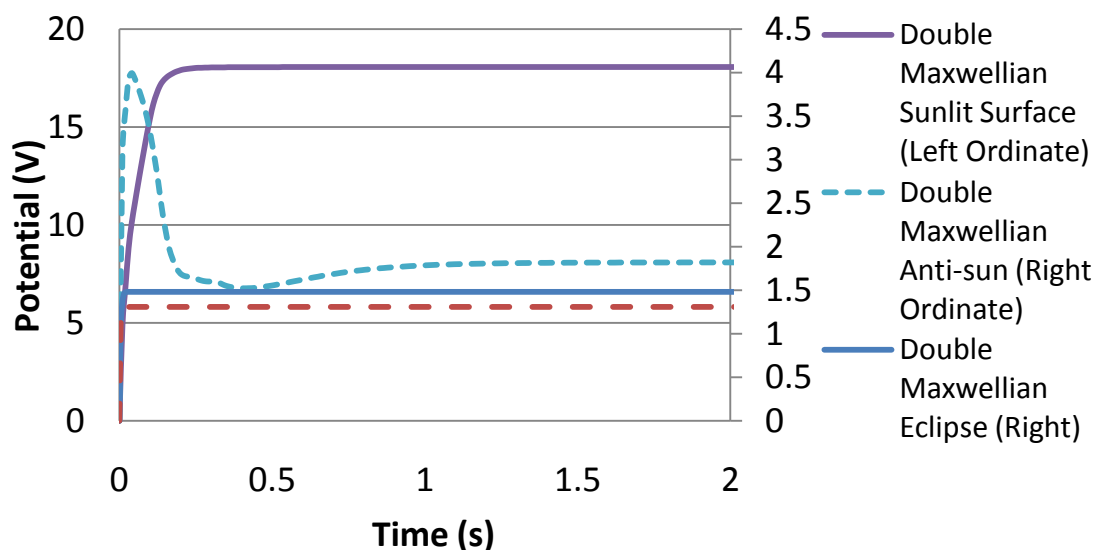
Because the atmospheric density is negligible at GEO altitudes and the magnetic field is very weak, the associated drag and electromagnetic interaction (Lorentz) forces are unlikely to affect the path of sub-droplets significantly. Electric fields between droplets in GEO during high magnetospheric conditions will be strong enough to produce significant repulsion forces between droplets. The next chapter will show how this can cause significant dispersion from the intended path in droplets charged much less strongly.



Interaction between non-uniform droplets formed through Coulomb breakup of larger droplets was not analyzed in this study and remains a potential obstacle to projecting droplet streams in GEO.

Figure 39 shows GEO results for a DC705 sphere in three nominal GEO environments. The top four curves show results from droplets simulated in the NASA Nominal GEO single and double Maxwellian charging conditions described in Chapter 2. The double Maxwellian environment was simulated in both eclipse and in sunlight. The difference in scales was necessary because of significant positive charging on the sun-facing side where potential reaches +18V. The plot of the minimum surface on a droplet in a double Maxwellian sunlit nominal GEO environment shows that the charge potential on surfaces opposite the sun only reaches +4V before equilibrating to +1.7V. Equilibrium charge in eclipse is reached very rapidly in all three nominal plasma environments and does not exceed +1.5V.

Simulations of droplet charging in nominal GEO conditions show that droplets will charge positively on all surfaces with the maximum charge on any surface reaching about +20V. High magnetospheric activity as strong as the NASA Worst Case just described is rare, having occurred only a handful of times since the space age (and monitoring) began.<sup>53</sup>



**Figure 39. Nominal GEO Environment DC705 Sphere Charging (first series plotted against left ordinate, other 4 plotted against right ordinate).**

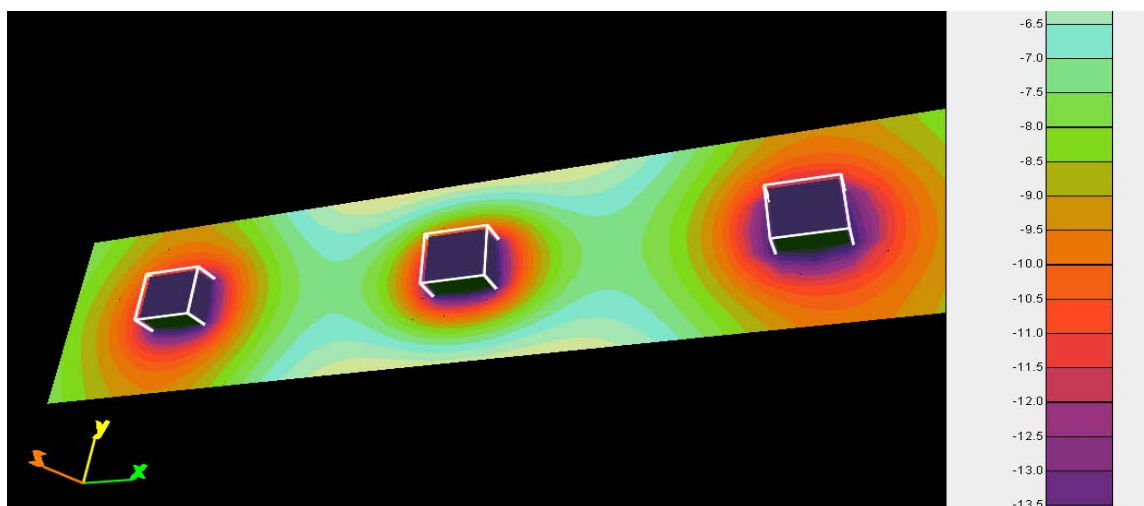
It typically takes 2-3 days for strong geomagnetic activity to dissipate, much longer than the 12 hours it takes for tandem satellites to cross paths following suspension of droplet streams. Moderate magnetospheric events could also charge droplets to levels where Coulomb breakup occurs.<sup>23</sup> One to three of these weaker solar events occur per solar cycle almost exclusively during the three years surrounding solar maximum. The effect of Coulomb breakup on droplet streams is discussed in the next Chapter.

#### **D. Results of LEO and Auroral Simulations**

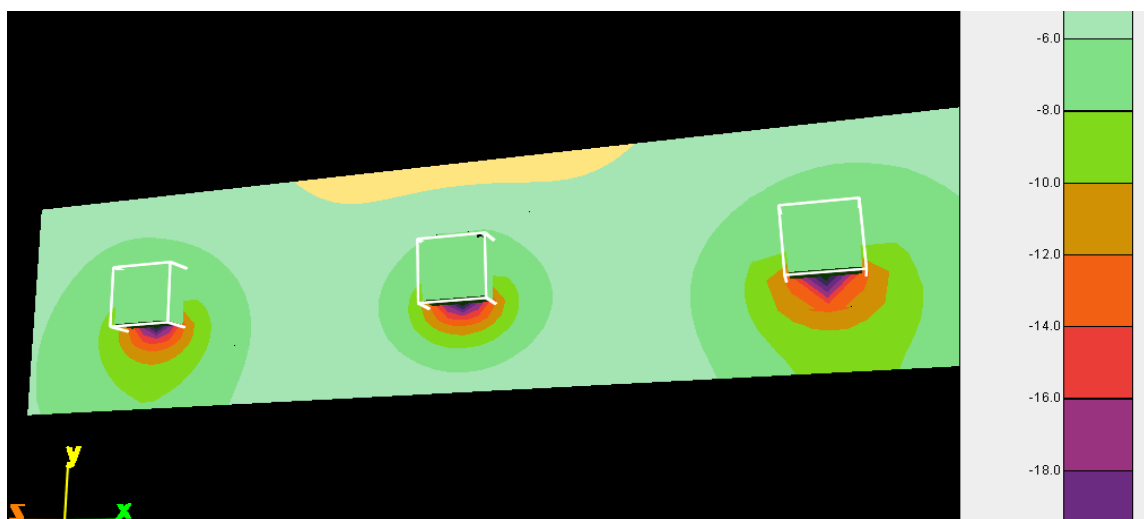
Simulations of DC705 droplets in LEO reveal a charging environment that is more benign than the nominal GEO environment described in the last section. Shielding by Earth's magnetic field prevents most high-energy particles from reaching low latitude LEO. Charging of droplets in LEO is mitigated by low energy positive and negative ions (cool plasma) in the ionosphere. NASCAP simulations were run with multiple spheres in a nominal single Maxwellian LEO environment with electron and ion energy and density specified by the International Reference Ionosphere (IRI) for the orbit of the International Space Station (ISS).<sup>32</sup> In sunlight, DC705 spheres reach a very small nearly uniform negative charge potential of -0.01V relative to the ambient plasma in less than a second. In eclipse, the same LEO environment resulted in a surface potential of -0.05V. By comparison, NASCAP charging of a Teflon sphere in the eclipsed ISS environment resulted in a charge potential of -0.67V. Similarly, a charging simulation of an isolated Teflon patch in 300km low latitude LEO using SPENVIS resulted in an equilibrium potential of -0.80V. These results match expectations of a benign charge environment in LEO dominated by low-energy plasma. The next chapter evaluates the impact of droplet charge on droplet streams and it will be shown that these low levels of charge are not expected to create any significant impediments to droplet stream operations.

NASCAP simulations show that auroral charging of droplets is highly dependent upon the plasma energy and density spectrum and, to a lesser degree, the presence of UV photons from the sun. The influence of low-energy positive ions impacting the ram and not the wake hemisphere results in a slight differential charging of these two hemispheres, even in eclipse, without the influence of photoemissions. The following images show electrostatic potential on and around three 2mm cubes spaced 6mm apart in the

eclipsed strong DMSP charging environment described by a Fontheim distribution in Chapter 2. Figure 40 shows the cubes after 0.01 seconds and reveals significant development of uniform sheaths around the droplets. Influence of the sheaths of the outer cubes causes the middle cube (or thousands of inner cubes) to have a thinner sheath in all directions perpendicular to the stream. Sheath thickness in the direction of the stream is greater and is roughly the same for outer and inner droplets.



**Figure 40. 2mm DC705 Cubes in Strong DMSP Eclipse Environment after 0.01 seconds.**

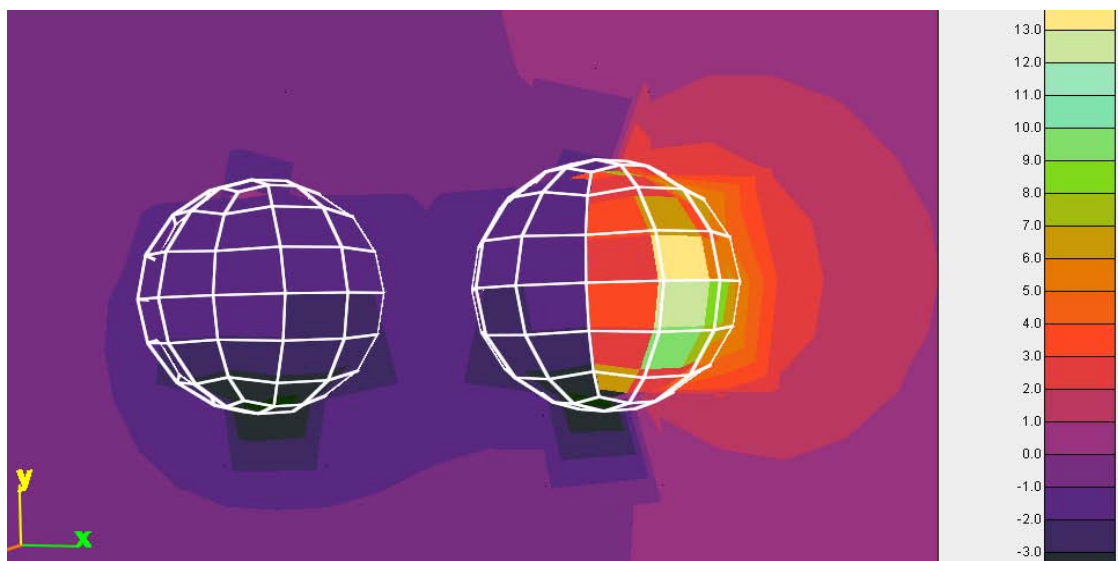


**Figure 41. 2mm DC705 Cubes in Strong DMSP Eclipse Environment after 0.5 seconds.**

As with GEO droplets, this overlap of sheaths results in less damping of electric fields acting between droplets. The effect of electric field damping by plasma sheaths on droplet interactions is addressed in the next chapter. The same three droplets are depicted in Figure 41 after 0.5 seconds.

At 0.5 seconds, surface charge is at equilibrium and the most negative charge potential (-25V) is on the wake surface while the most positive charge (-12V) is on the ram surface. Cube velocity is 7.5km/s in the “y” direction indicating that low-energy ions from the upper ionosphere are responsible for the charge mitigation seen on the ram side.

Charging in sunlight alters the charge seen on droplets in auroral space significantly. Surfaces on the sun-facing side charge positive and remain positively charged while shaded surfaces charge negatively as they do in eclipse. Figure 42 shows two DC705 spheres in an auroral environment with a level of elevated auroral activity that occurs several times during solar maximum and sometimes out of solar maximum due to geomagnetic activity. In addition, the sun is aligned with the x-axis so that one droplet is shaded by the other. Peak positive surface charge is +14V while peak negative charge is -4V.

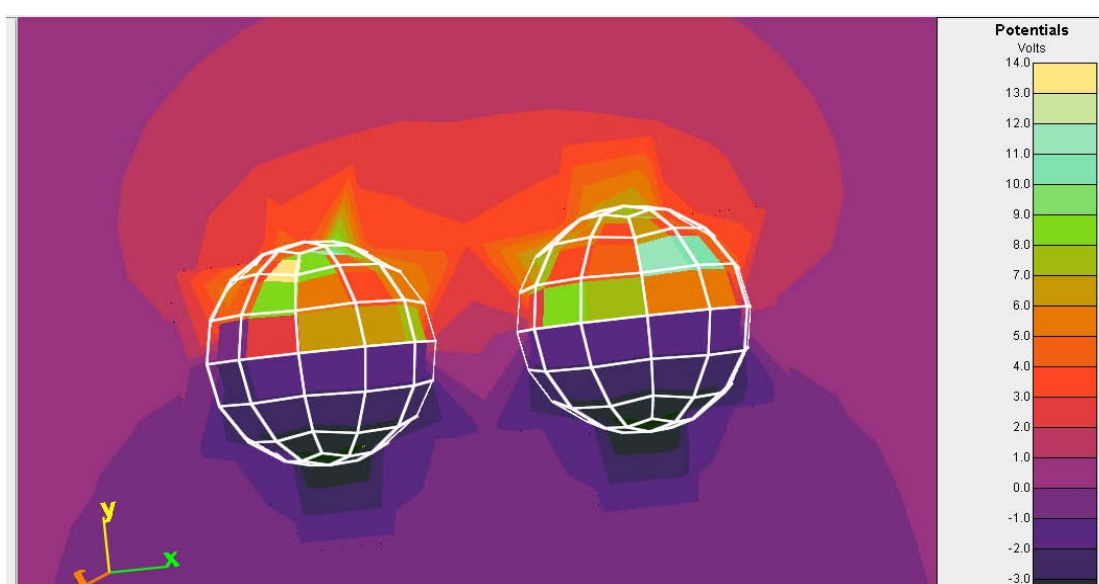


**Figure 42. DC705 Spheres in DMSP Sunlit Environment with Elevated Geomagnetic activity.**

Charging on the anti-solar half of the sunlit droplet is very similar to charging on the shaded droplet. Charging of the ram half of the sunlit hemisphere has the most positive surface element but, in general, does not show significantly more positive charging than the wake half of the sunlit hemisphere. Similarly,

the ram half of the anti-solar hemisphere and eclipsed droplet have a potential that is only about one volt more positive than surfaces on the wake hemisphere.

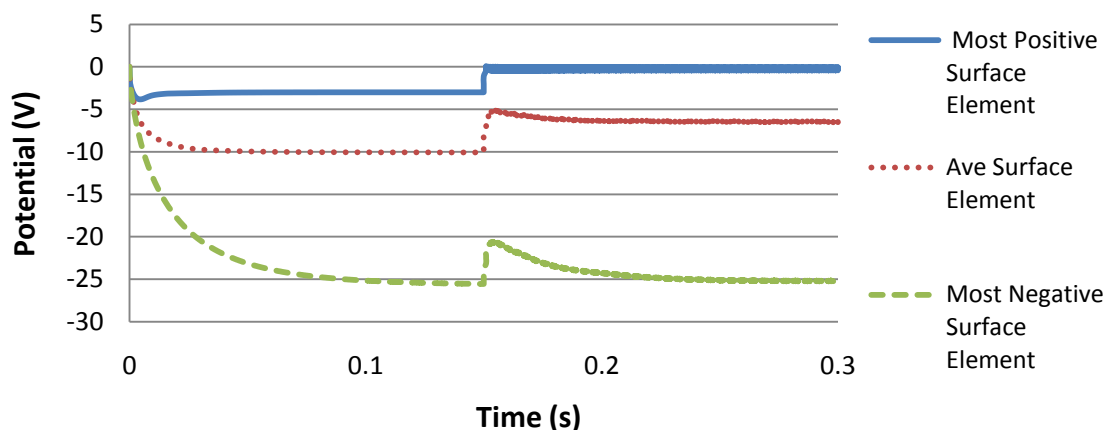
In order to further quantify the effect of both sunlight and ram ions acting on the same hemisphere, another simulation was run with the sun positioned in line with the ram direction (y-axis). Once again, two neighboring droplets were exposed to an environment with elevated auroral activity. Results in Figure 43 show that peak positive surface charge did not increase indicating that little ion deposition occurs in auroral space when a surface is already charged positively by photoemissions. This result matches expectations that a surface charged positively will repel low energy ions and attract low energy electrons present in the low-energy plasma of auroral space.



**Figure 43. DC705 Spheres in DMSP Sunlit Environment with Elevated Geomagnetic activity.**

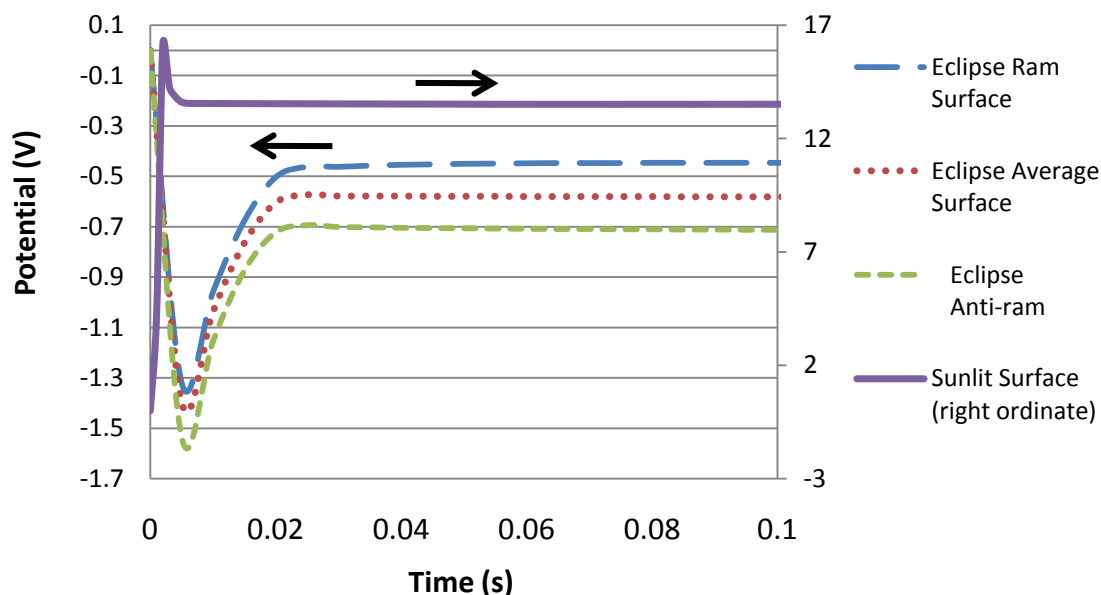
Often charge induced events occur on satellites during the transition from eclipse to sunlight. Dielectric components acquire a positive charge very rapidly while conducting components are still negatively charged. Such a dipolar situation can lead to arcing in spacecraft.<sup>23</sup> Arcing within a droplet is not likely because the liquid state allows Coulomb forces to dissipate concentrations of charge to other areas of the droplet. Arcing between a newly formed droplet and its parent spacecraft is highly dependent on the material used to construct the droplet generator and collector. Arcing was not analyzed in this study and it is assumed that suitable materials exist to mitigate arcing between the spacecraft and nearby droplets.

A simulation was conducted to quantify the effects of a droplet transitioning from eclipse to sunlight in a strong auroral charging environment. Results are shown in Figure 44, show that all surfaces charge negatively in eclipse with leading hemisphere surfaces assuming a more positive charge. Following solar exposure at 0.15 seconds, surface elements on the sun facing side rapidly charge positive with very little overshoot and then equilibrate to a nearly neutral potential. Interestingly, the most negative elements on the anti-solar hemisphere briefly charge more positive before returning to a potential near that of equilibrium eclipse. It is believed that this positive charging on the anti-sun side occurs because positive ions in the plasma sheath on the sunlit side are repelled by the, now positive, sunlit surface charge and migrate to the anti-sun side where ion deposition occurs.



**Figure 44. Transition from Eclipse to Sun in a Strong 800km Auroral Charging Environment.**

NASCAP simulations of nominal auroral conditions predict minimal negative charging in eclipse and significant positive charging on the sunlit side of droplets exposed to the sun. Figure 45 shows eclipse results in the bottom three curves plotted against the left ordinate. The top curve shows maximum potential on sunlit surface elements plotted against the right ordinate. Positive charging due to UV photoelectron emissions is both more rapid and of higher magnitude than negative charging in eclipse. Negative charging response on the anti-solar side is not shown in Figure 45 but is similar in onset and magnitude to eclipse charging shown in Figure 44.



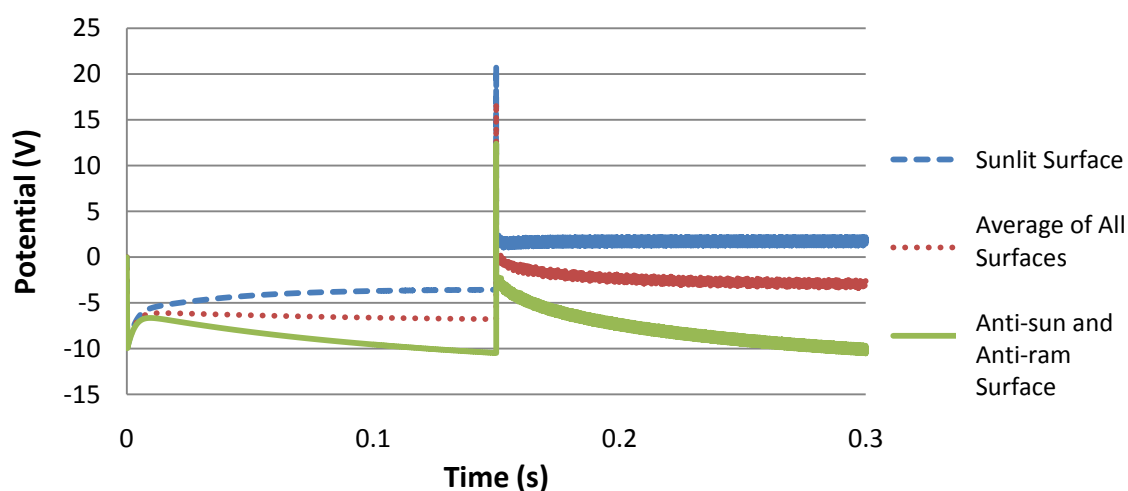
**Figure 45. Nominal Auroral Droplet Charging. Top curve shows Maximum Potential on Sunlit Surface Elements (right ordinate). Eclipse results are shown in the Bottom Three Curves (plotted against left ordinate). Ram Surfaces Acquire a Slightly more Positive Charge while and Sunlit Surfaces Charge more Strongly Positive.**

Because of the relative absence of low-energy atmospheric plasma above 1000km, the effects of auroral charging above this altitude were studied to compare with results from DMSP environment data collected in the 300-800km range. Simulations were run using six sets of Fontheim distribution data by the Freja satellite in auroral space at 1500km during strong, moderate, and nominal intensity periods of geomagnetic activity. Results showed negative charging on all surfaces in eclipse and negative charging on all but the sun facing surfaces in sunlight. Equilibrium charge results were similar to those that resulted from DMSP events analyzed. Parameters of the strongest of the six Freja charging events are listed in Table 2. This environment resulted in lower charging than simulations performed with the most severe DMSP environment data collected at altitudes 700km lower than that of the Freja satellite.

Because of the absence of low-energy plasma and the presence of more high-energy plasma, stronger equilibrium charging results at higher altitude is expected. This was not seen, probably because DMSP data has been collected for over four decades while Freja data exists for less than three years. Freja

collection began in 1992 and ended just three years later when the spacecraft failed. More long-term study of the high auroral zones and more Fontheim fits to high altitude data is needed before it can be concluded that the high auroral environment results in more charging of DC705 droplets. It is expected that further study of this environment will reveal that high auroral is a stronger charging environment for DC705 droplets than low auroral is.

High auroral charging of droplets experience negative charging in eclipse and positive charging in the sun much more abruptly than droplets at lower auroral altitudes. Without high-density low-energy plasma seen at lower altitudes, DC705 charges rapidly negative due to secondary electron emissions and charges rapidly positive due to photoemissions. The plot in Figure 46 shows the strong early response of a droplet in an eclipsed high auroral environment. Midway through the simulation emergence from eclipse into sunlight occurs along with a significant momentary jump in charge potential. This jump is significant but very short-lived and well below the several hundred volt potential needed to induce coulomb breakup in droplets 1mm in diameter or greater.



**Figure 46. Transition from Eclipse to Sun in a Moderate, High Altitude, Auroral Environment At 0.15 seconds, exposure to the sun occurs causing a momentary spike of +21V and establishes a new maximum (positive) equilibrium on the sunlit surfaces. The anti-solar side experiences a similar momentary spike of +12V before returning to negative charge equilibrium. In the simulation depicted the maximum number of time steps supported by NASCAP was used.**



The initial negative charging in the plot is caused by secondary electron emissions. This is followed by sheath formation and backscattering of electrons that result in some positive charging. Next, the ram hemisphere continues to charge slightly more positive as it impacts a weak flux of low-energy positive ions. The wake hemisphere charges negatively due to the preponderance of high-energy electrons impacting the entire droplet and the absence of low energy ions in the wake.

#### E. Summary of Droplet Charging in LEO, GEO, and Auroral Environments

Table 6 summarizes the results of more than a hundred NASCAP simulations of DC705 droplets in various environments. Shielding of high-energy particles by Earth's magnetic field and the presence of high numbers of low energy plasma particles makes low latitude LEO the most benign environment to operate in. Droplet charge potentials remain less than 2.1V despite high geomagnetic activity both in eclipse and in sunlight. It is shown in the next chapter that this level of droplet charge has minimal impact on droplet transit paths between satellites. Charge induced forces are especially small when compared to drag forces in LEO below about 500km.

**Table 6. Summary of Equilibrium Potentials (maximum sunlit surface and minimum eclipsed surface) and Time to Reach Equilibrium in the Environments Analyzed**

<b><u>Environment:</u></b>	<b><u>LEO</u></b>	<b><u>&lt;800km Auroral (DMSP)</u></b>	<b><u>1500km Auroral (FREJA)</u></b>	<b><u>GEO</u></b>
<b>Low Geomagnetic</b>	<b>+0V , -0.5V (sun, eclipse)</b>	<b>+1.5V, -2V</b>	<b>+2V, -14V</b>	<b>+18V, +1.5V</b>
<b>Nominal Geomagnetic</b>	<b>+0V , -1V</b>	<b>+4V, -16V</b>	<b>+6V, -25V</b>	<b>Not Analyzed</b>
<b>High Geomagnetic</b>	<b>+2V , -2V</b>	<b>+21V, -26V</b>	<b>Insufficient Data (3 years only)</b>	<b>-2kV, -13kV</b>

Analysis of auroral charging using environment data from DMSP spacecraft between 500 and 800km shows that charge will remain between -26V and +21V in and out of eclipse. Equilibrium potential is reached within 0.2 seconds without any significant overshoot of equilibrium potential in either sun or

eclipse. Negative charging due to electron deposition and secondary electron production is rapid but is then mitigated by low-energy ions within half of a second. These levels of charge potential will affect droplet impact dispersion to a level quantified in the next chapter along with methods of mitigation.

Sufficient Fontheim distribution data is not currently available to characterize the high auroral charging environment accurately during strong charging events. Droplet charging during moderate geomagnetic activity is characterized by rapid negative charging to magnitudes approaching those seen during strong charging events at lower altitudes. Photoemission charging of droplets in high auroral space is also rapid and results in spikes in voltage potential on all surfaces that are many times greater than the sunlit equilibrium charge but last just thousandths of a second. Further study of droplet charging in the high auroral environment is needed to accurately quantify negative charge potential during high magnetospheric activity.

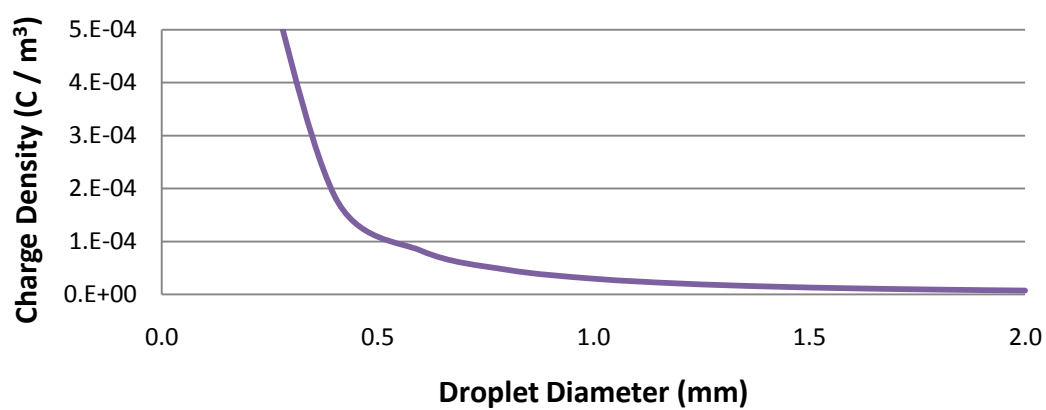
In the GEO environment, moderate and strong charging environments yielded negative charging large enough to cause Coulomb breakup of droplets in the size range considered for droplet streams in this study. The prime concern with breakup is that repelling electric field forces acting between sub-droplets will result in a larger stream impact area. This is especially if some sub-droplets are smaller than others are since smaller droplets are displaced more by electrostatic fields than large droplets. The impact of droplet breakup on droplet stream collection in GEO is discussed in the next chapter.

Once the voltage potential of a droplet is known, the total charge of the droplet is found by multiplying voltage by droplet capacitance:<sup>52</sup>

$$Q = VC \quad \text{where} \quad C = \sigma 2\pi d \epsilon_0 \quad (32)$$

where  $d$  is the sphere diameter,  $\sigma$  is Coulomb's constant, and  $\epsilon_0$  is the permittivity of free space ( $8.85\text{e-}12 \text{ C}^2/\text{nm}^2$ ). Charge density in Coulombs per cubic meter as a function of droplet diameter is shown in Figure 47 where bulk charge density decreases by a factor of  $8/d^2$  as droplet diameter is increased. This charge density relationship is in keeping with the findings of the famous Robert Millikan experiment of 1909 in which the discrete elemental charge of an electron or proton was first determined.<sup>52</sup> If a suspended charged droplet of oil is evaporated, the charge density of the droplet will increase until Coulomb forces overcome surface tension forces and the droplet breaks apart.<sup>54</sup> Similarly, for a given droplet voltage potential, the

average charge density decreases with the cube of the droplet radius. As a result, charge density decreases significantly when diameter is increased from 0.5 to 1.0mm but charge density decreases very little when droplet diameter is increased beyond 2mm.



**Figure 47. Droplet Charge Density as it relates to Diameter**

## Chapter 4: Effects of Electric and Magnetic Fields on Droplet Motion

This chapter discusses the impact of droplet charging on the droplet stream concept. Forces both internal and external to the droplets are analyzed. Coulomb forces that could overcome surface tension and break droplets up into smaller droplets are quantified. Lorentz and other forces due to the Earth's magnetic field and due to external electric fields are analyzed and quantified to show their impact on transiting droplets. Forces are quantified in terms of the estimated charging results presented in the last chapter, and the impact of those forces on different sized droplets is presented. A computer simulation code written for this study to quantify droplet repulsion due to inter-droplet electric fields is described and results presented. Taken together, these simulations provide an indication of how large of a collector would be required to capture a desired percentage of transiting charged droplets with a desired probability of success.

### A. Small Charge Induced Drift Forces Considered

Charged droplets interact with the Earth's magnetic field and produce forces that act on those droplets. Perturbation forces caused by the Earth's magnetic field will change droplet velocity magnitude, and/or direction, and potentially represent a significant challenge to projecting a droplet stream over a large distance, and receiving it on the other end. The strongest of these forces is the Lorentz force which acts perpendicular to both the droplet's velocity and the magnetic field lines and will be discussed at length later in this chapter.

Other charged particle interactions with Earth's magnetic field also cause perturbations to droplets in transit and cause drift. Chief among these are drift due to magnetic field gradients and drift due to magnetic field curvature. These forces impart a velocity to charged particles having a component of velocity acting perpendicular to the magnetic field,  $v_{\perp}$ , or parallel to the magnetic field,  $v_{\parallel}$ . The velocity induced by a magnetic field,  $\vec{B}$  is quantified by:<sup>20,28</sup>

$$\text{Grad-B Drift} \quad \vec{v}_{\nabla B} = \frac{mv_{\perp}^2}{2qB^3} (\vec{B} \times \nabla \vec{B}) \quad (33)$$

$$\text{Curvature Drift} \quad \vec{v}_d = \frac{mv_{\parallel}^2}{qB^2 R_{\text{curv}}} (\hat{R}_{\text{curv}} \times \vec{B}) \quad (34)$$

Both of these forces result from the fact that a charged particle, moving in a magnetic field will trace out a circular orbit perpendicular to the field. The period of this orbit (the cyclotron period) is given by:<sup>20</sup>

$$P = 2\pi \left( \frac{m}{qB} \right) \quad (35)$$

where  $q$  is the charge,  $B$  is the magnetic field strength, and  $m$  is the particle mass. Table 7 shows the cyclotron gyration period for a 1mm diameter DC705 droplet at five different voltage potentials. Also listed is the angle traversed in 50 seconds; the time it takes for a droplet to transit between satellites 1km apart at 20m/s transit velocity. The cyclotron periods of smaller (down to 0.2mm diameter) and larger (up to 2mm) droplets were also analyzed and found to have periods within an order of magnitude of those corresponding to 1mm diameter droplets.

**Table 7. Cyclotron Periods for 1mm Droplet at Several Voltage Potentials**

Voltage Potential (V)	Cyclotron Period (days)	Cyclotron Period (yrs)	Radians Traversed (in 50 sec)
50000	228	0.6	$1.6 \times 10^{-5}$
12000	951	2.6	$3.8 \times 10^{-6}$
500	22822	62.5	$1.6 \times 10^{-7}$
25	456432	1250.5	$8.0 \times 10^{-9}$

Since the cyclotron period is many years at the anticipated voltage potentials, 50 seconds represents only a small portion of that rotation period. Moreover, because of the relatively large mass of a droplet (as compared to the mass of a single charged particle) the radius of the rotation is quite large; tens of kilometers or more. The small angle and large radius of the cyclotron gyration experienced by a droplet during transit describes a nearly straight arc. The amount of drift induced by the cyclotron gyration is the amount of curve to this arc, which is very small. Even a 0.25mm diameter droplet with a three-minute

transit time drifts less than a tenth of a millimeter. For larger or faster droplets such as those preferred for LEO fluid stream propulsion, the drift amount is even less and can be ignored.

Another force that acts on charged particles in the space environment is polarization drift that results when an electric field,  $\vec{E}$ , is perpendicular to a magnetic field B-field. This drift is known as  $\vec{E}$  cross  $\vec{B}$  drift because its velocity is defined by the equation:

$$\vec{v}_E = \frac{\vec{E} \times \vec{B}}{B^2} \quad (36)$$

Weak electric fields do exist in the upper atmosphere of the auroral regions and will exist when droplets are in close proximity to satellites and other droplets. However,  $\vec{E} \times \vec{B}$  drift acts incrementally over many magnetic field-induced cyclotron orbits and thus has very limited affect on particles with long cyclotron periods. Relatively massive droplets (relative to ions) have very long cyclotron periods. Many years are required before  $\vec{E} \times \vec{B}$  drift will induce a small alteration of the cyclotron orbits caused by the magnetic field alone. The cyclotron orbits themselves were already shown to affect drift almost imperceptibly in the time scales being considered, thus  $\vec{E} \times \vec{B}$  drift is even smaller and can be neglected, at least for droplets larger than 0.2 mm in diameter and with charge potentials less than 50,000 volts. In this study, only droplets over 0.2 mm were analyzed and predictive modeling indicates nominal droplet voltage potentials below 10V. Indeed, the next section will show that useful droplet diameters with potentials more than several hundred volts will break apart.

It should be emphasized that Grad-B Drift, Curvature Drift, and Lorentz force are primarily a result of interactions with the Earth's magnetic field. Since the strength of this field drops with the cube of the distance from Earth's center, these forces are most significant in LEO and strongest over the geomagnetic poles. Magnetic field strength in GEO is more than two orders of magnitude weaker than in LEO.<sup>28</sup> Grad-B, Curvature, and Polarization Drift act on time scales that make the resulting drift insignificant (less than a millimeter) to droplets transiting for less than a few minutes. As a result, the only magnetic field interactions modeled in this study are those resulting from Lorentz forces. The following sections will describe the impact of charge on droplet drift and breakup in more detail.

## B. Lorentz Forces Caused by Earth's Magnetic Field

The magnetic field induced force that is of principle concern to droplet stream propulsion is the Lorentz force which acts in accordance with the equation:

$$\vec{F} = q (\vec{E} + \vec{V} \times \vec{B}) \quad (37)$$

Here,  $\vec{E}$  is any electric field present (in Newtons/Coulomb),  $\vec{B}$  is any magnetic field present (in Teslas),  $\vec{V}$  is the droplet velocity (in m/s) and  $q$  is the charge of the droplet (in Coulombs). In near Earth space, forces due to electric fields are at least an order of magnitude weaker than forces caused by Earth's magnetic field.<sup>20</sup> Electric fields between charged droplets are significant and are analyzed in the next section. The Earth's magnetic field is about twice as strong over the geomagnetic poles as it is over the equator. The magnetic poles are located near Tule, Greenland and Vostok Station, Antarctica so orbiting droplets with inclinations between 75 and 105 degrees are affected much more strongly by this force than those in lower inclination orbits.

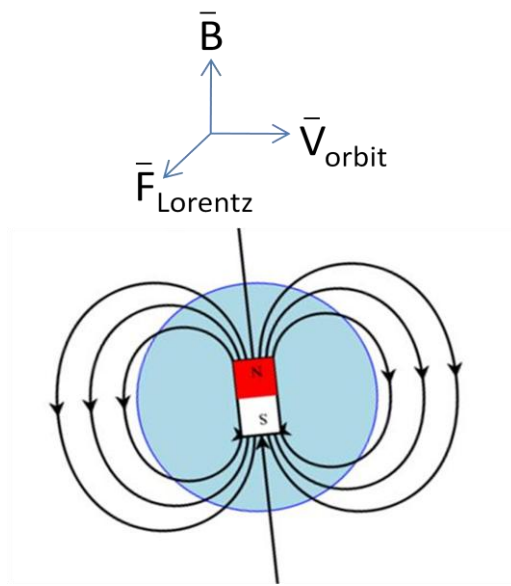
In terms of co-latitude ( $\theta$ ), the total intensity of the field in Teslas can be quantified by:<sup>28</sup>

$$\vec{B} = \frac{M}{r^3} \sqrt{3 \cos^2 \theta + 1} \quad (38)$$

The strength of the Earth's magnetic field is roughly twice as strong at the poles as it is at the equator for a given distance from Earth's center. At the geomagnetic north pole the magnetic field strength is 30-50  $\mu$ Teslas or 0.3-0.5 Gauss.<sup>33</sup>

The cross product of the droplet velocity  $\vec{v}$  and magnetic field  $\vec{B}$  results in a force acting perpendicular to both of these vectors. In Figure 48 the direction of the Lorentz force is shown for a satellite in polar orbit over the North Pole. The orbital plane lies in the V-B plane (on the page surface) and the Lorentz force is directed out of the page, in-line with the vector between two satellites flying side-by-side. There is also a Lorentz force induced by the transit velocity of the droplets moving between satellites but it is at least 750 times weaker than the primary Lorentz force induced by the orbital velocity. Because the primary Lorentz force acts nearly parallel to the path of transiting droplets, droplets are accelerated or slowed but the direction of droplet travel between satellites is altered very little. Lorentz forces are

strongest in polar orbits where the strongest portions of Earth's magnetic field are encountered and the orbit velocity is nearly perpendicular to the magnetic field. Everywhere in a polar orbit, the vector between side-by-side satellites is perpendicular to the magnetic field lines. Over the geomagnetic equator, the orbit velocity is parallel to the magnetic field and Lorentz forces are nearly zero.

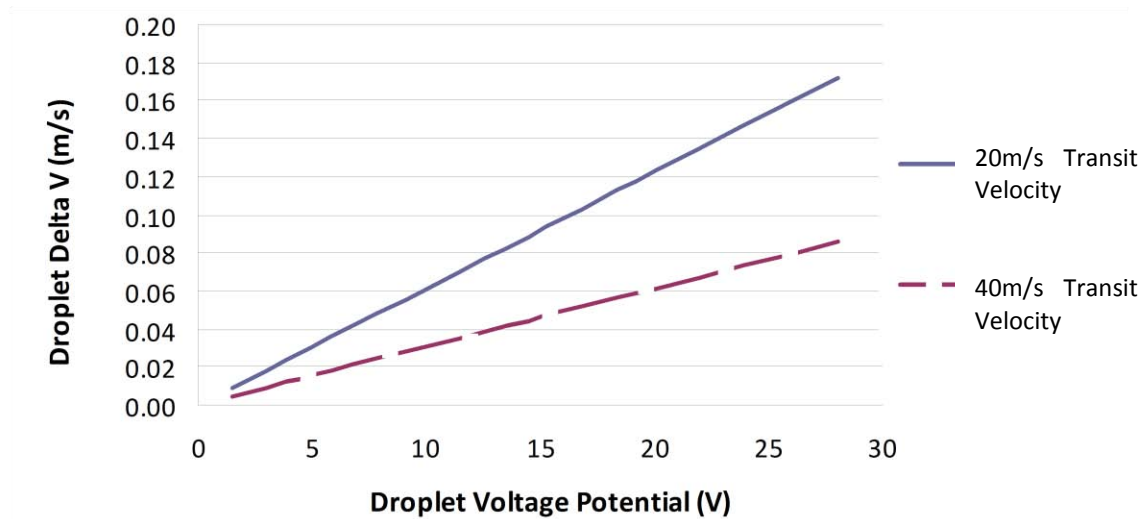


**Figure 48. Direction of Lorentz Force Defined by the Cross Product of the Charged Object's Velocity and External Magnetic Field.**

A polar orbit altitude of 300km was selected to analyze Lorentz force strength because it is near the lower limit of altitudes at which remote sensing satellites typically operate. The low altitude gives this orbit a relatively high orbit velocity and high magnetic field strength that result in high Lorentz forces. A 300km polar orbit is high enough that high-energy plasma can induce significant charging of droplets that transit between satellites as the spacecraft briefly passes through the auroral zones. Even in this worst-case orbit, Lorentz force strength will be quite weak. NASCAP modeling indicates droplet charge magnitude of more than 26 Volts below an altitude of 800km is unlikely even during periods of high geomagnetic activity. The Lorentz force acting on a 1mm droplet with a 26 volt potential is only  $1 \times 10^{-8}$  N. This small primary Lorentz force has little impact on the transit velocity of droplets. One stream is accelerated while the other is decelerated and the magnitude of acceleration is about a centimeter per second over a one-kilometer transit. A charge potential of 3300 Volts is required to completely stop a 1mm droplet launched



at 20m/s before it travels 1km. The velocity change for a 1mm droplet transiting between satellites at 300km altitude is shown in Figure 49 as a function of potential.



**Figure 49. Velocity Change due to Primary Lorentz Force at Nominal Charge Levels**

An interesting result of the acceleration and deceleration of droplets travelling in the opposite direction to one another is that the force acting on one satellite is less than the force acting on the other satellite. Although both droplets are released with the same velocity, one impacts the collecting satellite with slightly more velocity than the other one. Unchecked, spacecraft flying side-by-side will experience a small amount of drift toward and away from the centerline of their shared reference orbit. The differential speed of arriving droplets could be compensated for by increasing the exit velocity of one of the droplet generators, accomplished by increasing the chamber pressure. It may prove interesting to the scientific community to use the droplet stream as a measure of the charging environment by measuring the differential velocity of arriving droplets.

In addition to the primary Lorentz force, there is a secondary Lorentz force induced by the transit velocity of droplets moving between spacecraft through a magnetic field. Because transit velocity is so small relative to orbit velocity (<100m/s vs. >7500m/s), the resulting Lorentz force is extremely small. The table below shows the magnitude of secondary Lorentz force drift produced for various stream diameters

and transit velocities. An arbitrary 1000-volt droplet potential (relative to the ambient plasma) is assumed for all droplets analyzed. Drift distances are inconsequentially small, even at this high potential that is 40 times greater than peak charge potential seen in auroral modeling during worst-case geomagnetic events. The calculated results in Table 8 show that larger drops drift less than small ones. In this case, a four-fold increase in diameter results in about an eighty-fold decrease in drift. The data also shows that although increasing transit velocity does increase the Lorentz force, the resulting drift is less because of the shorter time of flight (TOF) in which the droplet is exposed to this force.

**Table 8. Secondary Lorentz Force Drift Due to Transit Velocity**

Drop Diam (mm)	Dist (m)	Speed (m/s)	TOF (s)	Drift (cm)
0.235	100	10.4	9.6	6.5E-04
0.235	1000	30	33.3	7.8E-03
1	100	3.5	28.6	1.2E-03
1	1000	30	33.3	1.0E-04
1	1000	100	10	9.1E-06

As a spacecraft transits the Earth in a polar orbit the magnitude and direction of Earth's magnetic field relative to droplet streams transiting between spacecraft is ever changing. Although drift due to the primary Lorentz force could never act perpendicular to the droplet transit path, the worst-case drift for this situation was calculated to quantify the upper limit for Lorentz drift. Figure 50 shows of a 1mm droplet transiting at 20 and 40 m/s, 300km with a worst-case magnetic field strength. The same chart also shows the resulting change in velocity (in m/s) for 1mm droplets transiting at the same two transit velocities. Lorentz force drift acts perpendicular to the transit velocity over the equator, however, the magnetic field is much weaker at this latitude making the possible drift amounts smaller than those seen in the chart.

The magnitude of drift seen in auroral space during high geomagnetic activity is less than three centimeters and could be collected without increasing the diameter of existing droplet collector designs. Only if droplet charge reaches a level of several hundred volts will Lorentz force drift be significant enough to hamper droplet collection. As shown previously, the likelihood of charging beyond 26V potential at altitudes below 800km is very low. Moreover, voltages high enough to produce significant Lorentz forces will likely result in droplet breakup and dispersion due to electrostatic forces discussed next.

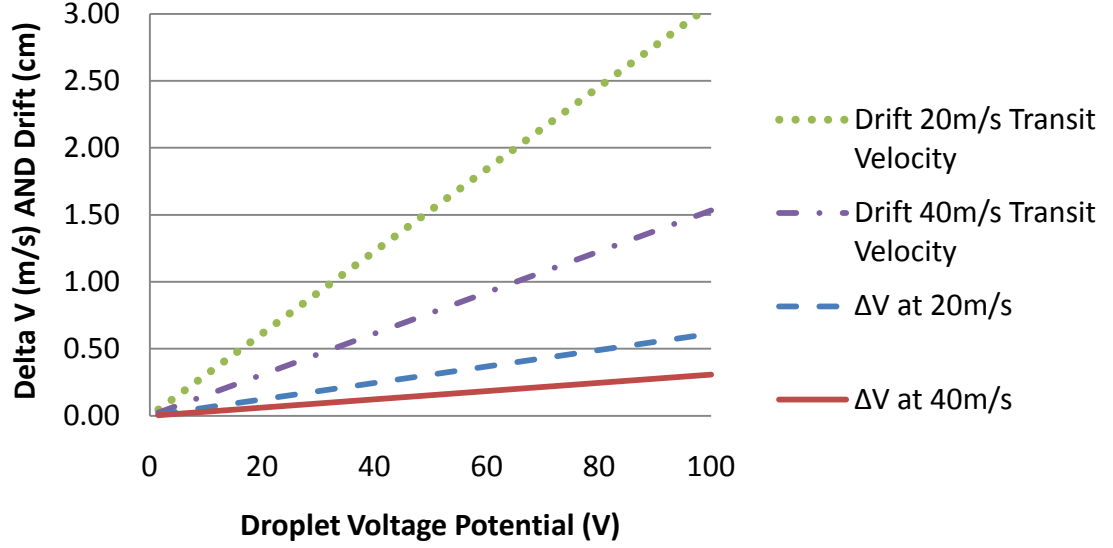


Figure 50. Worst-case Lorentz Drift and Velocity Change over a 1km Transit Distance.

### C. Charge Induced Droplet Breakup

If droplets reach a high enough level of charge, coulomb repulsion forces within the droplet will overcome surface tension forces and the drop will break into smaller droplets.<sup>55</sup> The force of surface tension as a function of droplet radius,  $r$ , is described by the following equation:<sup>51</sup>

$$F_{surf\ tension} = 2\pi r(T_{surf}) \quad (39)$$

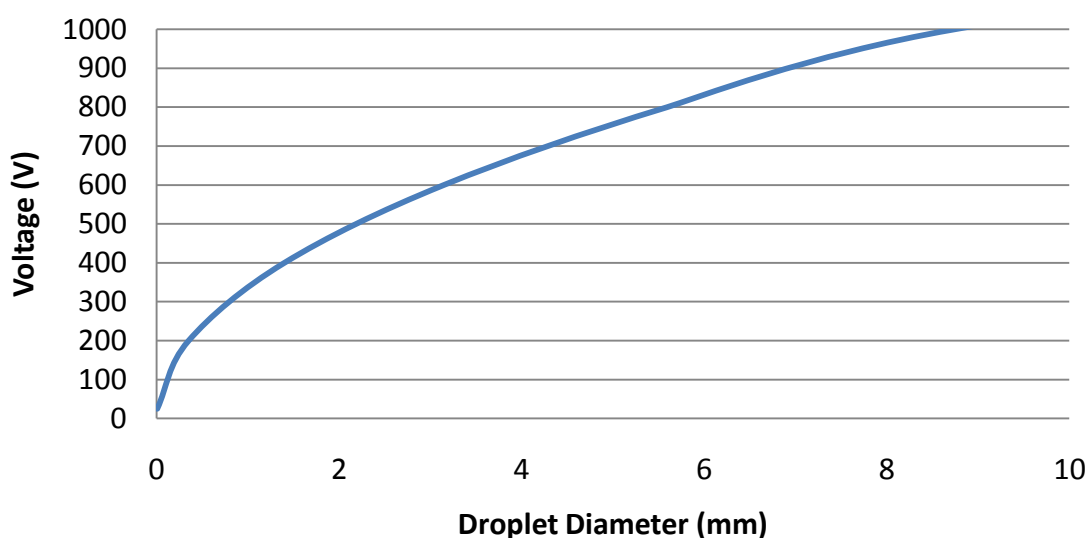
where  $T_{surf} = 0.0365$  N/m for DC705. Coulomb forces are described as a function of separation distance between volume centroids of each hemisphere, which equals two-thirds of the droplet radius:

$$F_c = \frac{\epsilon_0(Q_1Q_2)}{r_{sep}^2} \quad (40)$$

where  $Q$  is the total charge of each hemisphere and  $\epsilon_0$  is the permittivity constant of free space.

DC-705 was analyzed for its potential to break apart when exposed to significant charge levels. Droplet charge can be expressed as a function of voltage potential and droplet capacitance. Capacitance is directly proportional to droplet diameter and charge is directly proportional to capacitance so, for a given equilibrium voltage potential, larger droplets have greater charge. However, larger droplets also have greater surface tension forces holding them together than smaller drops. The increase in surface tension force with size is greater than the increase in coulomb repulsion forces caused by the increase in droplet charge.

Larger droplets can withstand greater voltage potential before breaking up. Droplets with a relative potential of 300 volts that are smaller than a millimeter in diameter will tend to break apart. Since the maximum anticipated charge potential on droplet surfaces in <800km polar orbit is less than 26 volts, breakup of droplets due to electrostatic self-interaction is not likely in any low altitude orbits. The minimum DC705 droplet diameter required to prevent breakup at 26 volts charge potential is less than one micron (.0055 mm). Figure 51 shows a curve representing the point where coulomb forces and surface tension forces are equal as a function of droplet size and voltage potential. Droplets with diameters smaller than those corresponding to the curve will break up. It is evident that large droplets can withstand potentials of more than 1000 volts without breakup.



**Figure 51. DC705 Droplet Breakup as a Function of Diameter and Voltage.**

In GEO, voltage potential during strong geomagnetic activity is likely to reach the point where droplet breakup will occur. Droplet breakup results in sub-droplets of different size with different drag properties. At low altitudes, these sub-droplets are decelerated differently producing a large area of impact at the collection site. At GEO altitudes drag is negligible and sub-droplets can be collected, provided electric fields between droplets do not repel each other off course. It is shown in the next section that some uniformly sized droplets streams with small gap distances have an impact radius of more than a meter due to droplet e-field interaction. Electric field interactions between sub-droplets will be even more pronounced than interactions between uniformly sized droplets. This is because of the relative mass difference between sub-droplets and because of their close proximity. Therefore, to avoid significant loss of fluid and possible spacecraft contamination, droplet streams in GEO must to be stopped prior to charge levels reaching the breakup point. This will probably require close monitoring of the charging environment with on-board sensors to stop droplet stream production if aspects of the local GEO plasma exceed certain thresholds. Since charging time in GEO can take several minutes, it may be possible to resume stream operations when spacecraft are closer. In this way, it may be possible to continue modified operations (and spacecraft cooling) and avoid collisions.

#### **D. Electric Field Forces Acting Between Droplets**

According to the Lorentz force equation an object with charge  $q$  exerts an electrostatic force on other charged objects that is equal to  $\vec{F} = q\vec{E}$ . Here  $\vec{E}$  is the electric field produced by the object and the magnitude of  $\vec{E}$  is equal to the electrostatic potential of the object. In spherical objects that are charged uniformly and are of like charge  $\vec{F}$  is repulsive and acts along the line connecting sphere centers. A spherical Gaussian surface is applicable to finding the electric field outside of the sphere by a point charge or a uniformly charged spherical shell or any other charge distribution with spherical symmetry.<sup>56</sup> Gauss' law, which is one of Maxwell's equations of electromagnetism, can be expressed as:

$$\oint_0^S \mathbf{E} \cdot d\mathbf{A} = \frac{q}{\epsilon_0} \quad (41)$$

where  $\mathbf{E}$  is the electric field strength, the vacuum permittivity constant  $\epsilon_0 = 8.854 \times 10^{-12} \text{ C}^2\text{N}^{-1}\text{m}^{-2}$ , and  $d\mathbf{A}$  is a differential surface area.  $S$  is a Gaussian surface, chosen so that it is concentric to and outside of the droplet surface enclosing the uniformly distributed charge  $q$ .

By the assumption of spherical symmetry, the integrand is a constant ( $4\pi r^2$ ) and can be taken out of the integral resulting in:

$$4\pi r^2 \hat{\mathbf{r}} \cdot \mathbf{E}(\mathbf{r}) = \frac{q}{\epsilon_0} \quad (42)$$

where  $\hat{\mathbf{r}}$  is a unit vector normal to the surface. Because the charge is symmetric within the sphere,  $\mathbf{E}$  also points in the radial direction, and is then equal to:

$$\vec{\mathbf{E}}(\mathbf{r}) = \frac{q}{4\pi\epsilon_0 r^2} \hat{\mathbf{r}} \quad (43)$$

Thus, Coulomb's law quantifies the electric field strength emanating from a charged droplet:

$$\mathbf{E}(\mathbf{r}) = \frac{q}{4\pi\epsilon_0 r^2} \quad (44)$$

The electrostatic potential (Coulomb potential) of an isolated sphere with charge  $q$  at a distance from the center,  $r$  is then:

$$\psi(r) = q/4\pi\epsilon_0 r \quad (45)$$

Results presented in Chapter 3 show that droplets in eclipse acquire a charge (usually negative) that is nearly uniform and therefore will produce electric field forces that repel each other. Sunlit droplets acquire positive charge on the sun facing side for a brief period before taking on a negative, or less positive, charge that remains less negative than the side opposite the sun. In most cases, uniformly charged droplets in eclipse represent the worst-case scenario for amplification of droplet angular dispersion because repulsion forces between droplets are strongest. Sunlit droplets are more positively charged on the sun-facing hemisphere and therefore have weaker repulsion forces than droplets that are uniformly charged, as they are in eclipse. The one exception to this rule, found in this study, is a sunlit droplet in GEO with nominal geomagnetic conditions.

Secondary electron production in GEO nominal geomagnetic conditions causes droplets to take on a positive charge, even in eclipse. Such a droplet can have a sunlit hemisphere with up to +20V potential and an anti-solar side charged to no more than +2V. Because strongly charged hemispheres must face the sun, it is not possible for any two +20V hemispheres to face (and therefore repel) each other. Thus, the worst-case repulsion in GEO nominal geomagnetic conditions results in a repulsion force comparable to that of two eclipsed droplets each uniformly charged to less than 7 volts. Since this force is less than that produced by droplets in several eclipsed environments the droplet repulsion between sunlit droplets was not analyzed in this study.

#### E. Droplet Drift Due to Electric Field Interactions

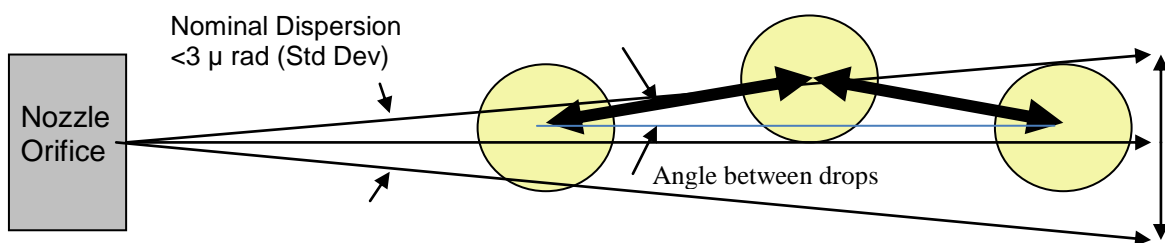
In the mid 1980s Muntz et al.**Error! Bookmark not defined.** and Dixon<sup>67</sup> showed silicon oil droplet streams can be generated and propagated in vacuum with excellent accuracy. They used a 30m drop tube in vacuum at the University of Southern California (USC) to record angular dispersion and velocity dispersion of droplet streams. Their research showed that DC704 droplet streams are produced with angular dispersions from centerline that follow a Gaussian distribution. Results of this testing are shown in Table 9 and indicate that an angular dispersion of less than 3 micro radians standard deviation is typical and that 1 micro radian is achievable for at least some droplet diameters and probably all.**Error! Bookmark not defined.**<sup>67</sup>

**Table 9. Direction and Speed Stability of DC704 Droplet Streams.**

<b>Droplet Diam (m)</b>	<b>Droplet Initial Velocity (m/s)</b>	<b>Std Deviation Velocity Variation (m/s)</b>	<b>Std Dev Angular Dispersion Angular Dispersion (rad)</b>
1.46x10 <sup>-8</sup>	24	0.00050	<1x10 <sup>-6</sup>
1.46x10 <sup>-8</sup>	49	0.00064	3x10 <sup>-6</sup>
1.46x10 <sup>-8</sup>	100	0.0011	2x10 <sup>-6</sup>

Even the largest angular dispersion standard deviation recorded (3 microradians) yields a seven-sigma estimate of less than one droplet exceeding a 21 microradian cone every 3 years. Thus, if only angular dispersion induced by nozzle manufacturing tolerances is considered, a collector only 3 cm in diameter could effectively guarantee no loss of droplets over a five-year mission with 1km separation between satellites.

USC researchers also measured speed dispersions from average stream velocity of DC704 in vacuum and concluded that speed dispersions of only  $10^{-5}$  times average velocity are typical but that  $10^{-7}$  is achievable through careful design of a droplet generator.<sup>71</sup> The work done in the 1980s on droplet angular and velocity dispersions provides a range of possible initial droplet displacements from which to analyze the effects of electric field interaction between droplets. Electric field forces of repulsion between droplets tend to dampen out stream velocity dispersions and amplify angular dispersions. Because droplets in a stream have trajectories with random angular dispersion, electric field forces between charged droplets will force them outside of the expected nominal cone of probability for uncharged droplets. Such an interaction is depicted in Figure 52 where a configuration of droplets is shown in which droplets interact with each other in such a way that the topmost droplet is forced outside of the nominal angular dispersion cone.

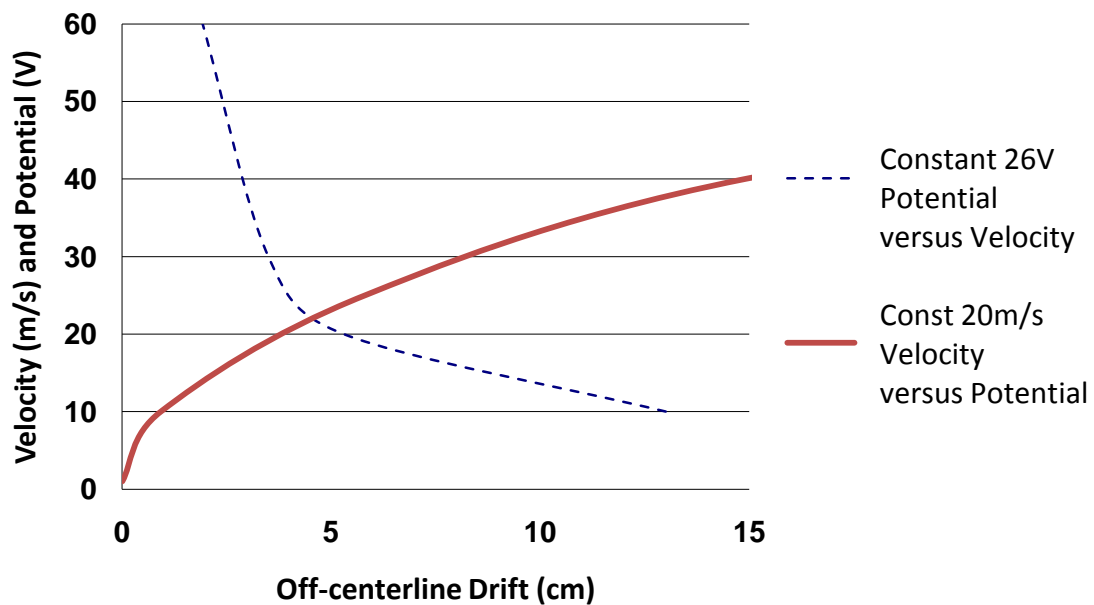


**Figure 52. Alignment of Charged Droplets Forcing Upper Droplet Out of Nominal Dispersion Cone.**

The amount of drift caused by two droplets that are fixed relative to a droplet offset as in Figure 52 with an angle between droplets of 1.5 micro radians was analyzed. In reality, a three-droplet scenario would result in significant lateral motion and significantly limit the amount of vertical drift. For this



preliminary analysis, it was assumed that any lateral displacement is arrested by forces from preceding and trailing droplets. Electric field strength ( $E$ ) was calculated using equation 44 and then the electrostatic force was determined by:  $\vec{F} = q \vec{E}$ . The force was applied to the displaced droplet and acceleration and position determined for a 0.1 second time interval. This process (Euler's method) was iterated over a 1km transit distance to determine the amount of off-centerline drift at the collection site. Drift results for 1mm diameter droplets spaced 1mm apart is depicted in Figure 53 as a function of both speed and charge potential. A higher speed results in less travel time and less time for Lorentz forces to act. Greater voltage potential relative to the plasma environment yields larger forces acting on neighboring droplets. The first curve shows drift as a function of drop velocity for a droplet potential of -26V that is the highest charge predicted in this study for the auroral regions. Above the elbow in the drift versus velocity curve, at approximately 25 m/s, the benefit of increasing transit speeds is less pronounced. Since pumping power is directly proportional to chamber pressure, which is directly proportional to droplet velocity, it is desirable to operate at stream-speeds above 25m/s for most tandem satellites in polar orbit. Increasing the diameter of droplets increases the electric field strength between droplets and increases the amount of expected drift. This is true even when spacing between droplets is increased commensurate with an increase in droplet diameter.

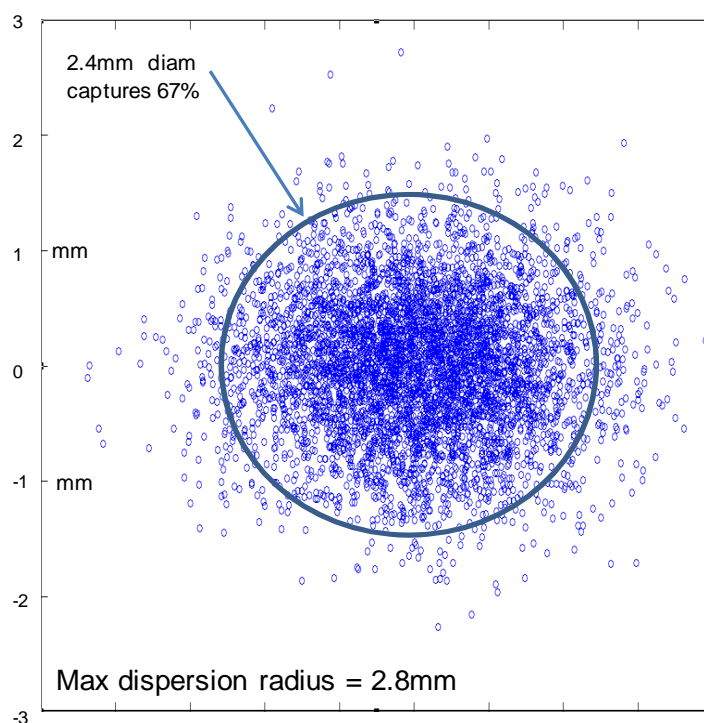


**Figure 53. Off-Centerline Drift of a 1mm Droplet during a 1km Transit as a Function of Velocity (for a 26V droplet) and as a Function of Potential (for a droplet transiting at 20m/s).**

#### **F. Computer Simulation of Electric Field Induced Droplet Dispersion**

The calculation of droplet drift associated with electric field interactions presented in the previous section was significant enough to warrant further quantification. Toward this end, a numerical model was developed to simulate the effect of electric field interactions between droplets transiting over a user specified distance. This code serves as a tool to analyze the impact of various droplet stream parameters such as charge, stream velocity, and droplet spacing on required collector size. The model takes droplet diameter, spacing, angular dispersion, velocity dispersion and charge potential as inputs and simulates droplet production and the three dimensional motion of droplets transiting a specified distance. The model then provides the impact location and distance from centerline and calculates a standard deviation of droplet dispersion from centerline. The code for the model can be found in Appendix 12.

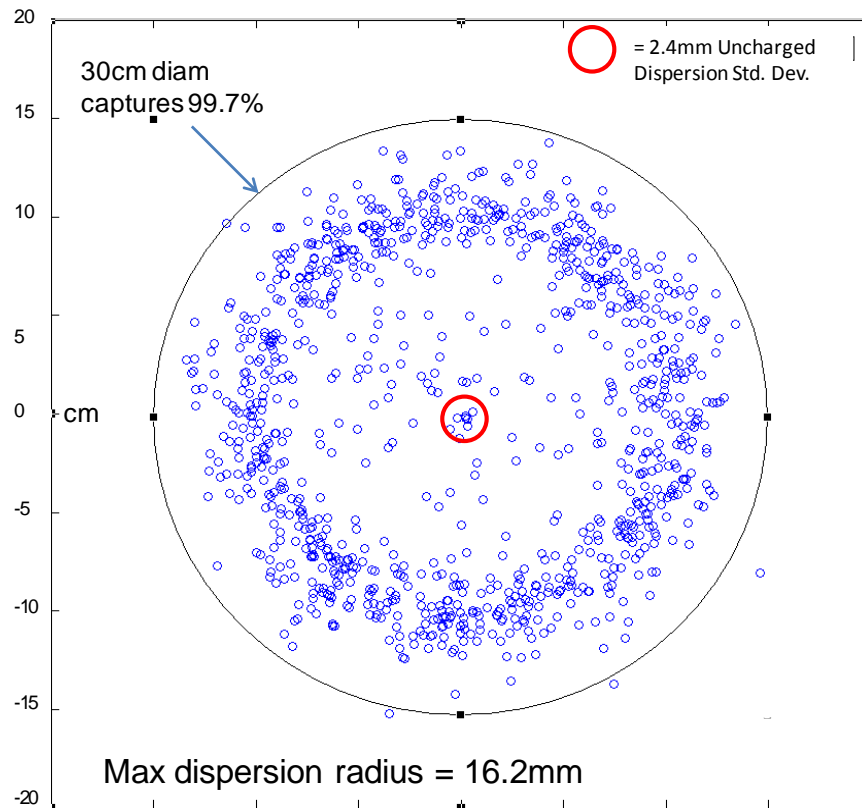
Without charging, the dispersion of droplet impact from centerline follows a normal distribution centered at the vector between satellites. This is shown in Figure 54 where 5000 uncharged droplets were simulated with an angular dispersion of  $2.4\mu\text{rad}$  (standard deviation).



**Figure 54. Dispersion Simulation Results for 5000 Uncharged Droplets after 50 second transit.**

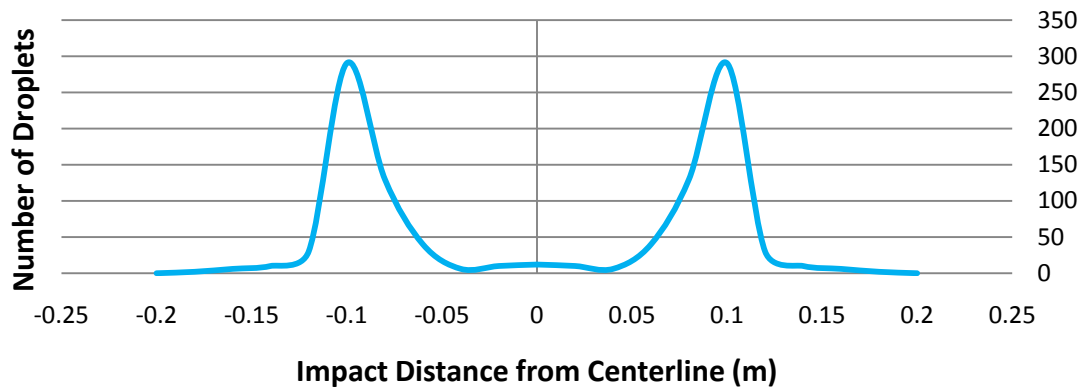
These uncharged droplets impacted no more than 3mm from the collector's center after 50 seconds of travel. This dispersion conforms to a normal distribution with the standard deviation of angular dispersion from stream centerline equal to values determined by USC researchers using DC704 droplet streams. Error! Bookmark not defined.

When droplets are uniformly charged their mutual repulsion results in significant dispersion from stream centerline that results in a ring shaped impact region at the droplet collector like the one depicted in Figure 55. The impact ring shown was created by simulating the transit of 1000, two-millimeter droplets each charged to 100V potential. The circle depicted in the figure has a radius that is three standard deviations from centerline, large enough to collect 99.7% of transiting droplets. By choosing an acceptable percentage of collected droplets, a corresponding standard deviation can be determined and the collector sized accordingly. For the example shown, a collector 60cm in diameter loses about 30 droplets in 5 years while a 70cm collector only loses one droplet in 5 years.



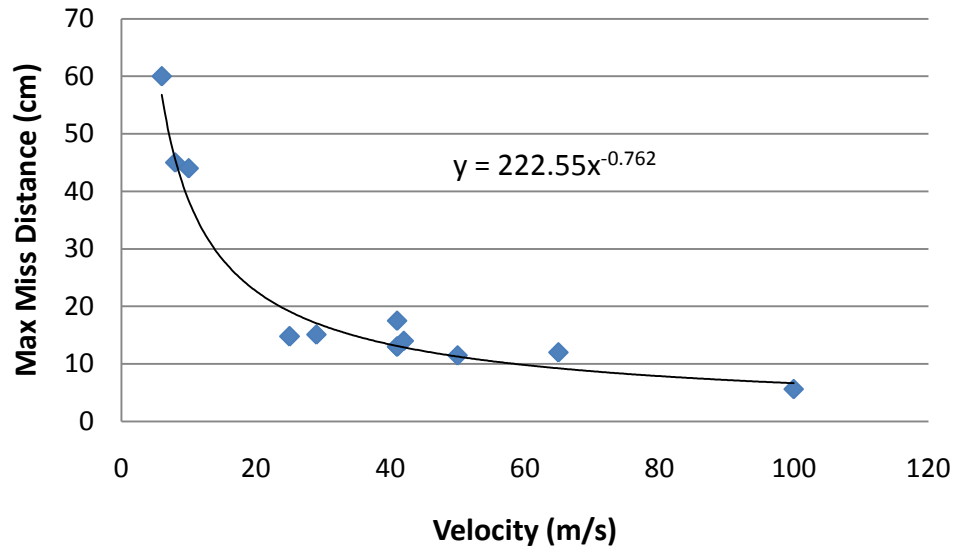
**Figure 55. Charged Droplet Impact Point for 2mm Droplets after 50 second Transit**

The histogram in Figure 56 shows absolute dispersion from a simulation mirrored in the negative half of the x-axis to show a histogram of the number of droplets impacting the collector as a function of distance from centerline.



**Figure 56. Histogram of Impact Distance from Centerline for a Droplet Stream Charged to 100V Potential.**

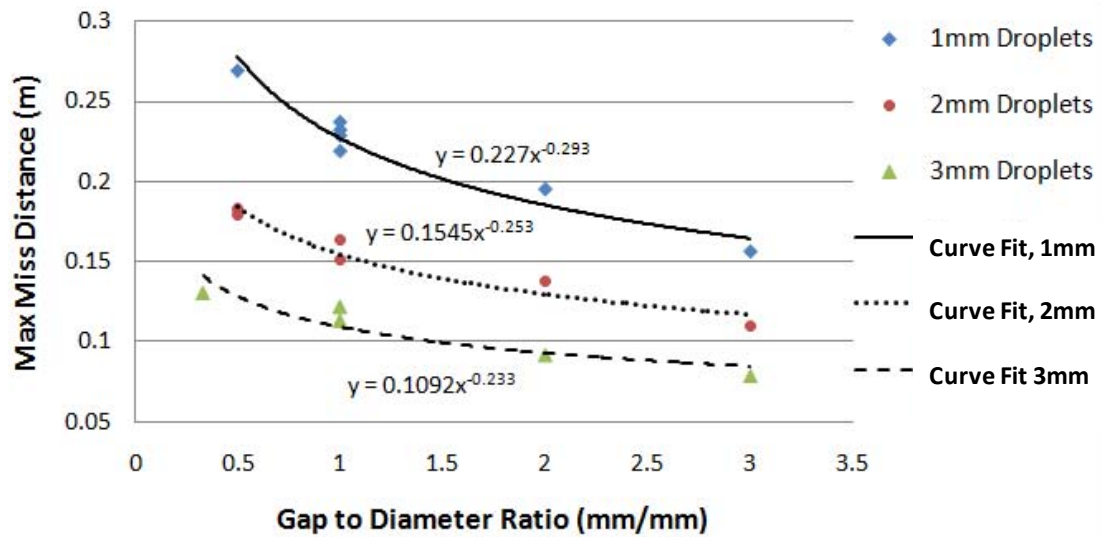
Stream parameters affecting dispersion include velocity, charge potential, droplet spacing, and droplet diameter. Increased velocity decreases dispersion by reducing the time droplets have to repel each other and then translate from centerline during transit.



**Figure 57. Maximum Miss Distance vs. Velocity for 100V Droplets. Diameter = 1 to 5mm, Spacing = 0.5 to 3 Diameters. Ratio of Diameter to Droplet Spacing =1 to 2.**

This is shown in Figure 57 where a power law curve fits the data best and shows a definite advantage to operating streams above 20m/s. Streams simulated had differing diameters and gap distances but all had a ratio of diameter to gap between 1.0 and 2.0.

Since the electrostatic force between droplets decreases with the square of the distance, it is expected that increasing the initial gap between droplets will substantially decrease the amount of drift from centerline experienced by transiting droplets. The effect of droplet spacing was analyzed by simulating three different droplet diameters produced with various gap to diameter ratios between 1/3 and 3. Each droplet simulated had a voltage potential of 100V, a stream speed of 29m/s, and a transit distance of 1km. Maximum miss distance of any droplet in each simulation is shown in Figure 58. At each droplet size the expected trend of decreasing miss distance with increasing gap distance is confirmed. Power law trend lines, applied to the data set for each droplet diameter indicate that the relationship between droplet miss distance and gap length becomes more linear as droplet diameter is increased.



**Figure 58. Results of Transit Simulations with Different Gap Distances between Droplets. Power Law Curve Fits to Simulation Data indicate an Inverse Relationship between Maximum Miss Distance and Droplet Diameter.**

A simulation of transiting droplets with voltage potentials near that predicted by NASCAP was performed to predict actual drift of droplets operating in an auroral environment. A 2mm diameter and 2mm gap distance stream transiting at 29m/s and charged to a 30V potential was simulated and maximum miss distances recorded. These miss distances were compared with those of an identical stream charged to 100V. The 100V stream had a maximum miss distance of 15.1cm while the 30V stream maximum miss distance was only 4.7cm. The same simulation of 30V droplets was performed with 1mm and 3mm droplets and yielded similar comparisons between 100V dispersion and 30V dispersions. These results indicate a nearly linear relationship between droplet potential and maximum drift, which supports the prediction of a linear relationship, at potentials above 25V, visible in the analytic results of Figure 53.

At potentials expected below 800km in auroral space, simulations of transiting charged droplets show that droplet drift is limited to less than about 5cm. The fact that the impact location of droplets conforms to a ring pattern complicates the collection of droplets since multiple droplet impacts at the same site may be required to overcome adherence to the collector surface and acceleration of the captured droplet to the collection site. Another simulation was performed in which gap distance between 2mm diameter, 30V droplets was increased to 8mm. The 4 to 1 gap to diameter ratio resulted in a decrease in impact ring

diameter from about 10cm down to about 6cm. Using solenoid valve droplet generator technology even longer gaps are possible, allowing effective mitigation of droplet dispersion due to inter-droplet interactions. Not accounted for, in these simulations, is plasma damping of electrostatic potential between droplets caused by sheath formation around each droplet.

### G. Plasma Damping of Electric Fields between Droplets

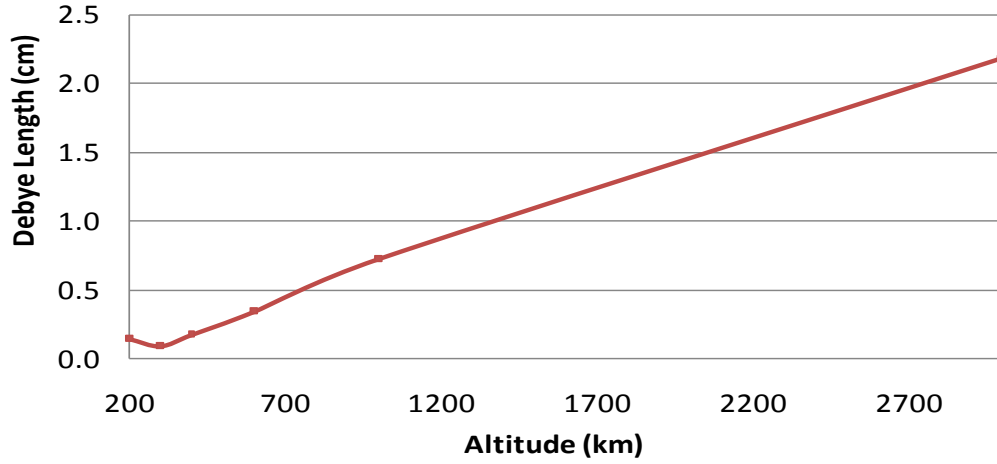
The electric field strength of a droplet in neutral space plasma is dampened, with distance, by a sheath surrounding the charged droplet. The sheath thickness can be estimated by finding the Debye length, which is about one-third the thickness of the sheath. For most materials, in space charging environments, electric fields strength is considered negligible several Debye lengths from the surface of a charged object. The Debye length is determined by the following relationship:

$$\lambda_D^2 = \frac{kT_e \epsilon_0}{n_0 q_e^2} \quad (46)$$

Where:  $\epsilon_0$  = the permittivity of free space  
 $q_e$  = the elemental charge  $1.6 \times 10^{-19}$  C  
 $k$  = Boltzmann Constant  $1.38 \times 10^{-23}$  J/K  
 $n_0$  = Plasma equilibrium density far from perturbations  
 $T_e$  = Plasma Temperature (about 1000K in LEO)

Debye length can be plotted as a function of plasma density that, in turn, is a known function of altitude. Using LEO plasma properties from Tribble,<sup>28</sup> Debye length versus altitude is plotted in Figure 59. Debye length is about 1mm at 300km and 2.2mm at 400km and therefore the sheath surrounding droplets is about 3-6mm thick below 400km. Between 200 and 300km plasma density increases and then drops off linearly above 300 km, this explains the dip in Debye length seen in the plot. Droplets at 400km will require at least 18mm spacing to shield droplets from neighboring electric fields interactions. At 1000km altitudes droplet spacing must be more than 30mm to avoid overlapping sheaths. Such spacing increases the

size and speed required of droplets considerably. Therefore, it is necessary to analyze the strength of electrostatic fields between droplets acting inside of overlapping sheaths.



**Figure 59. Debye Length as a Function of Altitude.**

The effect of the sheath is to shield the electrostatic field of the droplet, reducing the range over which it acts. The strength of a charged object's electric field can be related to its Debye length by the following relationship which arises from the kinetic properties of plasma and is known as the Debye screening potential:<sup>33</sup>

$$\psi = q / 4\pi\epsilon_0 r e^{-r/\lambda_D} \quad (47)$$

At distances less than a tenth of a Debye length from the droplet surface the  $(e)^{-r/\lambda_D}$  term is greater than 0.9 and electric field strength is approximated by the equation for electrostatic potential which can be simplified using Coulomb's constant,  $k_e$ , which is  $8.99e9 \text{ Nm}^2/\text{C}^2$ :

$$\psi = q / 4\pi\epsilon_0 r = k_e \frac{q}{r} \quad (48)$$

Thus, it is shown that the repulsive force between two uniformly charged spherical droplets that are less than  $1/5^{\text{th}}$  of a Debye length apart is given by Coulomb's equation:

$$F = k_e \frac{q^2}{r^2} \quad (49)$$



Since plasma shielding reduces the electric field strength and resulting force of repulsion, Coulombs equation yields the strongest force of repulsion possible between charged droplets. Droplet drift forces calculated with this equation result in a conservative estimate of droplet dispersion since plasma damping will decrease the amount of dispersion. NASCAP results, presented in Chapter 3, show that the amount of plasma damping between droplets is much less than the amount of plasma damping in other directions. Thus, dispersion results presented in the preceding sections of this chapter are accurate when gap distance is less than 0.2 Debye lengths. Results are somewhat conservative when gap distance is between 0.2 and 2 Debye lengths. With gap distances greater than two Debye lengths, plasma damping is expected to dampen droplet dispersion significantly and results should be considered very conservative.

Conservative estimates of droplet dispersion in streams with gap distances several droplet diameters long show that 99.7% of droplets will fall within a 4cm diameter dispersion ring. A 3-diameter gap distance is near the limit of traditional piezoelectric droplet generators. Gap distances of any length can be produced by micro-solenoid valve droplet generators, allowing electric field interactions to be virtually eliminated. Because micro-solenoid valve droplet generators allow electric field interactions to be virtually eliminated, plasma damping was not incorporated into the modeling of droplet dispersion performed for this study. If traditional droplet generators are used instead of solenoid valve types, then additional reduction in droplet dispersion that results from plasma damping of electric fields may be useful for more accurate estimates of impact area.

## Chapter 5: Droplet Charging Experimentation

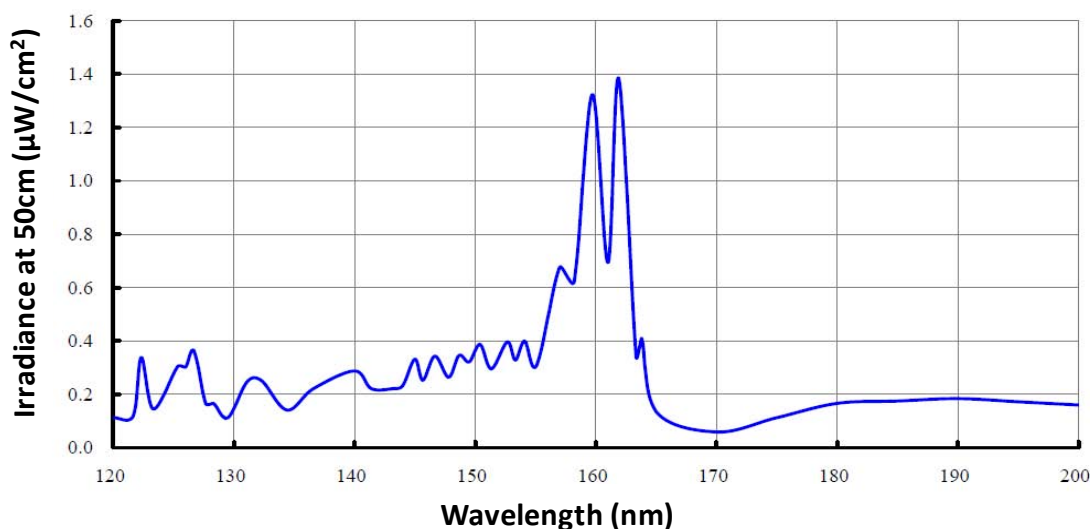
Two experiments were conducted in the study to quantify charging of silicone oil droplets that results from secondary electron production caused by photoemissions. Both experiments were carried out in a laboratory vacuum chamber and photoemission of electrons was accomplished by irradiation with an extreme ultraviolet (EUV) lamp. Droplet charge was measured and compared with levels predicted by NASCAP photoemission modeling of droplets. The main purpose was to validate photoemission charge modeling by NASCAP and to refine estimates of DC705 photoelectron yield. This property is used by NASCAP to predict current flow from a droplet due to electrons liberated by high-energy photons. A secondary goal of experimentation in this study was to devise a method of detecting stream impact location on a collector surface.

### A. Experimental Method and Setup

Two types of experiments were conducted in this study. In the first experiment, a fluid sample was irradiated with EUV light to determine if charging could be detected by a fluid filled capacitor. The second experiment irradiated individual droplets in free-fall and then measured their charge potential by deflecting them with an electrostatic field. A 30W EUV lamp made by Hamamatsu Corporation was used to irradiate droplets. This lamp emits photons primarily in the wavelength range of 120-200nm using a 0.5mm diameter Deuterium plasma source. Both experiments were conducted in vacuum to simulate the low-pressure space environment. The lamp radiates in a portion of the UV spectrum that is part of several named UV bands including UVC at 100 – 280nm (4.43-12.4 eV), Far UV at 115-200nm (6.20–10.8 eV), and Extreme UV between 30 and 115 nm (10.8–124 eV).<sup>57</sup> These ranges vary somewhat in the literature and lamp manufacturer's chosen term, EUV, is used in this dissertation.

The spectral radiance of the Hamamatsu L10266 Deuterium lamp used in this study is shown in Figure 60. Lamp irradiance can be compared to nominal solar irradiance and photoelectron yield, both displayed in Figure 27 in Chapter 3. Comparing the output of the lamp to the output of the sun, it is evident

that energy is distributed much differently along the electromagnetic spectrum. A large amount of the sun's radiation is concentrated at the Lyman-alpha radiation line, a spectral line of hydrogen located at 121.6nm. In contrast, no dominant peak lamp output exists in the range of wavelengths where significant silicon oil charging occurs. Instead there are two small peaks visible, one at 123nm where photoelectron yield is 0.054, and one at 127nm where yield is 0.040. The next peak of lamp spectral radiance is at 132nm where yield is only 0.023. Photoelectron yield at wavelengths above 140nm is less than 0.01.



**Figure 60. Spectral Radiance of 30W Deuterium Lamp Used to Simulate Solar EUV (From Hamamatsu, 2007).**

Koizumi et al.<sup>46</sup> showed that, even at peak yield wavelengths, only 7.3% of the photons impacting DC704 and 705 molecules actually liberate a photoelectron. They also found that photon energies above 10.4eV (below 122 nm) do not result in an increase in photoemission of electrons by DC704 and DC705. This is evident in Figure 27 where the dashed quantum yield line levels off at wavelengths below 112nm. Others<sup>32</sup> have shown that photoelectron yield follows a Gaussian distribution in all other materials tested to date. Thus, further increase in photon energy beyond 10.4eV is expected to result in a decrease in yield that roughly mirrors the decreasing curve at energies below 10.4eV.

The Inverse Square Law is used to calculate the decrease in radiation intensity as a function of distance from the radiation source:<sup>58</sup>

$$I = E(4\pi R^2)/(4\pi r^2) = E (R^2/r^2) \quad (50)$$

Where:  $I$  = irradiance at the surface of the outer sphere

$E$  = irradiance at the surface of the object

$4\pi R^2$  = surface area of the radiating object

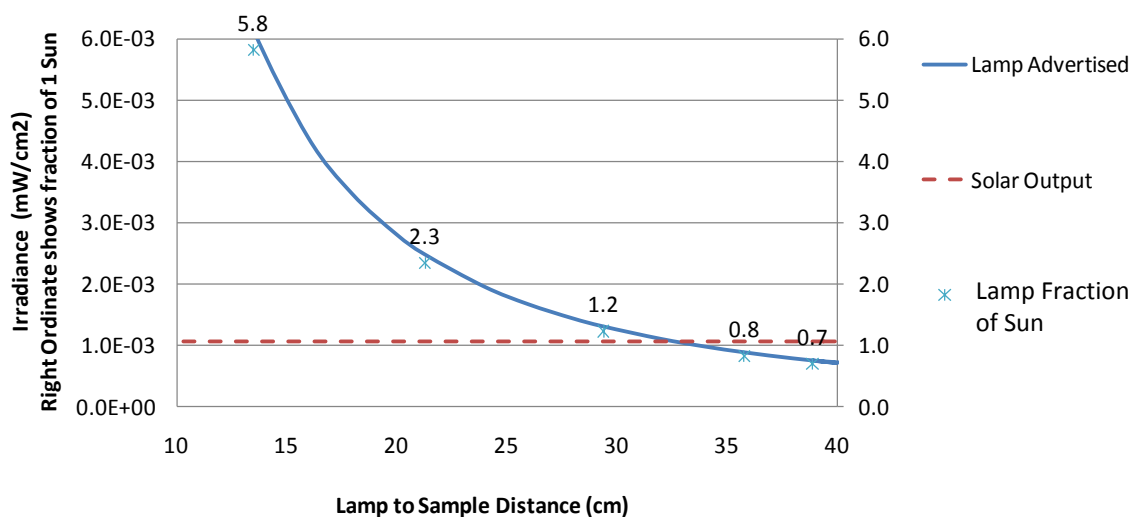
$4\pi r^2$  = surface area of the radiating sphere at the object of interest

The radius of the Sun ( $R$ ) is  $6.96 \times 10^5$  km while the average sun-Earth distance ( $r$ ) is  $1.5 \times 10^8$  km.  $E$  for the sun was determined using the Stefan Boltzmann equation (using Plank's Black Body assumptions for a mean surface temperature of 5800k) as  $7.35 \times 10^7$  W/m<sup>2</sup>. These values yield a total intensity of 1366 W/m<sup>2</sup>, which compares well with values reported by other sources for solar flux at the Earth's orbit.<sup>79</sup> Equation 50 was used to predict lamp irradiance as a function of distance for the various lamp positions tested.

The lamp is expected to lose 50% of its output in the first 1000 hours of use.<sup>59</sup> In this study, the lamp was turned off between tests and was run for less than 8 hours total time of use. No information on the nature of this drop in output was available but if it is assumed that the drop-off is linear, 8 hours results in less than a third of a percent loss of output. Irradiance levels were measured by a photodiode throughout testing (to a resolution of 0.01mW/cm<sup>2</sup>) and did not show any drop in lamp output over time. Photodiode monitoring of lamp output consistently measured irradiance to be at least 50% above advertised lamp output corrected for distance. Consequently, it was necessary to rely on company specifications of lamp irradiance. A complete discussion of why measured irradiance exceeded expected lamp output, along with photodiode results, is presented in Appendix 11. While photodiode monitoring did not provide an absolute measure of lamp irradiance, it was useful for determining lamp irradiance relative to other lamp positions.

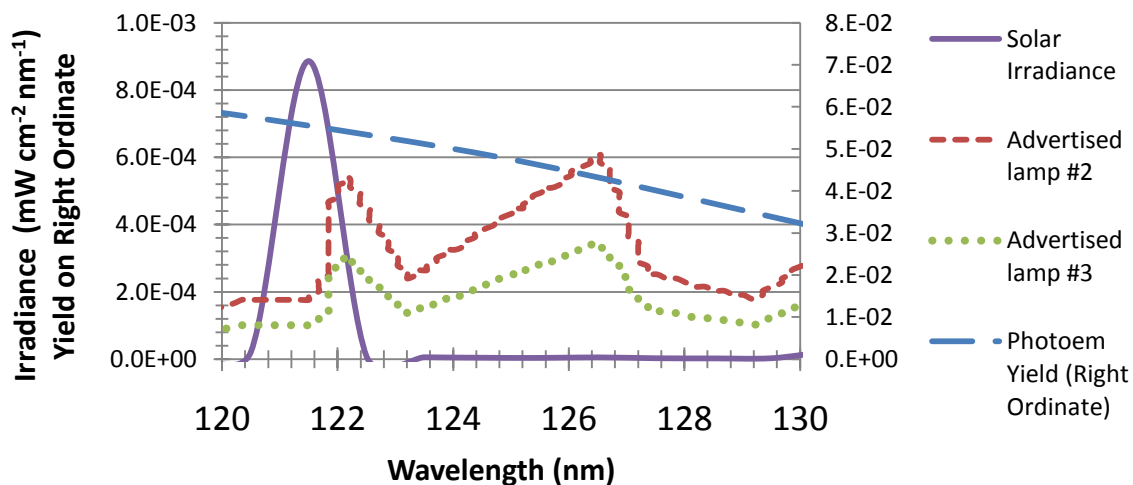
The dashed curve in Figure 61 shows peak solar intensity in the 121-123nm range plotted against the left ordinate. The solid curve shows advertised lamp irradiance in the 121-123 nm range as a function of distance from the lamp. Data markers with data labels show the fraction (or multiple) of solar irradiance at each of the five lamp positions tested. The EUV lamp produces nominal solar equivalent irradiance in the 121-123nm range when it is positioned 34.5 cm from the silicon oil sample. In this study, the greatest lamp-to-sample distance tested was 38.9cm or the equivalent of 0.7 times the sun's irradiance. The closest lamp position was 13.5cm and produced irradiance in the 121-123nm wavelength range 5.8 times greater than the sun. The closest (13.5cm) and second most distant (35.8cm) lamp positions were used in the charged

capacitor experiment while the other three positions; 21.3cm, 29.4cm, and 38.9cm were used in the droplet charging experiment.



**Figure 61. Comparison of Solar Irradiance at 121-123 nm to Lamp Irradiance**

Comparing lamp and actual solar EUV output between 121nm and 123nm does not capture a second spike in lamp output at 127nm that contributes significantly to silicon oil charging. Figure 62 shows nominal solar irradiance and advertised lamp irradiance in the range of 120-130nm for the third (29.5cm) and fifth (35.5cm) lamp positions corrected for distance.



**Figure 62. Solar and Lamp Irradiance with Photoemission Yield on Right Ordinate**

Irradiance at the other lamp position is omitted for chart clarity but parallels the curves associated with the lamp positions shown. Lamp data was extracted from Figure 60 using data extraction software and has an estimated error of <5%. Photoelectron yield reported by Issikawa and Gotto<sup>12</sup> is shown as a function of wavelength and plotted against the right ordinate.

A comparison of lamp-induced photoelectron current to sun induced photoelectron current was made by multiplying the irradiance curves for the sun and all three lamp positions by the yield at each corresponding wavelength and summing over the 120-160nm interval. The resulting sun and lamp photoelectron current levels are shown in Figure 63. The total current generated by the lamp over the 40nm range analyzed was then compared to the total current generated by the sun over the same interval. Using this more accurate method of comparison, the five lamp positions used in this study; 13.5, 21.3, 29.4 and 38.9 centimeters correspond to 4.85, **1.96**, **1.02**, 0.68 and **0.60** times solar intensity. The numbers in bold correspond to the solar equivalent intensity of the three lamp positions used in the droplet charging experiment while the other two intensities correspond to solar equivalent intensities used in the liquid capacitor experiment described next.

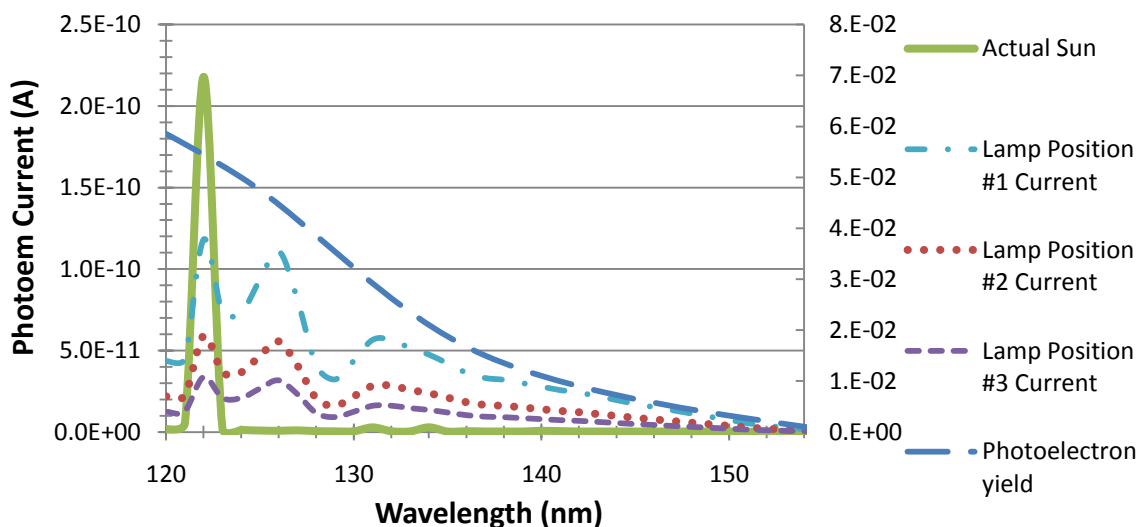
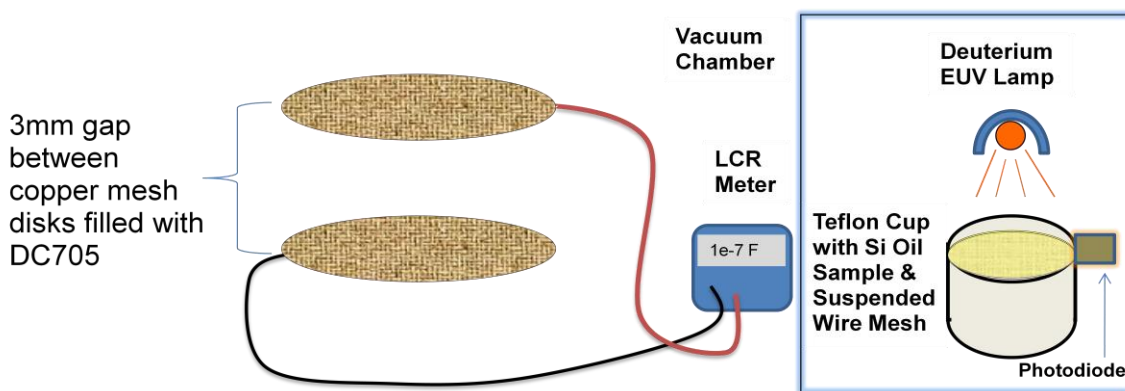


Figure 63. Photoelectron Currents for Lamp and Sun.

## B. DC705 Capacitor Charging Experiment Setup

In the first experiment, two parallel wire mesh disks were stacked within a 10mm deep Teflon dish as seen in Figure 64. Four 3mm cube shaped Teflon non-conducting spacers were used to separate the disks. The disks were submerged in silicone oil with the top disk residing just beneath the surface of the oil. Surface molecules of DC705 were charged positively by the UV lamp and, in the process, the plate nearest to the surface was charged negatively by the emitted electrons from the DC705. This setup is similar to that of a capacitor in which charged plates are separated by a dielectric material.



**Figure 64. DC705 Fluid Filled Capacitor Experiment Setup in which Change in Capacitance is Measured following Irradiation of DC705 with an EUV Lamp.**

The capacitance of a capacitor is determined by the charge on the plates divided by the voltage potential applied to the plates:

$$C = \frac{Q}{V} \quad (51)$$

For this experiment, a thermocouple was placed in series with the copper wire mesh disks to provide a small enough voltage to allow measurement of capacitance. The thermocouple was exposed to a constant temperature source, which resulted in a voltage output of 1.2e-6 V +/- 3e-8 V. This voltage was measured by a pico-ammeter with a sensitivity of 1e-11 V whose accuracy was verified with a NIST calibrated pico-ammeter. Capacitance of the copper and steel mesh capacitors was measured using an inductance,

capacitance, and resistance (LCR) meter designed to measure capacitance with a sensitivity of 1 pico Farad (1e-12 C/V).<sup>vi</sup>

The energy stored in a capacitor is equal to the work done to hold a charge,  $+q$  on one plate and  $-q$  on the other. Moving a small element of charge  $dq$  from one plate to the other against the potential difference  $V = q/C$  requires the work  $dW$  as shown in the following equation:<sup>60</sup>

$$dW = \frac{q}{c} dq \quad (52)$$

Integrating this equation over the interval of zero to the final plate charge ( $Q$ ) yields the work stored in a capacitor as in the following relationship:

$$W_{charging} = \int_0^Q \frac{q}{c} dq \quad (53)$$

The work required to produce the capacitance measured in the charged DC705 capacitor experiment was calculated and was found to be at least three orders of magnitude less than the lamp irradiance energy that reached the surface of the fluid. This matches the expectation that only a fraction of high-energy photons (less than 7%) that reach the surface will ionize DC705.

**Table 10. DC705 Capacitor Results.**

<b>DC705, Teflon Dish and Copper Mesh Experiment</b>	
Lamp Distance (cm):	<b>13.5cm</b>
Capacitance	12.78
Change (picoF):	12.90
	12.84
	12.98
Average (pF):	<b>12.88</b>
Standard Deviation:	0.09

---

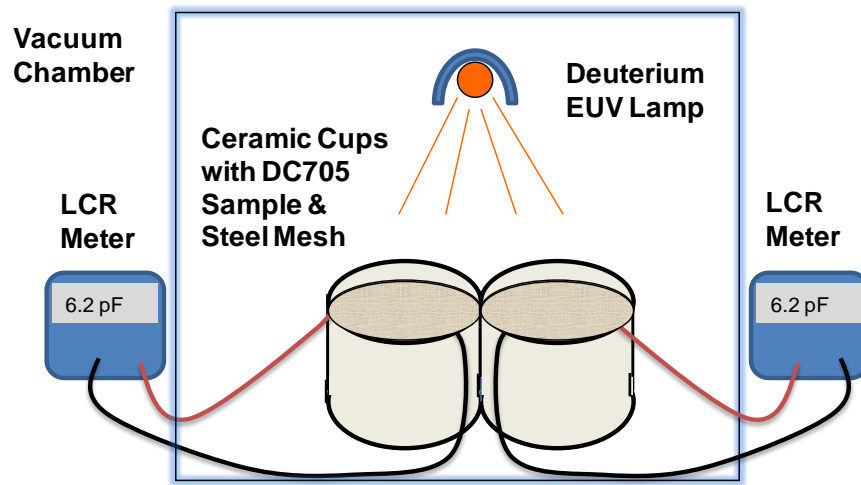
<sup>vi</sup> Agilent Inc. Company Product Description Website. Online:

<http://www.home.agilent.com/agilent/home.jsp?cc=US&lc=eng>. Accessed 14 Sep 2009.



In the silicone oil capacitor experiment the wire mesh disks were initially charged by the thermocouple yielding a capacitance of  $101.1 \pm 0.03 \text{ pF}$ . The UV lamp, positioned 13.5cm above the sample, was then used to illuminate the surface of the silicone oil which filled the holes in the top wire mesh but did not submerge the wire. Electrons emitted by silicone oil exposed to the UV lamp then charged the top plate of the capacitor changing the capacitance. The experiment was repeated four times and capacitance changed by the amounts shown in Table 10. Standard deviation of capacitance change was less than 1% of the average capacitance change, which demonstrates that a fluid filled capacitor can detect the presence of charged silicon oil with good consistency.

Another configuration of the DC705 capacitor experiment was conducted to compare variation of three parameters and to validate the results of the previous experiment. In the new configuration, smaller side-by-side ceramic cups with 4.2 cm inner diameters were centered 13.5cm beneath the UV light source as shown in shown in Figure 65.



**Figure 65. Second DC705 Capacitor Experiment Setup**

Two sets of 4.1cm diameter steel mesh disks with 1mm cube spacers were positioned in the bottom of the ceramic cups. Steel was selected over copper in this experiment because of its stiffness, which made it easier to form into identical mesh disks parallel to one another. Ceramic was selected over Teflon because it has a weaker dielectric strength and is therefore less likely to contaminate the experiment through photoemission of electrons.

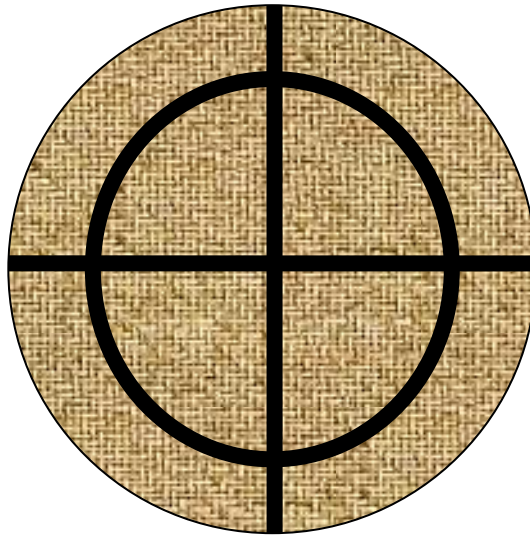
The first side-by-side configuration experiment consisted of two identical steel mesh capacitors in identical cups. One cup contained DC705 and one did not. No significant change in capacitance was observed in the capacitor without fluid confirming that DC705 is the source of charging and not some other component of the apparatus. The second side-by-side capacitor test configuration had two identical capacitors containing DC705 but with a covering on the inner diameter of one cup to shield the DC705 from EUV. This test eliminated the possibility that the ceramic rim of the cup, and not DC705, was the charging source for the wire mesh.

Following testing of side-by-side capacitors a single capacitor was tested several times at two different lamp distances. Table 11 lists the resulting change in capacitance from each exposure of DC705 to UV light at both lamp positions. Also listed is the ratio of values corresponding to the near lamp position divided by values associated with the more distant lamp position. The ratio of average capacitance change that results from exposure to the 13.5cm lamp position (near) versus the 35.8cm lamp position is 6.6. If the standard deviation of capacitance change in the far (35.8 cm) data set is subtracted from the average of the far capacitance change and the standard deviation of the near data is added to the average for near capacitance change, the resulting ratio of near to far is 7.04. This ratio of near to far capacitance is close to the ratio of the of near to far lamp distances squared, which is 7.03. Since capacitance is directly proportional to charge, this observation indicates that the relationship between EUV irradiance and the amount of charging of silicon oil by the lamp is nearly proportional to the square of the lamp distance. This result matches expectations since the number flux of impacting photons decreases with the square of the distance from the EUV source.

**Table 11. Capacitance Change in Second DC705 Capacitor Experiment.**

DC705, Teflon Dish and Copper Mesh Experiment			
Lamp Distance (cm):	<b>35.8cm</b>	<b>13.5cm</b>	<b>Ratio (near/far)</b>
Capacitance	0.91	6.39	6.9
Change (picoF)	1.02	6.45	6.3
	1.04	6.42	6.2
	0.95	6.49	6.8
Average (pF):	<b>0.98</b>	<b>6.44</b>	<b>6.6</b>
Standard Deviation:	0.06	0.04	

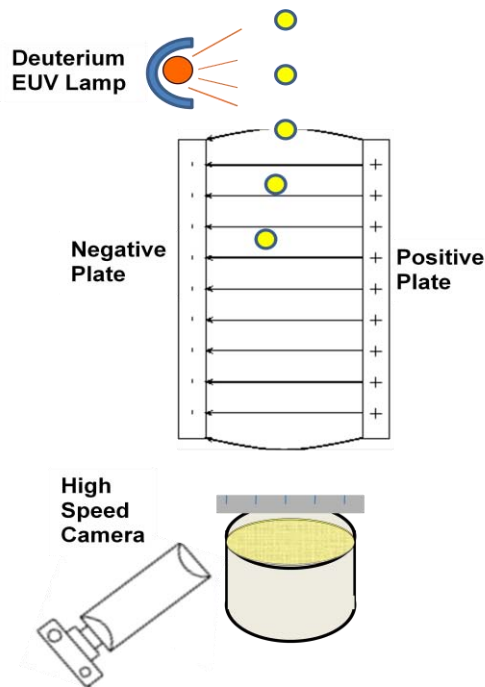
The ability to detect a change in capacitance caused by transfer of charge to a wire mesh has practical applications to an operational droplet stream system. An array of DC705 capacitors located on the surface of a droplet stream collector could allow detection of droplet impact location. Such sensors could provide feedback necessary to control pointing of droplet streams. Aiming of droplet streams can be accomplished by altering the attitude (yaw and roll) of the entire satellite or by pointing the nozzle of the droplet generator independently of the spacecraft. A possible array configuration is depicted in Figure 66. In this design the charge, current flow, or capacitance of each mesh segment is monitored independently of other segments. When charged droplets impact the mesh some of the oil passes through the mesh and lands on the collector surface while some adheres to the mesh. If a spinning collector is employed, the mesh sensor can be attached to the spinning collector forcing oil outward radially to the annular walls of the collector for collection. In a spinning sensor array, inner sensors would need to be offset from outer ones to avoid fluid flow from the inner segments to the outer ones.



**Figure 66. Droplet Impact Location Sensor composed of Separate Wire Mesh Capacitors, each Capable of Detecting Impacting Charged Droplets.**

### C. Droplet Charging and Deflection Experiment Setup and Method

A second silicon oil charging experiment was conducted in which falling droplets of DC704 were charged by UV light and then passed between two charged steel plates. Figure 67 shows a schematic of the setup of the experiment. The electric field between charged plates altered the path of the droplets, which was measured by high-speed camera imagery and then compared to uncharged droplet trajectories. In addition, trajectory information for droplets with and without UV exposure and with and without charged plates was recorded to rule out electrostatic displacement charging of droplets as a possible cause of droplet displacement. DC704 was used instead of DC705 because the charging properties are nearly identical<sup>12</sup> and the cost of DC704 is significantly less. DC704 also has a lower viscosity allowing droplet stream formation at lower pressure than with DC705.



**Figure 67. Charged Droplet Experiment in which Droplets are Charged with EUV then Deflected by Charged Plates. Displacement is Measured using High Speed Imagery.**

Droplet generation was accomplished by means of two leak-tight micro solenoid valves made by the Lee Corporation. Both valves were fitted with circular Sapphire orifices to promote uniformity of size

and velocity among droplets in the stream. Technical drawings for these valves are in Appendix 10, along with information on the driver circuit used to run the valve. Two Voltage sources and a function generator were used in concert with a spike and hold circuit to run the valve over a range of 1 to 900 Hz. The output of the circuit was monitored with an oscilloscope. A thermocouple was mounted to the valve to ensure the maximum allowed valve temperature of 160 C was not exceeded. The droplet stream was aligned with a ruler positioned across the fluid collecting cup to provide low-resolution measurement of lateral position. The ruler was mounted directly beneath the droplet generator with a 30-degree tilt from vertical. The off-vertical alignment of the ruler allowed measurement of fore and aft droplet displacement based on the position of impact of droplets on the ruler. From the perspective of the camera, the top of the ruler was further away than the base of the ruler so if a droplet landed 1mm lower on the ruler than the preceding droplet then it was displaced 0.58mm closer to the camera than the preceding droplet.

The charged plates were made of rigid 1.92mm thick polished steel. Plate dimensions were 88.57 mm by 26.21 mm. The plates were held in position by a precision machined, Teflon support structure and Nylon bolts. The Teflon support did not cover any part of the surface between plates where droplet passage occurs, and covered less than 5 mm of the outer edges of the plates at the entrance end. To minimize fringing fields, no holes were drilled into the plates. The gap between plates was maintained by the Teflon structure at the entrance and by Nylon spacers and bolts at the exit end of the plates. These were positioned to provide a 13.72 mm ( $\pm 0.005$ mm) gap measured at three positions along the length of the plates on both sides. The vertical orientation of the plates was determined to within less than a degree of vertical. Two adjustment screws were used to position the Teflon structure and hold the plates in the vertical position during and between tests. This vertical position was checked whenever modifications were made to the setup near the plate structure. A plumb bob was also suspended from the valve nozzle to ensure droplets entered the plates in the center of the opening of the droplet-charging path. This was done to prevent droplet impact with the negative plate. Prior to sealing the vacuum chamber, droplets were generated to verify that uncharged droplets were not impacting the plates. Once aligned, the plates were not disturbed until testing of all lamp positions was complete. This ensured a consistent droplet entrance location inside the gap between plates.

The EUV lamp was mounted to an ISO100 cross vacuum flange and positioned at one of three distances from the falling droplets using extension flanges. The plate assembly was mounted to the same ISO100 cross to ensure a perpendicular orientation of the plates with respect to the EUV lamp. In order to ensure droplets were exposed to EUV photons for the same amount of time, it was necessary to block some of the light using a toroidal aluminum shield positioned between the lamp and the droplet-charging path. This shield was repositioned with each lamp move to provide the same droplet charging path length ( $49.20\text{mm} \pm 0.13\text{mm}$ ) regardless of lamp distance from the droplets.

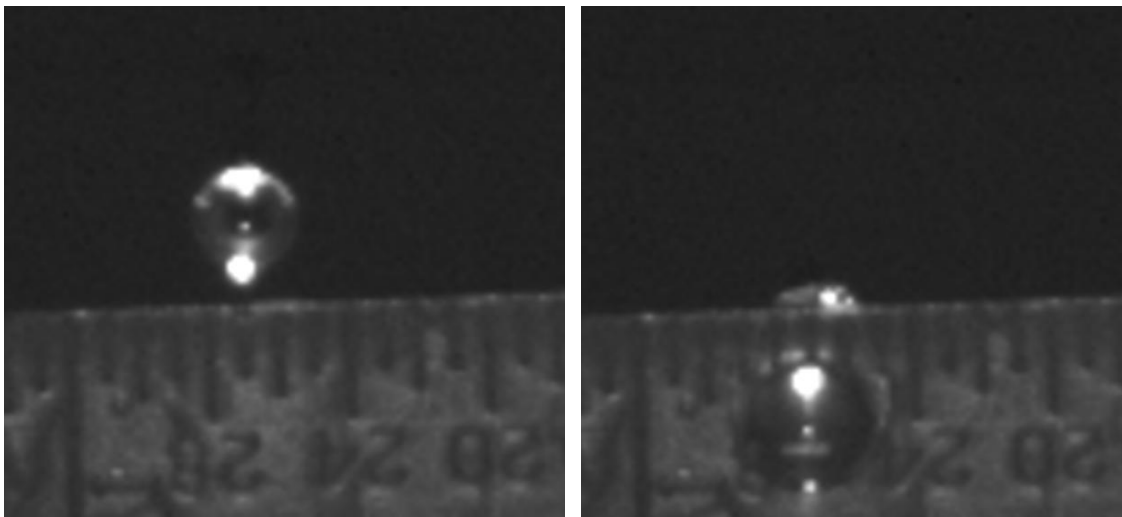
The shield was positioned using calipers with an estimated accuracy in lateral position of better than  $\pm 1\text{mm}$ . The change in charge path length corresponding to a 1mm error in shield position is 0.13mm for the closest (worst-case) lamp position, which was 21.30 cm away from the charge path. A 0.13mm change in charge path length is only a difference of 0.26% from the intended path length, which corresponds to less than 0.002 seconds out of a total exposure time of 0.070 seconds or less than a 2.8% uncertainty in exposure time. Use of the shield also prevented charging of the plate support structure (made of Teflon) and charging of the droplet generator nozzle by preventing EUV from reaching these components.

A photodiode was positioned next to the charging path to measure output of the lamp. The photodiode was held by a Teflon structure that was positioned inside an ISO-100 flange and extended the photodiode to within a centimeter of the actual droplet charge path. The photodiode support structure was shielded with aluminum foil to prevent charging that could have altered photodiode current output. This photodiode was located  $10\text{mm} \pm 0.5\text{mm}$  farther away from the lamp than droplet fall path in the middle of the spotlight. The photodiode was also positioned at two other positions below the spotlight center to verify that UV light was restricted to the charging path. When positioned so that the top of the photodiode was just below the intended edge of the EUV spotlight, photodiode current output decreased by 95% ( $\pm 5\%$ ). When the photodiode was positioned 10mm lower, the output was 97% ( $\pm 4\%$ ) less than the output measured at the center of the spotlight. Since photodiode output current is directly proportional to detected irradiance, this test confirmed that the shield was at least 90% effective at limiting the EUV spotlight to the intended droplet-charging path.

#### D. Droplet Charging Experimental Results

The first test series consisted of 84 droplet measurements, 24 at each of 3 lamp positions. These three lamp positions were 21.3, 29.4, and 38.9 centimeters, and are referred to in this section as lamp positions #1, #2, and #3 respectively. Four different levels of plate potential difference were tested at each lamp position; 0V, 1000V, 2000V and 3000V and 7-9 droplets were tested at each plate charge. The second and third testing series were identical to the first except that only two lamp positions were analyzed and the polarity of the plates was reversed. The polarity was reversed to help rule out electrostatic charge induction of droplets as a source of surface charge that would cause or contribute to displacement. The middle lamp position was not utilized in the last two series of tests, reducing the number of droplets analyzed to 60 in each series. In total, more than 200 droplets were measured using high-speed camera software to determine each droplet's diameter, displacement from a true vertical path, and velocity.

Plates were aligned perpendicular to the ruler and the viewing plane of the high-speed camera. Displacement of charged droplets resulted in lateral motion discernable in high-speed camera images. The Phantom 5 Camera recorded images at 1200 frames per second and has a post-processing tool that allows measurement of object position relative to a selected corner of the scene plane.



**Figure 68. Droplet Before and After Impact with a Ruler Tilted Away from Field of View.**

Scale was established by measuring a known distance in the scene (using the ruler) and then recording the diameter and position of successive droplets relative to that distance. For consistency, the lateral position was measured at the same two vertical locations along the fall path each time and the measurement point was always the left most point of the droplet. Similarly, droplet diameter was always measured horizontally. Velocity was measured just above ruler impact for approximately 10% of the droplets in each series. Velocity measured was 3.42m/s (+/-0.05m/s) for all three droplet sizes tested, which correlates to an initial nozzle velocity of less than 0.11m/s (+/-0.05m/s) when acceleration due to gravity is factored out.

Droplet diameter statistics for all 208 droplets measured are listed in Table 12. The range of diameters measured in each series was consistently less than 12% of the mean diameter and the standard deviation was consistently less than 2.6% of the mean droplet diameter. Diameter measurements were made at the same two points along the fall path and the average of the two measurements was used. The standard deviation from measured diameter was less than 2.6% of the average droplet diameter. This deviation compares well with conventional Rayleigh-type droplet generators using DC704 studied for the LDR program that had standard deviations from average diameter between 2% and 4% of average diameter.<sup>61</sup>

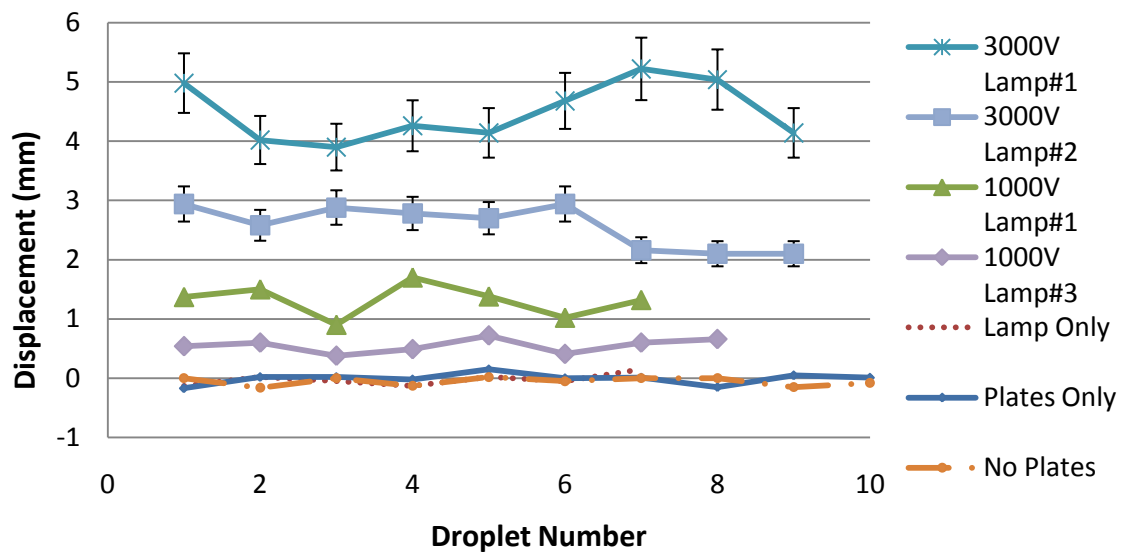
**Table 12. Droplet Diameter Statistical Results**

<b><u>Droplet Diameter Stats</u></b>	<b><u>Series 1</u></b>	<b><u>Series 2</u></b>	<b><u>Series 3</u></b>	
Mean	2.42	3.54	1.21	mm
Median	2.45	3.53	1.21	mm
Standard Deviation	0.062	0.087	0.030	mm
Std Dev % of Mean	2.58%	2.45%	2.46%	
Range	0.27	0.40	0.13	mm
Minimum	2.24	3.29	1.12	mm
Maximum	2.51	3.68	1.25	mm
Sample Count	85	62	61	droplets

Displacement results consistently show increasing displacement commensurate with increases in voltage potential applied to the plates. Displacement results for the 2.42mm diameter series are shown in Figure 69. The roughly 2.6% standard deviation in droplet diameter (and corresponding mass variation) causes a 6% variation in displacement measurement error. Error bars shown in two sets of data in the 2.4mm diameter



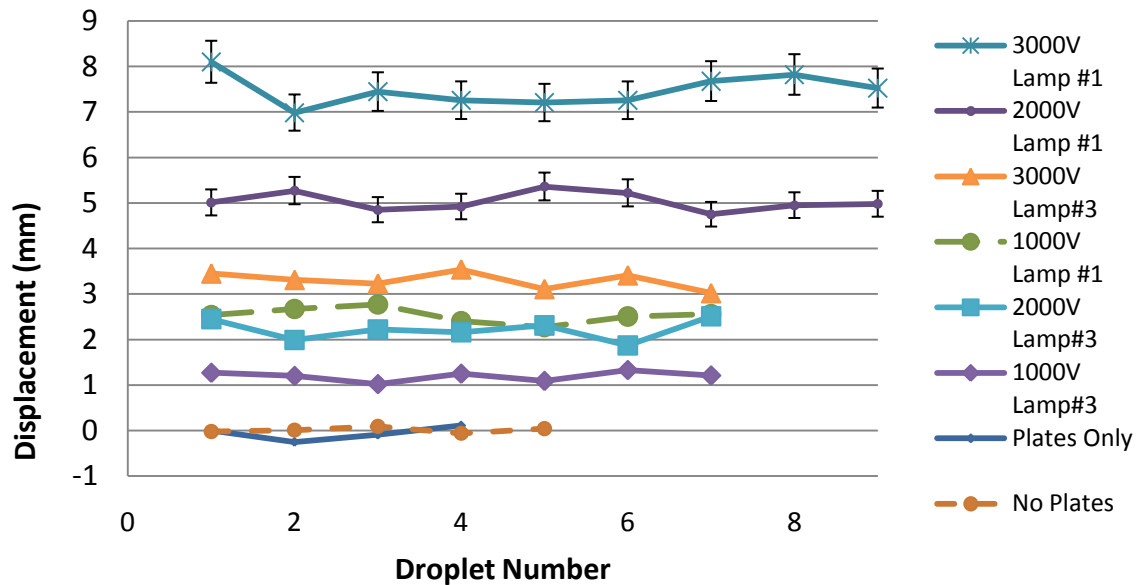
chart show the impact this 6% variation has relative to observed displacements. At observed displacements of less than a millimeter, the error bars are smaller than the data point markers in the plot and are not visible. At higher displacements, the error bars show that variations in droplet mass could account for a significant portion of the variation in displacement observed in the experiment. It is clear, however, that variability in droplet displacement is not entirely due to mass variability. Another possible explanation is rotation of falling droplets that would result in the charged hemisphere not facing the electric field directly and less displacement during passage through the plates.



**Figure 69. Displacement Results for the 2.4mm Diameter Droplet Series. Lamp# Refers to Lamp Positions 1, 2, and 3, which were positioned 21, 29, and 39 Centimeters, respectively, from the Droplet Charging Path.**

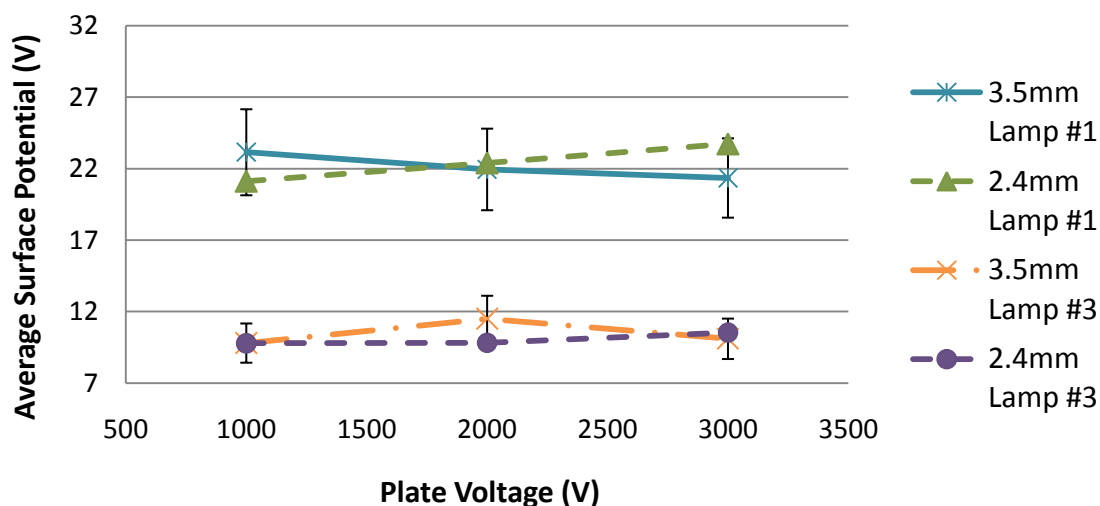
Displacement results in the 3.5mm diameter test series are similar in consistency to those of the 2.4mm series while dispersion of 1.2mm droplets is somewhat less than that of the larger droplets. Displacement of 1.2mm droplets is shown Figure 70 along with displacement error bars corresponding to the 5.9% standard deviation in droplet mass recorded for this series. The data series labeled “Plates Only” shows results of droplets that were not exposed to EUV. Variation in these droplet displacements is almost identical to variation among the data points labeled “No Plates” which had no voltage applied to the plates and the EUV lamp turned off. Because there is no significant difference between these two data sets, in all

three series, the possibility that electrostatic induction caused droplet displacement was ruled out. This is important because if electrostatic induction created a dipole charge on droplets, the resulting displacement of droplets would be indistinguishable from displacement caused by photoemission charging. The fact that no electrostatic induction occurs, even at plate voltage of 3000 volts, is strong evidence that photoemission of electrons is the dominant cause of droplet charging in the experiment.



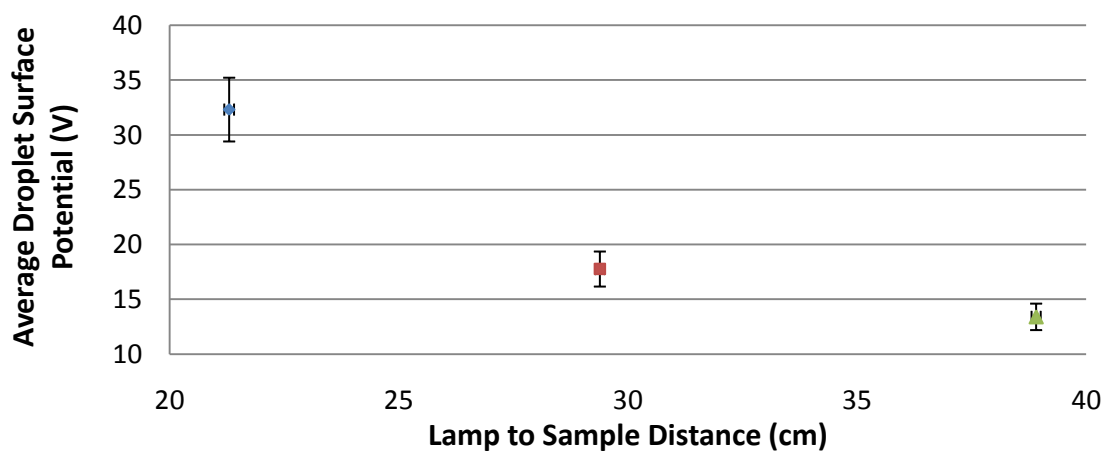
**Figure 70. Series 3 (1.2mm) Droplet Deflection Results. Lamp# Refers to Lamp Positions 1, 2, and 3, which were positioned 21, 29, and 39 Centimeters, respectively, from the Droplet Charging Path.**

Figure 71 shows average surface potentials corresponding to the average displacements recorded for two series of droplets as a function of the plate voltage applied to produce displacement. Vertical error bars, shown for the 3.5mm series, reflect variation in voltage due to one standard deviation in measured droplet displacement. Vertical error bars also reflect 6% error in voltage potential determination due to one standard deviation in droplet mass variation. The top curves correspond to droplets charged at lamp position #1 where irradiance is 2.34 times that of the sun. The bottom curves were charged by the lamp at position #3, which is 0.71 times as intense as the sun. Droplets of 1.2, 2.4, and 3.5mm all assumed very similar average surface potentials at each lamp position indicating that surface potential due to photoemissions is independent of droplet diameter.



**Figure 71. Average Droplet Potential at Nearest and Farthest Lamp Positions. Lamp# Refers to Lamp Positions 1 and 3, which were positioned 21 and 39 Centimeters, respectively, from the Droplet Charging Path. Error Bars Reflect One Standard Deviation in Measured Droplet Displacement as well as Uncertainty in Voltage Potential due to One Standard Deviation in Droplet Mass Variation.**

Figure 72 shows droplet potential as a function of lamp distance. Error bars reflect one standard deviation of displacements and one standard deviation of droplet mass.



**Figure 72. Droplet Potential as a Function of Lamp Distance. Vertical Error Bars Reflect One Standard Deviation in Measured Droplet Displacement and Droplet Mass Variation.**

Very small horizontal error bars show error associated with measuring lamp position relative to the charging path of the droplets. The drop in voltage potential with lamp distance matches expectation of an exponential relationship driven by a decrease in photon flux inversely proportional to the distance squared.

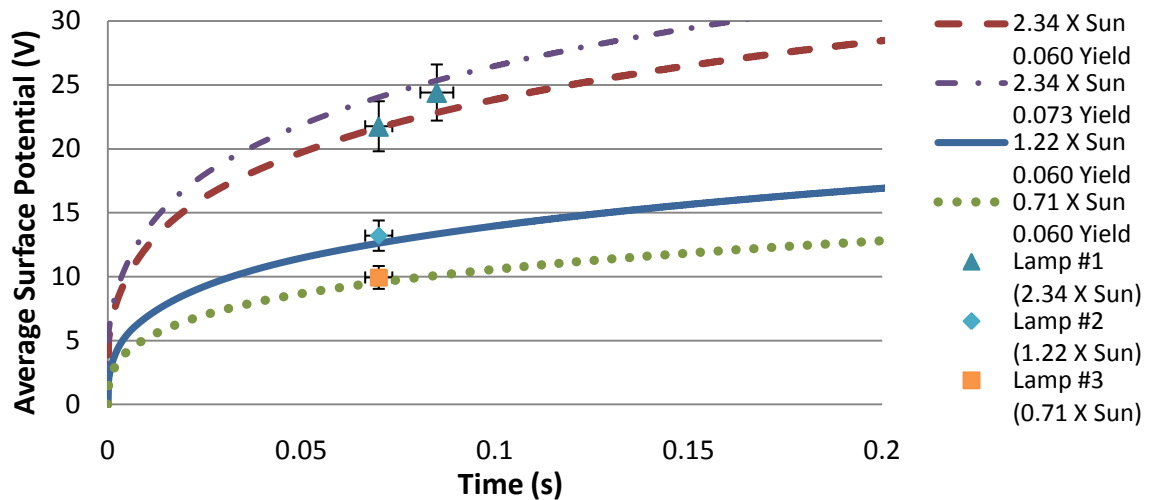
## **E. Comparison of Experimental Results to NASCAP Results**

Environmental conditions of the droplet charging and deflection experiment were simulated with NASCAP to compare measured droplet charge with predicted charge. The solar intensity in NASCAP was adjusted to match lamp intensity at the three lamp-to-droplet distances tested that correspond to 1.96, 1.02 and 0.60 times the intensity of the sun. Density and energy levels of electrons and ions in the NASCAP environment were lowered until further lowering had no impact on the equilibrium droplet charge. No attempt was made to measure plasma in the vacuum chamber but since the EUV lamp emits very few photons below the ionization potential of nitrogen, hydrogen, and oxygen, it is presumed that plasma levels in the chamber are very low.

Figure 73 shows NASCAP simulation results for DC704 droplets in an environment similar to that of the vacuum chamber used for droplet deflection experiments. Each curve in the chart represents simulation of a stationary DC704 sphere charged at a different solar intensity using a photoelectron yield of 0.60. Three data points are also plotted representing the average charge potential measured at each exposure level in the experiment. These data points are plotted at the time corresponding to their EUV exposure duration with horizontal error bars showing the error in computing exposure time.

Research by Issikawa and Gotto<sup>12</sup> showed a peak photoemission yield rate of 0.073 electrons per photon at wavelengths below 110nm (>10.5eV). The top curve in the chart shows NASCAP simulation results with nominal solar flux and a 0.07 photoemission yield. The resulting droplet charge is higher than that seen in the experiment, even at the closest lamp position. Lowering peak photoemission yield to 0.06 resulted in a droplet charge potential, after 0.07 seconds exposure time, very close to that seen in experimental droplets exposed to lamp position #1. A 0.06 peak photoelectron yield was found to result in droplet charge potentials at 1.02 and 0.60 suns that are less than half of a standard deviation below the

potentials measured in experiment. This is an indication that the appropriate peak yield to use in NASCAP modeling of silicon oil spheres is less than 0.073 and lies somewhere between 0.06 and 0.07.



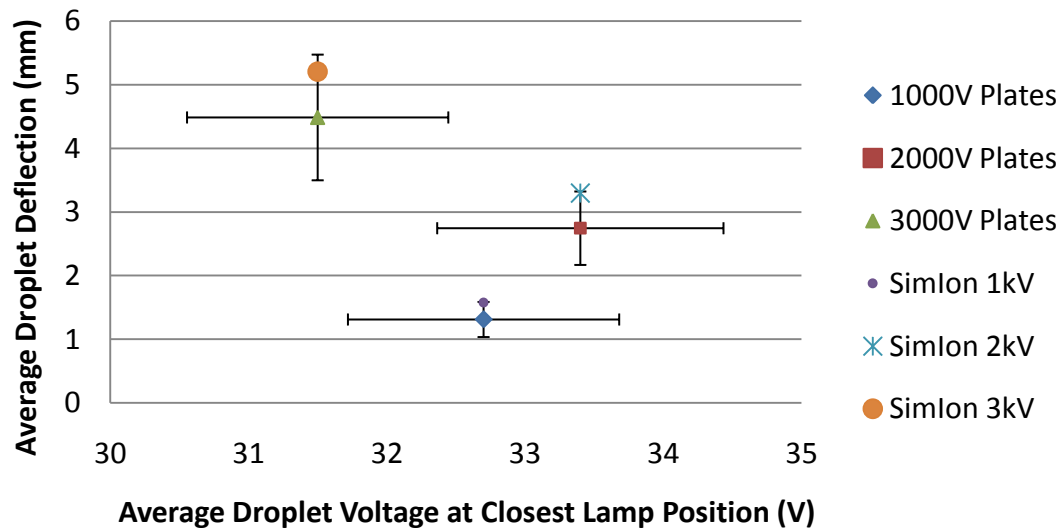
**Figure 73. Comparison of NASCAP and Experiment Results for DC704 Spheres. Lamp# Refers to Lamp Positions 1, 2, and 3, which were positioned 21, 29, and 39 Centimeters, respectively, from the Droplet Charging Path. Vertical Error Bars Reflect One Standard Deviation in Measured Droplet Displacement and One Standard Deviation in Voltage Potential due to Droplet Mass Variation.**

A peak photoelectron yield of 0.060 is less than a 14% change in yield from 0.073. To test the significance of this difference on droplet charge, two nominal sunlit GEO NASCAP simulations were run with yields of 0.073 and 0.06. The resulting maximum surface potentials were 18.5 and 17V respectively, roughly a 9% decrease in charge potential. Similar results were seen in nominal sunlit LEO (9.7% change) and in both nominal and strong sunlit auroral environments (6.3% and 4.5% respectively). These results indicate that NASCAP droplet charging predictions of sunlit droplets, determined using a photoelectron yield of 0.073, are accurate to within 10% and are slightly conservative. This difference is small enough that that 0.073 is appropriate to use in charging simulations and is slightly conservative for prediction of charge on both positively and negatively charged surface elements on sunlit spheres.

## F. Comparison of Experimental Results to SimIon Simulation Results

SimIon is a professional software package primarily used to calculate trajectories of charged particles in electric fields. This tool was used to simulate the droplet charging experiment for comparison with experiment results. SimIon allows users to input a configuration of charged plates and simulate charged particles passing between the plates. For this study, SimIon was configured with two charged plates and an ion starting above and centered between the plates. The charged particle was assigned a downward velocity that matched the actual average downward velocity droplets had while travelling between plates in the droplet charging experiment. The program will not simulate a charged particle with a mass as large as a droplet so the largest allowable particle was specified and the charge set to match the charge to mass ratio of DC704 droplets measured in experiment. SimIon plate voltages were matched to those in the experiment and deflection of each droplet occurring between the plates was recorded. The SimIon deflection results were then compared with actual droplet deflection results seen in the experiment.

The resulting predicted droplet deflection is shown in Figure 74 alongside actual droplet averages for 2.4mm droplets tested.



**Figure 74. Actual and SimIon Predicted Deflection of 2.4mm Droplets Charged at Closest Lamp Position. Error Bars Reflect One Standard Deviation in Measured Droplet Displacement as well as Uncertainty in Voltage Potential due to One Standard Deviation in Droplet Mass Variation.**

At all three plate voltage levels the SimIon deflection results are about 20% greater than the average actual deflection results seen in the experiment. The SimIon deflection predictions are consistently near the upper end of one standard deviation of the experiment deflection data recorded. The fact that SimIon predicts deflections that are within a standard deviation of actual average deflection indicates that the drift seen in the experiment is reasonable for the droplet charge to mass ratio measured in the experiment. Moreover, since SimIon uses a point mass assumption to model ion displacement and yields results similar to experiment, it supports the validity of using a point mass assumption to correlate droplet deflection with droplet surface charge.

## Chapter 6: Conclusions and Recommendations

Analyses of various aspects of the droplet stream propulsion concept show it is sound and at least an order of magnitude more efficient than high Isp electric propulsion systems at performing the same tandem satellite mission. A droplet stream system weighs about one-fifth as much as a comparable ion engine and consumes about 1000 times less power. The relatively low required operating power of droplet stream propulsion effectively makes it an enabling technology for side-by-side tandem formation satellites. In addition, a droplet stream propulsion system contains most of the components needed in a Liquid Droplet Radiator (LDR). Such a radiator is more efficient than conventional radiators on a mass basis and its use offsets the mass of conventional thermal control system mass in most satellites. Many components such as collectors and pumps were developed and tested as part of the LDR program and are well suited to droplet stream propulsion with only minor modifications.

In this study, charging of DC705 droplets in space was analyzed with numerical methods for the first time. More than 200 simulations were performed using carefully researched material properties and environmental parameters. Simulation results presented in Chapter 3 indicate that, under nominal geomagnetic conditions, transient and equilibrium droplet potential is less than 10V relative to the ambient plasma in the LEO, auroral, and GEO environments. During periods of high geomagnetic activity auroral space can charge droplets to potentials approaching -30V.

Strong geomagnetic activity may induce strongly negative levels of charge in droplets in GEO and possibly in high auroral space. Analysis in Chapter 4 shows that charge can reach thousands of volts in GEO during high magnetospheric activity and can induce droplet breakup as Coulomb forces overcome surface tension. Charging events of this magnitude are expected every 8-11 years. Droplet charging is slow in GEO and short transits limit the amount of charge acquired, preventing Coulomb breakup of droplets. Short transits also minimize off-course drift of charged droplets caused by interactions with other charged droplets or sub droplets. Lorentz forces will cause polar orbiting droplets to accelerate in a direction perpendicular to both the orbital velocity and Earth's magnetic field. For polar orbiting tandem satellites, this acceleration of droplets is primarily in a direction that will increase or decrease transit speeds. Lorentz force acceleration is small compared to droplet acceleration due to drag or electric fields and is unlikely to



affect the required collector size significantly. In GEO and low-latitude LEO, Earth's magnetic field is much weaker and Lorentz force accelerations are insignificant relative to other forces acting on droplets.

Droplet mutual repulsion due to electric field interactions is strongest when droplets are uniformly charged. Nearly uniform charging occurs when droplets charge in eclipse. Repulsion forces can be significant enough to create a large circular droplet impact area that increases required collector size. Simulations of transiting droplets show that electric field interactions can be mitigated by increasing the gap distance between droplets. Traditional piezo-electric droplet generators must break up a continuously flowing fluid column projected from an orifice before the column extends more than three orifice diameters. Columns extending more than 3.15 diameters experience Rayleigh breakup droplets into non-uniform sized droplets. Rayleigh breakup limits the gap distance that can be generated by traditional droplet generators to less than two droplet diameters.

A relatively new type of micro-solenoid valve was evaluated and tested in this study to determine its effectiveness at droplet stream production. The ability of micro solenoid valves to produce droplets at any desired gap distance makes them more desirable than conventional droplet generators for fluid stream propulsion. Existing models are sufficient for most GEO satellites but are too small and slow to separate spacecraft in LEO with masses over 200kg. However, current designs are scalable and prototype valves have been produced with much higher operating frequencies. Micro valve produced droplet uniformity was tested in this study and found to be comparable to, if not better than, that of conventional piezoelectric droplet generators.

Droplets charged with EUV light and subsequently deflected by charged plates allowed for quantification of droplet charge. Charge potential of more than 200 droplets with three different diameters was measured. Three different lamp positions and three different electric field strengths were used to provide a range of charge levels and amounts of deflection. Results show similar voltage potentials for different sized droplets charged at the same level of UV irradiance. Measured droplet potentials for each lamp position were compared with NASCAP charge predictions for droplets exposed to solar irradiance equivalent to lamp output. Results show that NASCAP prediction of droplet charging is accurate to within 10%. This correlation of modeled and actual photoemission charging provides significant validation of this aspect of the NASCAP algorithm used to predict droplet charge. Moreover, since NASCAP predictions of

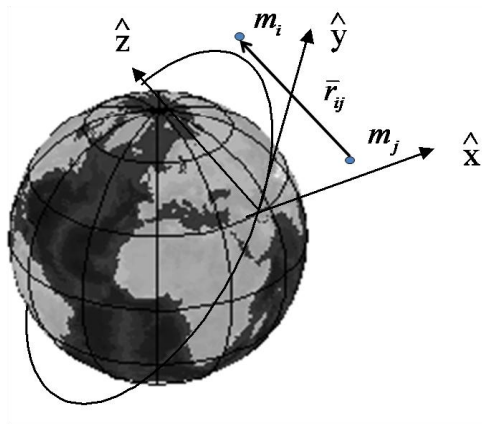
droplet charge were consistently slightly less than that measured in experiment, NASCAP provides a slightly conservative estimate of charging in sunlit droplets.

More experimentation is warranted before droplet stream propulsion is ready for operational implementation. In particular, repeated and extended exposure of DC705 to atomic oxygen is needed. Atomic oxygen testing of DC705 that was done as part of the LDR program was inconclusive enough to warrant further study. Droplet charging with high-energy electrons and protons could be performed in droplet charging experiments to refine estimates of secondary electron yield in droplets. Such experiments would validate or refine DC705 material properties used by NASCAP. A relatively simple experiment performed on a single satellite in space could validate many aspects of this study such as drift due to drag, droplet charge measurement (in auroral regions if possible), charged droplet interactions at various droplet sizes and spacing, and long-term viscosity changes to DC705.

This study has shown that the major concerns surrounding implementation of this novel concept in satellite propulsion are significant but quantifiable. These impediments can be mitigated through the use of sensors, techniques, and systems identified by this study and described in this dissertation. The goal of this study was not to prove that droplet stream propulsion is viable, but merely to quantify the challenges associated with it. The greatest unknown, droplet charging, has been quantified and found to pose challenges to stream collection that can be effectively mitigated through careful selection of stream parameters like droplet spacing, velocity, and diameter.

## Appendix 1: Tandem Satellite Propulsion Needs and Droplet Stream Capabilities

It has been shown by Tragesser<sup>2</sup> that satellites can maintain a side-by-side formation with a given distance between them if a force is applied to each spacecraft displacing them from a reference orbit between them. Without this force they tend to converge toward the centerline of the reference orbit and



**Figure 75. Reference Frame used in Development of Equations used to Describe the Forces Required to Maintain Tandem Satellite Formation Position (From Tragesser, 2007).**

converge half an orbit later. This closure rate is quantified mathematically by the Clohessy-Wilshire (CW) equations of motion that describe the motion of a satellite as it is influenced by other satellites sharing the same reference orbit and held in position relative to one another by forces associated with momentum exchange:<sup>2</sup>

$$m_i(\ddot{x}_i - 2n\dot{y}_i - 3n^2x_i) = \sum_{j=1}^N \bar{u}_{ij} \cdot \hat{x} \quad (54)$$

$$m_i(\ddot{y}_i + 2n\dot{x}_i) = \sum_{j=1}^N \bar{u}_{ij} \cdot \hat{y} \quad (55)$$

$$m_i(\ddot{z}_i + n^2z_i) = \sum_{j=1}^N \bar{u}_{ij} \cdot \hat{z} \quad (56)$$

Here:  $m_i$  = the  $i$ th satellite mass,

$n$  = the mean motion (average angular orbital velocity) of the reference orbit in rad/s,

$\bar{u}_{ij}$  = A repulsive force caused by momentum exchange between satellites  $i$  and  $j$ ,  
 $x$ ,  $y$ , and  $z$  = satellite displacement from the reference orbit as depicted in Figure 75.

Assuming that thrust acts along the relative position vector (as it must for exchanged droplet streams) yields the following equation:

$$\bar{u}_{ij} = \alpha_{ij} \frac{\bar{r}_{ij}}{|\bar{r}_{ij}|}, \quad \alpha_{ij} > 0 \quad (57)$$

where  $\alpha_{ij}$  = the magnitude of the momentum exchange force between the  $i$ th and  $j$ th satellite,  
 $\bar{r}_{ij}$  = the position of the  $i$ th satellite relative to the  $j$ th satellite.

Looking at the cross track axis ( $\hat{z}$ ) motion for two satellites only and solving for a steady-state condition by setting the time derivatives to zero results in the following equations:

$$m_1 n^2 z_1 - \alpha_{12} \frac{(z_1 - z_2)}{|z_1 - z_2|} = 0 \quad \text{and} \quad m_2 n^2 z_2 - \alpha_{12} \frac{(z_2 - z_1)}{|z_2 - z_1|} = 0 \quad (58)$$

Solving these equations simultaneously yields the following relationship, which requires that the center of mass of the two satellites reside at the centerline of the reference orbit:

$$z_1 = -\frac{m_2}{m_1} z_2 \quad (59)$$

Solving Equation 59 for the magnitude of the force required, in LEO, to maintain position relative to the other satellite yields:

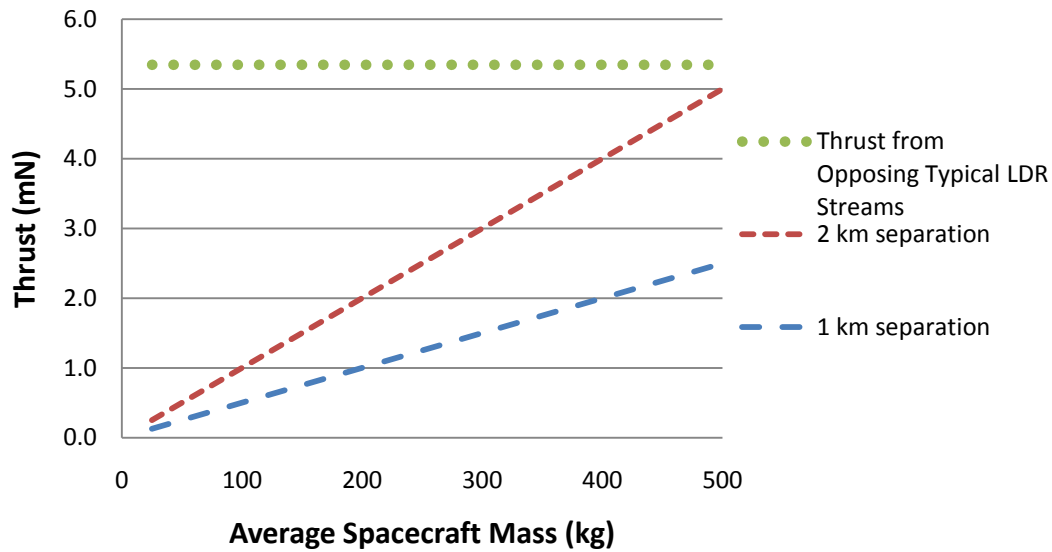
$$\alpha_{12} = m_1 n^2 z_1 = -m_2 n^2 z_2 \quad (60)$$

Thus, it is shown that the thrust needed to maintain the position of tandem cross-track satellites is a function of the masses of the satellites, the desired distance between them and their orbital mean motion. Acceleration is more pronounced at lower altitude orbits where orbital mean motion is high, but even large (>1000km) tandem satellites can be held in position relative to each other in LEO by a single droplet stream pair with untested but feasible droplet diameter and velocity.

In Geosynchronous Earth orbit (GEO), mean motion is small and the corresponding low thrust needed to maintain tandem satellite separation is shown in Figure 76. The thrust required in GEO, in Newtons, is roughly equal to:

$$\alpha_{12} = m_1 z_{12} (5e - 9) \quad (61)$$

where  $z_{12}$  is the baseline distance between spacecraft. Figure 76 shows thrust required in GEO as a function of satellite mass for 1 and 2 km separation distances along with thrust from a droplet stream.



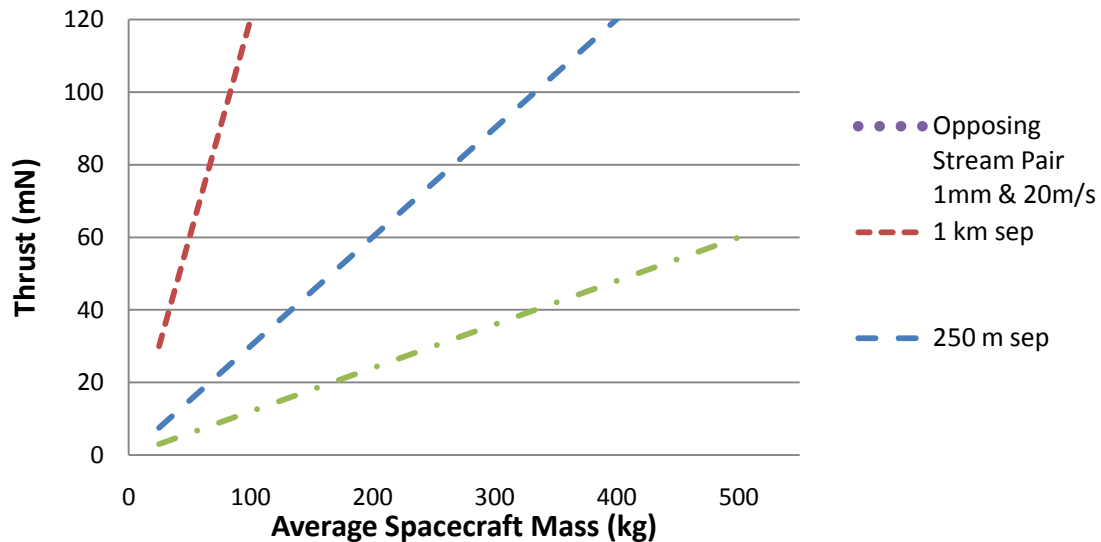
**Figure 76. Thrust Required in GEO and Produced by LDR Streams**

The droplet stream in Figure 76 has a diameter of 0.25 mm and a stream velocity of 16m/s which is much smaller and slower than is possible. Droplet streams of this size and speed were demonstrated for the LDR program both at 1-g and in drop tower microgravity testing in the U.S. and in Japan.<sup>6,64</sup> LDR applications favor small droplets to maximize the surface to volume ratio and increased rate of radiative heat loss. Slow drops are also favored for LDR applications to maximize time radiating while transiting about a meter. The largest LDR streams tested had a diameter of 1mm and a speed of 20m/s. Little effort has gone into demonstrating larger or faster streams because they are less efficient for use in LDR applications.

In LEO and Polar orbits mean motion is much higher than in GEO and the forces required to maintain a tandem satellite formation are three orders of magnitude greater in LEO than in GEO. The thrust, in Newtons, required for a 600km orbit is roughly equal to:

$$\alpha_{12} = m_1 z_{12} (1.2e - 6) \quad (62)$$

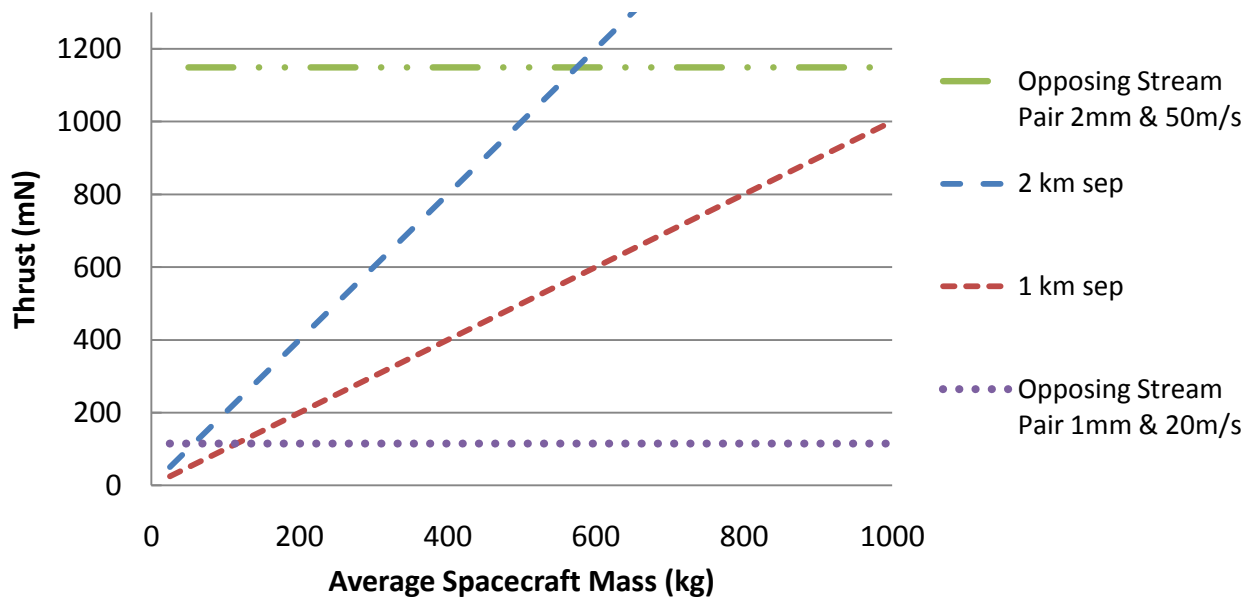
Figure 77 shows thrust required as a function of spacecraft average mass and separation distance, compared to the force of thrust that is generated by a single pair of opposing droplet streams. The thrust produced is based on momentum produced by opposing 1 mm diameter streams with 1mm spacing between droplets and a velocity of 20 m/s. This size and velocity represents the limit of size and velocity of uniform droplet streams tested by NASA in the 1980's for the LDR program. It is apparent from Figure 77 that unless uniform droplet streams larger and/or faster than this can be generated, spacecraft weighing more than 100 kg will require more than one stream pair to maintain 1km spacing.



**Figure 77. Thrust Required in LEO and Maximum Demonstrated Stream Capabilities**

For LDR applications, multiple streams pose little challenge for either stream generation or collection. Several LDR concepts propose millions of droplet streams focused on a single droplet collector for large space structures such as solar power generating satellites. However, small defects or obstructions in the droplet generators will alter the path of droplet streams and could cause collision of droplets. There is a demonstrated propensity for colliding droplets to coalesce into a single larger droplet that has a velocity

vector that will still reach the stream collector over short distances.<sup>62</sup> Over long transit distances drag and charge related forces have more time to act and droplets of different diameters will travel very different paths. This is the principle reason why it is more desirable to produce a pair of opposing streams pairs that can each be aimed at a single collector. This ensures that only one droplet size is collected by each satellite reducing the probable impact circle and corresponding collector size and mass. An impact site detection sensor is proposed later in this report that enables feedback to a droplet stream pointing control system. It would be challenging for such a sensor to distinguish between multiple streams impacting a collector. Use of single opposing streams limits the amount of thrust that can be produced by previously tested droplet stream size and velocity as illustrated in Figure 77. However, as Figure 78 shows, relatively small increases in speed and diameter beyond those that have been demonstrated yield significant increases in propulsive effect.



**Figure 78. LEO Thrust Required as a function of Spacecraft Mass and Thrust Possible by Increasing Diameter and Velocity Slightly**

Figure 78 shows the thrust provided by an increase of droplet diameter to 2mm and an increase in velocity to 50m/s. This velocity is half of what has been demonstrated already with 0.146mm silicone oil droplets.<sup>67</sup> Although examples of silicon oil streams larger than 1mm diameter were not found in the

literature, fluid mechanics theory does not preclude larger sizes. In a 1986 fluid stream applications study, Muntz & Dixon proposed 3mm diameter droplet streams for transport of materials and noted that, “It is relatively straightforward to accelerate unit density liquid or slurries to speeds as high as 1000 m/s; a more common value might be 300 m/s.”<sup>66</sup> In this study, uniform droplet streams with diameters of up to 1.5mm were produced with velocities in the 5m/s range and a frequency of approximately 0.5 Hz. Individual droplets with consistent diameters as large as 3.5mm were produced in vacuum for this study. An increase to 3mm at 100m/s expands allowable spacecraft mass beyond 6000 kg with 3km separation in LEO.



## Appendix 2: Past Droplet Stream Research

Proposals for the use of droplet streams in space first appeared in the literature in the 1980s where they saw great interest and development as a mechanism for heat dissipation on high-powered satellites such as the International Space Station and a Lunar Base. Droplets of low vapor pressure streamed through space are cooled by radiation as they travel to a collector. Liquid Droplet Radiator (LDR) collectors were typically positioned about a meter away from the droplet generating nozzles and collected droplets were then pumped back to the satellite heat source to begin another cycle. Figure 79 shows a basic schematic of the concept applied to removing heat from a generic thermal load.<sup>63</sup>

Testing of weightless droplet streams in a drop tower is ongoing by researchers at Hokkaido University, Japan, who published results as recently as 2002.<sup>63,64</sup> Droplet stream technology development has resulted in working components that can be used off-the-shelf in a droplet stream propulsion system. Most LDR technology development focused on collector design and several types of collectors and droplet generators were developed and tested by NASA and the Air Force. These studies resulted in at least two viable designs, both of which exhibited minimal loss of fluid due to splashing.

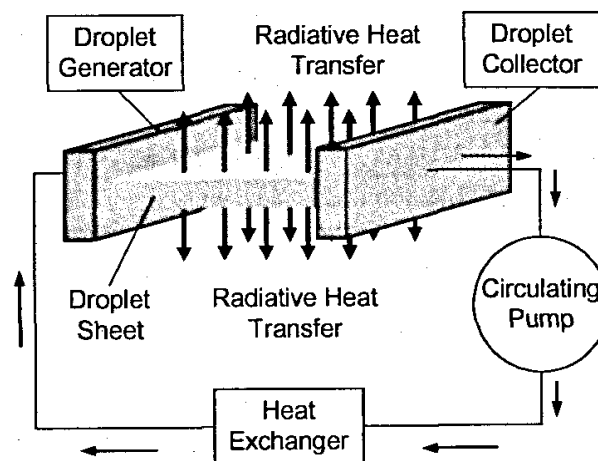
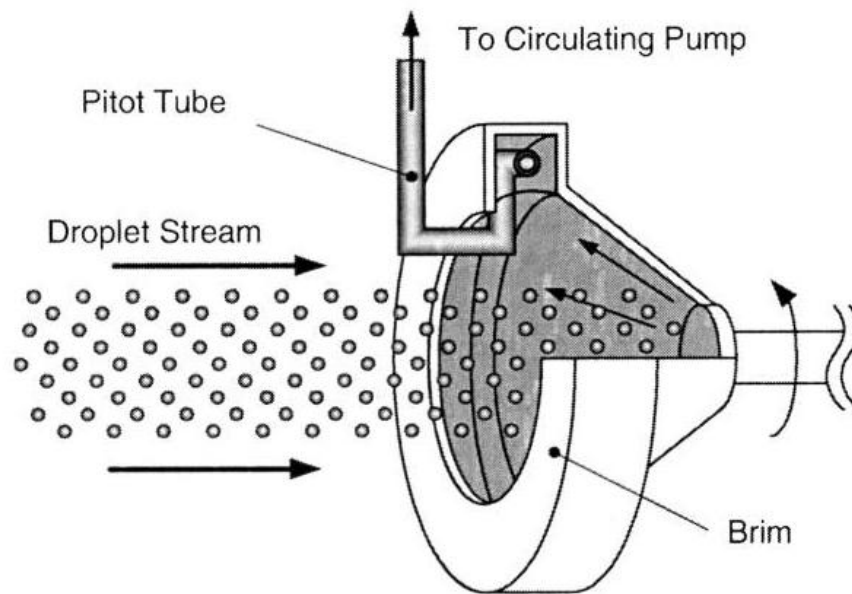


Figure 79. Liquid Droplet Radiator Concept (from Totani et al., 2002).

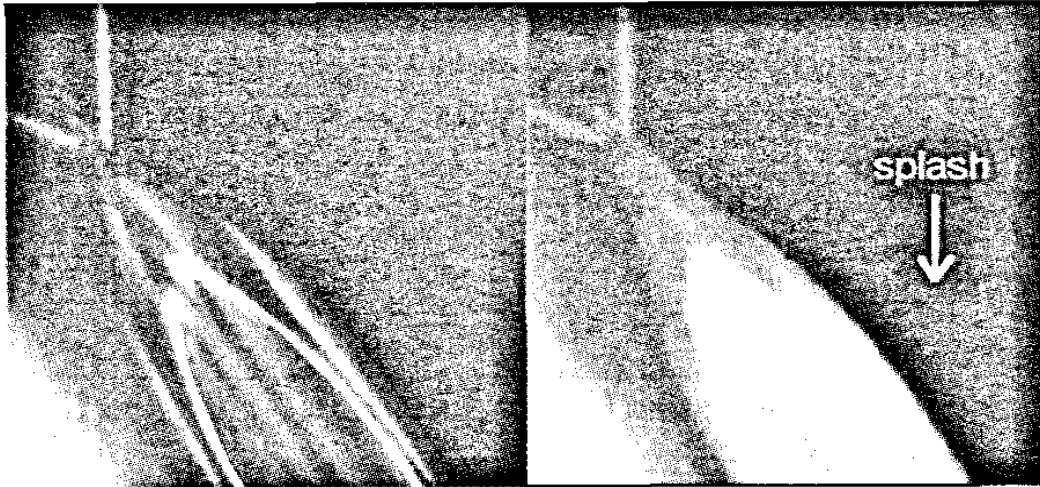
The most effective design for long distance droplet stream collection is likely a rotating cylindrical drum design like the one depicted in Figure 80. Entering droplets are forced into a collection channel where a pitot tube, immersed in fluid, collects and circulates the fluid into the receiving satellite for heating and pressurization. Collectors like this one have seen extensive development and testing by the USAF<sup>7</sup> and NASA<sup>6</sup> as well as by Japanese researchers.<sup>65</sup> USAF testing showed that droplets as large as 1mm in diameter and up to 20m/s velocity can be successfully collected with little, if any, loss of droplets due to splashing.<sup>6</sup> Because of the relative maturity of droplet stream collector technology, collector design was not investigated in this study beyond determining required collector diameter needed to prevent loss of droplets due to environmental factors.



**Figure 80. Silicon Oil Rotating Collector. (from Totani, et al., 2006).**

One of the findings that emerged from testing of LDR candidate fluids is that streams of uniform diameter and spacing tend to minimize splashing on the surface of a stream collector. This is illustrated in Figure 81 that shows images from a weightless drop tower experiment in which an aluminum plate was impacted by two silicone oil streams.<sup>65</sup> Both streams have an incidence angle of 35 degrees but the first stream is driven at a frequency that results in uniform droplet size while the second stream is much slower and droplet formation is more random. The result is droplet interactions at the collision surface that result

in numerous small droplets that are liberated from the impact surface. These liberated droplets appear white in the figure. In nominal geomagnetic charging conditions, droplets will impact quite close to each other and a non-uniform stream could result in fluid loss due to splashing.



**Figure 81. Collection of Uniform (left) and Non-uniform (right) Droplet Streams (from Totani et al., 2002)**

In addition to splash losses, non-uniform droplet streams are undesirable because they present considerable challenges to the propagation of a stream over long distances. Non-uniform droplets have different mass and ballistic coefficients and will drift off of the intended path by varying amounts. The causes of drift of droplets in a stream are a significant impediment to droplet stream collection in space and are the major focus of this study. Major sources of drift include droplet charging and atmospheric drag; both will be discussed in detail in the chapters that follow.

Droplet streams are mentioned in the early LDR literature by Muntz, et al.<sup>66</sup> and Dixon<sup>67</sup> as a possible mechanism for long distance transfer of high vapor pressure fluids encased within low vapor pressure droplets. These researchers also proposed liquid stream propulsion as a method of low contamination propulsion, and as a means of momentum exchange for vehicles docking with a space station.<sup>66</sup> In support of these propulsion concepts, and LDR, Muntz and Dixon studied velocity variations in direction and magnitude in DC704 droplet streams at the University of Southern California (USC) in a 6

meter vacuum drop tube.<sup>66, 67</sup> Aside from the USC work, it appears that no one has studied long distance droplet transit and no one has studied droplet charging in space and the challenges this poses to fluid transfer between satellites over more than a few meters.

### Appendix 3: Heat Transfer Considerations for Fluid Stream Propulsion

Heat loss during transit is a concern because of the potential challenges associated with collecting frozen or partially frozen droplets. Solid droplets might bounce off a collector while partially frozen droplets require heating in order to process them for subsequent transits. This study analyzed both radiative heat transfer from the droplets and heat transfer within the droplets to determine if heat transfer to the surface would keep pace with radiation from the surface. If conduction of heat is sufficient to prevent solid outer shell formation then convection of heat increases heat transfer to the surface and further reduces the chance of shell formation. Analytic and numerical analysis shows that the heat transfer rate within droplets due to conduction exceeds heat transfer from droplets due to radiation. As a result, it was not necessary to quantify convective heat transfer within the droplets since convective transfer.

Radiative heat transfer from DC705 in space has received considerable attention in the LDR literature but these studies have focused on radiative heat transfer from sheets and columns of droplet streams and not individual droplets.<sup>65</sup> **Error! Bookmark not defined.** None of the LDR designs proposed droplet stream transit distances of more than a few meters or exposure times of more than a few seconds. In this study thermal heat loss was analyzed for several droplet sizes with the goal of developing an envelope in which droplets of various sizes and transit velocities can be used over various transit distances while avoiding any freezing of the droplet surface. Two thermal models were developed using radiation parameters from the LDR literature and materials properties from Dow Corning. These models were then compared with results from simulations performed with a professional spacecraft thermal modeling tool called Thermal Desktop.

Predicting the freezing point of DC705 is not as straightforward as it is for most common liquids. The polymer is an amorphous solid with a glass transition temperature of about -120°C (153 K) depending

upon the purity of the sample.<sup>vii</sup> Glass transition temperature is defined as the temperature above which a rearrangement of atoms or molecules in an amorphous solid can occur. It is considered the temperature where liquid polymers transition to a brittle glass like state and solid polymers transition to a rubbery state. A technical representative for Dow Corning also cited testing that revealed that crystals can form in some of their silicone oil products at -50C (223 K). The same Dow Corning representative felt confident in stating that no crystallization of DC705 would occur above -45 C (228 K).<sup>vii</sup> Most LDR literature assumes a freezing point of 200K which is significantly greater than glass transition temperature. A received temperature limit above glass transition temperature allows for additional cooling that will occur on the collector before collected fluid is pumped into the receiving spacecraft. A received temperature margin above freezing will likely eliminate the need to heat the collector surface.

It is possible to collect solid droplets and then melt them in a surface film of warm fluid injected onto the collector or sprayed onto the collector by additional droplet generators on the receiving satellite. Warm fluid directly injected into the collector would prevent bouncing of solid droplets and melt them as well. The chief consideration for collecting solid droplets is splashing of fluid on the collector that could result in loss of fluid. Despite this concern, collection of solidified metals (Lithium) was examined for the LDR and was found to be feasible without significant fluid loss. Collection of solid droplets was not considered in this study and modeling, presented next, indicates that it is not necessary to design a system capable of solid droplet collection.

Prior to modeling radiative heat transfer in DC705 droplets, it was necessary to determine if the rate of heat conduction within the droplet is high enough to prevent surface freezing. Consider a droplet with an inner temperature of 300K and a surface temperature of 228K. If the surface is assumed to radiate to a background temperature of zero Kelvin then this is the maximum radiative heat loss for a droplet that is on the verge of forming crystals. Setting the maximum radiative heat flow equal to the necessary

---

<sup>vii</sup> Telephone conversations and email correspondences with several Dow Corning technical representatives. Numbers quoted are courtesy Mr. Travis Hein, Technical Information Center, Dow Corning Corporation. June, 2008.

conductive heat flow needed to replace heat lost at the surface through radiation yields the minimum required conduction coefficient  $k$ . Using an emissivity of 1.0, the minimum conduction coefficient is equal to 0.004 W/mK which is significantly less than the advertised conduction coefficient from Dow Corning of 0.1 W/mK. Thus, heat transfer within the droplet will exceed the rate of radiative heat transfer from the droplet surface and temperatures should be nearly uniform within the droplet.

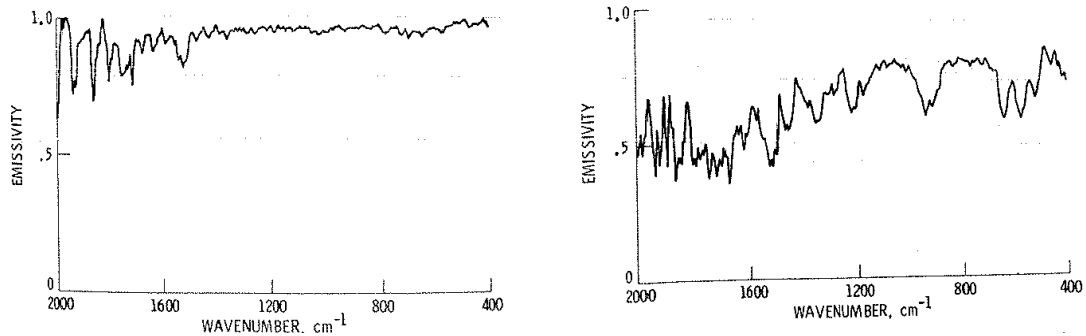
To help quantify how reasonable the uniform droplet temperature assumption is, a radiation equivalent Biot number was calculated. Biot numbers less than 0.1 indicate that the lumped capacitance method of determining the temperature of a cooling body over time can be used with less than 5% error.<sup>68</sup> Table 13 shows calculated values for radiation equivalent Biot numbers for a 1mm diameter DC705 droplet at various initial temperatures. These values are consistently below 0.01 indicating that uniform temperature throughout the droplet is a reasonable assumption. This was later confirmed by a spacecraft thermal modeling tool called Thermal Desktop which showed a maximum difference of only 3 °C between the surface and center of the droplet over a 100 second exposure time in eclipse.

**Table 13. Radiation Equivalent Biot Numbers for a 1mm Droplet**

Initial Temperature		Biot #
50 C	122 F	0.0034
40 C	104 F	0.0031
30 C	86 F	0.0028
20 C	68 F	0.0026

Definitive information on the thermal emissivity of a single stream of DC705 droplets was not found in the literature, however, emissivity of a thin film of DC704 was tested by Teagan and Fitzgerald.<sup>69</sup> The results of their testing are shown in Figure 82 and indicate that the emissivity varies as a function of film thickness tested. A 1987 NASA LDR status report quoted a value of 0.61 +/- .05 for emissivity of DC705 in droplets that were 0.6 millimeters in diameter but listed no source of this information or results for droplets of different diameters.<sup>6</sup> The same 1987 NASA report stated that emissivity of a single droplet

or droplet stream had not been determined. NASA emissivity studies focused on determining the emissivity of a sheet of tightly spaced droplet streams many streams thick.



**Figure 82. Emissivity Results for DC704 Samples; 0.6mm thick film on the left, 0.3mm on the right (from White, 1987)**

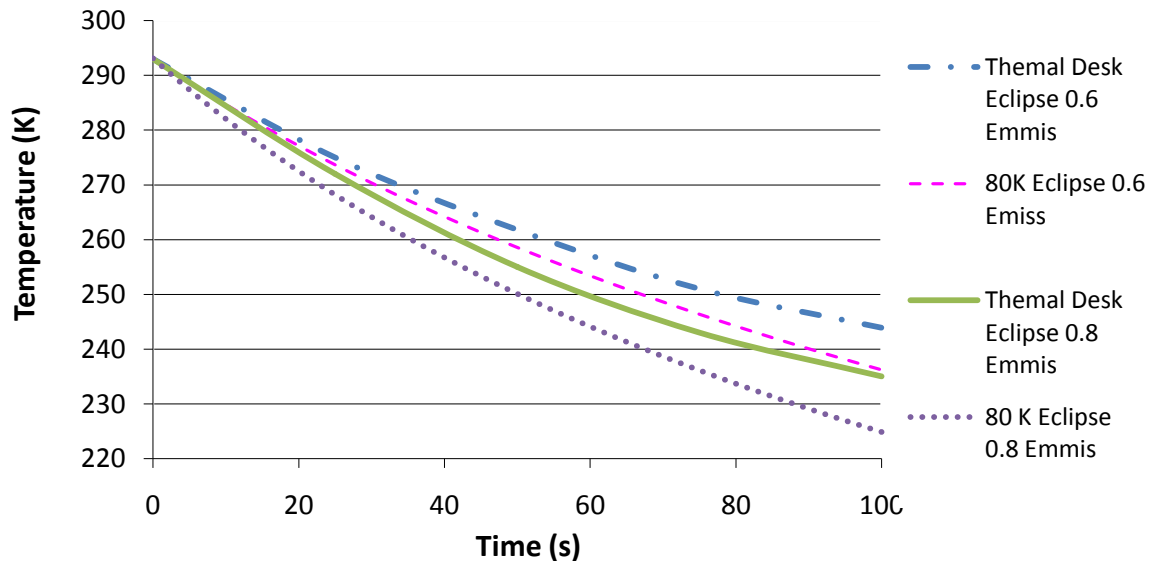
The NASA estimate of 0.61 for emissivity of a 0.6mm DC705 droplet fits the data for a 0.3mm thick film of DC704 in the figure above closely. This implies that a droplet of DC705 that is larger than 0.6mm has an emissivity that is higher than 0.61. In fact, more recent research by Totani et al. quotes a value of 0.8 for 0.25mm diameter droplets of a silicon oil called KF-96, which is described as equivalent to DC705 and has properties nearly identical to those of DC705.<sup>62</sup> This lack of consistent data for emissivity of DC705 makes thermal analysis of heat loss during transit somewhat imprecise. It is clear, however, that droplets greater than 1mm in diameter will have an emissivity greater than 0.6. For this study, three values: 0.6, 0.8, and 1.0 were used to determine the amount of radiative heat loss that will cause droplets to begin to freeze in eclipse as a function of droplet size.

Two Microsoft Excel spreadsheets were created for this study to simulate heat loss in transiting droplets over time. Droplets of various sizes and exposure times were analyzed with the spreadsheets and then compared with results from a professional spacecraft design tool called Thermal Desktop. Thermal Desktop employs a nodal mesh to model temperature throughout a body over time. Analysis with this tool confirmed that heat transfer within a droplet is efficient enough to prevent more than a 5°C differential between the core and the surface. All three models used in this study analyze droplets in full sun and eclipse. Full sun conditions include direct radiation from the sun as well as reflected albedo and earthshine from the Earth. USAF researchers determined the absorptivity of DC705 to be 0.08 which is used in all



three models. **Error! Bookmark not defined.** Specific heat and droplet density are available from Dow Corning and are 1530 J/kg-K and 1097 kg/m<sup>3</sup> respectively. Earth albedo was assumed equal to 31% of direct sunlight (1368W/m<sup>2</sup>). Earthshine is the only radiation source considered in eclipse and is a constant 237W/m<sup>2</sup>. Both models assume incoming radiation incident on an area equal to the cross sectional area of a droplet sphere.

The two models differed in the manner in which the droplets radiate. In one model, the droplet radiated to 80K space in all directions. This method is used by Totani et al.<sup>63,65</sup> to determine temperature loss of LDR fluid streams. Results from a simulation of 1mm droplets cooled with the 80K method are shown in Figure 83 along with the results of temperature loss determined by Thermal Desktop simulation using identical thermal properties for DC705. Eclipse results for two different emissivities are shown for the 80K model and for Thermal Desktop:

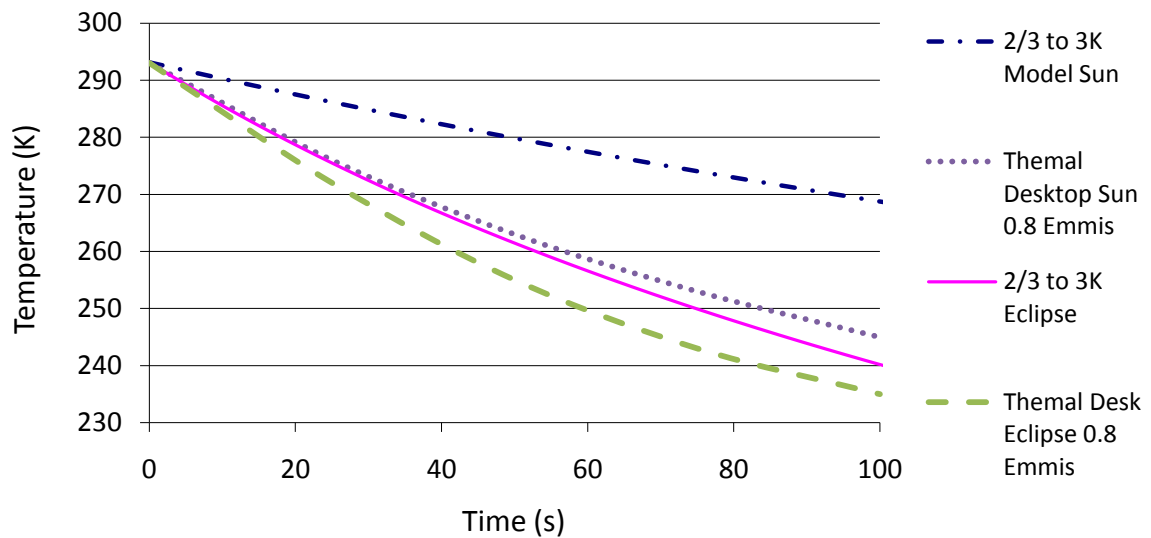


**Figure 83. Spherical Radiation to 80K Model vs. Thermal Desktop Results (1mm diam in eclipse).**

The 80K thermal model yields slightly more heat loss than the Thermal Desktop model. The models were run for 100 seconds which is twice as long as necessary to transit 1km at 20m/s. Even with the most conservative emissivity and most conservative model it takes 70 seconds for a relatively small (1mm) droplet at 20 C to cool enough for any crystallization to occur. It takes 2 minutes and twenty seconds to

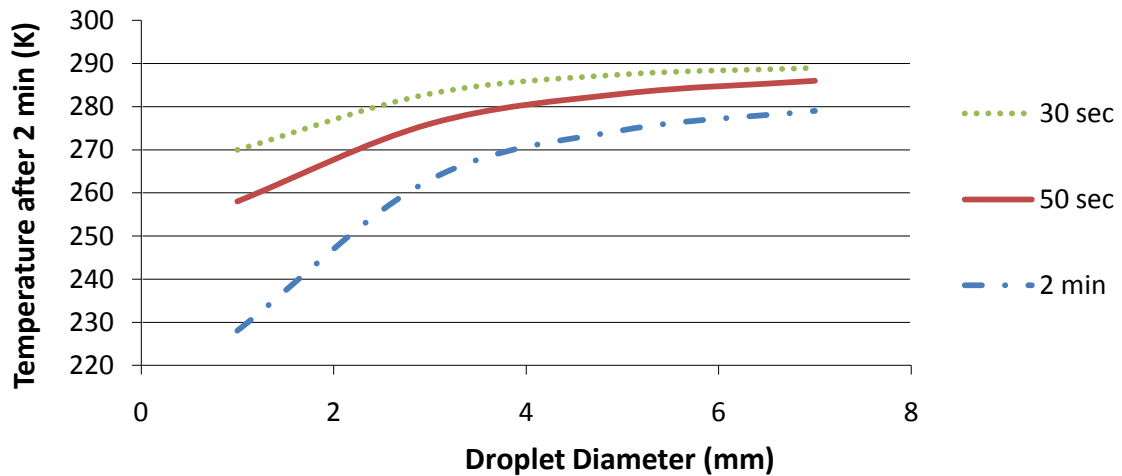
reach 200K, the freezing point published by NASA LDR researchers. Larger droplets take longer to freeze due to their greater mass to surface area ratio.

The second model generated for this study radiated from 2/3 of the droplet surface area to an environment at 3 K. Results are shown Figure 84 and indicate that the 2/3 model is less conservative than the Thermal Desktop and 80K models. The 2/3 model under predicts heat loss when compared to the Thermal Desktop and 80K models in sunlit conditions. The 2/3 model also underpredicts heat loss in eclipse when compared to the other two models though it is much closer. For this study, the two conservative models (80K and Thermal Desktop) were used for comparison of heat loss in droplets.



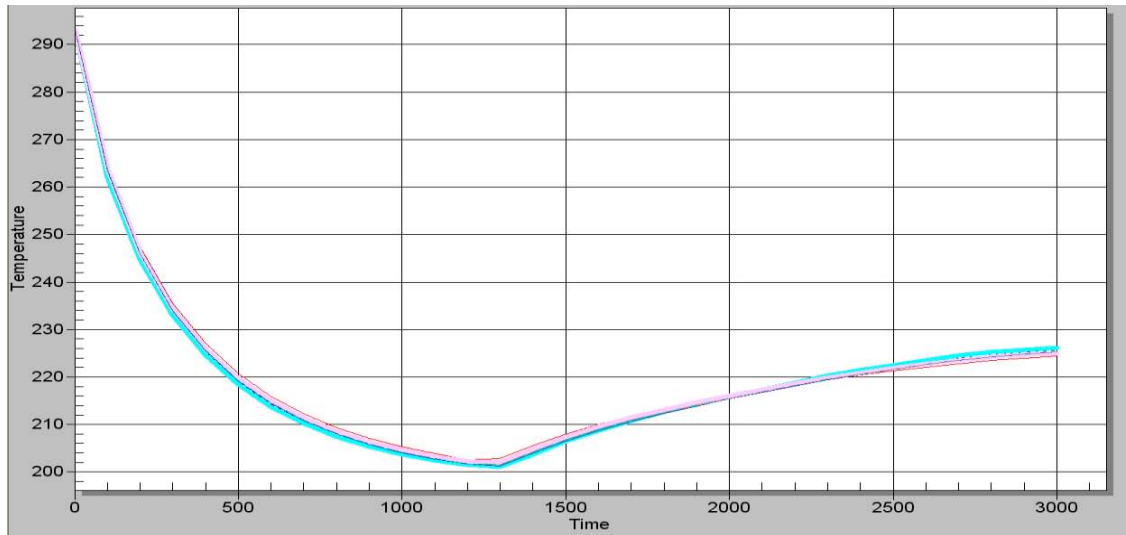
**Figure 84. Cooling Results for 1mm droplet using "2/3 to 3K" Model and Thermal Desktop**

A comparison of droplet cooling at 4 different diameters was made using the model radiating in all directions to an 80K environment. Results, in Figure 85, show that temperature loss in larger droplets is significantly less than in smaller droplets.



**Figure 85. Equilibrium Temperature for Various Diameters and Exposure Times (0.61 emissivity)**

A 2mm droplet was simulated in eclipse using Thermal Desktop for 3000 seconds to observe how cold it would get and then how quickly it would heat up once it entered full sunlight. The results are presented in Figure 86 and indicate that a droplet 2mm in diameter or larger takes more than 10 minutes to reach the freezing point of 200K. The chart also indicates that frozen 2mm droplets should melt when exposed to full sun after leaving eclipse. Larger droplets are likely to never reach the freezing point of DC705 during an entire eclipse period of a low Earth orbit. By eliminating earthshine in the model an estimate of the time to reach 200K in GEO eclipse was made. The resulting time to freeze for a 1mm droplet in GEO was 141 seconds. Using this time to freeze, and the maximum uniform stream speed (100m/s) from the literature, one can assume that transit distances of at least 14km are reasonable without freezing. At 20m/s a 1mm droplet can travel several kilometers without freezing and much greater distances are possible with larger droplets.



**Figure 86. 2mm Droplet Cooled in Eclipse then Exposed to Full Sun (Temperature vs. Time)**

Spacecraft designers employing droplet stream propulsion will have to consider the loss of heat from the spacecraft that occurs because of transiting droplet streams. This amount heat loss is small for a typical spacecraft but will reduce the need for conventional radiators. This is especially true if extra fluid is injected into the collector to help facilitate droplet collection or prevent pump cavitation. Heat loss in droplets increases as droplet diameter decreases and Table 14 shows the rate of heat loss for stream pairs of three small sizes at two different speeds transiting 100 meters and providing similar levels of thrust.

**Table 14. Radiation from Fluid Stream Pairs at Similar levels of Thrust (100m Transit)**

<b>Drop Diam</b>	<b>Full Sun</b>	<b>Eclipse</b>	<b>Velocity</b>	<b>Thrust</b>	<b>Stream Pairs</b>
<b>1mm</b>	<b>0.24 W</b>	<b>2.05 W</b>	<b>3.5 m/s</b>	<b>6.2 mN</b>	<b>1</b>
<b>.25 mm</b>	<b>0.18 W</b>	<b>1.38 W</b>	<b>16 m/s</b>	<b>7.0 mN</b>	<b>1</b>
<b>.1 mm</b>	<b>5.07 W</b>	<b>52.9 W</b>	<b>3.5 m/s</b>	<b>6.3 mN</b>	<b>315</b>

A single 1mm stream loses heat at a rate of 2 Watts in eclipse and ¼ Watt in the sun travelling very slowly at 3.5m/s. Increasing this speed to 35m/s decreases the heat loss of the stream by an order of magnitude

while increasing the travel distance to a kilometer increases the heat loss an order of magnitude. Larger droplets provide the same impulse as smaller droplets with a slower transit speed and can therefore lose more heat than a comparable stream. The droplet stream can be tailored to the needs of the satellite and even altered in flight to manage spacecraft temperatures.

#### Appendix 4. Droplet Stream Formation

Lord Rayleigh observed a fluid stream will break up into randomly sized droplets within a distance of 3.15 to 3.18 stream diameters. He went on to show that a cylindrical column of water will break up into evenly spaced droplets if the stream is supplied with a steady vibration with a wavelength greater than the stream's circumference. Later Weber derived stream formation relationships that account for fluid viscosity and a pressure differential between the chamber and ambient environment. **Error! Bookmark not defined.** The process developed by Rayleigh by which a column of fluid is broken up into droplets is shown in Figure 87 and is typical of modern droplet stream generators. Formation of droplet streams in this manner is relatively mature technology and many droplet stream generators are available for low viscosity fluids.

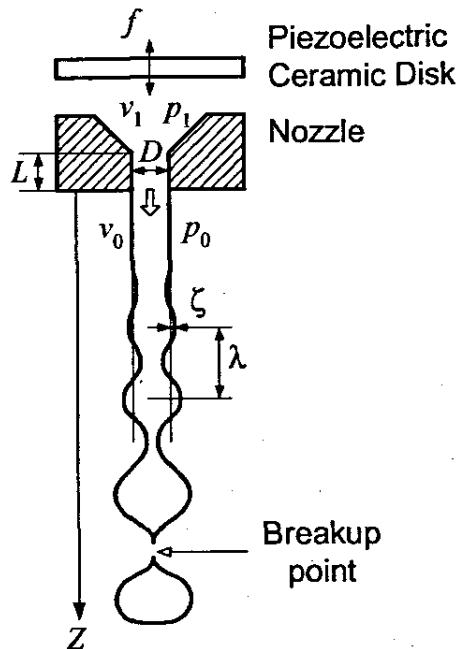


Figure 87. Transformation of Fluid Column to Droplet Stream (from Totani et al, 2002)

In the droplet generator depicted, a piezoelectric disk (or cylinder) produces a vibration that propagates through a volume of pressurized fluid and is focused by a converging nozzle at a nozzle orifice. Without vibrations a column of fluid is projected through the orifice and eventually breaks up into random

diameter droplets. Rayleigh derived the optimum wavelength ( $\lambda$ ) that will produce instability in the column of fluid most rapidly which is given by the formula:<sup>70</sup>

$$\lambda_{optimum} = 4.508D \quad (63)$$

If the mechanical disturbance of the piezoelectric disk is sinusoidal then a stream of uniform size droplets is created. The spacing between droplets is constant and is equal to the disturbance wavelength given by

$$\lambda_{uniform} = f/v_0 = 3.5D \text{ to } 7D \quad (64)$$

where  $f$  is the piezoelectric vibration frequency and  $v_0$  is the fluid column velocity. Testing has shown that uniform droplets are produced if  $\lambda$  is between 3.5 and 7 times the fluid column diameter. Also, the minimum column velocity needed to form a jet from a capillary tube is given by<sup>70</sup>

$$v_{0min} = \sqrt{8\sigma/\rho D} \quad (65)$$

where  $\sigma$  is the surface tension and  $\rho$  is the density of the fluid and  $D$  is the nozzle and fluid column diameter. The droplet size  $d$  may be calculated by equating the droplet volume to the volume of a length of the nozzle cylinder equal to  $\lambda$  and is given by

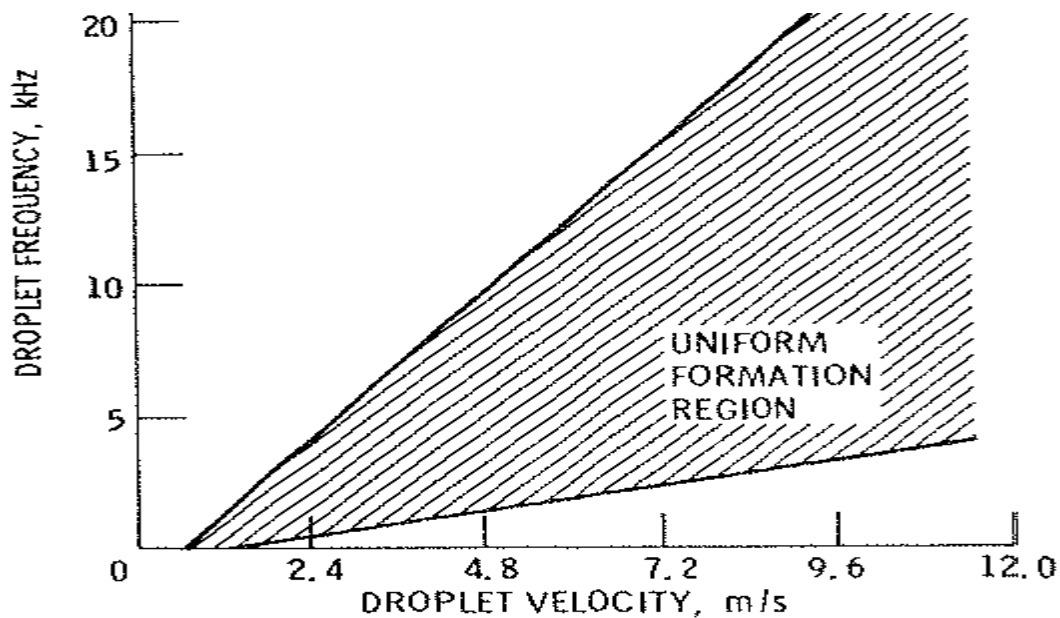
$$d = 1.145\sqrt[3]{\lambda D^2} \quad (66)$$

Since  $\lambda$  must be between  $3.5D$  and  $7D$  for uniform droplet production,  $d$  must lie between  $1.74D$  and  $2.19D$ . None of the equations above impose a limit on the diameter or maximum velocity of generated droplets.

Silicon oil droplet streams of demonstrated diameter and speed are not sufficient to meet the propulsion needs of medium and large tandem LEO satellites without using multiple streams. For large LEO satellites, larger and faster streams than those demonstrated to date offer several advantages. Besides providing more momentum transfer, large and fast droplets are advantageous because they experience less drift due to drag and Lorentz forces, discussed later in this report. Uniform silicone oil droplet stream velocities of up to 100m/s have been demonstrated with droplet diameters of 0.146mm.<sup>71</sup> Slower droplet streams of up to 1mm diameter have also been demonstrated.<sup>6</sup> As shown, the governing equations do not

restrict the diameter or speed of silicon oil droplet streams but demonstrations of faster, larger, uniform streams were not found in the literature.

The chart in Figure 88 contains DC704 droplet stream analysis that shows an expanding range of frequencies compatible with various droplet velocities.<sup>71</sup> This chart reveals that as droplet speed is increased the range of frequencies corresponding to uniform droplet streams is shifted slightly higher. It also shows that the range of frequencies that will produce uniform streams is widened. This is further evidence supporting the viability of producing droplet streams faster than those tested to date. For a given stream velocity and range of droplet production frequency droplet diameter is a function of orifice size. A larger orifice allows more fluid to pass through before the jet is broken by the next pressure wave.



**Figure 88. Uniform Droplet Formation Envelope (from Muntz and Dixon, 1984).**

Electronic micro valve technology has advanced significantly since NASA and the USAF curtailed LDR development work in the late 1980's. Solenoid valves purchased off-the-shelf can now provide an alternative to piezoelectric vibration droplet generation. Such technology offers advantages over piezoelectric generators during the startup or shutdown phase of stream operations when the first and last droplets are created. In a piezoelectric driven system, a column of fluid that is pressurized and beginning to exit the nozzle is disturbed by a pressure wave propagating through the liquid oil medium behind the column. The oil must reach operational pressure in the chamber before exiting the nozzle to achieve the



intended droplet size and velocity. Synchronizing wave propagation and fluid pressurization so that the first droplet has the desired size and velocity is a significant technical challenge that apparently was not addressed by the LDR development program. Since typical LDR transit distances are less than a meter, the amount of off-course drift of a non-uniform droplet is probably not very significant. Drift of a non-uniform droplet that is transiting a kilometer is two orders of magnitude greater and may miss the collector entirely.

There is no theoretical upper limit on droplet size or transit velocity, but faster drops require more pressure. Limited available power and mass limitations for pressure vessels on-board spacecraft impose practical limits on stream velocity. As an example, a 0.15 mm diameter droplet stream generated by USC researchers using DC704 which is less viscous than DC705 (39 cst for DC704 vs. 175 cst for DC705) required a chamber pressure of 500 psi to produce a stream speed of 49m/s and 1400 psi to reach 100m/s.<sup>71</sup> Larger droplets can be generated with larger nozzle orifices which reduces the ratio of flow area to channel surface area reducing shear forces and reducing the pressure required significantly. Reservoir pressures were calculated using droplet generation relationships developed by Muntz and Dixon<sup>71</sup> and applied to DC705. The chamber pressure was adjusted to achieve the desired velocities and accounts for head pressure losses using the Darcy–Weisbach equation. This equation yields a friction factor in terms of the Reynolds number as shown in the following equation.<sup>72</sup>

$$\Lambda = \frac{64}{Re} , \text{ where } Re = \frac{2\rho v r}{\eta} , \quad (67)$$

where:  $\Lambda$  = Darcy Friction Factor equal to the ratio of nozzle exit to entrance pressure (<1)

$Re$  = Reynolds number

$\rho$  = Fluid density (kg/m<sup>3</sup>)

$v$  = Fluid Velocity (m/s)

$r$  = Nozzle orifice radius (m)

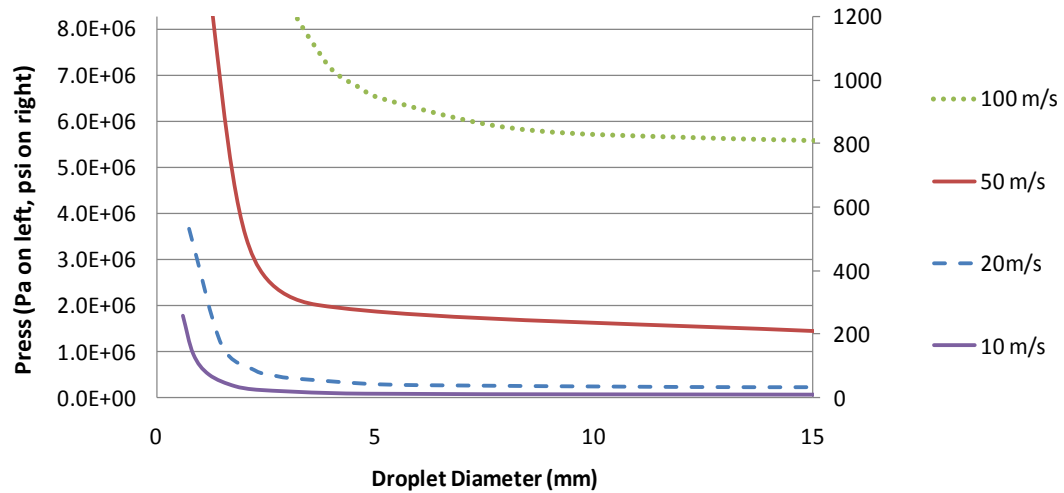
$\eta$  = Dynamic fluid viscosity (Pa·s)

Pressure losses through the nozzle are then given by the equation:

$$P_{exit} = \Lambda P_{enter} \quad (68)$$

Figure 89 shows pressure required as a function of droplet diameter at several stream velocities. Each velocity curve has an inflection point where decreasing droplet diameter results in dramatically increased pressure. Larger droplets require less pressure for a given transit speed which reduces pumping

power required. Lower pressure also limits component mass since containment vessels and feed lines can have thinner wall construction. In most cases, designers will want to select droplet velocity and diameter so as to stay to the right of the inflection points of Figure 89.



**Figure 89. Droplet Velocity and Chamber Pressure for Several Orifice Diameters**

Applying Newtonian fluid power equations to the pressures required to generate velocities between 10 and 100 m/s yields the fluid power required to generate the requisite pressures. Applying gear pump efficiencies of about 80% yields an estimate of the electrical power required to pump fluid for a droplet stream propulsion system.

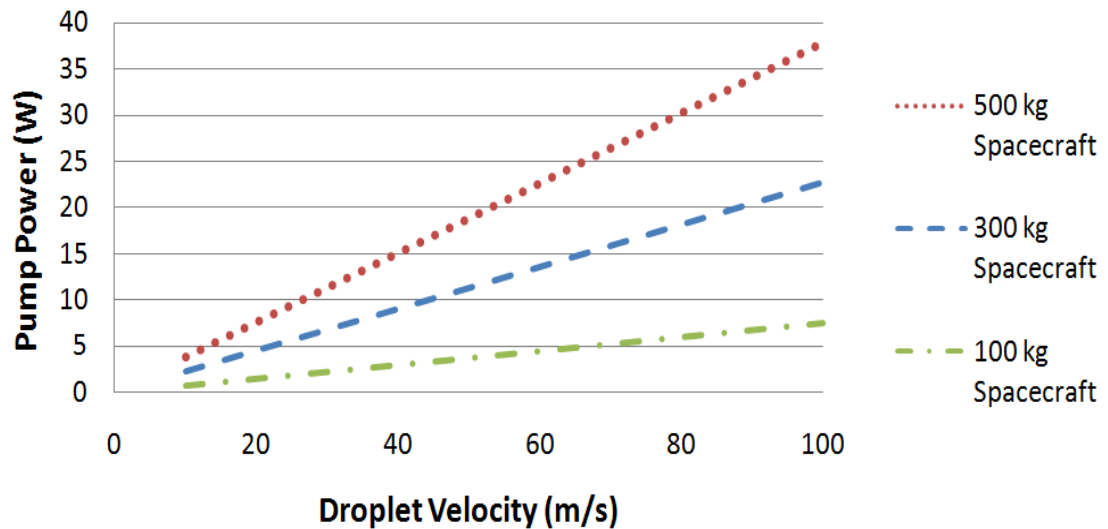
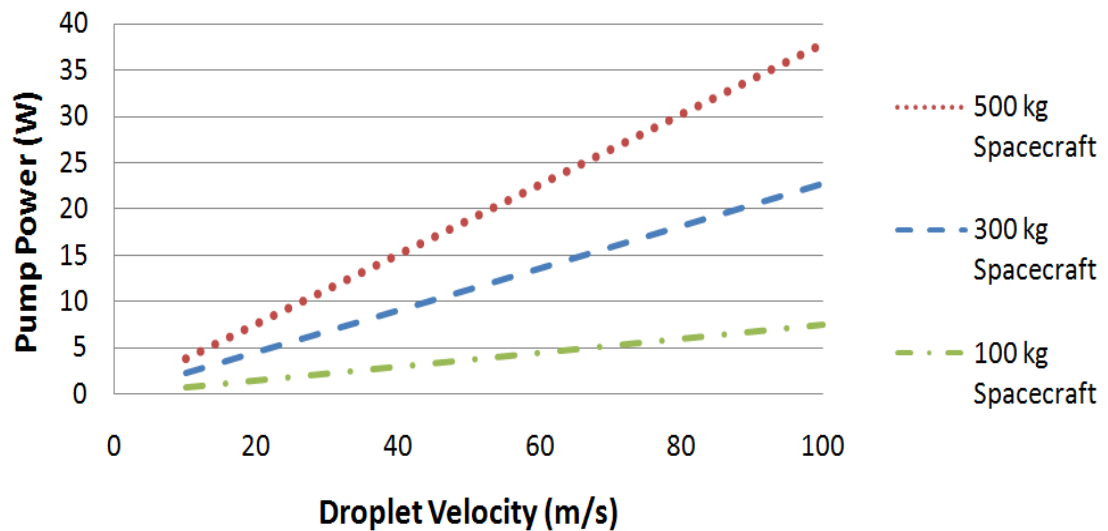


Figure 90 shows power required to run 80% efficient pumps to provide requisite pressures for tandem spacecraft in a 300km orbit. Curves for three spacecraft masses all with 1km separation are shown. The mass shown is the average mass of each spacecraft. For velocities below 50m/s pump power required represents a relatively small portion of the power budget of satellites in the respective class shown. At speeds above 50 m/s power required is significant enough that some spacecraft might need to stop or slow droplet streams to save power.



**Figure 90. Electrical Power Required Generating Fluid Pressures at 1km Spacing in LEO**

When a piezoelectric droplet generator is started disturbance waves must be synchronized with the fluid column emanating from the nozzle. Consequently the first droplet generated has a different diameter than subsequent droplets. These lead droplets will follow different flight paths than the droplets that follow because of the way drag and other forces affect them. This may result in the loss of lead droplets at system startup and resulting loss of fluid or contamination of the receiving satellite by a droplet that is larger or smaller than the rest in the stream. This is probably not a significant problem for a pair of tandem satellites if it only occurs once in the life of the system, however, it may be necessary to suspend operations for a few minutes every time the spacecraft pass through the auroral regions during periods of high geomagnetic activity.

It also may be necessary to interrupt droplet stream production if a droplet generator nozzle becomes clogged, misaligned, or altered slightly by the space environment. Aiming a misaligned nozzle by changing the attitude of the spacecraft might impede collection or increase the likelihood of collision of droplets from opposing streams. In this situation droplet stream operations can continue if streams are sent in one direction at a time. The ability to start and stop stream generation frequently without generation of non-uniform sized leader droplets is possible with micro valve droplet generators. Solenoid valves also make possible, the transfer a single droplet between satellites as a test before attempting to transfer an entire stream. For these reasons, micro solenoid valves are better suited to droplet stream production than piezoelectric driven systems.

Two relatively new types of solenoid valves were chosen for evaluation and droplet generation during experiments in this study. Both valves are made by the Lee Company and were used to produce droplet streams and uniform droplets on demand for experiments done in a vacuum chamber. The valves used in this study can operate at 0 to 1200 Hz, in vacuum, with a pressure differential of up to 827 kPa (120 psi).<sup>73</sup> These valves can operate for at least 250 million cycles allowing a non-stop operating duration at 1 Hz of nearly 8 years. If longer life is needed, several redundant valves can be installed and used in sequence over the life of the satellite. According to a Lee Applications Engineer, similar valves are currently used in operational spacecraft; sealing propulsion feed lines against vacuum.<sup>viii</sup> The Lee valves used in experiments for this study were able to produce droplets in vacuum while supplying pressurized fluid to a vacuum environment at pressures approaching 900kPa (120psi). The valves tested in this study were only operated at 448kPa (65psi) differential pressure whereas pressures as high as 6MPa (850 psi) may be desired to produce droplet streams with velocities of 100m/s. The need for high-speed droplets is diminished if solenoid valve droplet generators are utilized instead of piezoelectric generators because a solenoid generator can produce larger gaps between droplets.

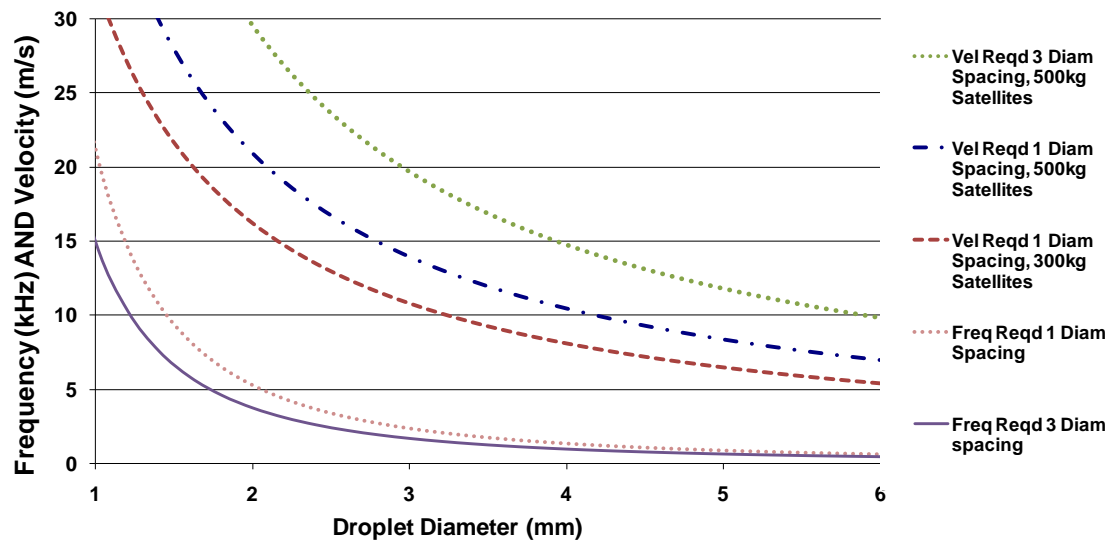
Another advantage of a solenoid valve over a piezoelectric system is that the spacing between droplets can be much greater. Piezoelectric driven droplet generators can only produce uniform droplet

---

<sup>viii</sup> Private Communication with Lee Company Applications Engineer, Mr. Eric Brown.

streams within a certain range of operating frequencies and velocities and the amount of spacing between droplets is restricted to distances slightly less or slightly greater than the diameter of droplets in the stream. In contrast, a solenoid valve can remain closed for any desired length of time between droplets generated. One focus of this study was on the dispersion of droplets caused by electric field interactions between droplets. It will be shown in later sections that this dispersion represents a significant challenge to droplet stream collection at certain stream diameters and speeds. One simple way to combat electric field dispersion is to provide more separation between transiting droplets. A solenoid valve generation system provides spacecraft designers and operators with more flexibility to change spacing between droplets in response to environmental changes or changing mission requirements.

Larger droplets allow slower transit velocities and less drift due to drag and electric field interactions. The chart in Figure 91 shows the velocity required (upper right curves) and the required operating frequency (lower left curves) as a function of droplet size at three different droplet gap distances. The chart shows that tripling the distance between droplets from 1 droplet diameter to 3 diameters increases the stream velocity required to maintain 1km spacing between two 500kg spacecraft by about 50%.



**Figure 91. DC705 Required Velocity and Operating Frequency for a Range of Droplet Diameters**

Another advantage of increased spacing between droplets is a decrease in required operating frequency. This effect is not as pronounced as the decrease in operating frequency that results by increasing droplet

diameter. Figure 91 shows that increasing droplet diameter brings the required operating frequency down from the range of Piezoelectric generators into the range of off-the-shelf solenoid valve technology like the Lee valves used in this study which can operate at 1.2kHz.

There is a significant reduction in required velocity of a 3mm droplet versus a 1mm droplet for maintaining position of two 500kg satellites at 1km. One diameter spacing data is also included for a pair of 300kg satellites showing similar relative velocity reductions. For the 500kg satellites in this particular mission, use of a 3mm droplet instead of a 1mm droplet reduces the required velocity and the required operating pressure to a level where off-the-shelf valves operate currently. The Lee valves used in experiments for this study could generate droplet streams with speeds above 10m/s using just 414 kPa (60psi) reservoir pressure. These valves consume less than 500mW peak power for 3ms to open the valve and then less than 200mW while the valve is held open during droplet formation.<sup>73</sup>

Higher operating pressure valves are on the horizon as evidenced by recently developed micro valves that employ piezoelectric stack actuators bonded onto silicon valve components. Such valves have demonstrated “leak-tight” operation at differential pressures up to 1000psi using just 180mW for continuous operation at 100 Hz.<sup>74</sup> Solenoid valve technology has progressed enough to produce droplet streams in a vacuum with a broad range of diameters, speeds, and gap distances that make them very attractive for use in droplet stream propulsion applications. Yet the valves used for experiments in this study were developed for use in inkjet printers not for droplet stream propulsion. If valve manufacturers turn their attention to designing a valve specifically for droplet stream propulsion it is likely that they will develop valves that can operate at higher differential pressure and a greater range of orifice diameters.

## Appendix 5. Evaporation Losses and Additional Fluid Requirements

GEO satellite propulsion needs are low and can be satisfied by a single opposing pair of droplet streams using already proven stream size and velocity. Droplet streams of demonstrated size and speed extended over a 1km distance require less than 100mL of Silicone Oil in transit at any one time. This volume and mass amounts to less than a half-cup or quarter pound of fluid. The need for additional fluid beyond that which is in transit will be discussed later but, even after accounting for expected fluid loss and extra fluid needed to ensure correct collector and pump operation, the impact of fluid propulsion on a typical GEO satellite's mass budget is quite small.

In LEO where the propulsion need is much greater, the need for larger droplet diameters results in a need for more fluid in transit. The chart in Figure 92 compares fluid in transit over a 1km distance between two 300km LEO satellites. Droplet stream speed has a significant effect on the amount of fluid in transit because slower droplets spend more time in transit and because the slower speed requires more fluid mass to provide the requisite momentum. A transit velocity of only 10m/s requires about 5 liters of fluid in transit to maintain 1km spacing of 500kg satellites whereas a transit velocity of 50m/s has about 70 ml of fluid in transit.

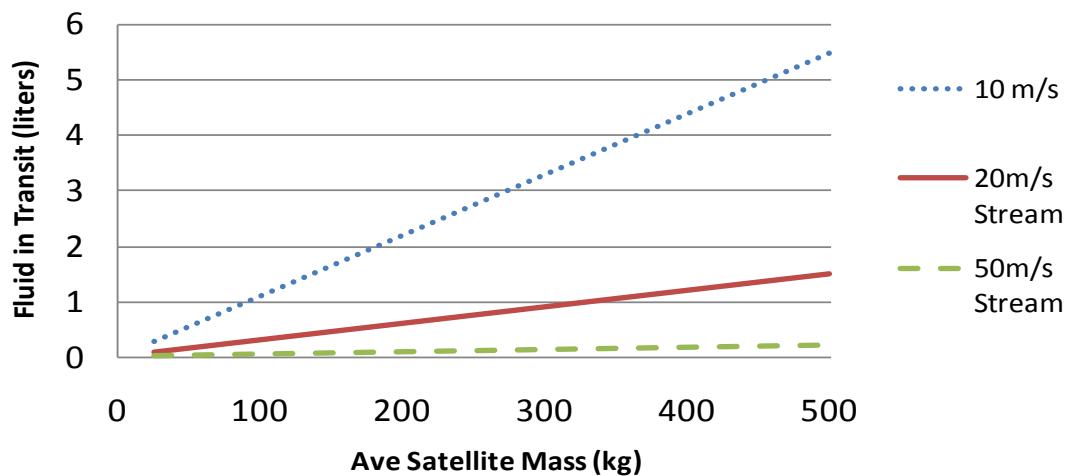
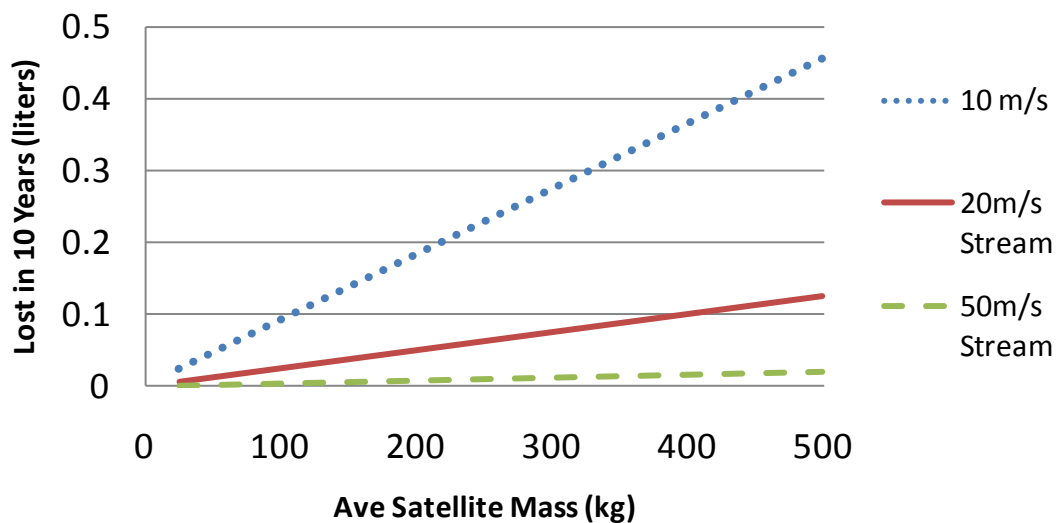


Figure 92. Fluid in Transit 1km Spaced LEO Satellites

In addition to the fluid in transit, standing fluid is needed in the collector to ensure system feed lines remain submerged. There could be as much standing fluid in the collector as there is in transit,<sup>8</sup> doubling the total amount required. Additionally, more fluid is required for circulation between the collector and ejector nozzle and some will probably be employed for thermal control (heat transfer) within the spacecraft. It might even be useful to actively cool the spacecraft with additional fluid streams generated on the end of a boom and directed toward the spacecraft collector. Such a system might reduce overall spacecraft mass by reducing or eliminating the need for radiators and heat pipes. Tagliafico and Fossa<sup>75</sup> showed that an LDR is capable of removing 250-450 W per kilogram of LDR component mass whereas advanced heat pipes are limited to about 66 Watts per kilogram of component mass. An LDR operating in conjunction with a droplet stream propulsion system could share some of the same components, particularly the collector, and may only require about one-fifth the mass of a comparable conventional thermal control system.

Evaporation of DC705 in LEO vacuum conditions was studied by NASA contractors for the LDR program. Testing showed an evaporation rate of 1 stream volume in 30 years at fluid temperatures below 52°C.<sup>6</sup> These LDR estimates of fluid lost due to evaporation are conservative because the droplet diameter used by LDR researchers to determine the evaporation rate is only 0.25mm compared with droplets more than 1mm in diameter primarily considered in this study.



**Figure 93. Loss of DC705 Fluid due to Evaporation in 10 Years for 1km Spacing in LEO**



The surface to volume ratio of typical LDR droplets is 4 times greater than the ratio for a 1mm droplet and 12 times greater than the ratio for a 3mm droplet. Secondly, evaporation estimates are based on a 52°C fluid temperature that results in a vapor pressure that is 4 orders of magnitude higher than DC705 vapor pressure at 25°C. Ignoring the effects of temperature and assuming a droplet diameter of 1mm results in the total fluid losses after a 10-year period shown in Figure 93. The advantage of faster streams is apparent as the fluid amount lost at stream speeds of 50m/s is about 4% of that lost at 10 m/s. This difference is due to the amount of fluid in transit, and time exposed to vacuum, both decrease with higher transit speed.

Based on current LDR designs, it is estimated that about twice the amount of fluid in transit will be needed onboard each spacecraft to account for reservoir and feed line volume. A droplet stream propulsion system will have less feed line length than a conventional LDR design because there is no need to pump fluid from a collector attached to a boom on the spacecraft. Another 10% of transit fluid is needed to account for fluid losses due to evaporation during a 10-year mission.<sup>63</sup> Additionally, it may be necessary to pump fluid directly to the collector to aid in collection of the incoming stream. This could require an amount comparable to two-thirds of the fluid in transit. Adding up all the amounts of fluid needed beyond that in transit yields an amount roughly equal to 3 times the amount of fluid in transit. If the amount in transit needed to maintain 1km separation of two 500kg satellites in LEO at 20m/s is tripled the result is a total fluid mass of 9kg for each satellite. This represents less than 2% of the total spacecraft mass and displaces some mass otherwise needed for a conventional thermal control system.

## Appendix 6. Effects of Drag in LEO

The drag force due to atmospheric particles acting on a surface element of area  $A$ , normal to the object's orbital velocity  $v$ , is quantified by the well known equation:

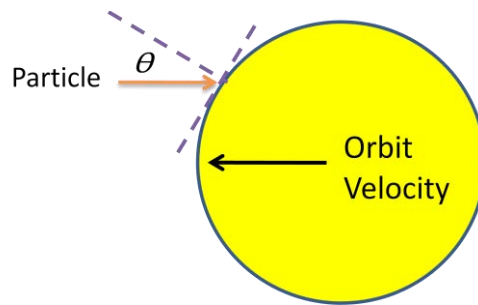
$$F_d = \frac{1}{2} \rho_{\infty} v^2 C_d A \quad (69)$$

where  $\rho_{\infty}$  is atmospheric neutral density and  $C_d$  is a dimensionless drag coefficient defined by:

$$C_d = 2(1 + f(\theta)) \quad (70)$$

where  $\theta$  is the angle of incidence of the impacting particles to the surface normal as shown in Figure 94.

Determining  $f(\theta)$  is difficult because of the nature of atomic collisions. A particle may scatter elastically like a reflection in a mirror (specular reflection) or it may adhere long enough to establish thermal equilibrium with the surface and then scatter randomly (diffuse reflection). Material properties, surface temperature, impacting species type, and other factors all play a role in determining the nature of collisions. The majority of collisions are at least partially diffuse reflections. This makes an analytical prediction of  $C_d$  difficult and experimentally determined  $C_d$  values are usually needed for accurate analysis.<sup>76</sup>



**Figure 94. Angle of Incidence of Particles Impacting a Droplet.**

It is costly and complex to simulate the various species and conditions a material will be exposed to in various space environments in the laboratory. Most accurate assessments of  $C_d$  come from analysis of actual satellites exposed to varying atmospheric conditions that fluctuate primarily with solar cycles. The

liquid radiator program analyzed droplet streams that were typically less than a meter in length. Thus, only a simplified drag analysis of droplet drag was performed for that program using a  $C_d$  of 2.0 which is typical for spherical satellites. For this study, a more accurate analytic prediction was made for transiting droplets at 300km altitude.

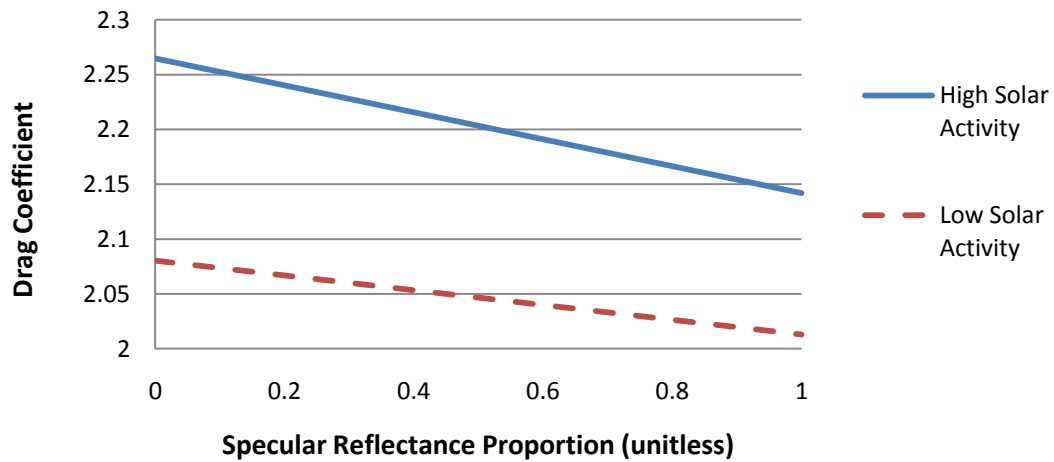
Bird has shown that the drag coefficient,  $C_d$ , for a sphere is approximated by the following relationship:<sup>77</sup>

$$c_D = \frac{2S^2 + 1}{\pi^{1/2} S^3} (e^{-S^2}) + \frac{4S^4 + 4S^2 - 1}{2S^4} \text{erf}(S) + \frac{2(1 - \epsilon)\pi^{1/2}}{3S} \left( \frac{T_w}{T_\infty} \right)^{\frac{1}{2}} \quad (71)$$

where  $T_w$  is the surface temperature,  $T_\infty$  is the free stream temperature and  $S$  is defined by the following equation:

$$S = v_0 \beta \quad S = v_0 \beta \quad \text{where} \quad \beta = \sqrt{M/2kT_\infty} \quad (72)$$

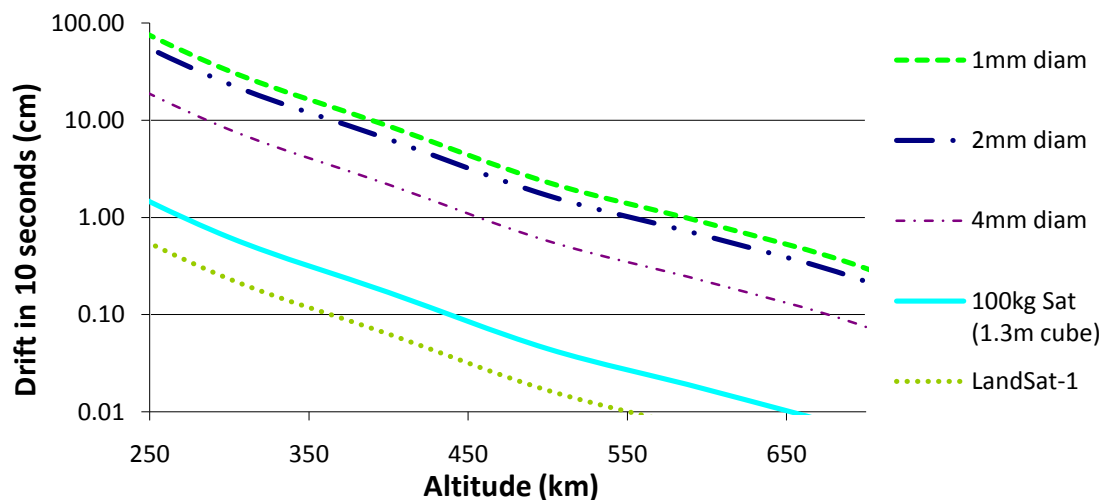
$M$  is the mass of the incoming species and  $k$  is Boltzmann's constant ( $k = 1.38\text{e-}23$  J/K) which relates energy at the particle level and temperature at the bulk level. The values of  $C_d$  were analyzed at 300km where free stream temperature is about 2000K during high geomagnetic activity and the predominant species is atomic oxygen. Drag coefficient is shown as a function of specular reflectance ( $\epsilon$ ) in Figure 95 and is less than 2.26:



**Figure 95. Drag Coefficient vs. Specular Reflectance of Neutrals at 300km**

Small droplets transiting between tandem satellites have a larger ratio of surface area to volume than their host spacecraft. As a result, droplets are affected more by drag and opposing streams in LEO will travel in an arc as they travel between satellites. The amount of drift caused by this drag will vary over time as a function of the atmospheric density that varies with geomagnetic activity and with the altitude of the formation. The effect of drag on the deceleration of DC705 droplets was analyzed for various altitudes in LEO at solar maximum when the atmospheric density is highest at LEO altitudes. A drag coefficient of 2.26 is used which is slightly more conservative than a typical  $C_d$  for a smooth spherical satellite in LEO.<sup>78</sup> Results of this analysis are shown in Figure 96 where droplet deceleration (drift off centerline) during 10 seconds of transit is presented as a function of orbit altitude. The expected deceleration of a small, 1.3m cube satellite and Landsat 1 is shown for comparison.

Deceleration of a 4mm droplet is roughly 10 times greater than that of the satellites considered while a 1mm droplet is expected to decelerate about 80 times more than their host satellites. Droplets less than 4mm in diameter will drift at least 10cm off centerline course in a 10 second period at 300km altitude. This is significantly more than the deceleration on a 100kg, 1.3m per side cube shaped satellite at the same altitude which only moves about half a centimeter due to drag. The drift due to drag at 450km is roughly an order of magnitude less than that at 300km and another order of magnitude lower at 650km.



**Figure 96. Drift off Centerline of Droplets and Satellites Due to Drag During 10 Seconds of Transit**

Drag deceleration of droplets is a compelling reason to operate tandem formations at higher altitudes. However, a droplet transiting between satellites can be aimed at a lead angle that accommodates the drift rate of droplets relative to the satellites. The expected drift rate is predictable since it changes gradually as the atmosphere changes in response to geomagnetic activity. A prototype sensor that can detect the impact location of collected droplets was tested as part of this study and is described in chapter 5. A system of such sensors could detect stream impact location providing feedback to the control system aiming the droplet stream. Such a system might also enable unprecedented accuracy in measurement of atmospheric density as a function of altitude and location in the upper atmosphere.

## Appendix 7. Effects of Solar Radiation Pressure

Droplets transiting between spacecraft will experience a very slight acceleration due to solar radiation pressure (SRP). The magnitude of the acceleration of droplets is the same in GEO as it is in LEO and is in the direction opposite the sun. The magnitude of the force is simply the SRP (4.6 micro Pascals) times the cross sectional area of the droplet  $A$  times the coefficient of reflectivity  $c_r$ . DC705 is translucent with a solar absorptive coefficient, determined in LDR experimentation, of 0.08.<sup>6</sup> The coefficient of transmissivity and reflectivity for DC705 and other candidate silicone oils was not found in the literature but must sum to less than 0.92 since absorptivity is 0.08. Since the fluid transmits visible light transmissivity is more than zero and reflectivity is less than 0.92. Solar pressure was assumed to act in a direction normal to the cross sectional area of the droplet and force was determined using the following equation:<sup>79</sup>

$$F_{SR} = -p_{SR}c_RA \quad (73)$$

where  $F_{SR}$  = Force contributed by the solar radiation pressure,  $p_{SR}$  = Force per unit area exerted by the solar radiation (4.6 micro Pascals).  $c_R$  = Coefficient of reflectivity of the object,  $A$  = Area of the object exposed to the solar radiation.

The table below lists results of an analysis of SRP effects on the drift of two of the smallest diameter droplets exposed to solar pressure for 50 seconds. Coefficients of solar reflectivity  $c_R$  were analyzed between 0.2 and 1.0. Even the slowest (10m/s) and smallest droplets (0.235mm) considered in this study will drift less than 2 centimeters over a 1km transit distance.

**Table 15. Drift of Droplets due to Solar Radiation Pressure in 50 seconds**

Reflectivity	1mm Diameter Drift (cm)	0.235mm Diameter Drift (cm)
0.4	0.22	0.41
0.6	0.25	0.47
0.8	0.28	0.53
0.9	0.29	0.56
1.0	0.31	0.59

Droplets over 1mm in diameter will drift less than 3 mm while transiting one kilometer at the relatively slow speed of 10m/s. These results show that drift due to SRP is very limited especially in droplets with diameters of 1mm or greater and will not play a significant role in determining the requisite collector size.

## Appendix 8. Effects of Atomic Oxygen on Candidate Fluids

At LEO altitudes below about 650km the principle chemical specie is neutral atomic oxygen with a relative kinetic energy of about 4-5eV.<sup>81,32</sup> When an atomic particle is absorbed by the surface of a body in space, energy is transferred from the particle to an atom or molecule on or near the surface of the body. Often, the transfer of energy results in a change in the electronic structure of the atom or molecule impacted. If the transfer of energy is high enough it can lead to the removal of an electron from an atom within the surface material. If energy from the impacting particle is in excess of that required to liberate an electron, that energy may be imparted to the kinetic energy of the now free electron. If this kinetic energy is high enough, the electron may exit the material completely. In more energetic collisions, the impacted molecule is excited into a repulsive state that leads to subsequent dissociation. Sometimes this imparts enough energy to a dissociated fragment for it to break free of the material completely. Dissociation can happen even if the fragment is beneath other surface molecular layers. If this happens in a solid material it may results in loss of the overlying layers leading to erosion of material beyond just the fragment ionized by the impacting particle. This process is called sputtering and can have significant impact on surface material properties in solids.

Sputtering of liquid Gallium-Indium alloy was studied by Dumke, et. al.<sup>80</sup> They found that 85% of sputtered atoms originate in the surface monolayer at atomic oxygen incident energy levels of 15keV while 70% of sputtered atoms come from the surface monolayer when incident energy is 25 keV. They also found that the angle of incidence was important to determining sputtering yield and showed that both liquid targets fit a  $\cos^2\theta$  yield function. These results indicate that sputtering, as a mechanism for removal of surface material occurs in liquids and indicate that DC705 could experience some loss of fluid due to sputtering. Quantifying this loss of fluid will require further study and probably testing of DC705.

A preliminary study of the effects of atomic oxygen bombardment on DC705 was conducted by NASA contractors as part of the LDR program.<sup>81</sup> This study focused on indications of depolymerization of DC705 molecules and found evidence of discoloration of the fluid after high-energy bombardment by ionized and dissociated air molecules with a plasma asher. These samples were then analyzed by infrared spectroscopy to identify molecular changes. This testing revealed the presence of hydroxyl functional



groups in DC705 samples exposed for 43.5 hours. Hydroxyl groups would evaporate in the vacuum environment of the study but the mass of a 2g sample increased 3.5% in this test indicating that hydroxyl groups were attached to larger molecules, possibly directly to DC705 molecules. The same study reported an increase in viscosity of exposed samples but did not quantify the increase. Further testing of atomic oxygen effects on DC705 is certainly warranted before a fluid stream system is employed in space. Such testing was beyond the scope of this study. If testing reveals atomic oxygen to be a significant hazard to DC705 it may be necessary for tandem satellites to operate at high altitude; atomic oxygen densities are significantly lower above 800km.<sup>28</sup>

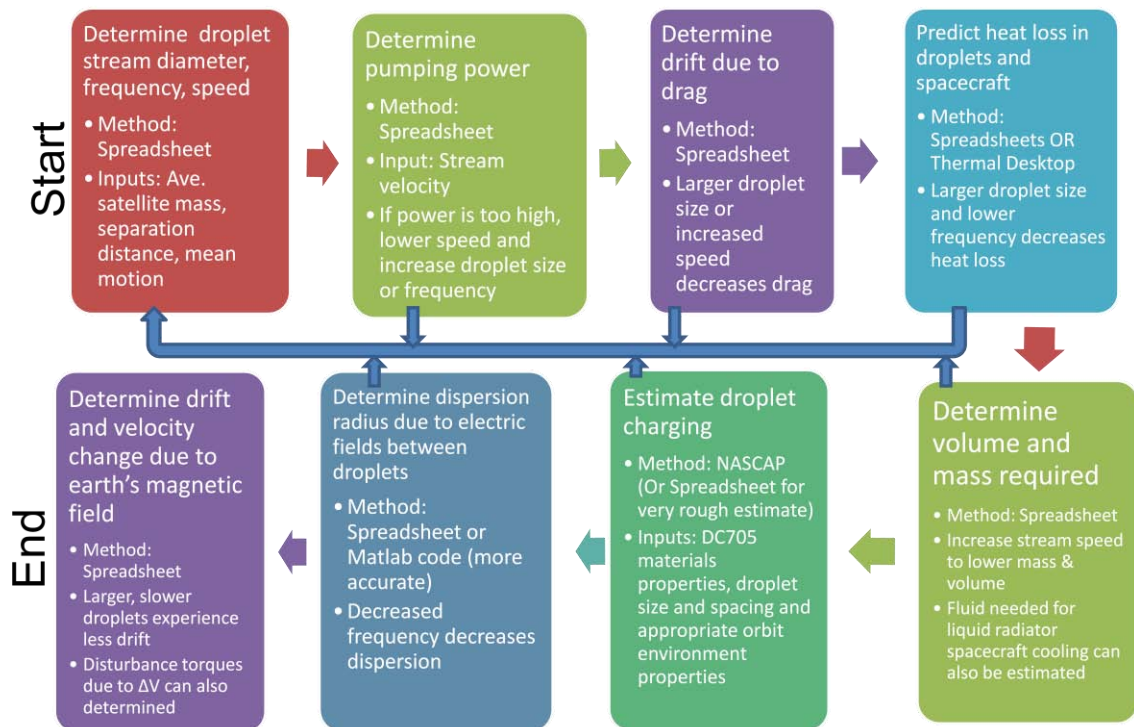
## **Appendix 9: Optimization and Design Tools**

Once it was established that the droplet stream propulsion concept is viable for a range of satellites in several different orbits, an effort was made to establish guidelines for optimizing a droplet stream system to particular missions. This research led to the development and implementation of tools that can be used to select droplet stream parameters that best suit the needs of a specific orbit, satellite pair, and separation distance. Using these tools the optimum droplet stream propulsion system (or at least a range of options) can be determined for a given set of spacecraft parameters that include mass, mean motion, separation distance, inclination, expected mission duration, expected spacecraft (fluid) temperature, and allowable contamination by droplets missing the collector.

Eight different Microsoft Excel spreadsheets were created for analysis of various aspects of droplet stream propulsion. The design process begins by using one of these spreadsheets to identify droplet stream sizes and speeds appropriate to the proposed average satellite mass and separation distance. Next a second spreadsheet is used to determine the pumping power required for the selected stream size and compared to spacecraft power budgets. If the power required is too high, then larger droplets and slower speeds can be selected to lower the pumping power. Once droplet size is selected, a third spreadsheet will determine the amount of drift due to drag and solar radiation pressure. A fourth spreadsheet is then used to predict thermal heat loss in both the droplets and host satellites to ensure droplet size is large enough to avoid freezing of droplets or overcooling of satellites while in eclipse. Two spreadsheets exist for this purpose. One is slightly more conservative than Thermal Desktop modeling and one is slightly less conservative. It is believed that Thermal Desktop will provide the most accurate heat loss prediction and should be employed at some point in the design process. Next, a fifth spreadsheet determines the amount of fluid needed in transit and estimates total fluid needed. This spreadsheet can also be used to estimate fluid volume and mass required to operate additional on-demand cooling of the spacecraft through fluid cooling directly on the droplet collector without transit between satellites.

The next step in the design process is to determine the charge of droplets. A spreadsheet was written to estimate charge using empirical formulas not specific to DC705. This spreadsheet is often accurate to a first order approximation but can be off by two orders of magnitude or more during high

geomagnetic activity. It is recommended that NASCAP be used to simulate droplet charging using the materials properties identified in this study. Once droplet charge is known, a sixth spreadsheet is used to predict a first order approximation of droplet dispersion due to electric field interactions between droplets. If dispersion from centerline is significant, the Matlab code developed to simulate behavior of an entire stream should be used. This code allows selection of the number of droplets allowed to miss the collector over the mission duration and outputs a collector diameter corresponding to a cone radius that is of sufficient multiples of standard deviations to catch all but the specified number of droplets. A seventh spreadsheet will predict off-course drift of transiting droplets due to Lorentz forces induced by Earth's magnetic field. This same spreadsheet can be used to predict changes in transit velocity caused by the Lorentz force and the magnitude of the resulting disturbance torque on the host satellites for comparison to attitude control capabilities. The design process up to this point is described by the flow diagram in Figure 97:



**Figure 97. Design Process for a Droplet Stream Propulsion System**

Once an appropriate droplet stream diameter size, speed, gap distance is determined, the corresponding drifts can be added up to determine the requisite collector size. The drift due to drag can be reduced by aiming the streams with a droplet generator pointing platform or the spacecraft's own attitude determination and control system. Addition of an impact location detection system provides feedback to a pointing system that can compensate for other drift forces. Both of these measures will allow a reduction in collector diameter that can be quantified by using some of the tools just described along with known (or predicted) spacecraft capabilities.

The design process was performed to design a notional system operating at 300km in a polar orbit. Two 500 kg spacecraft were selected with a separation distance of 1km and a mission duration lasting 7 years. It was determined that a 3mm, 27m/s droplet stream with a 33.2 cm collector is suitable for the mission inputs shown in Table 16. This table also gives an estimate of system mass and power requirements and compares these with equivalent parameters for an ion engine propulsion system.

**Table 16. Notional Mission Parameters and Resulting Stream Propulsion Specifications**

Inputs:					
Orbit Inclination	98	Deg	Outputs:		
Orbit Altitude	300	km	Stream Velocity Needed	26.9	m/s
Mission Duration	7	years	Collector Minimum Diameter	33.2	cm
Ave spacecraft Mass	500	kg	Cooling Provided (eclipse)	2.7	W
Separation Distance	1000	m	Cooling Provided (in full sun)	2.4	W
Contamination	0.1	g/year	Propulsion System Mass	16.1	kg
Number of Streams	1	per sat	Radiator Mass Savings	1.2	kg
Operating Frequency	1.2	kHz	No Ion Engine - Mass Savings	80.4	kg
Droplet Diameter	3	mm	Net Mass Savings	81.6	kg
Spacecraft Temp	50	Deg C	Estimated Power Required	14.4	W
	122.0	Deg F	Estimated Power Savings	2057.6	W

The droplet stream system shows significant advantages over ion engines with significantly less mass required and 2 orders of magnitude less power required. These parameters are more in-line with typical mass and power allocations for the propulsion system of a 500kg satellite. For this notional spacecraft scenario, it can be argued that a droplet stream propulsion system is an enabling technology. It is unlikely

that spacecraft designers would be able to provide the power or be willing to allocate the mass needed to perform this mission with ion engines.

## **Appendix 10: Lee Solenoid Micro Valve Specifications**

(next page)



## PRODUCT DATA SHEET

### VHS MICRO-DISPENSE VALVES

The Lee VHS Series Micro-Dispense Valves are high-speed, two-way solenoid valves designed for applications that require microliter and nanoliter dispense volumes such as high-throughput screening and drug discovery.

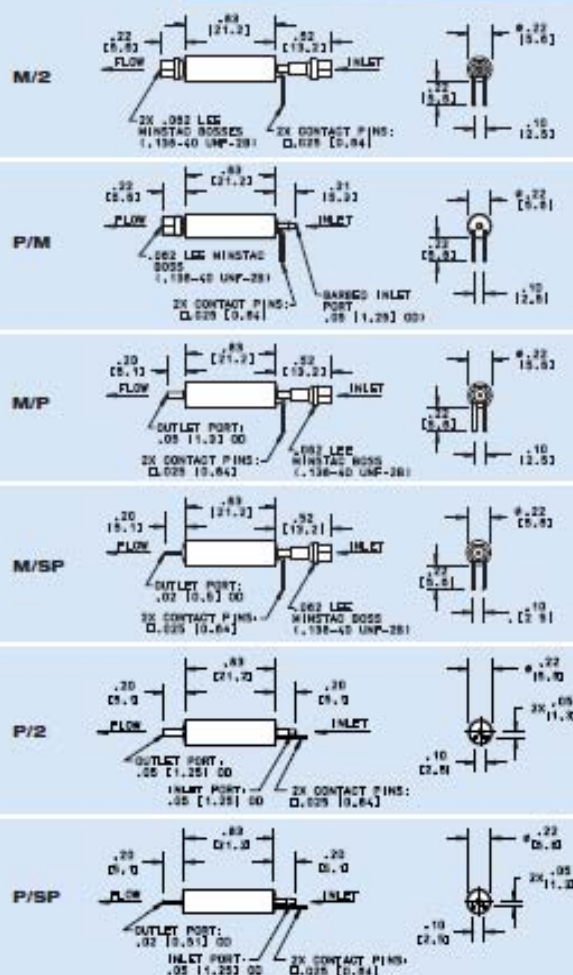
The VHS valves are offered in multiple porting configurations, including 062 MINSTAC® ported models. 062 MINSTAC port options allow simple, compact, leak-proof connections to 0.062" OD Teflon® tubing or direct coupling to Lee 062 MINSTAC nozzles. These nozzles can be removed easily to change the dispense range and offer a broad range of micro-dispense options from a single valve. A special MINSTAC safety screen is also available for "last chance" protection in critical applications.

The VHS valves require a spike and hold circuit for proper operation. Special drive circuits (IECX0501350) and starter kits (IKTX0322000A) are available for lab and prototyping work.

The Lee VHS valves are available in 4 standard seal materials and 2 operating voltages (12 and 24 vdc). However, special configurations such as custom ports and electrical connections are also available. Please contact your local Lee Sales Engineer for additional technical assistance and application information.

MINSTAC® is a registered trademark of The Lee Company.

Teflon® is a registered trademark of Dupont-Dow.



THE LEE COMPANY, 2 PETTIPAUD RD., P.O. BOX 424, WESTBROOK, CT 06498-0424

Tel: 860-399-6281

Fax, Order Entry: 860-399-7058



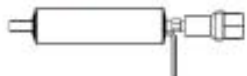
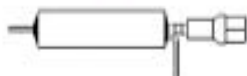

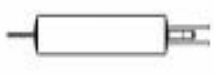

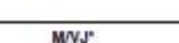
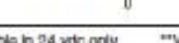

Fax, Technical Information: 860-399-7037

Web: www.TheLeeCo.com

PDS 57 9/05



### LEE VHS MODELS

Configuration	Voltage	Material	Part Number	Ohms	Pressure (psi)	Volume Range**
	12	EPDM	INX0511400A	4,750	120	40+ nl
	24		INX0514300A	4,750	120	
	12	FCR	INX0511850A	4,750	120	
	24		INX0517500A	4,750	120	
	12	PFE	INX0516350A	4,750	10	
	24		INX0514100A	4,750	10	
	12	SI	INX0507900A	4,750	120	
	24		INX0507950A	4,750	120	
	12	EPDM	INX0514800A	4,750	10	40+ nl
	24		INX0514850A	4,750	10	
	12	FCR	INX0508000A	4,750	10	
	24		INX0508050A	4,750	10	
	12	PFE	INX0515000A	4,750	10	
	24		INX0515050A	4,750	10	
	12	SI	INX0508100A	4,750	10	
	24		INX0508150A	4,750	10	
	12	EPDM	INX0511950A	4,750	120	40+ nl
	24		INX0514750A	4,750	120	
	12	FCR	INX0520850AA	4,750	120	
	24		INX0508200A	4,750	120	
	12	PFE	INX0512700A	4,750	10	
	24		INX0516450A	4,750	10	
	12	SI	INX0508250A	4,750	120	
	24		INX0508300A	4,750	120	
	12	EPDM	INX0514900A	11,000	120	10+ nl
	24		INX0514950A	11,000	120	
	12	FCR	INX0514650A	11,000	120	
	24		INX0508350A	11,000	120	
	12	PFE	INX0516200A	11,000	10	
	24		INX0516250A	11,000	10	
	12	SI	INX0516100A	11,000	120	
	24		INX0508400A	11,000	120	
	12	EPDM	INKA1224212H	4,750	10	40+ nl
	24		INKA2424212H	4,750	10	
	12	FCR	INX0508450A	4,750	10	
	24		INX0514550A	4,750	10	
	12	PFE	INX0511900A	4,750	10	
	24		INX0516550A	4,750	10	
	12	SI	INX0508500A	4,750	10	
	24		INX0508550A	4,750	10	
	12	EPDM	INKA1226212H	11,000	10	10+ nl
	24		INKA2426212H	11,000	10	
	12	FCR	INX0508600A	11,000	10	
	24		INX0508650A	11,000	10	
	12	PFE	INX0507000A	11,000	10	
	24		INX0516500A	11,000	10	
	12	SI	INX0508700A	11,000	10	
	24		INX0508750A	11,000	10	
Configuration	Orifice	Material	Part Number	Ohms	Pressure (psi)	Volume Range**
	.003"	EPDM/Butyl	INKA2437210H	110,000	10	10-50 nl
	.005"		INKA2457210H	50,000	10	20-200 nl
	.007"		INKA2477210H	21,000	10	30+ nl
	.003"	EPDM	INKA2438210H	110,000	10	10-50 nl
	.005"		INKA2458210H	50,000	10	20-200 nl
	.007"		INKA2478210H	21,000	10	30+ nl
	.003"	FCR	INX0509100A	110,000	10	10-50 nl
	.005"		INX0509150A	50,000	10	20-200 nl
	.007"		INX0509200A	21,000	10	30+ nl
	.003"	EPDM/Butyl	INX0507150A	110,000	120	10-50 nl
	.005"		INX0509000A	50,000	120	20-200 nl
	.007"		INX0515500A	21,000	120	30+ nl
	.003"	EPDM	INX0508800A	110,000	120	10-50 nl
	.005"		INX0508850A	50,000	120	20-200 nl
	.007"		INX0508900A	21,000	120	30+ nl
	.003"	FCR	INX0509250A	110,000	120	10-50 nl
	.005"		INX0509300A	50,000	120	20-200 nl
	.007"		INX0515350A	21,000	120	30+ nl

\*Available in 24 vdc only      \*\*Values based on water dispense @ 10 psi

THE LEE COMPANY, 2 PETTIPAUT RD., P.O. BOX 424, WESTBROOK, CT 06498-0424

Tel: 860-399-6281

Fax, Order Entry: 860-399-7058

Fax, Technical Information: 860-399-7037

Web: www.TheLeeCo.com

PDS 57 9/05

## Appendix 11: Photodiode Specifications and Output

Monitoring of lamp output at all 5 lamp positions was accomplished using an SXUV series photodiode made by International Radiation Detectors, Inc. (IRD). This  $1\text{cm}^2$  diode has a nearly constant response of  $0.020\text{--}0.022\text{ mA/mW}\cdot\text{cm}^2$  to UV between 90 and 390nm. This sensor has better than 2% uniformity between manufactured sensors and guaranteed response stability of less than 3%.<sup>82</sup> Testing performed by IRD in conjunction with the National Institute of Standards (NIST) showed no discernable change in SXUV photodiodes when exposed to 10 eV photons for several hours. There was no way to measure the accuracy of the particular photodiode received, however a verification of functionality procedure was performed and the photodiode current output fell within the range of expected response.<sup>ix,82</sup> Error in lamp irradiance measured by photodiode was expected to be less than 5% off of actual lamp output.

In reality, lamp output, measured by the photodiode, showed a difference from expected lamp output of 57% to 88% and was consistently higher than the expected lamp output. In Figure 98 predicted lamp output is displayed alongside solar output and measured lamp irradiance levels. The plot shows average photodiode measured irradiance at all five distances tested. The maximum difference from the average is incorporated into the vertical error bar for each lamp position. The first and third lamp positions were associated with the DC705 capacitor experiment while the other three irradiance measurements were recorded during droplet charging experiments.

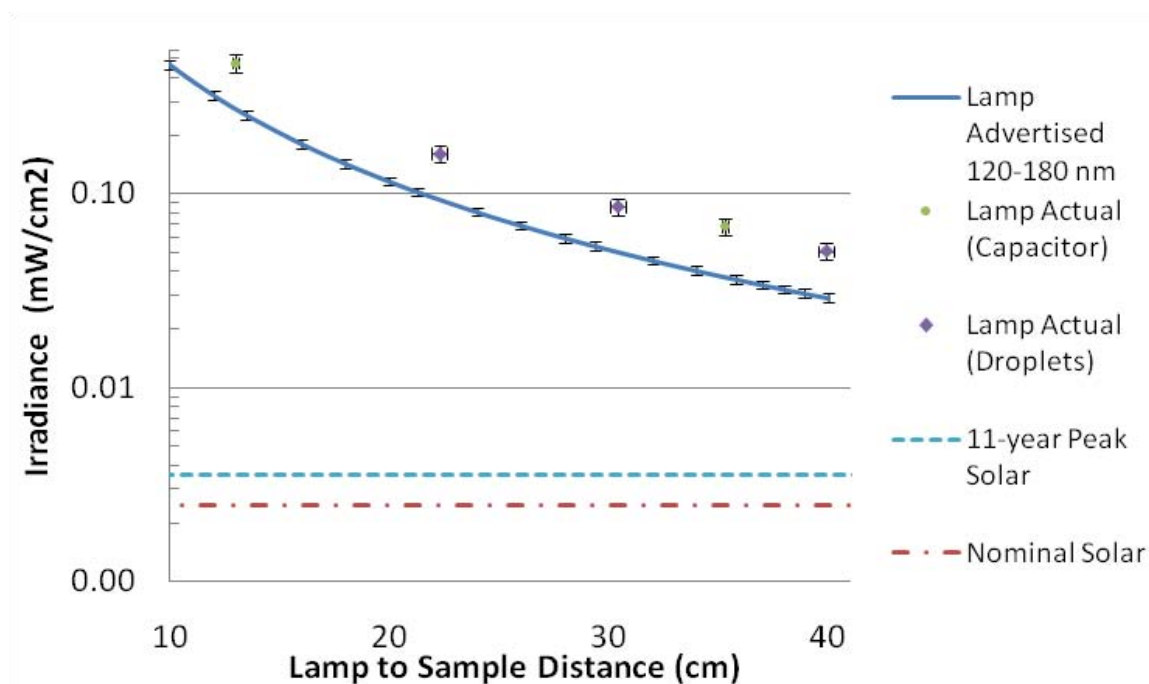
Sample to diode distance was more accurately measured in the capacitor experiment because calipers could be extended directly from the lamp-mounting flange to the diode. In the droplet experiment the diode was positioned in the center of a series of horizontal tubes making it necessary to measure the length of each tube and the distance from the flange edge to the charging path. Measurement error was estimated by measuring each distance three times and using the maximum variation as the range of error expressed in the error bars. Horizontal error bars on lamp output data also account for a  $\pm 0.5\text{mm}$  tolerance on position of

---

<sup>ix</sup> Personal communications with Dr. Raj Korde at International Radiation Detectors, Torance, CA. Aug, 2008.



the Deuterium source described in lamp owner's manual. Vertical error bars account for advertised photodiode response accuracy, and a maximum of 7% variation in advertised photodiode response over the 120-180nm wavelength range.<sup>82</sup>



**Figure 98. Measured and Advertised Lamp Output between 120-180 nm**

One explanation for the difference between observed irradiance and advertised lamp output is a known variation in photodiode response at photon energies near 10eV. National Institute of Standards testing of a similar IRD photodiode at photon energies between zero and 160eV found measured response to be about 1% higher than that predicted.<sup>83</sup> A more likely explanation for the difference between measured and advertised lamp output is that the lamp radiates at wavelengths above the wavelengths for which there is spectral lamp output data. Lamp literature acknowledges that there is irradiance from 115 to 400nm but Hamamatsu only has data for lamp output between 115 and 200nm. An Applications Engineer for Hamamatsu stated that lamp output is believed to drop considerably above 200nm but could not quantify this drop.<sup>x</sup> With a darkened laboratory, there was a faint burgundy colored illumination visible inside the

<sup>x</sup> Personal communication with Mr. Rich Deneen, Customer Support Engineer, Hamamatsu Corporation.

chamber when the lamp was operating. Visible violet light extends from 380 to 450nm and the color burgundy is around 400nm.<sup>52</sup> Thus, there is evidence of lamp radiation at wavelengths between 200 and 400nm that is not accounted for by the advertised lamp output curve but is measured by the photodiode.

If the predicted lamp output of  $0.156\mu\text{W}/\text{cm}^2/\text{nm}$  at 200nm is assumed to extend into the range of wavelengths between 200nm and 400nm the total irradiance at these wavelengths is  $31\mu\text{W}$ , more than double the expected output of the lamp between 120 and 200nm. If average irradiance above 200nm is assumed to drop to about 35% of the 200nm level, the additional irradiance between 200 and 400nm is enough to account for the difference between predicted lamp irradiance from Hamamatsu and irradiance measured by photodiode. Light above 200nm does not charge silicon oil so the light causing higher photodiode response than expected does not affect charging of droplets. For this study, it was assumed that lamp output at wavelengths of interest to droplet charging (below 150nm) matched the advertised spectral lamp output.

During NIST testing of a similar IRD photodiode at photon energies between 0 and 160eV it was noted that, "...measured response is significantly higher than predicted [by the company]." Gullikson et al.<sup>83</sup> report that the difference, "...is likely due to an increasing contribution of carriers (holes) from the oxide [surface in the diode]. The apparent oxide contribution can be very significant in the region around 10 eV." A plot of the NIST test results indicated that the difference was about 10% and the instrument used has a 4% error.<sup>83</sup> 10eV corresponds to a peak in lamp output and a critical portion of the spectrum for DC705 charging in space, however, in terms of total irradiance, 120-130nm represents less than 10% of total lamp output. A 10% increase of 10% of the total spectral output is only a 1% overall increase over advertised lamp output.

---



global TwoPI Rad

```

##### Ask User for stream parameters#####
scenario_name = 'test' %INPUT('Give this scenario a name','s');
d = 2 %INPUT('Input desired droplet diameter in mm (recommend 1 to
4)');
#####freq = INPUT('Input desired droplet production frequency in
Hz (any number from 0 to about 20000 is reasonable, 1200 is max
solenoid freq)');
Volts = 100 %INPUT('Input anticipated droplet voltage potential in
Volts (rec 100 for Polar, 30 for <60 deg inclination LEO)');
T = 7 %INPUT('Input desired satellite mission duration in years');
Orbit = 1 %INPUT('Input 1 for Polar Low Earth Orbit, 2 for LEO
inclined < 60 deg, 3 for GEO ');
L = 1000 %INPUT('Input desired separation distance between satellites
in meters');
Msat = 500 %INPUT('Input spacecraft average mass in kg (mass of one
spacecraft if they have same mass)');
Vdisp = 1e6 %INPUT('Input Std Dev of Droplet velocity dispersion from
Vave 1e-6 is somewhat conservative 1e-7 is possible');
Adisp = 3e-6 %INPUT('Input Std Dev of Droplet Directional dispersion
from straight line to other spacecraft 1e-6 is possible 3e-6 is
conservative');
D = 5 %INPUT('Input number of droplets to analyze (recommend 100)');
Sigma = 7 %This defines the area of the collector - 7 should only
allow ~8 drops lost in 10 years (with only nominal dispersion).

```

```

%%%%%%%%%%%%%%%%%%%%%%%%%%%%%%%%%%%%%%%%%%%%%%%%%%%%%%%%%%%%%%%%%%%%%%%%%%%%%%
%fprintf(outfile,' Echo Check Input Data for:
');fprintf(outfile,'%15s\n\n',scenario_name);
%fprintf(outfile,'      Droplet Diameter              =
');fprintf(outfile,'%12i  mm\n',d);
%fprintf(outfile,'      Droplet Generation Frequency =
');fprintf(outfile,'%12.8f  Hz\n',freq);
%fprintf(outfile,'      Droplet Voltage Potential    =
');fprintf(outfile,'%12.8f  Volts\n',Volts);
%fprintf(outfile,'      Mission Length                =
');fprintf(outfile,'%12.8f  Years\n',T);
%fprintf(outfile,'      Satellie Separation Distance =
');fprintf(outfile,'%12.8f  meters\n',L);
%fprintf(outfile,'      Ave Spacecraft Mass          =
');fprintf(outfile,'%12.8f  kg\n',Msat);
%fprintf(outfile,'      Velocity Dispersion Coef.    =
');fprintf(outfile,'%12.8f  Unitless\n',Vdisp);
%fprintf(outfile,'      Angular Dispersion Coef.      =
');fprintf(outfile,'%12.8f  Unitless\n',Adisp);
%fprintf(outfile,'      Total # Droplets to Analyze   =
');fprintf(outfile,'%12.8f  Droplets\n\n',D);
%fprintf(outfile,'      Sigma to Define Area of Impact Cone =
');fprintf(outfile,'%12.8f  Droplets\n\n',D);

```

```
%%%%%%%%%%%%%%%%%%%%%%%%%%%%%%%%%%%%%%%%%%%%%%%%%%%%%%%%%%%%%%%%%%%%%%%% Convert inputs to working units %%%%%%%%%%%%%%
d=d/1000;
T=T*3600*365;
```

```

%%%%%%%%%%%%%%%%%%%%%%%%%%%%%%%%%%%%%%%%%%%%%%%%%%%%%%%%%%%%%%%%%%%%%%%%%Calculate initial constants and conditions %%%%%%%%%%%%%%%
Eps = 8.85E-12; %%permittivity of free space (c^2/Nm^2)
dens=1097 %%kg/m^3 1097foDC705
Vol_d=4/3*pi*(d/2)^3
mass_d=dens*Vol_d

If Orbit=1 %%Sets min Vave to provide needed thrust in LEO%%
    Vave=1e-6*Msat*L/mass_d/freq
End
If Orbit>2 %%Sets min Vave to provide needed thrust in GEO%%
    Vave=5e-9*Msat*L/mass_d/freq
End
If 2*d*freq>Vave %%Sets velocity to min reqd for selected freq
    Vave=2*d*freq
End

V_Gaussian=randn(1,D); %%Returns a standard distrib pseudorandom values
0 to 1 for dispersion from Vave%%
Angle_Y_Gaussian=randn(1,D); %%Returns a standard distrib pseudorandom
values 0 to 1 for disp from straight line X axis%%
Angle_Z_Gaussian=randn(1,D); %%Returns a standard distrib pseudorandom
values 0 to 1%%

dt = 0.1*(freq)^-1; %%Step time should be smaller than period tween
drops(1/freq) increase to decrease run time but decr to improve
accuracy%%
Q=4*Pi*Eps*(d/2)*Volts; %%Charge=Voltage * Capacity of sphere%%

Vmag(1:D,1)=V_Gaussian*Vdisp+Vave; %%Finds magnitude of intital
velocity%%
Ay=Angle_Y_Gaussian*Adisp; %%Assigns a normal distributed angle in y
dir +/- rad%%
Az=Angle_Z_Gaussian*Adisp; %%Assigns a normal distributed angle in Z
dir +/- rad%%

%% Define initial Velocity %%
Vi(1:D,2)=Vmag*Sin(Ay(1:D)) %%Y comp of velocity intital%%
Vi(1:D,3)=Vmag*Sin(Az(1:D))
Vi(1:D,1)=sqrt(Vmag^2-(Vi(1:D,2))^2-(Vi(1:D,3))^2) %% in X dir is
mag^2-xcomp^2-ycomp^2%%
V=Vi;

%%%%%%%%%%%%%%%%%%%%%%%%%%%%%%%%%%%%%%%%%%%%%%%%%%%%%%%%%%%%%%%%%%%%%%%%% Begin droplet generation and simulating motion
%%%%%%%%%%%%%%%%%%%%%%%%%%%%%%%%%%%%%%%%%%%%%%%%%%%%%%%%%%%%%%%%%%%%%%%%%
t=dt;
n=1; %%1 drop was formed at time 0%%
If t<1/freq*D+trans_time %% If time less than time to make drops and
transit then update position%%
    P(1:n,2:4)=P+V*dt; %% Update Position and output to file%%
    fprintf(outfile,'Droplet Number and Position X,Y,Z (X is
Transit Vector) : ');fprintf(outfile,'%12.8f\n',P);
    %%INSERT Update Velocity with Drop interactions%%

    If P(n,2)>L %%If the position in X dir exceeds transit distance
than send final position to another outfile%%

```

```

        %% ADD fprintf(final_disp_outfile,'Droplet Number and
Position Y,Z (origin is collector center):
');fprintf(final_disp_outfile,'%12.8f\n',P(1:n,3:4));
        Pfinal(n,2,3,4) = P(n,2,3,4);
        P(0:n,2,3,4)=0; %Sets position of drops that would be
        %collected to zero Velocity of these drops should be zero
too
        V(0:n,2,3,4)=0;

%%%%%%%%%%%%%%%%%%%%%%%%%%%%%%%%%%%%%%%%%%%%%%%%%%%%%%%%%%%%%%%%%%%%%%%%Animation%%%%%%%%%%%%%%%%%%%%%%%%%%%%%%%%%%%%%%%%%%%%%%%%%%%%%%%%%%%%%%%%%%%%%%%%
        %% 2 ways to animate this one looked best:
        %% Movie: It becomes more effective to save a predetermined
number of frames as bitmaps and to play them back as a movie. First,
decide on the number of frames,
        nframes = 50;
        %% Next, set up the first plot as before, except using the
default EraseMode (normal).
        Frame = plot(P(3),P(4),'.');
        set(Frame,'MarkerSize',18);
        look=1.2*Sigma_angle;
        axis([-look look -look look])
        axis square %%Try circle!!%
        grid off
        %%Generate the movie and use getframe to capture each
frame.
        for k = 1:nframes
            set(Frame,'XData',P(3),'YData',P(4))
            M(k) = getframe;
        end

        If n<D %%keep making droplets until you reach D (as long as
enough timesteps have passed - see next %%
            If t >or= 1/freq-n %%If the time is greater than the
period btwn droplets MINUS #drops, then add a drop%%
                n=n+1;
            End
        End
    End
End

%%%%%%%%%%%%%%%%%%%%%%%%%%%%%%%%%%%%%%%%%%%%%%%%%%%%%%%%%%%%%%%%%%%%%%%%Output functions%%%%%%%%%%%%%%%%%%%%%%%%%%%%%%%%%%%%%%%%%%%%%%%%%%%%%%%%%%%%%%%%%%%%%%%%
save finalP.dat Pfinal -ascii %creates an ASCII file called finalP.dat
containing

plot(Pfinal(3),Pfinal(4)); %%Plot the final location
    %% The legend command provides an easy way to identify the
individual plots.
    %% legend('sin(x)', 'sin(x-.25)', 'sin(x-.5)')

%%Finally, play the movie 3 times.
movie(M,3)

```

## Bibliography

- Ashley, J., V. Tung, R. Anderson, R. Richie, Inelastic interactions of electrons with polystyrene: calculations of mean free path, stopping powers and CSDA ranges, IEEE Trans Nucl Sci, NS-25, p. 1566, 1978.
- Everhart, T., Simple theory concerning the reflection of electrons from solids, J Appl Phys, 31, p. 1483, 1960.
- Fontheim, E., S. Fung, J. Winningham, Classification of auroral precipitation fluxes by characteristic parameters and their effects on the coupling of the precipitation to the ambient ionosphere. Advances in Space Research 10(6): 183-186. 1990.
- Hakim, R., R. Olivier, H. St-Onge, The Dielectric Properties of Silicone Fluids. IEEE Trans. Electrical Insulation. Vol. 12, pp. 36-370, 1977.
- Jackson, J. Classical Electrodynamics (3rd ed.). Wiley. ISBN 0-471-30932-X. 1998.
- Juhasz, A. , D. Chubb, Design Considerations for Space Radiators Based on the Liquid Sheet (LSR) Concept. NASA Technical Memorandum 105158. Prepared for the 26th Intersociety Energy Conversion Engineering Conference, Boston, Massachusetts, August 4-9, 1991.
- Lord Rayleigh: On the Instability of Jets, Proceedings of London Mathematical Society, Vol. 10, No.4, 1878.
- McAfee, W. Determination of energy spectra of backscattered electrons by use of Everhart's theory. J Appl Phys, 47, p. 1179, 1976.
- NASA Glen Research Center, Thermo Mechanical Systems Branch  
<http://www.grc.nasa.gov/WWW/tmsb/concentrators.html>  
 [accessed Sep 29, 2006].
- Purcell, E. Electricity and Magnetism. McGraw-Hill. ISBN 0-07-004908-4. 1985.
- Stannard, P., I. Katz, L. Gedeon, J. Roche, A. Rubin, M. Tautz, Validation of the NASCAP model using spaceflight data, AIAA Paper AIAA 82-0269, 1982.
- Sutton, G., O. Biblarz, Rocket Propulsion Elements, 7<sup>th</sup> ed. John Wiley & Sons, Inc. 2001.
- Tipler, P., G. Mosca. Physics for Scientists and Engineers (Extended Version) (5th ed.). Freeman Press. ISBN 0-7167-4389-2. 2004.
- Totani, T., T. Kodama, K. Watanabe, H. Nagata, I. Kudo, Numerical and Experimental Studies on Circulation of Working Fluid in Liquid Droplet Radiator. Acta Astronautica, #59 (2006) pp. 192-196. Available On-line 23 May 2006. [www.elsevier.com/locate/actaastro](http://www.elsevier.com/locate/actaastro).

## References

---

- <sup>1</sup> Zink, M., Krieger G., Fiedler H, Moreira L. The TanDEM-X Mission: Overview and Status. Proceedings of the Geoscience and Remote Sensing Symposium, 2007. IGARSS 2007. IEEE International 23-28 July 2007 Page(s): 3944 - 3947
- <sup>2</sup> Tragesser, S. Static Formations Using Momentum Exchange Between Satellites. AIAA/AAS Astrodynamics Specialist Conference, August 18-21, 2008.
- <sup>3</sup> Sandau, R., H. Röser and A. Valenzuela. Small Satellites for Earth Observation. Springer Press, Netherlands © 2008.
- <sup>4</sup> Mattick, A., A. Hertzberg. Liquid Droplet Radiators for Heat Rejection in Space. Journal of Energy 5 (6) (1981) 387–393.
- <sup>5</sup> Muntz, E., M. Dixon, Applications to Space Operations of Free-Flying, Controlled Streams of Liquids. Journal of Spacecraft, Vol. 23, No. 4, July-August 1986.
- <sup>6</sup> White, K. Liquid Droplet Radiator Development status, AIAA Paper 87-1537, June 1987.
- <sup>7</sup> Grumman Aerospace. Liquid Droplet Radiator Collector Component Development AFRPL TR-85-082, 1985.
- <sup>8</sup> Pfeiffer, S. Conceptual Design of Liquid Droplet Radiator Shuttle-Attached Experiment. Grumman Space Systems, NASA Contract Report 185165, October 1989.
- <sup>9</sup> Totani, T., Kodama, T., Nagata, H., Kudo, I., Thermal Design of Liquid Droplet Radiator for Space Solar-Power System. Journal of Spacecraft and Rockets, Vol. 42, No. 3, May-June 2005.
- <sup>10</sup> Santovac 5 Technical Data Sheet. Available on-line: [www.santovac.com/techdata](http://www.santovac.com/techdata) [accessed Sep 27, 2008].
- <sup>11</sup> Comparison of Diffusion Pump Fluids. Varian Inc., Available on-line: <http://www.varianinc.com/cgi-bin/vacpower?cc1=110&cc2=162&classcode3=689&cid=KNNMNPKNFO> [accessed Sep 27, 2008].
- <sup>12</sup> Issikawa, K., K. Goto. Secondary Electron Emissions from Diffusion Pump oils I. Japanese Journal of Applied Physics, Vol. 6, No. 11, November 1967.
- <sup>13</sup> White, F. Fluid Mechanics. 6th Ed. McGraw Hill, © 2009.
- <sup>14</sup> Tagliafico, A., M. Fossa. Liquid Sheet Radiators for Space Power Systems. Proc Instn Mech Engrs Vol 213 Part G. © 1999
- <sup>15</sup> EADS Astrium Corp. Space Propulsion Website: [www.cs.astrium.eads.net/sp/](http://www.cs.astrium.eads.net/sp/) [accessed Sep 29, 2009].
- <sup>16</sup> Dumke, M., T. Tombrello, R. Weller, R. Housley and E. Cirinc, Sputtering of the Gallium-indium Eutectic Alloy in the Liquid Phase. Surface Science. Volume 124, Issues 2-3, Jan 2, 1983. Pg. 407-422.
- <sup>17</sup> Katz, I., D. Parks, M. Mandell, J. Harvey, D. Brownell, S. Wang and M. Rotenberg. A Three Dimensional Dynamic Study of Electrostatic Charging of Materials NASACR-135256



---

SSS-R-77-3367. July, 1977.

<sup>18</sup> Present, R. Kinetic Theory of Gases. McGraw-Hill Book Company. © 1958.

<sup>19</sup> Miyamoto K. Plasma Physics and Controlled Nuclear Fusion. Springer-Verlag Press, Heidelberg. © 2005.

<sup>20</sup> Chen, Francis. Introduction to Plasma Physics. Harper Press, Chicago, © 1984.

<sup>21</sup> NOAA SPACE ENVIRONMENT SERVICES CENTER: Solar Proton Events Affecting the Earth Environment, Preliminary Listing, 1976 – present. Online: <http://umbra.nascom.nasa.gov/SEP/seps.html> [accessed Oct 29, 2008].

<sup>22</sup> Space Environments Office, NASA Marshall, <http://see.msfc.nasa.gov/> [accessed May 29, 2009].

<sup>23</sup> Hastings, D., Garrett, H., Spacecraft Environment Interactions. Cambridge University Press. © 1996.

<sup>24</sup> Eriksson, A.I. and Wahlund, J.E. Charging of the Freja Satellite in the Auroral Zone IEEE Transactions on Plasma Science, Volume: 34, Issue: 5, Part 2, Pgs: 2038-2045 Oct. 2006.

<sup>25</sup> Garrett, H., S. DeForest, An analytical simulation of the geosynchronous plasma environment, Planetary Space Science, 27:1101-09, 1979.

<sup>26</sup> Purvis, C., H. B. Garrett, A. C. Whittlesey, N. J. Stevens, Design Guidelines for Assessing and Controlling Spacecraft Charging Effects, NASA TP 2361, 1984.

<sup>27</sup> Garrett H., A. Whittlesey. Spacecraft Charging Requirements and Engineering Issues. ©AIAA, 2005.

<sup>28</sup> Tribble, A. The Space Environment. Princeton University Press, © 1995.

<sup>29</sup> Chen, F., R. Huddleston (ed.) Plasma Diagnostic Techniques. Academic Press, New York, 1965

<sup>30</sup> Garrett, H. and C. Pike, ed. Space Systems and Their Interactions with Earth's Space Environment. Progress in Astronautics and Aeronautics, Vol 71. AIAA. 1980.

<sup>31</sup> Katz, I., D. Parks, M. Mandell, J. Harvey, D. Brownell, S. Wangand, M. Rotenberg. A Three Dimensional Dynamic Study of Electrostatic Charging of Materials NASACR-135256 SSS-R-77-3367. July, 1977.

<sup>32</sup> Hastings, D., H. Garrett, Spacecraft Environment Interactions. Cambridge University Press. © 1996.

<sup>33</sup> Parks, G. Physics of Space Plasmas An Introduction. 2<sup>nd</sup> Ed. Westview Press. © 2004.

<sup>34</sup> Brebbia, S. Boundary Element Methods, Springer Verlag, New York, 1981.

<sup>35</sup> Huddleston, R. (ed.) Plasma Diagnostic Techniques. Academic Press, New York, © 1965.

<sup>36</sup> Bird, G., Molecular Gas Dynamics. Oxford University Press, © 1976.

<sup>37</sup> Katz, I., D. Parks, M. Mandell, J. Harvey, S. Wang, and J. Roche, NASCAP, A three dimensional charging analyzer program for complex spacecraft, IEEE Trans on Nucl Sci, NS-24,

6, p. 2276, 1977.

<sup>38</sup> McAfee, W. Determination of Energy Spectra of Backscattered Electrons by use of Everhart's Theory, *Journal of Applied Physics*, Vol. 47, p. 1179, 1976.

<sup>39</sup> Issikawa, K., K. Goto, Secondary Electron Emissions from Diffusion Pump Oils. *Japanese Journal of Applied Physics*, Vol. 6, No. 11, November 1967.

<sup>40</sup> Darlington, E. and V. Cosslett, Backscattering of 0.5 - 10 keV Electrons from Solid Targets, *J Phys D5*, 22, p. 1969, 1972.

<sup>41</sup> Frederickson, A., D. Cotts, J. Wall, F. Bouquet, *Spacecraft Dielectric Material Properties and Spacecraft Charging*. American Institute of Aeronautics and Astronautics. 1986.

<sup>42</sup> Feldman, C. Range of 1-10 keV Electrons in Solids, *Phys. Rev.* 117, p. 455, 1960.

<sup>43</sup> Data available online from the Laboratory for Atmospheric and Space Physics Interactive Solar Irradiance Datacenter: <http://lasp.colorado.edu/lisird/LISIRD> [Accessed May, 2009].

<sup>44</sup> Laboratory for Atmospheric and Space Physics at the University of Colorado in Boulder, Colorado. <http://lasp.colorado.edu/sorce/index.htm> [Accessed May 9, 2009].

<sup>45</sup> NASA Goddard Earth Sciences Data and Information Services Center, <http://disc.sci.gsfc.nasa.gov/> [Accessed May 9, 2009].

<sup>46</sup> Koizumi, H., S. Lacmann, Light-induced Electron Emission from Polymethylphenyl Siloxane Oils. *IEEE Transactions on Dielectrics and Electrical Insulation*, Vol. 3 No. 2, April 1996, pg. 233.

<sup>47</sup> Space Environment Information System (SPENVIS) website maintained by the European Space Agency. <http://www.spennis.oma.be/> [Accessed Nov 30, 2009].

<sup>48</sup> Mandell, M., I. Katz, J. Hilton, J. Minor, D. Cooke, NASCAP-2k, A Spacecraft Charging Analysis Code for the 21st Century, AIAA Paper 2001-0957, AIAA Aerospace Sciences Meeting & Exhibit, 39th, Reno, NV, Jan. 2001.

<sup>49</sup> Katz, I., D. Parks, M. Mandell, J. Harvey, D. Brownell, Jr., S. Wang, M. Rotenberg, A Three Dimensional Dynamic Study of Electrostatic Charging in Materials, NASA CR 135256, 1977.

<sup>50</sup> Davis, V.A., B.M. Gardner, M.J. Mandell, I.G. Mikellides, SAIC San Diego, CA. Version 3.1 User's Manual. Prepared for the Space Environments and Effects Program NASA Marshall Space Flight Center Under Contracts #NAS8-00143 and #NNM04AB37C. Report #SAIC 02/2047-R1. July 2005.

<sup>51</sup> Dow Corning Technical Library. Available online. <http://www.dowcorning.com>. [Accessed Nov, 2009].

<sup>52</sup> Serway, R. *Physics for Engineers and Scientists*. 2nd Edition. Saunders College Publishing. ©1986.

<sup>53</sup> NOAA SPACE ENVIRONMENT SERVICES CENTER: Solar Proton Events Affecting the Earth Environment, Preliminary Listing, 1976 – present. Online: <http://umbra.nascom.nasa.gov/SEP/seps.html> [Accessed Jun, 2009].

- 
- <sup>54</sup> Fong, S., N. Black, P. Kiefer, R. Shaw, An Experiment on the Rayleigh Instability of Charged Liquid Drops. *American Journal of Physics*. 75 (6), June 2007.
- <sup>55</sup> Pickett, G. Presentation online: Self Assembly of Charged Polymers 2008. Department of Physics and Astronomy, California State University Long Beach. <http://www.csulb.edu/~gpickett/PhysicsSDSU.pdf> [Accessed Jan, 2009].
- <sup>56</sup> Tipler, P. and M. Gene, *Physics for Scientists and Engineers (Extended Version)* (5th ed.). W.H. Freeman Press, © 2004. ISBN 0-7167-4389-2.
- <sup>57</sup> Pankratz, C. LASP Interactive Solar Irradiance Datacenter (LISIRD). Presentation. Laboratory for Atmospheric and Space Physics (LASP), University of Colorado, Boulder, CO. <http://lasp.colorado.edu/lisird/LISIRD%20AGU%20Fall%202007%20-%20Pankratz.pdf> [Accessed Dec 11, 2009].
- <sup>58</sup> NASA Goddard Earth Sciences Data and Information Services Center GES DISC, <http://disc.sci.gsfc.nasa.gov/> [Accessed Feb, 2009].
- <sup>59</sup> Hamamatsu Corporation, L1026 EUV Lamp users manual. © 2007.
- <sup>60</sup> Jackson, J. *Classical Electrodynamics* (3rd ed.). Wiley. © 1998. ISBN 0-471-30932-X.
- <sup>61</sup> Schneider J. and C. Hendricks, *Review of Scientific Instruments*. 35, 1349 (1964).
- <sup>62</sup> Totani, T., Kodama, T., Watanabe, K., Nagata, H., Kudo, I. Experimental Study on Convergence of Droplet Streams. *Z-Tec Publishing, Bremen Microgravity Science Technology*. XVII-3. 2005.
- <sup>63</sup> Totani, T., M. Itami, H. Nagata, I. Kudo, A. Iwasaki, S. Hosokawa, Performance of droplet generator and droplet collector in liquid droplet radiator under microgravity, *Microgravity Science and Technology* 13 (2) (2002) 42–45.
- <sup>64</sup> Tsuyoshi, T. Masahiro, I. Harunori, N. Performance of Droplet Emitter for Liquid Droplet Radiator under Microgravity. *Transactions of the Japan Society of Mechanical Engineers*, VOL.68; NO.668; (2002) 1166-1173.
- <sup>65</sup> Totani, T., Kodama, T., Nagata, H., Kudo, I., Thermal Design of Liquid Droplet Radiator for Space Solar-Power System. *Journal of Spacecraft and Rockets*, Vol. 42, No. 3, May-June 2005.
- <sup>66</sup> Muntz, E., M. Dixon, Applications to Space Operations of Free-Flying, Controlled Streams of Liquids. *Journal of Spacecraft*, Vol. 23, No. 4, July-August 1986.
- <sup>67</sup> Dixon, M. Droplet Velocity Dispersion Device. *AIAA student Journal*. Spring, 1985.
- <sup>68</sup> Incropera, F.P., Dewitt, D., Bergman, T., Lavine, A.S. *Fundamentals of Heat and Mass Transfer*, Sixth Edition, John Wiley & Sons, © 2007.
- <sup>69</sup> Teagan, W., K. Fitzgerald, Preliminary Evaluation of a Liquid Belt Radiator for Space Applications. NASA CR-174807, 1984.
- <sup>70</sup> J. Stricker and D. Sofer, Monosize droplet stream generator. *Rev. Sci. Instrum.* 62 (12), December 1991. © 1991 American Institute of Physics.

- 
- <sup>71</sup> Muntz, E.P., Orme, M. Characteristics, Control, and Uses of Liquid Streams in Space. AIAA Journal, Vol. 25, No. 5. 1985. Pg. 746.
- <sup>72</sup> White, F. Fluid Mechanics. McGraw-Hill, © 1998.
- <sup>73</sup> Electro-Fluidic Systems Technical Handbook. Release 7.1. The Lee Company. 2008.
- <sup>74</sup> Yang, E., C. Lee, J. Mueller, T. George, Leak-Tight Piezoelectric Microvalve for High-Pressure Gas Micropropulsion. Journal of Microelectromechanical Systems, VOL. 13, NO. 5, OCTOBER 2004 799.
- <sup>75</sup> Tagliafico, A., M. Fossa. Liquid sheet radiators for space power systems. Proc Instn Mech Engrs Vol 213 Part G. © 1999.
- <sup>76</sup> John, J. Gas Dynamics. 2<sup>nd</sup> Ed. Prentice Hall, © 1984.
- <sup>77</sup> Bird, G., Molecular Gas Dynamics. Oxford University Press, © 1976.
- <sup>78</sup> Wertz, J., W. Larson (ed.) Space Mission Analysis and Design. Kluwer Academic Publishers, ©1991.
- <sup>79</sup> Larson, G., J. Wertz, Spacecraft Mission Annalysis and Design.
- <sup>80</sup> Dumke, M., T. Tombrello, R. Weller, R. Housley and E. Cirinc, Sputtering of the Gallium-indium Eutectic Alloy in the Liquid Phase. Surface Science. Volume 124, Issues 2-3, Jan 2, 1983. Pg. 407-422.
- <sup>81</sup> Gulino, D., C. Coles. Oxygen Plasma Effects on Several Liquid Droplet Radiator Fluids. J. Spacecraft, Vol 25, No. 2, March-April 1988.
- <sup>82</sup> User's Manual for SXUV Photodiode. International Radiation Detectors, Torance, CA. Aug, 2008 – Feb, 2009.
- <sup>83</sup> Gullikson, E., R. Korde, L. Canfield, R. Vest. Stable Silicon Photodiodes for Absolute Intensity Measurements in the VUV and soft X-ray Regions. Journal of Electron Spectroscopy and Related Phenomena. 80 (1996). 313-316.